Modeling and Theoretical Design Methods for Directed Self-Assembly of Thin Film Block Copolymer Systems

by

Adam Floyd Hannon

B.S. Physics
B.S. Polymer & Fiber Engineering
Georgia Institute of Technology (2009)

Submitted to the Department of Materials Science and Engineering
in partial fulfillment of the requirements for the degree of

Doctor of Science in Materials Science and Engineering

at the

MASSACHUSETTS INSTITUTE OF TECHNOLOGY

June 2014

Author . . . . . .
Department of Materials Science and Engineering
May 22, 2014

Certified by. . . . . .
Caroline A. Ross
Toyota Professor of Materials Science and Engineering
Thesis Supervisor

Accepted by . . . . . .
Gerbrand Ceder
R. P. Simmons Professor of Materials Science and Engineering
Chair, Departmental Committee on Graduate Students

Modeling and Theoretical Design Methods for Directed Self-Assembly of Thin Film Block Copolymer Systems

by

Adam Floyd Hannon

Submitted to the Department of Materials Science and Engineering
on May 22, 2014, in partial fulfillment of the
requirements for the degree of
Doctor of Science in Materials Science and Engineering

Abstract

Block copolymers (BCPs) have become a highly studied material for lithographic applications due to their ability to self-assemble into complex periodic patterns with feature resolutions ranging from a few to 100s nm. BCPs form a wide variety of patterns due the combination of their enthalpic interactions promoting immiscibility between the blocks and the bonding constraint through their chain topology. The morphologies formed can be tailored through a directed self-assembly (DSA) process using chemical or topographical templates to achieve a desired thin film pattern. This method combines the traditional top-down lithographic methods with the bottom-up self-assembly process to obtain greater control over long range order, the local morphology, and overall throughput of the patterns produced.

This work looks at key modeling challenges in optimizing BCP DSA to achieve precision morphology control, reproducibility, and defect control. Modeling techniques based on field theoretic simulations are used to both characterize and predict the morphological behavior of a variety of BCPs under a variety of processing conditions including solvent annealing and DSA under topographical boundary conditions. These methods aid experimental studies by saving time in performing experiments over wide parameter spaces as well as elucidating information that may not be available by current experimental techniques. Both forward simulation approaches are studied where parameters are varied over a wide range with phase diagrams of potential morphologies characterized and inverse design approaches where given target patterns are taken as simulation input and required conditions to produce those patterns are outputted from the simulation for experimental testing. The studies ultimately help identify the key control parameters in BCP DSA and enable a vast array of possible utility in the field.

Thesis Supervisor: Caroline A. Ross
Title: Toyota Professor of Materials Science and Engineering

Acknowledgments

Life has been a journey with many twists and turns for me, and so many people have contributed to the man I have become. With so many positive influences through the years, a few paragraphs of acknowledgments will surely fall short of fully recognizing everyone that has had an impact on my life. So please forgive me if you read this and do not find your name and feel you had a noticeable impact on my journey to become a doctor of Materials Science and Engineering. Most importantly I want all these blessings that were bestowed on me to go forth to others I come into contact and help others grow and mature just like I have done.

I firstly want to thank my parents Ronny and Alice Faye for raising me in a loving Christian home and teaching me the important things in life and how to truly love others by serving others first forsaking myself. I am grateful for my siblings Lisa, Chuck, and David all being my first set of friends in life and being there to look up to as I grew even though they picked on me a lot being the baby of the family (more so Chuck and David than Lisa). I am very thankful for my Maw-Maw, my only living grandparent, and for my Nanny, who considers me family though she is only technically my siblings' grandmother. I am thankful for my Pop Grover though I only knew him for a short time as he passed away when I was 4 years old. I am thankful for my Aunt Carolyn who in some ways was a second mother to me growing up babysitting me when my parents had to be away. I am thankful for my Aunt Jane and Uncle Ernie, who were very influential growing up. I am thankful for my Aunt Mary Nell and her husband Uncle Richard, and the memories of being with her and my mom growing up. I am thankful too for all my other aunts and uncles, including my Uncle Roger, Uncle Mutt, Uncle Buddy & Aunt Myra, Aunt Ruth, and Aunt Juanita. I am thankful for my many cousins, especially Laura and Jessica, Faye, Kim, Theresa, Joe, Jan, Ricky, Ashley, Keith, and Sheri. I am thankful for the familes of my siblings including Harvey, Christina, and Jill and the nieces and nephews they helped bring into my life including Abigail, Alison, Andrew, Macey, Madison, Mason, and William.

I thank my home church, Sharon Baptist Church, for the support through years and teaching me the values of life, especially the Myers family, the Baileys, the Brooks, the Smiths, the Johnsons, the Harrisons, the Greenes, the Wilkersons, the Banks, the Shoupes, the Foressters, the Pettits, the Gleadalls, the Moons, and Pastor Glenn and his family. I am grateful for my hometown of Loganville growing up and all the people that helped in my growth there. I am thankful for my many friends growing up including Jesse H., Zach H., Alex G., John K., Peter B., Richard G., Dan D., Adam A., Clay N., Nick B., Jenna S., Chelsea P., Emily R., Jenni B., Kerry C., Valerie C., Heather B., Kelsey M., Aleena M., Shanessa F., Kimberly M., Laura B., Charlie Permetus G., Kim A., and Jennifer C.

I am thankful for all the teachers I had through grade school, especially Coach Hobbs in 6th grade math, Mrs. Sue Dado in 8th grade science, Mrs. Perry in 9th grade Honors Biology, Coach Evans in 10th Grade Honors Algebra II, Ms. Sargent in 10th Grade Honors English, Mrs. Luck in 10th grade Latin, Mr. Wisdom in 11th grade Honors Pre-Calculus and 12th grade AP Calculus, Mrs. Hood in 12th Grade AP Literature, and Mrs. Roberts in 12th grade AP Chemistry. I am also thankful for my piano teachers Crystal, Mrs. Charlene, and Mrs. Ree as music has been a major component of my life in inspiring my scientific thought process.

I am very thankful for my undergraduate institution of Georgia Tech (GT) and the community there that helped me to grow into a researcher capable of performing at the level required at MIT. I am thankful for many of my friends at GT including Cale N., Walter M., Lucas R., Anisha A., Jena B., Jordan B., Katie C., Anne C., Haley C., Joyce F., Kate H., Whitney K., Tallulah P., Darlene S., Deborah S., Margaret T., Aaron B., William L., Zach S., and Richard H. I am thankful for my GT professors that taught me the skills I needed for higher level learning, mentored me in my academic studies, and inspired me to pursue lifelong learning including Yonathan Thio, David

Bucknall, Mohan Srinivasarao, Meisha Shofner, Wallace Carr, David Collard, Martin Flannery, James Gole, Ahmet Erbil, Anselm Griffin, Walter de Heer, David Smith, and Deidre Shoemaker.

Since coming to MIT, I've met so many people that have helped me through the five years of perseverance in pursuing this doctoral degree. I am so thankful for my church family at Cambridgeport Baptist Church where the community has been so supportive of me in spiritual growth. I am especially thankful for Pastor Dan and his family, Mama Dot, Tracy W., the Bothewell family, Bill B., Michael D., Brian & Emily W., and Paul & Kristin C. I am thankful for the different members of my Bible study group there during my time in Cambridge including Joel C., Darcy K., Rachel Y., Aaron & Cynthia K., Colton B., Todd & Christa S., Andrew, Amy, & Madeline E., Harriet R., Mike R., Alex M., Becky A., Kunle A., Dawsen Y., Derik F., Sunday T., Kim T., Melanie V., Hannah P., Markus & Christina A., Sharon P., and Karolyn C. I'm thankful for my friends I met in the Graduate Christian Fellowship at MIT including Albert & Amalia A., Eric & Victoria J., Joe & Kayleen M., Ming & Yukkee P., Doug & Samantha S., Annie C., Peng S., Poru L., Charis T., Christina L., Amanda S., Sam E., David M., Asa A., Andrew B., Nigel C., Mark K., David K., John L., Gerald P., Louis T., Tunde A., Jonathan B., Courtney J., Andong L., Dan M., Angie A., Anya B., Katie R., Joyce Z., Janet C., Charlene C., Diana F., Diana J., Alice K., Alli H., Megan J., Becky T., Helen W., and Kevin F.

I am grateful for my roommates at Tang Hall my first few years including Andrew S., Yulei S., Pat S., Eugene S., Ben J., and Jame D. I am thankful for other friends from Tang including Nan L., Eric M., and Xiaoyu W. I am thankful for my wonderful roommates from my last two years who have become brothers to me in George K., Keith L., Sam P., and S. Yong. I am very thankful to Marcus & Emily G. for being such great friends and for getting married at such a convenient time for me to move into his old apartment. I am thankful for my sisters in Tang of Heather B., Michelle C., Wei-Shan C., and Stephanie L. for letting me hang out at there place all the time and playing games with me. I am thankful for Pete D., Fabrice K., and Brandon S. for studying the Bible with me one semester. I am thankful for Aaron B., Phil N., and Justin M. for the fun nights playing MTG and for Sam G. putting up with us when we played at Justin's place.

I am thankful for all the friends I made in DMSE including Charles & Michelle S., Reid V.L., Richard B., Jordan C., Tim Z., Sabrina Y., Billy W., Jon S., Sophie N., Adam J., Jane W., Jongho K., Satoru E., and Liz R. I am grateful for the members of the Ross group I befriended with whom I did not directly work including Mehmet O., Dong H.K., Nicolas A., Mark M., Juan M., and Jean C. I am thankful for my friends and coworkers in my research who enabled a lot of the projects presented in this thesis including Rafal M., J.G. S., Amir T.K.G., Sam N., J.B. C., Professor Karl Berggren, Brent K., Hsieh C., Y.J. K., Yi D., Hong K.C., and Karim, R.G. I am very thankful for Wubin B. being such a great friend and coworker. I am especially thankful for Kevin G. being a great friend and coworker and the support of his loving wife Susan and two daughters and them letting me come over to hang out.

I am very grateful for the various financial sponsors of my research through my five year tenure at MIT including the Office of Naval Research, Semiconductor Research Corporation, Taiwan Semiconductor Manufacturing Corporation, Global Foundries, and the National Science Foundation.

I am thankful for my MIT professors that guided me through my first few years and with whom I had classes or TAed under including Gerbrand Cedar, Samuel Allen, Robert Cohen, Jeffrey Grossman, and Polina Anikeeva. I am very thankful for Professor Alfredo Alexander-Katz guiding me in understanding the fine nuances of SCFT without which this thesis would not have been possible. I am also very thankful for my advisor Professor Caroline Ross for giving me the opportunity to take on the research projects contained in this thesis and for all her support, advice, and mentorship without which I would not have been inspired to examine the block copolymer systems I did nor been able to do so. Ultimately I thank God, the creator of the universe, so that we are even here to study these complex systems examined in this thesis.

Contents

List of Figures

List of Tables

Chapter 1

Introduction and Motivation

1.1 Motivation and Outline of Thesis

Block copolymers (BCPs) have become of great interest for lithographic applications over the past decade due to their ability to self-assemble into high resolution patterns with $\approx 10 - 100$ nm periodicity[1–28]. This range of features sizes makes BCPs a prime candidate for the fabrication of next generation patterned media and microelectronic devices to continue the trend of "Moore's Law"[29] since the current methods for producing features on the low end of this size range, 193 nm immersion lithography, is limited to ≈ 25 to 30 nm features[30] while electron beam lithography (EBL) can reach ≈ 5 to 10 nm size features but is limited by throughput[31]. The patterns produced from BCP systems can be used for the fabrication of a variety of devices including nanowires, filtration membranes, graphene ribbon transitions, flash memory, and patterned magnetic recording media[32–39]. Traditional photolithography methods can only reliably produce features toward the middle of this range[30]. BCP self-assembly alone can only produce the necessary feature sizes needed for next generation nanolithographic processes, but cannot achieve the long range order and precise pattern placement necessary for fabricating memory storage and integrated circuit devices. To achieve such results, directed self-assembly (DSA) uses the combination of the bottom-up BCP self-assembly with other top-down patterning processes to achieve the local morphology control and long range order needed.

The goals in nanolithography ultimately are to manufacture nanoscale devices using a large enough throughput, extremely small resolution of features, low cost materials and processes, high reproducibly in the generated patterns, and locally complex structures. Techniques such as extreme ultraviolet (EUV) photolithography, nano imprint lithography, and EBL address these different goals to some extent with some more than others, but

none all optimally. Although EBL can generate arbitrary patterns with very small resolution, throughput yields are quite low and the overall process is quite expensive. On the other hand, EUV photolithography has great reproducibility and high throughput, but can only resolve features ≈ 30 nm at best, is somewhat costly, and is limited by the original patterned generated since the process replicates a pattern from a mask. Similarly, nano imprint lithography has advantages in great reproducibly with high throughput, but the original stamp must be produced via another nanolithographic technique such as EBL.

BCPs have the potential to solve these problems as they can produce a large surface area of features in a single spin casting step in thin film systems, their feature size limit can be reduced by increasing the Flory-Huggins interaction parameter χ and lowering the degree of polymerization N[40–43], are generally quite cheap to synthesize, and locally complex features can be reproduced using appropriate thermal and/or solvent annealing conditions with appropriate topography and/or surface chemistry[5,6,44,45]. Here DSA is required to fully access these benefits of locally complex and reproducible features in producing the topographical or chemical templates.

BCP DSA is still considered an emerging technology according to the International Technologies Roadmap for Semiconductors with industrial implementation coming along slowly due to precise morphological control, pattern reproducibility, defectively, and noninvasive metrology needing further study[46,47]. One way to address these problems is by using simulation methods that reduce experimentation time and costs to determine the DSA boundary conditions necessary to achieve a given optimized reproducible target structure[48].

Self-consistent field theory (SCFT) simulations have been the standard simulation tool for modeling BCP systems, allowing the prediction of what equilibrium morphologies will form under various boundary conditions reflecting a variety of DSA surface chemistries and topography[49]. Now through the use of inverse design optimization algorithms, the development of DSA templates is now achievable as well for a given target morphology[50,51]. Thus these simulations methods are starting to allow for the design of arbitrary target structures limited only the essential pattern components chosen to build up the target structures. This thesis examines these simulation methods, how they have been applied to

various BCP DSA systems and annealing conditions, how they can be applied to other similar systems, and how they can be improved and optimized.

This chapter examines the general concepts of BCP self-assembly. The general principles used in the simulations and modeling approaches for these systems are explored through the basic thermodynamic criteria used in studying them. Experimental processing and annealing methods used to reach equilibrium structures in BCP thin films are examined. General concepts of DSA are explored as well.

Chapter 2 details all the important nuances of the SCFT simulations implemented in finding equilibrium and metastable morphologies. Various partition functions of interest for thin film BCP systems are examined. Relaxation schemes for reaching the final states of interest are presented and discussed. Methods for solving the underlying differential equations involved in calculating the partition functions in the simulation are presented. How boundary conditions are implemented for a variety of physical systems is also discussed.

Chapter 3 looks at ways solvent vapor annealing (SVA) has been used in particular to reach a variety of thin film morphologies with high tunability. The experimental methods used to perform such annealing are first examined. Two approaches to modeling the SVA system is then examined; an implicit model is first examined where effective physical parameters are used for computational simplicity and then an explicit model is examined where solvent added is modeled as a separate species in the simulation at the cost of increasing simulation parameter space. Simulation results are then compared with experimental results.

Chapter 4 looks at thin film systems with no topographical templating or DSA effects. Both two dimensional (2D) and three dimensional (3D) simulation results are explored for a variety of substrate surface energy conditions. Results are compared with experimental observations where appropriate.

Chapter 5 looks at many different kinds of DSA templating effects on thin film systems. Hierarchical templating using topographical patterns generated from other BCP thin films are examined using 3D simulations and compared with experimental results. Studies using hexagonal arrays of post are examined in both 2D and 3D simulations and

those results compared with experiments as appropriate. Rectangular arrays of posts used for templating the BCP thin films are examined in 2D and 3D simulations and compared with experimental results. BCPs confined in square and circular holes are examined as well in 2D and 3D simulations and compared with experimental results where appropriate.

Chapter 6 examines an inverse design algorithm used to develop DSA templates for complex target structures. A comparison is made with this approach and a general design rule approach. The inverse design algorithm itself is presented in full nuanced detail. Results using the algorithm for a variety of target structures in 2D simulations are compared with experiments. Suggested modifications for the algorithm are presented and discussed.

Chapter 7 concludes this thesis by examining potential future work that can be done based on observations in these studies and limitations encountered in current methodology. Studying dynamical SCFT simulations are proposed to try to capture kinetic effects not captured in the current relaxation schemes. Suggestions are made for examining multicomponent systems such as triBCPs with three distinct blocks for reaching a more diverse morphology set. Potential approaches to modeling nanoparticle containing systems are proposed. Additionally, suggestions for making more detailed experimental comparison of simulation results possible through new characterization techniques are explored.

1.2 Introduction to Block Copolymers (BCPs)

BCPs are polymers that are composed of at least two distinct chemical monomers each making up a long segment blocks of the chain[40,41]. Many potential architectures of BCPs are possible depending on how the blocks are covalently bonded and are shown in Figure 1.1.

Since the different blocks normally have dissimilar chemistry, there is generally a positive enthalpy associated with the blocks trying to mix making them immiscible. Coupling this with a low free energy contribution from entropic mixing since the number of possible spatial configurations is reduced in polymer systems due to the monomers being connected along the chain, micro phase segregation occurs below an order-disorder

transition (ODT) temperature. For a system of two homopolymer blends, the normalized Gibbs free energy of mixing ΔG_{mix} from the Flory-Huggins theory of mixing is given as

$$\frac{\Delta G_{mix}}{kT} = \frac{f_A}{N_A}\ln(f_A) + \frac{f_B}{N_B}\ln(f_B) + f_A f_B \chi$$

where k is Boltzmann's constant, T is temperature, f_A is the volume fraction of the minority blend component, f_B is the volume fraction of the majority blend component, N_A is the degree of polymerization of the minority component, N_B is the degree of polymerization of the majority component, and χ is the segemental Flory-Huggins interaction parameters between the two species[43].

By examining the condition where the chemical potential is both a saddle point and inflection point, the observation is made that for a homopolymer blend with equal degrees of polymerization, micro phase separation will occur for $\chi N > 2$ when $f_A = 0.5$. For a diBCP, the above equation no longer applies in terms of the entropic contribution being further constrained by the covalent bonding between the two blocks; this effect results in the critical $(\chi N)_{crit}$ of BCP for micro phase separation to be higher than the equivalent homopolymer blend system. For a symmetric diBCP $(\chi N)_{crit} \cong 10.5$ while for an ABA triBCP system is $(\chi N)_{crit} \cong 18.0$, with N now designating the total length of the copolymer chain[40,41,52].

Full macro phase separation cannot occur in BCP systems like in homopolymer blends because of the covalent bonding between blocks, so ordered structures form instead with natural periodicities designated by the length L_0 on the order of the radius of gyration R_g of the polymer. For diBCP systems, this period is given as $L_0 \cong \sqrt{6} R_g (\chi N)^{\frac{1}{6}}$ in the high χN regime. In the bulk form of diBCP systems, structures such as close-packed spheres, hexagonally packed cylinders, cubic gyroid, and lamellae are all possible depending on the volume fraction f_A and χN. Both SCFT simulation studies and experiments have explored and documented the theoretical phase diagram for bulk diBCPs as shown in Figure 1.2[42,52].

When examining thin film BCP systems, additional free parameters become available that affect the final morphology formed. These parameters include the film thickness t and the air polymer surface energies for both blocks $\gamma_{A/air}$ and $\gamma_{B/air}$ as well as

the substrate polymer surface energies for both blocks $\gamma_{A/sub}$ and $\gamma_{B/sub}$. This leads to the formation of phases such as perforated lamellae phase over gyroids compared with the bulk or a differentiation between perpendicular and parallel to substrate morphologies in cylinders and lamellae. These additional parameters give greater control over what morphologies are formed from a given copolymer sample as they can be varied locally on a sample through surface chemistry or topography treatment to affect local morphological behavior making hybrid morphologies on the same sample as shown in Figure 1.3 for different surface chemistry conditions.

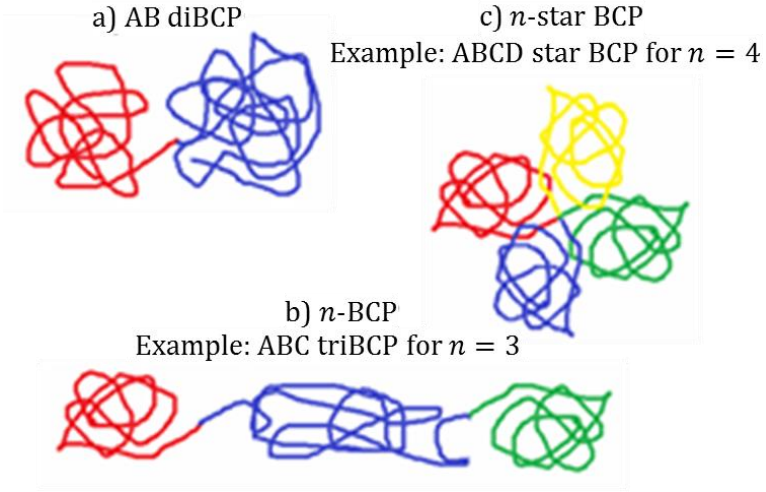

Figure 1-1: Potential BCP architectures: a) a simple diBCP with two distinct chemical blocks connected via a single covalent bond, b) a more general linear *n*-BCP with *n* segments covalently bonded in a series fashion (here specifically a triBCP with *n* = 3), c) an *n*-star BCP where the covalent bonds of the *n* blocks branch out from a central location in the copolymer (here specifically a 4-star BCP with *n* = 4).

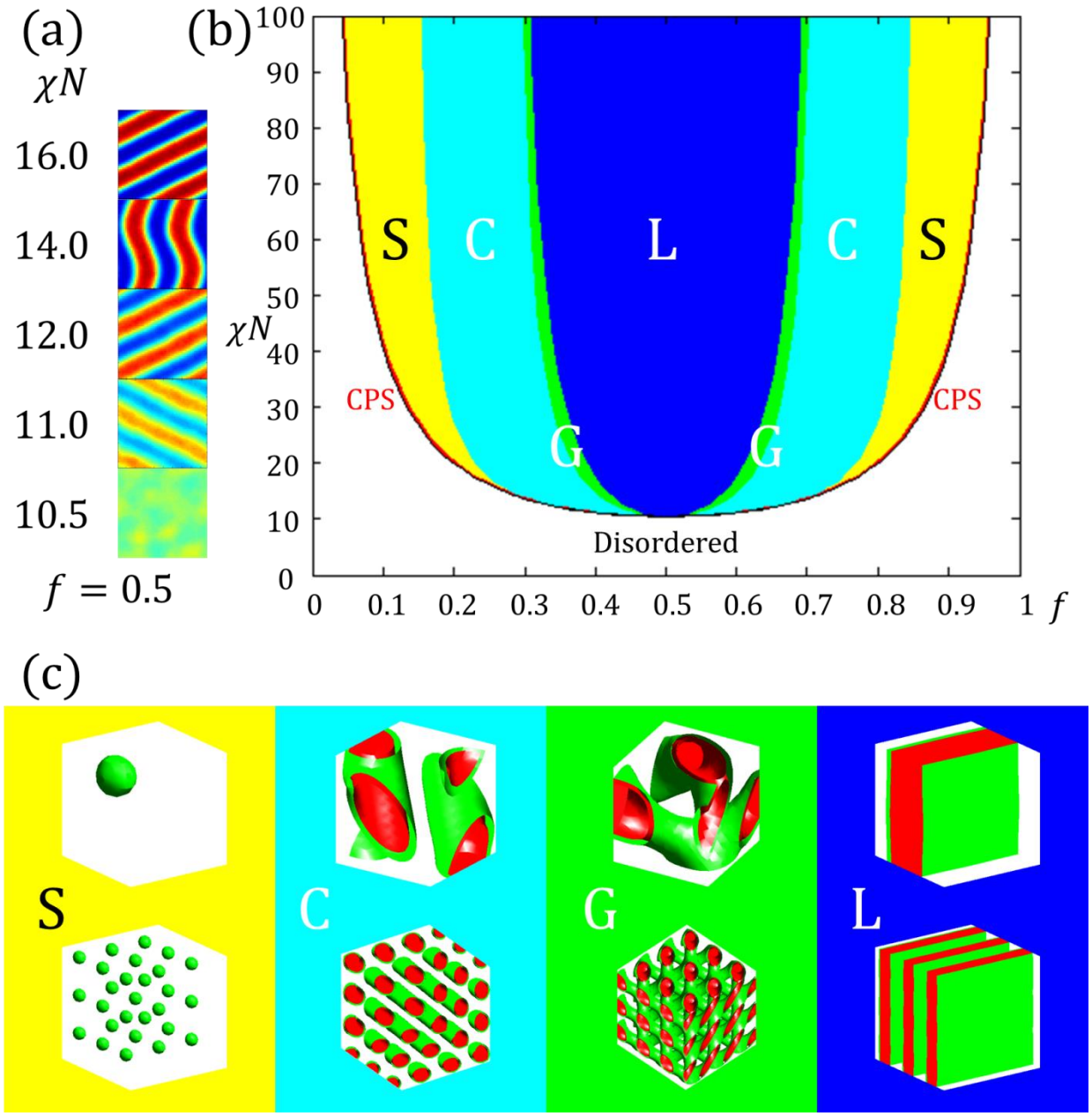

Figure 1-2: (a) 2D SCFT simulation results that show the transition from disordered phase at χN = 10.5 to ordered lamellae as χN increases for f = 0.5. Red regions are A rich and blue regions B rich. (b) Bulk diBCP phase diagram. S stands for sphere (yellow), C for cylinder (teal), G for gyroid (green), L for lamellae (blue), and CPS for close-packed spheres (red)[42]. (c) 3D SCFT simulation results for S, C, G, and L with top image being a single unit cell and bottom three unit cells concatenated for clarity seeing overall structure. Green regions are boundaries between A and B blocks and red regions are A rich regions.

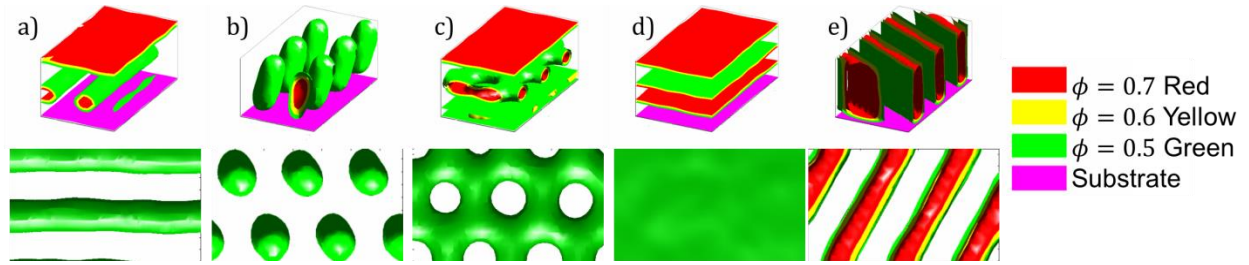

Figure 1-3: SCFT results showing possible morphologies under a variety of surface energy conditions and film thicknesses. The top images show a side angle tilted view of the 3D structure of the thin film and the bottom images shows a top-down cut through view of the structure. The plots show isosurfaces of the local normalized density ϕ of the minority block with red being 0.7, yellow 0.6, and green 0.5. Purple indicates the substrate in the side view images. a) Majority block preferential substrate and minority block preferential air interface results in parallel to the substrate cylinders with χN = 14.0, f = 0.34, and t = $1.5L_0$. b) Neutral preferential substrate and air interface results in perpendicular to the substrate cylinders with χN = 14.0, f = 0.32, and t = $1.5L_0$. c) Minority block preferential substrate and air interface results in perforated lamellae with χN = 14.0, f = 0.40, and t = $2.0L_0$. d) Majority block preferential substrate and minority block preferential air interface results in parallel to the substrate lamellae with χN = 14.0, f = 0.5, and t = $1.5L_0$. e) Neutral preferential substrate and air interface results in perpendicular to the substrate cylinders with χN = 14.0, f = 0.5, and t = $1.5L_0$.

1.3 Modeling and Theory

In order for a model to capture the necessary physics to simulate realistic behavior of BCP systems under a variety of conditions, the underlying thermodynamics variables governing how BCPs behave need to be identified and measured experimentally. As already mentioned, the core set of control variables in thin film self-assembly for diBCPS have been identified as χ, N, f, $\gamma_{A/air}$, $\gamma_{B/air}$, $\gamma_{A/sub}$, $\gamma_{B/sub}$, and t. Thus whatever model one uses to study the system should incorporate these variables or make assumptions about why the variables are not being explicitly considered.

Here two main approaches for modeling BCP systems are presented. In the first approach, analytical free energy models are derived for various morphologies and compared under a variety of conditions to determine which morphology is the lowest energy equilibrium structure. In the second approach, SCFT simulations are performed that use a single chain partition function model of a copolymer chain to calculate an equilibrium structure for a given discretized unit cell without prior knowledge of the final state.

1.3.1 Free Energy Comparison

For situations where potential morphologies BCPs self-assemble into are known, free energy models can be developed to distinguish what conditions cause those morphologies to have the lowest free energy. In these models, there are generally two key components: a surface energy component based on the interface between the blocks and a chain stretching component based on strain induced on the system.

As a simple example, a rough estimate of the locations of the strong segregation (high χN) transitions between body centered cubic (BCC) spheres to hexagonal close-packed cylinders to lamellae morphologies can be calculated just using the free energy of the bulk unit cell assuming no external strain is applied to the system. In these calculations, the natural period length L_0 is assumed to be constant for all three phases due to the system being in the strong segregation regime and thus the chains are strongly stretched. The surface free energy of the system will in general be of a form $F_{sur} = \gamma_{AB} A_{int}$ where γ_{AB} is the interfacial surface energy and related to χ for the polymers such that $\gamma_{AB} \cong \frac{kT}{a^2}\sqrt{\frac{\chi}{6}}$ and A_{int} is the surface area between blocks, where a is the Kuhn monomer length. Considering unit cells for the three phases, the BCC phase will have 2 spheres of minority block in a unit cell, the hexagonally close-packed cylinders a single minority phase cylinder per unit cell, and the lamellae one sheet of minority lamellae per unit cell. Schematics for the unit cells with relevant variables are shown in Figure 1.4.

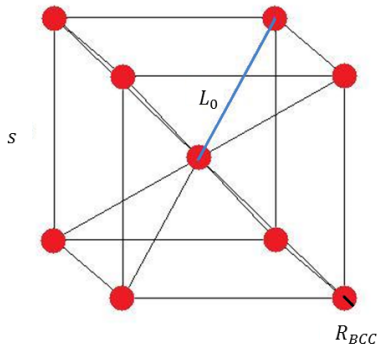

BCC Spheres

$$V_{BCC} = s^3 = \frac{8L_0^3}{3\sqrt{3}}$$

$$V_{BCC_A} = 2\frac{4\pi R_{BCC}^3}{3}$$

$t \equiv$ Unit Cell Thickness (Into Page)

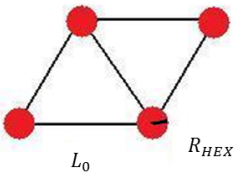

Hexagonal Close-Packed Cylinders (Top Down View)

$$V_{HEX} = \frac{\sqrt{3}L_0^2}{2}t$$

$$V_{HEX_A} = \pi R_{Hex}^2 t$$

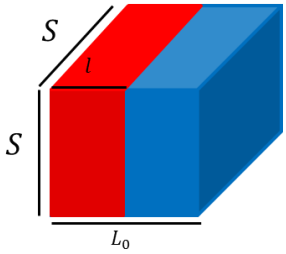

Lamellae

$$V_{LAM} = L_0 S^2$$

$$V_{LAM_A} = lS^2$$

Figure 1-4: Unit cell schematics for simple surface energy model comparison of bulk phases of a diBCP with the volume equations for their unit cell and volume for their minority component. Left: BCC spheres. Middle: Hexagonal close-packed cylinders. Right: Lamellae.

From the unit cell schematics, the volume fraction of minority block in each can be calculated as follows: for the BCC spheres $f = \frac{V_{BCC_A}}{V_{BCC}} = \frac{\sqrt{3}\pi R_{BCC}^3}{L_0^3}$, for hexagonal close-packed cylinders $f = \frac{V_{HEX_A}}{V_{HEX}} = \frac{2\pi R_{HEX}^2}{\sqrt{3}L_0^2}$, and for lamellae $f = \frac{V_{LAM_A}}{V_{LAM}} = \frac{l}{L_0}$. This implies in terms of the natural polymer periodicity $R_{BCC} = \sqrt[3]{\frac{f}{\sqrt{3}\pi}}L_0$, $R_{HEX} = \sqrt{\frac{f\sqrt{3}}{2\pi}}L_0$, and $l = fL_0$. Additionally, by assuming the volume of minority block is equal across unit cells for a given volume fraction, one can easily show $t = \frac{8R_{BCC}^3}{3R_{HEX}^2} = \frac{16}{9}L_0$ and $S^2 = \frac{\pi R_{HEX}^2 t}{l} = \frac{8}{3\sqrt{3}}L_0^2$. Each surface free energy is then a function of f with $F_{sur_{BCC}} = \gamma_{AB}2(4\pi R_{BCC}^2) = \gamma_{AB}8\pi\left(\frac{f}{\sqrt{3}\pi}\right)^{2/3}L_0^2$, $F_{sur_{HEX}} = \gamma_{AB}(2\pi R_{HEX}t) = \gamma_{AB}\frac{32\pi}{9}\sqrt{\frac{f\sqrt{3}}{2\pi}}L_0^2$, and $F_{sur_{LAM}} = \gamma_{AB}2(S^2) = \gamma_{AB}\frac{16}{3\sqrt{3}}L_0^2$. Plotting these surface free energies normalized by $\gamma_{AB}L_0^2$ shows that BCC spheres has the lowest surface energy for $f < 0.14$, hexagonal close-packed cylinders the lowest surface energy for $0.14 < f < 0.28$, and lamellae the lowest surface energy for $f > 0.28$ as shown in Figure 1.5. These values are very close to the ranges observed experiementally, although

real systems tend to have broader polymer interfaces and the actual transition f tend to be higher than these values for real systems with finite χ.

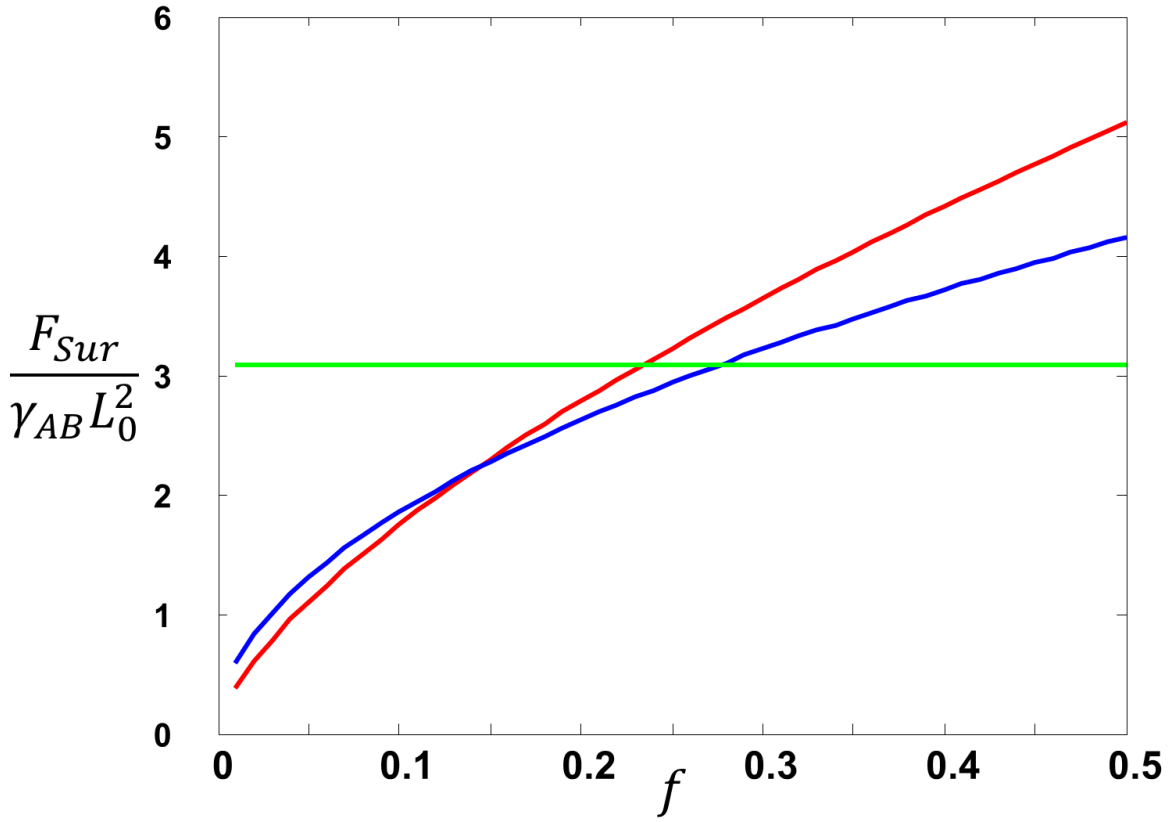

Figure 1-5: Plot of the normalized surface free energies for BCC spheres (red), hexagonal close-packed cylinders (blue), and lamellae (green) in the high segregation limit.

The previous model demonstrates using free energy comparisons can greatly elucidate the parameters necessary to reach desired morphologies. The next example looks at a system where strain energy is more of a dominating factor than surface energy. This example is for a DSA system that will be examined in more detail later in the thesis.

The change in free energy due to strain of a BCP under a given hexagonal array of posts can be modeled as an affine deformation, where the strain affects both the conformational entropy and the interfacial energy. The derived expression for a BCP is thus

$$\frac{\Delta F}{kT} = \frac{2Na}{L}\sqrt{\frac{\chi}{6}} + \frac{1}{2}\left(\frac{L^2}{4Na^2} + \frac{4a\sqrt{N}}{L} - 3\right)$$

where L is the BCP lattice spacing that is strained, a is the statistical Kuhn monomer segment length, and N is the number of Kuhn segments. By substituting $L = \frac{L_{post}}{\sqrt{i^2+j^2+ij}}$, where i and j are the post lattice type indices, one can calculate the reduced free energy per chain for different post lattices and see where a given commensuration of spheres is the lowest energy structure[49]. More details of these considerations will be examined in Chapter 5 for hexagonal post array DSA studies.

In general, these free energy relationships have a form as follows

$$\frac{\Delta F}{kT} = \frac{\Gamma}{\lambda} + \alpha\lambda^2 - \beta$$

where Γ is a constant related to the surface free energy and some components of strain, α is a constant related to the strain free energy, β is a constant related to the affine nature of deformations, and λ is the length deformation parameter such that $\lambda = (\Gamma/2\alpha)^{1/3}$ when the system is at equilibrium. This means that L_0 for the system is $L_0 = (\Gamma/2\alpha)^{1/3}$. For the previous example for hexagonal posts, $\Gamma = 2a\left(N\sqrt{\chi/6} + \sqrt{N}\right)$, $\alpha = 1/8Na^2$, and $\beta = -3/2$. If free energy curves are produced from SCFT calculations, a best fit for these parameters can be performed to gain insight into the physics of the system.

In both free energy calculation examples presented here, a key piece of knowledge was the form of the free energy function for potential morphologies. When the morphologies are simple geometric lattice structures as in the first case or only have a difference in lattice positioning as in the second case, free energy calculations are a powerful tool in predicting what morphologies will form under a given set of conditions. However, for more complicated systems where the morphologies may have mixed or complicated symmetries or the free energy is a function of two or more variables in different directions, such free energy calculations are limited in their ability to be of use. In these cases a more sophisticated approach is necessary and thus simulation methods are better suited to such situations. Free energy analysis of course can in principle still be done with these simulations by producing simulated free energy curves.

1.3.2 Self-Consistent Field Theory (SCFT)

SCFT simulations have been the standard methods for modeling and predicting the phase behavior of BCP systems. Similar to how density function theory has become the standard method for calculating electron cloud densities in the semiconductor community, SCFT allows the polymer community a means to calculate the morphologies of various polymer blend systems[52–55].

The central idea of the theory is that one can rewrite the partition function Z as a functional of a free energy Hamiltonian H. This Hamiltonian rather than being a function of individual particle or monomer positions is instead recast as a function of density fields ρ and chemical potential fields Ω that are themselves a function of spatial coordinates. Mathematically one can then write the partition function as follows

$$Z = \int e^{\frac{-H[\rho,\Omega]}{kT}} D\rho D\Omega$$

where the fact ρ and Ω are functions of the real space coordinates $\mathbf{r} = \{\boldsymbol{x}, \boldsymbol{y}, \boldsymbol{z}\}$ has been suppressed for clarity. D here represents integration over a function. How the actual H depends on ρ and Ω depends upon chain architecture and the number of distinct species in the system and will be examined in more detail in Chapter 2.

Knowing the partition function for an ensemble of interest, the goal of SCFT is to determine ρ^* and Ω^*, the mean field solutions that dominate the partition energy functional and satisfy the saddle point SCFT conditions

$$\left.\frac{\delta H}{\delta \rho}\right|_{\rho^*} = 0 \text{ and } \left.\frac{\delta H}{\delta \Omega}\right|_{\Omega^*} = 0$$

These conditions are in general referred to as a mean-field approximation, but in the polymer community they are referred to as the SCFT condition since they satisfy the self-consistent solution of a mean-field theory[53]. Care should be taken when solutions are found to these equations as they only represent a general saddle point solution, meaning solutions found might be local minima or metastable solutions rather than a global

minimum solution. Ultimately finding ρ^* and Ω^* corresponds to determining the morphology of interest under the specified conditions of a given simulation.

For a given BCP system, the Hamiltonian needs to be derived from the corresponding partition function and an algorithm developed to relax the fields to self-consistently solve for the saddle point solutions. For most polymer systems, the standard Gaussian chain partition function is the starting point, although there are other chain models that are better suited for certain systems such as the worm-like chain. A Hubbard-Stratonovich transformation is applied to the partition function to convert the particle based partition function to a polymer density and field representation. For certain systems, the partition functional can be further simplified to eliminate the density field component entirely and make the problem simply solving for the chemical potential fields. Specific BCP systems, ways of satisfying the SCFT conditions, and ways of solving for the partition functions and thus the real space density fields will all be examined in Chapter 2.

For numerical implementation, a unit cell system is devised using a N_X by N_Y by N_Z discrete grid of points each representing a real space location. All field and density variables are then represented as 3D matrices of this size with all calculations done on these matrices. Periodic boundary conditions are normally applied to the system, but since boundary conditions are a key parameter of interest in thin film and DSA studies details of implementing various kinds of boundary conditions including local topography and surface chemistry are discussed in Chapter 2. Depending on the system of interest, unit cell dimensions can vary from a commensurate cell with dimensions on the order of L_0 to several times that for large system studies where defect analysis is desired.

1.4 Experimental Annealing Methods

Having theoretical methods to predict morphologies formed by BCPs is all well and good, but for real world applications to be implemented and the theory to be validated, experimental comparison must be performed. SCFT has been an excellent tool in reproducing the results of many experiments involving chemical patterning and topographical templating[49,56–60].

In studying thin film BCP systems, experiments normally follow a similar routine. A substrate is chosen (usually silica based) either used bare or functionalized with a polymer brush layer to change surface chemistry as well as increase polymer mobility on the substrate. These brush layers are normally low molecular weight homopolymers of one of the blocks in the BCP and are attached by using a hydroxyl terminated homopolymer that when spun cast and then thermally treated will bond to the silica substrate. BCP is then spun cast onto the substrate using an appropriate solvent with concentration and spin speed calibrated to get a uniform desired cast film thickness. An annealing step is then performed to guide the BCP film to the desired equilibrium morphology. Three different kinds of annealing, thermal annealing, solvent vapor annealing, and annealing with a top coat, will be discussed shortly in detail. Morphologies are then examined using some microscopy technique that depends upon the copolymers used and what kinds of contrast there is between the two blocks. As an example, siloxane based polymers have a high etch selectivity to oxygen plasma etching while organic based blocks are easily etched away by such plasmas, so reactive ion etching is generally used to etch away the organic block in such BCPs leaving the siloxane based block exposed for characterization via scanning electron microscopy[44].

In the experiments explored and compared with simulations in this thesis, a variety of molecular weight polystyrene-*b*-polydimethylsiloxane (PS-PDMS) with high χ values and excellent etch selectivity using oxygen plasma reactive ion etching were used[1,2,49,56–61].

In comparing simulation results with experiments, there will usually be disagreement with experimental results in various situations. These differences are normally due to oversimplification of the real system or not considering all the effects of all potential variables when the disagreement is from the modeling side of things. Such differences can then be used as learning experiences to improve the model. As an example, a DSA system simulation explored the effects of PS functionalized hydrogen silsesquioxane (HSQ) posts and oversimplified the system trying to model the self-assembly in 2D and the simulation results did not agree with the experimental ones. In changing the model to a 3D unit cell with appropriate film thickness and post dimensions, the SCFT reproduced the experimental results as shown in Figure 1.6[57]. Alternatively, a 2D model could still be used,

but effective parameters such as an effective 2D volume fraction that corresponds to the area fraction of the in plane 3D structure would have to determined. A simpler theory is desired to explain experimental observations, but in general more detail added into the model will allow for better experimental comparison.

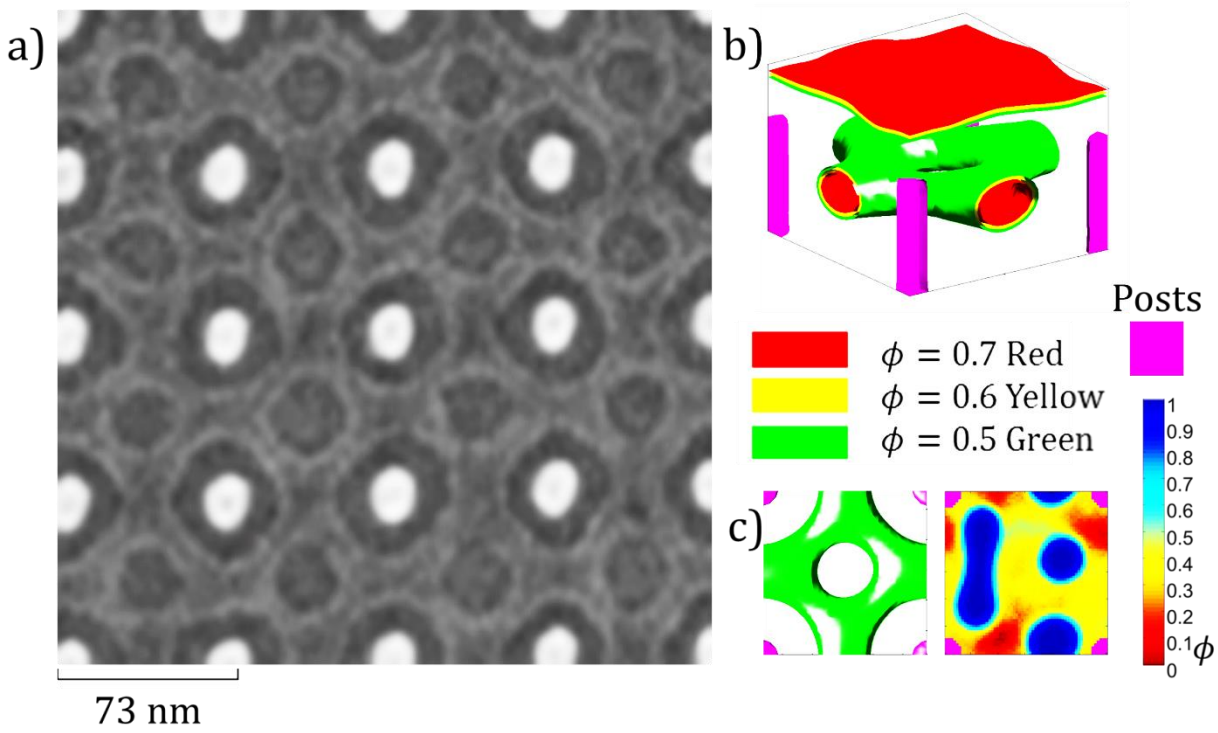

Figure 1-6: a) Experimental result for a given square symmetry DSA post array where BCP formed square symmetry perforated lamellae. HSQ post features are white, hardened PDMS is light grey, and dark grey regions are where PS was before etching. b) 3D SCFT simulation result showing same structure as experiment. Parameters for the simulation were χN = 30, f = 0.32, $1.00L_0$ tall posts, $0.71L_0$ diameter posts, $1.50L_0$ thick films, and a square posts period of ≈ $2.00L_0$. c) Top-down view of 3D SCFT results compared with 2D SCFT result using same base parameters showing the 2D model does not produce the expected structure. Density scales for the structures are shown as well for the PDMS[57].

1.4.1 Thermal Annealing

In order to be able to process BCPs and preserve the desired equilibrium morphology at room temperature, at least the majority block thermal glass transition temperature T_g should be larger than room temperature so that once the system is quenched the morphology does not continue to change on time scales before final characterization or application can be performed. All methods used to apply a thin film of BCP to a substrate

will require further processing to achieve desired equilibrium morphologies since as cast morphologies will either be disordered or based on the way the sample was coated. Defect annihilation also requires such annealing, so some kind of external treatment must be performed to rid the sample of these undesired features and guide the BCP toward the target lower energy state. Thermal annealing can achieve these goals by increasing the temperature of the sample to near or above the maximum T_g in the BCP system and giving the polymer chains enough thermal energy to diffuse and reptate. One can model the temperature required for such diffusion to take place using an activated reptation model with a Rousian dynamics diffusion coefficient $D = D_0 e^{\frac{-\Delta E}{kT}}$ where D_0 is dependent on the degree of polymerization and ΔE is an energy barrier proportional to χN. Estimates for when diffusion begins to become difficult are already below the critical χN for microphase segregation in diBCPs of 10.5 with a value of $\chi N \cong 7.6$ already showing slow diffusion[62]. Since χ is an inverse function of temperature, achieving the temperatures required to properly thermal anneal a given BCP become more difficult with increased χ values that are desired for getting smaller periodicity structures. Thus thermal annealing is limited in either being used on lower molecular weight or lower χ polymers. The final volume fraction of the polymer is also fixed in thermal annealing limiting access to different kinds of morphologies based on the BCP used.

Even though thermal annealing can remove defects and push systems toward their equilibrium morphologies in a simple setup of just applying heat, letting the system sit at that temperature, and then letting the system cool back to ambient temperature, difficulties arise in determining the optimal times of keeping the system heated and how quickly to quench the systems. If the molecular weight or χ is too large the time to anneal will be on the order of days or longer and thus is not practical for most applications. Additionally, thermal annealing cannot be used to control the natural bulk morphology of the BCP as the main control parameter is χ and thus volume fraction is a fixed parameter based on the polymer used. Thus if experimentation requires a new morphology or periodicity synthesis of a new BCP of a different molecular weight and volume fraction would be required.

In general thermal annealing is a simple technique to perform experimentally and modeling thermal annealing in simulations is straight forward as one has to primarily just match the effective χ parameter the real system encounters at the annealing temperature and possibly try to model quenching from that effective χ to the room temperature value. However, in many applications where high χ materials are desired to produce small features and more control over the effective volume fraction is desired without synthesizing new polymers, other annealing methods should be used.

1.4.2 Solvent Vapor Annealing (SVA)

The most studied alternative approach to thermal annealing is solvent vapor annealing (SVA). In SVA, a thin film of BCP is placed in either a chamber containing solvent vapor or in a closed flow system device that flows in solvent. These solvents are generally either neutrally preferential between the blocks or block selective and mixed in controlled proportions that enable selective swelling of the two blocks and thus control over the effective volume fraction of the system. Unlike thermal annealing where there is little change in thickness of the film, SVA is a very thickness dependent process especially for monolayer initial thicknesses and the film can swell to many times the original film thickness for both monolayer spun cast film thicknesses and thicker films, where a monolayer means an initially L_0 thick sample of polymer using the bulk natural period as reference. As long as the initial film thickness is uniform and the swelling thickness monitored during the annealing process, long range ordered structures that are now a function of the solvent volume fractions can be obtained as the solvents penetrate and plasticize the film to increase mobility of the chains and thus drive the system toward an equilibrium morphology in the swollen state.

Experimentally issues that arise from such an annealing setup is maintaining control of solvent vapor pressures and ensuring the system is saturated and well mixed. These issues are easily addressed using a flow control setup[59]. Another issue is the potential of sample dewetting into island and hole structures due to multiple commensurable morphologies being possible between different film thicknesses. This issue is usually addressed by calibrating the best initial film thickness and monitoring the swelling

behavior to ensure the correct commensurate swollen film thickness is obtained before quenching the sample to maintain the swollen equilibrium morphologies.

Modeling such behavior can become daunting especially if experiments are performed in such a way that nonequilibrium structures are preserved due to the swollen film not being fully equilibrated before quenching. When films are very thick, concentration gradients become important and quenching dynamics can affect the final morphology[63]. For the most part, films studied in this thesis will not be greater than $2L_0$ thick when swollen and such concentration gradient effects are expected to be negligible. Two approaches to modeling solvent annealing are presented for cases where equilibrium has been reached with an implicit model with effective parameters and an explicit model with solvent considered as a separate simulation species in Chapter 3. These methods along with more explicit details of experimental comparison will be discussed in Chapter 3.

1.4.3 Top Coats

One of the main issues with SVA is the fact the film thickness is free to evolve under the solvent atmosphere conditions imposed upon the system and thus ensuring an equilibrium film thickness is reached requires in situ monitoring and control to both make sure the target thickness is reached and no dewetting occurs. Additionally for high χ polymers, realizing neutral surface air interfaces for achieving perpendicular to the substrate morphologies can be difficult. An alternative approach to this is through the use of a top coat. By constraining the BCP film between a top coat and the substrate, uniform film thickness is guaranteed throughout the film along with a prescribed surface energy based on the top coat[64]. The top coat can be loaded with solvent depending upon the material and thus SVA performed using the method[65] or a simple thermal anneal can be performed on a hard top coated system. One obvious disadvantage with such an approach is developing a means to remove the top coat without damaging the sample and any solvent annealing will be limited to how much solvent the top coat can allow to deswell from itself or if the top coat is semipermeable.

In this thesis no simulations were performed that explicitly tried to model an experimentally top coat annealed system. However, most of the implicit SVA simulations

used a constrained film thickness in the simulations and thus can effectively be compared to the equivalent top coat annealed system of interest. Thus future work that may incorporate such strategies can use these models as a starting point in developing appropriate surface energy top coats.

1.5 Directed Self-Assembly (DSA)

In all the previous annealing approaches examined, none of them guaranteed complete long range order with low defect densities, complete reproducibility, or the ability to create locally complex morphologies. Through the use of DSA, all three of these issues can be overcome and BCP self-assembly implemented in a quality control manner for industrial applications. DSA is implemented primarily in one of two ways, either local chemical patterning or topographical templating, sometimes referred to as graphoepitaxy[5,6].

In chemical patterning, the substrate is modified by some lithography method to change the local surface chemistry and thus modify the surface energy to interact with the BCP differently across the sample. Groups such as Thomas Russell and Paul Nealey have demonstrated such techniques with lamellar polystyrene-*b*-poly(methyl methacrylate) (PS-PMMA) on silicon oxide and gold patterned stripes[22] and cylindrical and lamellar PS-PMMA using EBL or UV interference lithography to pattern periodic lines with periodicities analogous to L_0 of the BCP, respectively[66,67]. Many other examples of such chemical templating exists for a wide variety of BCP morphologies[5,9,21,68–72]. Depending upon whether these chemical patterns are commensurate with the overlying BCP film, the BCPs will self-assemble to attempt to minimize the energy with underlying pattern. Using these methods thus allows control of the morphology across a thin film when the features produced are perpendicular to the substrate; however, the effect is local at best when the BCP tends to form parallel to the substrate features due to large air interfacial energy differences observed in high χ polymers and thus the method is limited in patterning such morphologies.

In topographical templating, a physical surface feature such as a trench or array of posts is fabricated using another lithography method that creates hard features on the substrate the BCP must self-assemble around. The method has been used to align parallel

to the surface features such as cylinders and spheres and control their internal morphology[1,2,4,56–58,60,61]. Patterning with trenches is usually done using photolithography to create regions over 200 nm wide in which the BCP cylinders or spheres must align or pack into a commensurate way or else would incur high strain energy penalties for making sharps bends or incommensurate packing. Patterning with posts is usually done with EBL to vector scan a region on a substrate with a grid layout of posts and expose a resist material such as HSQ to create an array of tall and thin features that will influence the orientation of cylinders or packing of spheres due to the local strain imposed on the polymer chains. Posts can be further functionalized with homopolymer brush to modify their surface chemistry to influence whether the majority or minority BCP features wet the post or a repelled and compressed by the posts. By combining these patterning techniques and creating valid models to predict the behavior of the BCP under a variety of patterning conditions, one can in essence create an unlimited array of structures by locally varying post positions and chemistries.

1.6 Summary

BCP DSA shows great promise as a way to manufacture complex patterns for transferring into functional devices. However, the parameter space for creating such complex structures is immense. While bulk diBCPs only have 2 free parameters that govern their equilibrium morphologies, thin films of diBCPs already increase the number of free parameters to 5 by combining the surface energy parameters of the two blocks for the top and bottom surfaces, solvent annealing adds a minimum of 3 extra free parameters per solvent type incorporated when explicitly modeling them, and adding posts, chemical patterning, or other topography adds many more degrees of freedom in position, feature size, etc. To account for all the parameters, the SCFT models must either make simplifying assumptions or be very careful to hone in on the parameters that affect the morphology in a given situation the most.

The rest of this thesis will explore sets of studies where different assumptions for such parameters were made and how the models were either simplified or advanced in order to capture the physics of these systems. Starting in Chapter 2 with basic descriptions

of all the potential tools that can be used in SCFT, systems studied using SVA (Chapter 3), unpatterned thin films (Chapter 4), DSA thin films of many different types (Chapter 5), and trying to reverse engineer parameters in a very complex case through an inverse design approach (Chapter 6) will all be examined and then reflected upon for future applications in Chapter 7. The ultimate hope of these modeling approaches is to zone into the key fundamental parameters needed to create complex target patterns using BCPs while reducing the need for a multitude of experiments. One should simply be able to use the simulation results to design experiments that are already close to the final necessary conditions to create a desired target morphology.

Chapter 2

Simulation Theory and Methodology

2.1 Introduction

All SCFT simulations performed in the studies discussed in this thesis are based upon the work and theory developed by Glenn Fredrickson and his collaborators[53–55]. The theory states that the partition function of the system Z can be expressed as a functional of a Hamiltonian $H[\rho, \Omega]$ instead of individual monomer positions $\vec{\boldsymbol{r}}$ where Ω is the set of chemical potential fields and ρ is the set of polymer densities. For the diBCP systems studied, the Hamiltonian can be expressed in terms of just Ω such that $Z = \int e^{-H[\Omega]}\, D\Omega$. Knowing $H[\Omega]$ from Z, the mean field configuration Ω^* that is assumed to dominate the partition energy functional is found using the equation $\frac{\delta H[\Omega]}{\delta \Omega}\Big|_{\Omega^*} = 0$. This mean-field approximation results in solutions Ω^* that are saddle points in the energy phase space and thus can correspond to either local minimum, metastable, or global minimum energy states of the system. As defined the Hamiltonian is related to the free energy for such a solution as $F = k_B T H[\Omega^*]$. In more general cases, the density fields need to be considered explicitly in terms of the saddle point equations. In Section 2.2 of this chapter, various partition function models and their corresponding Hamiltonians are discussed.

In general, the simulations were evolved using a random initial field configuration; this makes sure the system can generate several solutions over multiple simulations if there are multiple metastable state solutions for a given set of conditions. An alternative approach to this is if potential solutions are known, the simulations can be seeded with these expected structure field solutions and allowed to evolve to test whether that structure was stable under the given conditions. Usually for confined systems there is only one dominant solution, so convergence to the same saddle point for these simulations was

confirmed by running simulations several times with the same structure always being observed.

Once H for a given system is known, a relaxation scheme is developed to evolve Ω and more generally ρ in a way that will produce solutions that satisfy the SCFT condition $\frac{\delta H[\Omega]}{\delta \Omega}\Big|_{\Omega^*} = 0$ and if ρ is explicitly used $\frac{\delta H[\rho,\Omega]}{\delta \rho}\Big|_{\rho^*} = 0$. These schemes are usually made to find saddle point solutions as fast as possible or to try to model realistic dynamics of the system being studied. In Section 2.3 of this chapter, such approaches will be discussed.

In mean field theories, an approximation is usually made to consider the interactions between objects in the system are mediated by some average field interaction. In polymer systems, this amounts to considering the interactions of all chains as being equivalent to that of a single chain partition function Q. This term will appear in H for all systems examined with there being a different Q for every distinct chain component in the system. One can show that this single chain partition function is solved from a well known second order differential diffusion equation known as the Fokker-Planck equation.[73,74] Thus in order to solve the SCFT equations, Q must be solved during every step and this is by far the most computationally expensive step of the simulations. In Section 2.4, three different methods are examined for solving this equation and explanations given why the pseudo-spectral method was implemented in the studies of this thesis.

For numerical computational purposes, the system is evolved in an N_x by N_y by N_z discrete point grid each representing a real space location. All variables are represented as 2D or 3D matrices of this grid size. These finite computation limitations mean the system must have some sort of boundary conditions to be physically relevant. In Section 2.5, how boundary conditions are enforced in different situations are discussed as they play a key role in determining the physics of a given system.

2.2 Inhomogeneous Polymer Equilibrium Theory

In all models presented, one starts with a particle based partition function Z for the polymer chain type considered, develops the interaction potential $U(\vec{\boldsymbol{r}}^{\boldsymbol{n}})$ between all monomers in all n chains, and then converts this partition function to a field based function

using a Hubbard-Stratonovich transformation that also decouples interactions among particles leaving only the auxiliary fields that govern the physics of the system as the functional parameters[53]. In this thesis, only a Gaussian chain model for polymers is considered since the experimental PS and PDMS examined are all considered to exhibit random coil behavior.

For all polymer chains considered, the canonical partition function is given as

$$Z(n,V,T) = \frac{1}{n!\,(\lambda_T^3)^{nN}} \prod_{j=1}^{n} \int D\vec{\mathbf{r}}_j \, e^{-\beta U(\vec{\boldsymbol{r}}^{\boldsymbol{n}})}$$

where n is the number of Gaussian chains in the system, $\lambda_T = \frac{h}{\sqrt{2\pi m k_B T}}$ with h being Planck's constant and m the mass of the chain, V is the volume of the system, N the degree of polymerization of each chain, and $\beta = \frac{1}{k_B T}$. $U(\vec{\boldsymbol{r}}^{\boldsymbol{n}}) = U_0(\vec{\boldsymbol{r}}^{\boldsymbol{n}}) + \bar{U}(\vec{\boldsymbol{r}}^{\boldsymbol{n}})$ where U_0 is the short-range intramolecular potential energy contribution which for Gaussian chains is given as

$$U_0(\vec{\boldsymbol{r}}^{\boldsymbol{n}}) = \frac{3k_B T}{2b^2} \sum_{j=1}^{n} \int_0^N ds \left| \frac{d\vec{\mathbf{r}}_j(s)}{ds} \right|^2$$

and $\bar{U}(\vec{\boldsymbol{r}}^{\boldsymbol{n}})$ is a pair potential function that accounts for the intermolecular interactions between nonadjacent monomers in the chains. This pair potential function is given approximately as

$$\bar{U}(\vec{\boldsymbol{r}}^{\boldsymbol{n}}) \approx \frac{1}{2} \sum_{j=1}^{n} \sum_{k=1}^{n} \int_0^N ds \int_0^N ds' \bar{u}\left(\left| \vec{\mathbf{r}}_j(s) - \vec{\mathbf{r}}_k(s') \right| \right)$$

Where $\bar{u}$ is a pair potential of mean force for a given model. Once this pair potential function is known, a transformation is applied to partition function and the partition function is left now as only a functional of auxiliary fields ρ and Ω.

2.2.1 Homopolymer Partition Function

In the case of a homopolymer, the main physical effect to consider for non-adjacent intermolecular pair interactions is the exclude volume effect[75,76] with the pair potential of mean force being given by a delta function multiplied by the excluded volume parameter u_0 such that $\bar{u} = k_B T u_0 \delta(\vec{\mathbf{r}})$. The value of u_0 thus dictates the kind of environment the homopolymer resides with a negative value representing a poor solvent condition, a positive value a good solvent condition, and a value of zero a theta solution or homopolymer melt[43,77]. For the formulism presented, however, having a negative value of u_0 will result in an unbound collapse of the local polymer density onto itself with no repulsive potential thus this model is restricted to good solvents or the theta condition.

In order to get the homopolymer partition function to the appropriate form to make it a functional of density and chemical potential fields, the microscopic segment density operator is introduced as

$$\hat{\rho}(\vec{\mathbf{r}}) = \sum_{j=1}^{n} \int_0^N ds \delta\left(\vec{\mathbf{r}} - \vec{\mathbf{r}}_j(s)\right)$$

which upon substituting into the potential of mean force gives the relationship

$$\bar{U}(\vec{\boldsymbol{r}}^{nN}) = \frac{1}{2} \int d\vec{\mathbf{r}} \int d\vec{\mathbf{r}}' \hat{\rho}(\vec{\mathbf{r}}) \bar{u}(|\vec{\mathbf{r}} - \vec{\mathbf{r}}'|) \hat{\rho}(\vec{\mathbf{r}}') - \frac{1}{2} nN\bar{u}(0)$$

with the second term here simply being the subtraction of self-interactions in the first term. Now using $z_0 \equiv e^{\frac{\beta N \bar{u}(0)}{2}} \lambda_T^{-3N}$ and the functional transformation

$$F[\hat{\rho}] = \int D\rho F[\rho] \int D\omega \, e^{i \int d\vec{\mathbf{r}} \omega(\vec{\mathbf{r}}) [\rho(\vec{\mathbf{r}}) - \hat{\rho}(\vec{\mathbf{r}})]}$$

the partition function $Z(n, V, T)$ can be rewritten as

$$Z = \frac{z_0^n}{n!} \int D\rho \int D\omega \prod_{j=1}^{n} \int D\vec{\mathbf{r}}_j \, e^{-\beta U_0 + i \int d\vec{\mathbf{r}} \omega(\rho - \hat{\rho}) - \frac{\beta}{2} \int d\vec{\mathbf{r}} \int d\vec{\mathbf{r}}' \rho \bar{u} \rho}$$

where explicit dependence of $\vec{\mathbf{r}}$ for ω, ρ, $\hat{\rho}$, U_0 and $\bar{u}$ has been dropped for simplicity. This partition function now has interactions decoupled through the use of the auxiliary fields ω and ρ. Finally noting that the n polymer chain path integrals factor as follows

$$\prod_{j=1}^{n}\int D\vec{\mathbf{r}}_j\, e^{-\beta U_0 - i\int d\vec{\mathbf{r}}\omega\hat{\rho}} = \left\{\int D\vec{\mathbf{r}}\, e^{\frac{-3}{2b^2}\int_0^N ds\left|\frac{d\vec{\mathbf{r}}(s)}{ds}\right|^2 - i\int_0^N ds\omega(\vec{\mathbf{r}}(s))}\right\}^n = (\xi_0 Q[i\omega])^n$$

where in the last equality the knowledge of the form of the single polymer partition $Q[i\omega]$ has been used as well as ξ_0 denoting the configurational part of the Gaussian polymer partition function. The total partition function thus simplifies to the following functional

$$Z = Z_0\int D\rho\int D\omega\, e^{i\int d\vec{\mathbf{r}}\omega(\vec{\mathbf{r}})\rho(\vec{\mathbf{r}}) - \frac{\beta}{2}\int d\vec{\mathbf{r}}\int d\vec{\mathbf{r}}'\rho(\vec{\mathbf{r}})\bar{u}\left(|\vec{\mathbf{r}}-\vec{\mathbf{r}}'|\right)\rho(\vec{\mathbf{r}}') + n\ln Q[i\omega]}$$

where $Z_0 = \frac{(z_0\xi_0)^n}{n!}$. In this form the Hamiltonian $H[\rho,\omega]$ is given as

$$H[\rho,\omega] = -i\int d\vec{\mathbf{r}}\omega(\vec{\mathbf{r}})\,\rho(\vec{\mathbf{r}}) + \frac{\beta}{2}\int d\vec{\mathbf{r}}\int d\vec{\mathbf{r}}'\rho(\vec{\mathbf{r}})\bar{u}(|\vec{\mathbf{r}}-\vec{\mathbf{r}}'|)\rho(\vec{\mathbf{r}}') - n\ln Q[i\omega].$$

At this point the necessary Hamiltonian needed to implement SCFT for a homopolymer system has been described. Further simplifications can be done by specifying the exact form of $\bar{u}(|\vec{\mathbf{r}}-\vec{\mathbf{r}}'|)$ such as the case for a good solvent with a positive constant u_0 that allows the ρ field to be integrated out of the equation leaving the following $Z = Z_0\int D\omega e^{-H[\omega]}$ where $H[\omega] = \frac{1}{2u_0}\int d\vec{\mathbf{r}}[\omega(\vec{\mathbf{r}})]^2 - n\ln Q[i\omega]$.

2.2.2 BCP Partition Function

For BCPs, there are more than one distinct monomers in the system that usually have repulsive interactions characterized by a positive Flory-Huggins parameter χ[43,77]. To account for these interactions, a local pairwise potential between dislike polymer segments is introduced. For a diBCP system, this pairwise potential has the form

$$\beta U_1\left(\vec{\mathbf{r}}^{(f_A n_A + f_B n_B)N}\right) = \nu_0\chi\int d\vec{\mathbf{r}}\hat{\rho}_A(\vec{\mathbf{r}})\,\hat{\rho}_B(\vec{\mathbf{r}})$$

where A and B signify the two distinct blocks, ν_0 is the inverse of the monomer density ρ_0, and U_1 is simply added to the potential terms in the partition function previously described

in 2.2.1. Additionally to account for incompressibility, a term $\beta U_2\left(\vec{\mathbf{r}}^{(f_A n_A + f_B n_B)N}\right) = -\kappa\frac{\nu_0}{2}\int d\vec{\mathbf{r}}\left(\rho_A + \rho_B - \rho_0\right)^2$ is added to the system, such that in the limit $\kappa \to \infty$ the system is fully incompressible. The total partition function thus takes the following form $Z = \frac{z_0^{(f_A n_A + f_B n_B)N}}{n_A! n_B!}\prod_{j=1}^{n_A}\int D\vec{\mathbf{r}}_j \prod_{k=1}^{n_B}\int D\vec{\mathbf{r}}_k\, e^{-\beta U_0 - \nu_0\int d\vec{\mathbf{r}}\rho_A\chi\rho_B + \kappa\frac{\nu_0}{2}\int d\vec{\mathbf{r}}(\rho_A+\rho_B-\rho_0)^2}$.

Converting this to field variable vectors $\boldsymbol{\omega} \equiv [\omega_A, \omega_B]$ and $\boldsymbol{\rho} \equiv [\rho_A, \rho_B]$ as before using the delta function relationships yields the following expression for the diBCP partition function

$$Z = Z_{AB_0}\int D\boldsymbol{\rho}\int D\boldsymbol{\omega}\, e^{i\int d\vec{\mathbf{r}}\boldsymbol{\omega}\cdot\boldsymbol{\rho} + \frac{-\nu_0}{2}\int d\vec{\mathbf{r}}\boldsymbol{\rho}\boldsymbol{\chi}\boldsymbol{\rho}' + n\ln Q[i\omega] + \kappa\frac{\nu_0}{2}\int d\vec{\mathbf{r}}\left(\rho_A+\rho_B-\rho_0\right)^2}$$

where the vector form of the fields has been used to simplify the expression for considering n-BCPs later with $\boldsymbol{\omega}\cdot\boldsymbol{\rho} = \omega_A\rho_A + \omega_B\rho_B$ and $\boldsymbol{\rho}\boldsymbol{\chi}\boldsymbol{\rho}' = [\rho_A \quad \rho_B]\begin{bmatrix}0 & \chi\\ \chi & 0\end{bmatrix}\begin{bmatrix}\rho_A\\ \rho_B\end{bmatrix}$. Denoting the following relationships $\rho_+ = \rho_A + \rho_B$, $\phi_x = \frac{\rho_x}{\rho_0}$, and $i\omega = \mu$, and upon substituting them into the partition function equation, the general field Hamiltonian for BCPs with any number of components and with normalized field parameters is inferred in matrix form as

$$H[\boldsymbol{\phi},\boldsymbol{\mu}] = \rho_0\int d\vec{\mathbf{r}}\left(\frac{1}{2}\boldsymbol{\phi}\boldsymbol{\chi}\boldsymbol{\phi}' - \boldsymbol{\mu}\cdot\boldsymbol{\phi} - \frac{\kappa}{2}(\phi_+ - 1)^2\right) - n\ln Q[\boldsymbol{\mu}]$$

where $\equiv \begin{bmatrix} 0 & \chi_{12} & \chi_{13} & \cdots & \chi_{1m}\\ \chi_{12} & 0 & \chi_{23} & \cdots & \chi_{2m}\\ \chi_{13} & \chi_{23} & 0 & \cdots & \chi_{3m}\\ \vdots & \vdots & \vdots & \ddots & \vdots\\ \chi_{1m} & \chi_{2m} & \chi_{3m} & \cdots & 0\end{bmatrix}$, $\boldsymbol{\mu} \equiv [\mu_1, \mu_2, \ldots, \mu_m]$, $\boldsymbol{\phi} \equiv [\phi_1, \phi_2, \ldots, \phi_m]$, for m blocks. $\phi_+ \equiv \sum_{i=1}^{m}\phi_i$

For the case of diBCPs, the $\boldsymbol{\chi}$ matrix $\begin{bmatrix}0 & \chi\\ \chi & 0\end{bmatrix}$ is diagonalizable with eigenvalues $-\chi$ and χ with corresponding eigenvectors $\frac{1}{\sqrt{2}}[1 \quad 1]$ and $\frac{1}{\sqrt{2}}[1 \quad -1]$ respectively. Using the linear algebra identity $VDV^{-1} = M$ where V is a matrix with columns composed of the eigenvectors of M and D is a diagonal matrix of the eigenvalues of M with each corresponding to the appropriate column of V, the following change of basis in density operators is possible[78].

$$\frac{1}{2}\boldsymbol{\phi}\boldsymbol{\chi}\boldsymbol{\phi}' = \frac{1}{2}[\phi_A \quad \phi_B]\begin{bmatrix}0 & \chi\\ \chi & 0\end{bmatrix}\begin{bmatrix}\phi_A\\ \phi_B\end{bmatrix} = \frac{1}{4}[\phi_A \quad \phi_B]\begin{bmatrix}1 & 1\\ 1 & -1\end{bmatrix}\begin{bmatrix}\chi & 0\\ 0 & -\chi\end{bmatrix}\begin{bmatrix}1 & 1\\ 1 & -1\end{bmatrix}\begin{bmatrix}\phi_A\\ \phi_B\end{bmatrix}$$

$$[\phi_A \quad \phi_B]\begin{bmatrix}1 & 1\\ 1 & -1\end{bmatrix} = [\phi_A + \phi_B \quad \phi_A - \phi_B]$$

$$\therefore \phi_+ \equiv \phi_A + \phi_B$$

$$\phi_- \equiv \phi_A - \phi_B$$

H can then be rewritten as a function of these normalized density operators

$$H[\boldsymbol{\phi}, \boldsymbol{\mu}] = \rho_0 \int d\vec{\mathbf{r}} \left(\frac{1}{4}(\phi_+^2 - \phi_-^2) - \boldsymbol{\mu} \cdot \boldsymbol{\phi} - \frac{\kappa}{2}(\phi_+ - 1)^2 \right) - n \ln Q[\boldsymbol{\mu}]$$

Upon substituting this expression back into the partition function, taking a Hubard-Stratnovich transformation of the partition function, taking the limit as $\kappa \to \infty$, and factoring out dimensional parameters such as $n, R_g,$ and N the Hamitonian reduces to the following form as a function of $\Omega_+ = N(\mu_A + \mu_B)/2$ and $\Omega_- = N(\mu_A - \mu_B)/2$

$$H[\Omega_+, \Omega_-] = C \left(\int d\vec{\mathbf{r}} \left((2f - 1)\, \Omega_- + \frac{\Omega_-^2}{\chi N} - \Omega_+ \right) - V \ln(Q[\Omega_+, \Omega_-]) \right)$$

where $C = \frac{\rho_0 R_g^3}{N}$ is a dimensionless concentration in terms of ρ_0 the monomer concentration and R_g the radius of gyration of the polymer, $\vec{\mathbf{r}}$ is the position in real space, Ω_+ is the pressure-like chemical potential field conjugated to the total normalized density ϕ_+, Ω_- is the exchange interaction chemical potential field that drives microphase separation and is conjugate to the difference normalized density ϕ_-, V is the volume of the simulation unit cell, and $Q[\Omega_+, \Omega_-]$ is the single chain partition function of the BCP.[49,54,55] Since C multiplies all the terms in the Hamiltonian, in the limit of $C \to \infty$, the SCFT approximation becomes exact since Ω^* will be the only available state and thus the lowest energy structure in this limit. This statement is equivalent to saying that in the long chain limit SCFT becomes an exact theory.

2.2.3 Monoatomic Solvent Partition Function

In the previous cases the single chain partition function Q corresponds to Gaussian chain of length N that is found by solving for the propagator functions q that are found by solving the Fokker-Planck equation to be discussed in Section 2.4. For the case of monomer

solvents, the single chain partition function becomes a monatomic fluid partition function Q_{Sol} that is simply given by

$$Q_{Sol} = \int d\vec{\mathbf{r}} e^{\Omega_{Sol}(\vec{\mathbf{r}})}$$

where Ω_{Sol} is the position dependent field for a given block selective or neutral solvent and the normalized density of the solvent is given by

$$\phi_{Sol}(\vec{\mathbf{r}}) = \frac{e^{\Omega_{\mathrm{Sol}}(\vec{\mathbf{r}})}}{Q_{Tot}} f_{Sol}$$

where f_{Sol} is the volume fraction of the solvent and Q_{Tot} is the total partition function that includes any other chain contributions. How such a total partition function is built up for multicomponent systems is examined in the next Section 2.2.4.

2.2.4 Multicomponent Blends and Partition Functions

For multicomponent blends systems, there are two main ways of having multiple constituents in a system. One way is having distinct chain components with different chain architecture. In this situation multiple constituent partition functions must be considered and combined appropriately to account for all distinct components introduced into the system studied. The other way is introducing distinct chemistries through distinct field parameters for each chemically distinct species. These species need not necessarily be distinct chain components as in the case of BCPs where all the distinct chemical species are bonded together in some predefined architecture.

To examine how constituent partition functions are combined for blends with different chain architectures, only two distinct chemical species (AB systems) are considered for simplicity. Each chain type will now be designated as a component and each chemistry type will be designated as a species. Here each distinct component has a distinct density operator ϕ_i and partition function Q_i, but the interactions between components of the same species are mediated through only the two fields Ω_+ and Ω_-. The incompressibility condition for the system is now defined for the sum of all densities of the components with their subspecies. The total partition function is just the product of the

individual ones, $Q_{Tot} = \prod_{i=1}^{p} Q_i$ where p represents the total number of components in the system. The resulting Hamiltonian for AB systems is thus

$$H[\Omega_+, \Omega_-] = C\left(\int d\vec{\mathbf{r}}\left((2f-1)\,\Omega_- + \frac{\Omega_-^2}{\chi N} - \Omega_+\right) - V\sum_{i=1}^{p}\ln(Q_i)\right).$$

Each *i*th component can be either a solvent of type A or B, homopolymer of A or B with different molecular weight, diBCP of different molecular weight, ABA or BAB triBCP of different molecular weight, etc. The N in the χN in the expression now explicitly refers to the largest molecular weight component with most complexity (e.g. for a blend of an ABA triBCP with A homopolymer, N would refer to the molecular weight of the ABA triBCP) chosen to define the length scales of the simulation unit cell.

For systems with more than two distinct species, the more general Hamiltonian

$$H[\boldsymbol{\phi}, \boldsymbol{\mu}] = \rho_0 \int d\vec{\mathbf{r}}\left(\frac{1}{2}\boldsymbol{\phi}\boldsymbol{\chi}\boldsymbol{\phi}' - \boldsymbol{\mu}\cdot\boldsymbol{\phi} - \frac{\kappa}{2}(\phi_+ - 1)^2\right) - n\ln Q[\boldsymbol{\mu}]$$

must be used. Since the $\boldsymbol{\chi}$ matrix in a general *c* number of species system will not generally have an eigenvector that allows ϕ_+ to be a basis vector for the density operators, attempting to reduce the Hamiltonian to only a function of the chemical potential fields $\boldsymbol{\mu}$ is no longer as trivial as the two species case and a simple relaxation scheme that is numerically stable is hard to develop for such cases. Thus for such systems explicit use of the density fields and chemical potential fields are suggested. For the most part all systems explored in this thesis work only consider two species at most, but for future potential work purposes the general case for *c* species is presented.

2.3 Relaxation Schemes

In order to find solutions that satisfy the SCFT conditions without prior knowledge of what equilibrium morphologies are possible for a given set of conditions, a numerical way to relax the fields toward equilibrium solutions must be developed that is stable. For cases where only the final equilibrium morphology is of interest, a steepest decent or similar approach is used where the states obtained during the evolution of the algorithm are evolved in a way to reach a saddle point solution as fast as possible without becoming

numerically unstable. For cases where dynamics are important, a dynamical relaxation scheme can be implemented where each iteration is broken into a time relaxation of a set number of steps to try to capture realistic dynamical evolution of a given system. Usually such simulations are best utilized if an initial melt or solution state of the system is known such that state can be seeded as a starting point for the simulation and a dynamical pathway be evolved from the starting point.

These are not the only valid methods trying to satisfy the saddle point conditions. By screening all the available space groups, Matsen found the lowest energy structures; this however is only practical for completely periodic boundary conditions[52]. A Monte-Carlo scheme can be used to sample the function directly as de Pablo has done, but the chains are described in a particle based way in this method[6,79].

Since the *ab initio* methods discussed here in general will yield potentially different solutions for a given set of initial conditions, a statistical sampling using the same system parameters but varying the initial field conditions are performed by using a different randomized seeding for the initial field state. An example of the results of such randomized initial seeding is shown in Figure 2.1 for a set of eight 2D SCFT simulations using boundary conditions with a hexagonal post array lattice of DSA features templating a diBCP. Here a number of simulations were performed using different initial seeding keeping everything else constant in the simulations. An $N_x = 84$ by $N_y = 48$ size grid was used with $\chi N = 18$, $f = 0.25$, and a fixed post spacing of $L = 3.6L_0$. Random initial states were seeded using the date and time of the simulation submission.

The expected equilibrium structure for these conditions is of a ⟨3 1⟩ lattice (meaning by starting at a post, going through 3 dots along one axis of the BCP dot structure lattice and then changing direction and going 1 more dot, a neighboring post will be found; more details of this notation is discussed in Chapter 5) based on the post spacing; several of the simulations indeed show symmetry related versions of this lattice. Still, there were often simulations with different seeding that got stuck in metastable states with defects such as the minority dot structures not being 6-fold coordinated or being locally periodic. In these situations metastable structures were found with the simulation converging to a local energy minimum structure and not the global minimum structure which is confirmed by

comparing the normalized Hamiltonian evaluated using the chemical potential fields for these structure solutions. Experiments performed for this system for this post spacing showed both ⟨3 1⟩ and ⟨4 0⟩ lattices forming thus showing that identifying such possible metastable structures is important in using SCFT to predict potential morphologies that can form[2].

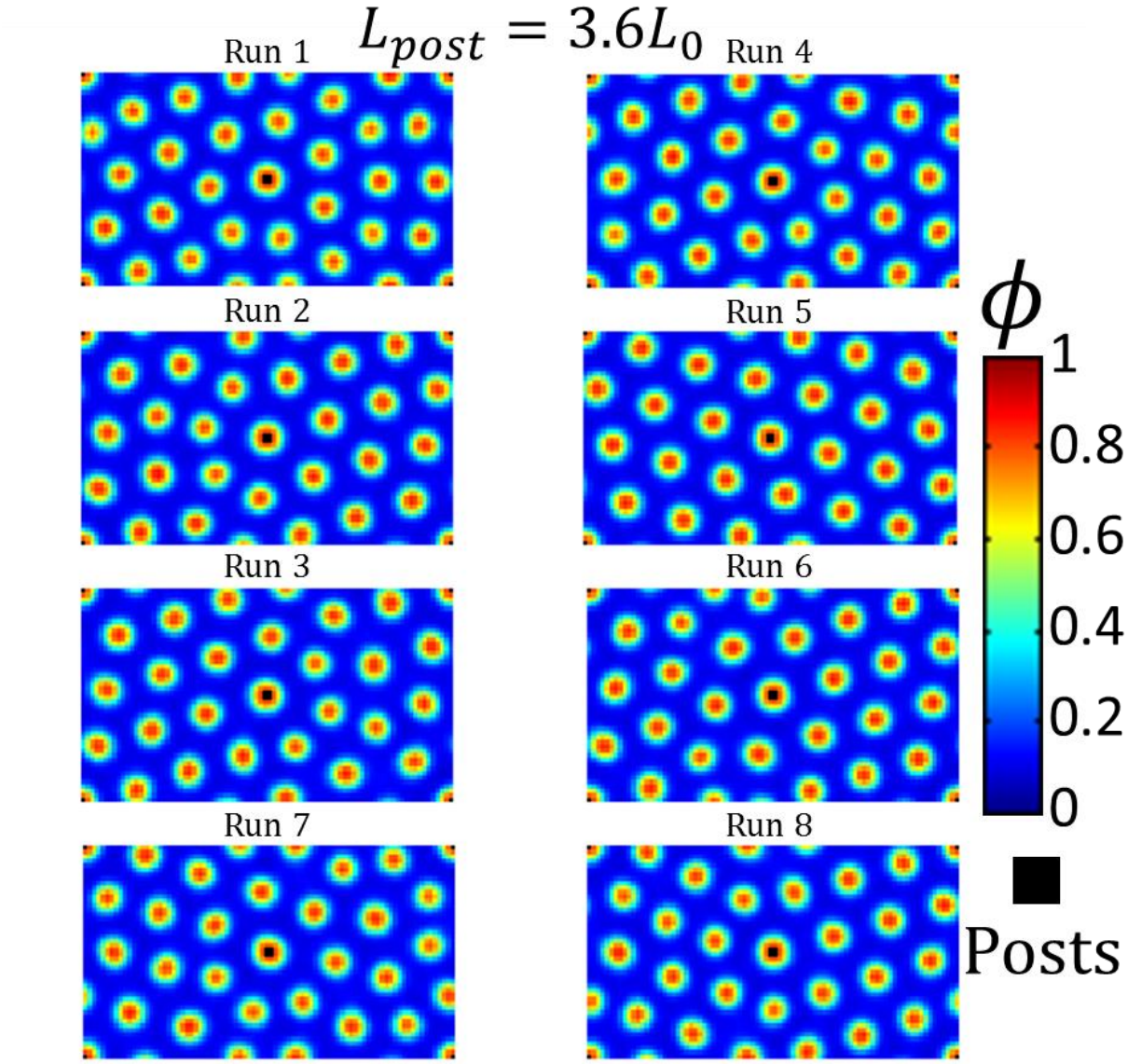

Figure 2-1: Eight 2D simulation results for a diBCP with hexagonal post array boundary conditions with post spacing $3.6L_0$ using different initial seeding. Only Run 5 showed a complete defect free ⟨3 1⟩ lattice. The others results appear to have similar underlying symmetry but with defects. Posts are at corners and middle of cells[49].

2.3.1 Steepest Decent

The steepest decent method seeks to find a way to satisfy the SCFT condition as quickly as possible by relating the partial differential of the Hamiltonian with respect to the fields with a pseudo-dynamical field derivative. In general this relation takes the following form

$$\frac{\delta\Omega}{dt} \equiv \lambda \frac{\delta H}{\delta\Omega}$$

where the variable λ is a time evolution constant that determines the rate at which the pseudo-dynamical field evolution takes place. In general one would like λ to be as large as possible to get the system to fall into the saddle point solution quickly, but if set too large numerical instabilities can occur and the system rather than converge become unstable. For every independent Ω field in the system, a λ parameter must be determined. Thus for a given simulation system, these constants must be optimized before simulations studies for various conditions can be tested to ensure numerical stability in known solutions first. Thus for increasing number of fields, finding stable relaxation schemes becomes more difficult and for most of the work in this thesis two species AB systems are studied for simplicity in using the steepest decent relaxation schemes. Once the saddle point solution is found, the equation goes to 0 and the simulation is complete.

Using this kind of scheme, one can apply this method to determine the first order steepest decent relaxation equations for a diBCP or more general a blend with two distinct chemical species. There are two independent fields for these two species systems, Ω_+ and Ω_-, and thus two saddle point conditions that need to be satisfied as follows

$$\frac{\delta\Omega_+}{dt} = \lambda_+ \frac{\delta H}{\delta\Omega_+} \text{ and } \frac{\delta\Omega_-}{dt} = \lambda_- \frac{\delta H}{\delta\Omega_-}$$

where λ_+ and λ_- are determined numerically. Using the Hamiltonian previously derived for these systems, the relaxation equations are determined as follows

$$\frac{\delta\Omega_+}{dt} = \lambda_+ C(1-\phi_+) \text{ and } \frac{\delta\Omega_-}{dt} = -\lambda_- C\left(2f - 1 - \phi_- - \frac{2\Omega_-}{\chi N}\right)$$

Numerically then if a simulation iteration is represented by j, the value of the Ω fields at iteration $j+1$ can be found as follows

$$\Omega_{+,j+1} = \Omega_{+,j} + \lambda_+ C\left(1 - \phi_{+,j}\right)$$

$$\Omega_{-,j+1} = \Omega_{-,j} - \lambda_- C\left(2f - 1 - \phi_{-,j} - \frac{2\Omega_{-,j}}{\chi N}\right) + \lambda_- \eta(\vec{\mathbf{r}})$$

Here the function $\eta(\vec{\mathbf{r}})$ is random Gaussian introduced used in complex Langevin dynamics to add noise to the system to promote the system to get out of shallow energy wells and thus only fall into deep wells[54]. For the two species systems studied in this thesis the parameters $\lambda_+ = 5.0$ and $\lambda_- = 0.0033$. Additionally, Ω_+ is not necessarily updated each iteration of a simulation. Instead a root mean square difference in the deviation of $\phi_+$from unity is calculated each iteration and if the value is too large the pressure fields are updated and if not only the exchange fields are updated. When the pressure fields are updated, the average value of the fields are subtracted since the pressure fields are invariant to a constant value[80]. For this selection of time constants, the simulations generally take anywhere from 10,000s to 100,000s of iterations to find saddle point solutions depending upon the size and dimensionality of the system.

2.3.2 Dynamic Methods

As previously discussed, the steepest decent method for relaxing the field does not produce true dynamics. To address this issue a dynamical approach can be used[53,81–86]. In these methods, an assumption is made that the longest wave length components of the fields will also be the slowest relaxing variables such that viscoelastic coupling effects can be neglected. With this assumption, the density fields will evolve with the following simple dynamical scheme

$$\frac{\partial}{\partial t}\rho(\vec{\mathbf{r}}, t) = \Lambda \nabla^2 \frac{\delta H[\rho, \mu]}{\delta \rho(\vec{\mathbf{r}}, t)}$$

with the chemical potential fields being computed using the saddle point equations from these instantaneous dynamical density field solutions

$$\frac{\delta H[\rho, \mu]}{\delta \mu(\vec{\mathbf{r}}, t)} = 0$$

where the appropriate Hamiltonian would be used for a given polymer model. Additionally for models that consider incompressibility, the pressure field must be chosen to satisfy these equations as well.

Many modifications on these dynamic schemes can be made depending on the model and the field parameters used. The main issue with any such model though is that the dynamical scheme must be solved and is an expensive computational step. In this thesis, such schemes are not implemented as the dominant factors that influence the final morphology appear to be topographical feature constraints and surface energies. However, there is evidence kinetic effects do play a role in thick solvent annealed samples and thus future studies should examine these effects. One recent study has examined such effects for thick films undergoing various quench rates with neutral preferential solvent conditions and thus there is definitely plenty of potential application for these kind of studies[87].

2.4 Solving the Fokker-Planck Equation

For the general case of a single chain Gaussian coil polymer, the single chain partition function Q is found by solving for the single chain partition propagators q using the diffusion equation known as the Fokker-Planck equation and then summing over q for the chain. Q is thus given as

$$Q[\boldsymbol{\mu}] = \frac{1}{V}\int d\vec{\mathbf{r}} q(\vec{\mathbf{r}}, s = 1, \boldsymbol{\mu})$$

and q is given from the Fokker-Planck equation

$$\frac{\partial q(\vec{\mathbf{r}}, s, \boldsymbol{\mu})}{\partial s} = \frac{R_g^2}{N}\nabla^2 q(\vec{\mathbf{r}}, s, \boldsymbol{\mu}) - \boldsymbol{\mu}\big(\boldsymbol{\phi}(\vec{\mathbf{r}}, s, \boldsymbol{\mu})\big) q(\vec{\mathbf{r}}, s, \boldsymbol{\mu})$$

with initial conditions

$$q(\vec{\mathbf{r}}, 0, \boldsymbol{\mu}) = 1$$

where s is the normalized length along the polymer chain with $s = 0$ corresponding to one end designated as the initial end of the chain and $s = 1$ corresponding to the opposite end or terminal end of the chain. Depending on chain architecture, this equation will have different $\boldsymbol{\mu}$ applied to the chain at different locations along the chain. As an example, for a diBCP with volume fraction f, $\boldsymbol{\mu}$ is given as follows

$$\boldsymbol{\mu} = \begin{cases} \Omega_A = \Omega_+ + \Omega_- & s < f \\ \Omega_B = \Omega_+ - \Omega_- & s \geq f \end{cases}$$

meaning that as q is solved forward in s that the chemical potential field used in the Fokker-Planck equation is changed for different values of s.

From these equations, the normalized densities can be computed using the relationship $\phi(\vec{\mathbf{r}}) = \frac{\rho(\vec{\mathbf{r}})}{\rho_0} = \frac{1}{Q}\int_{f_0}^{f_s} ds q^\dagger(\vec{\mathbf{r}}, 1-s, \boldsymbol{\mu}) q(\vec{\mathbf{r}}, s, \boldsymbol{\mu})$ where $q^\dagger$ is the propagator found by solving Fokker-Planck equation starting at the $s = 1$ end of the chain. Here f_0 and f_s are the f values for the given block (e.g. $f_0 = 0$ and $f_s = f$ for the A block). For homopolymers $q^\dagger = q$ from symmetry, but for BCPs the asymmetry from the block makes the forward propagator q and reverse propagator $q^\dagger$ different. Finding this reverse propagator only matters in calculating the density and the total partition function is the same regardless of which one is chosen. With this framework now in mind of how the partition function is found for Gaussian chains, three numerical ways of solving the Fokker-Planck equation will be examined. Solving for the propagators is the most computationally expensive step in SCFT and thus understanding the advantages and disadvantages of different methods is crucial in deciding upon a numerical technique to use for a given simulation.

2.4.1 Real Space Methods

Real space methods are in general the easiest methods to implement in solving second order partial differential equations such as the Fokker-Planck equation. In these methods, the system is first discretized in space into N_x by N_y by N_z grid points and along the chain into N_s statistical monomer segments. The differential operators are approximated using various finite differences between current and previous solutions divided by the discretization of the appropriate dimensions related to the inverse of the number of grid points in that dimension. Although these methods are in general easy to implement, they are usually computationally the slowest methods to solve for the propagators, require combinations of future and old solutions in order to get more accurate solutions, and are conditionally unstable for certain discretization conditions and dimensionalities. One of the

best real space methods is the Crank-Nicolson scheme that is unconditionally stable in 1D[88]. Due to the tridiagonal form of the matrix used to solve for q in 1D systems, the method appears very nice, but in higher dimensions this is no longer the case and in 3D the system is no longer unconditionally stable. Due to the slower computation times and inherent stability issues under certain dimensionality constraints with these methods, such methods were not used in the studies in this thesis.

2.4.2 Spectral Methods

For spectral methods, the differential equations are solved using knowledge of Fourier space modes that are essential constituents of the propagator solutions. Strict spectral methods choose a prescribed space group set of Fourier basis functions and use those functions to solve for the appropriate modes that satisfy the Fokker-Planck equation under the given field constraints. This approach is fine and computationally fast when the relevant modes are known, but in the most general cases this is not the case.

A more general approach is what is known as the pseudo-spectral method. In this approach, the Fokker-Planck equation is rearranged to a form where the different prefactors in front of q are grouped and treated as a mathematical operator in real space making the problem an eigenvalue and eigenvector type problem. The problem is then solved by applying a Fourier transformation on the propagator, an exponential argument representing the differential operator in Fourier space applied to this Fourier transformed q, and the altered function returned to real space through an inverse Fourier transformation. This process gives a numerical solution of q at a new step along the chain, so this process is repeated along the whole chain until the entire q is built up. By far this is one of the most computationally efficient algorithms in solving for the propagators due to the Fast Fourier Transformation algorithms available[89]. For all the studies in this thesis, the pseudo-spectral method was implemented. See the previous work of Fredrickson for more details of this method[61].

2.4.3 Lattice-Boltzmann Method

Recently a method for solving Fokker-Planck equations was implemented that allows for local refinement of the grid[90]. Whereas a fixed grid size is required for the previously

discussed real space and spectral methods, the lattice-Boltzmann method allows local refinement of grid points for getting fine structure details at things such as surfaces, interfaces, and near topographical features or nanoparticles. In general the method is more computationally expensive than the pseudo-spectral method, but for a given set of discretization parameters the algorithm converges faster, though such conditions must be optimized on a case by case basis. The general methodology for this method can be found in the recent work of Chen *et al*[90]. This method is referenced here as it can potentially be applied in future work where fine details of such features may need to be modeled to fully understand the factors influencing the morphology behavior of BCPs under topographical boundary conditions or with nanoparticle inclusion.

2.5 Boundary Conditions

To model the constraints of a given system, boundary conditions must be made to reflect the real space physical constraints encountered by the BCPs in experiments. For the simplest systems considered, periodic boundary conditions are automatically implemented since BCP systems are periodic in nature with length scales of L_0. For the more general constraints of thin films, surface chemistries, and topographical boundaries, additional boundary conditions are added to the system that yield a variety of interesting physics. Specifically in these cases for two chemical species systems or AB diBCPs, the exchange Ω_- fields were constrained to a values of W_i to model different preferential surfaces and the pressure-like Ω_+ fields were constrained to a value of P to model topographical features. As noted earlier in the section on solving the Fokker-Planck equation, the fields applied for a given chain species are composed of linear combinations of the exchange and pressure fields. Similar approaches for modeling boundary conditions of different types are applied locally to points defined to represent local interfaces, surface chemistry, and topographical features. These different kinds of constraints in general are of the form

$$\mu_{i,ext}(\vec{\mathbf{r}}) = P\sigma_+(\vec{\mathbf{r}}) + \sum_j W_j \sigma_{-,j}(\vec{\mathbf{r}})$$

where σ_+ and $\sigma_{-,j}$ are matrices of zeroes and ones of the size of the discretized system where a one value means the field value there is fixed by the mask feature constraint and a zero means those fields are allowed to evolve freely. Here j different kinds of preferential surface chemistries are considered and the subscript "ext" indicates that the field is constrained by the "external" boundary conditions chosen for the simulation. The total chemical potential for species i is then

$$\mu_i(\vec{\mathbf{r}}) = \mu_{i,ext}(\vec{\mathbf{r}}) + \left(1 - \sigma_+(\vec{\mathbf{r}})\right) \cdot \left(1 - \sigma_-(\vec{\mathbf{r}})\right) \cdot \left(\Omega_+(\vec{\mathbf{r}}) \pm \Omega_-(\vec{\mathbf{r}})\right)$$

where the $\pm$ depends on if i is the A or B species for $+$ or $-$ respectively. A schematic representation of how these mask boundary conditions are implemented is shown in Figure 2.2 for the case of thin films in 2D, 3D, and for 3D rectangular posts arrays in thin films.

2.5.1 Periodic Boundary Conditions

Periodic boundary conditions are necessary in modeling most BCP systems due to their periodic nature in addition to normal simulation considerations such as having to perform simulations on a finite grid and computational time increasing with grid size meaning larger systems take longer to simulate. In the pseudo-spectral method, periodic boundary conditions are naturally considered as the chosen basis are plane waves that have the constrained periodicity assigned to the simulation grid dimensions[53]. These periodic constraints are considered both for large cell calculations (dimensions in multiple directions much larger than L_0) or for unit cell calculations where the dimenions are assigned length scales based on the known symmetries of the underlying BCP morphology expected for equilibrium. The opposite case of periodic boundary conditions, having a completely confined unit cell in all directions, requires more care and consideration and various confinements will be examined in the following sections.

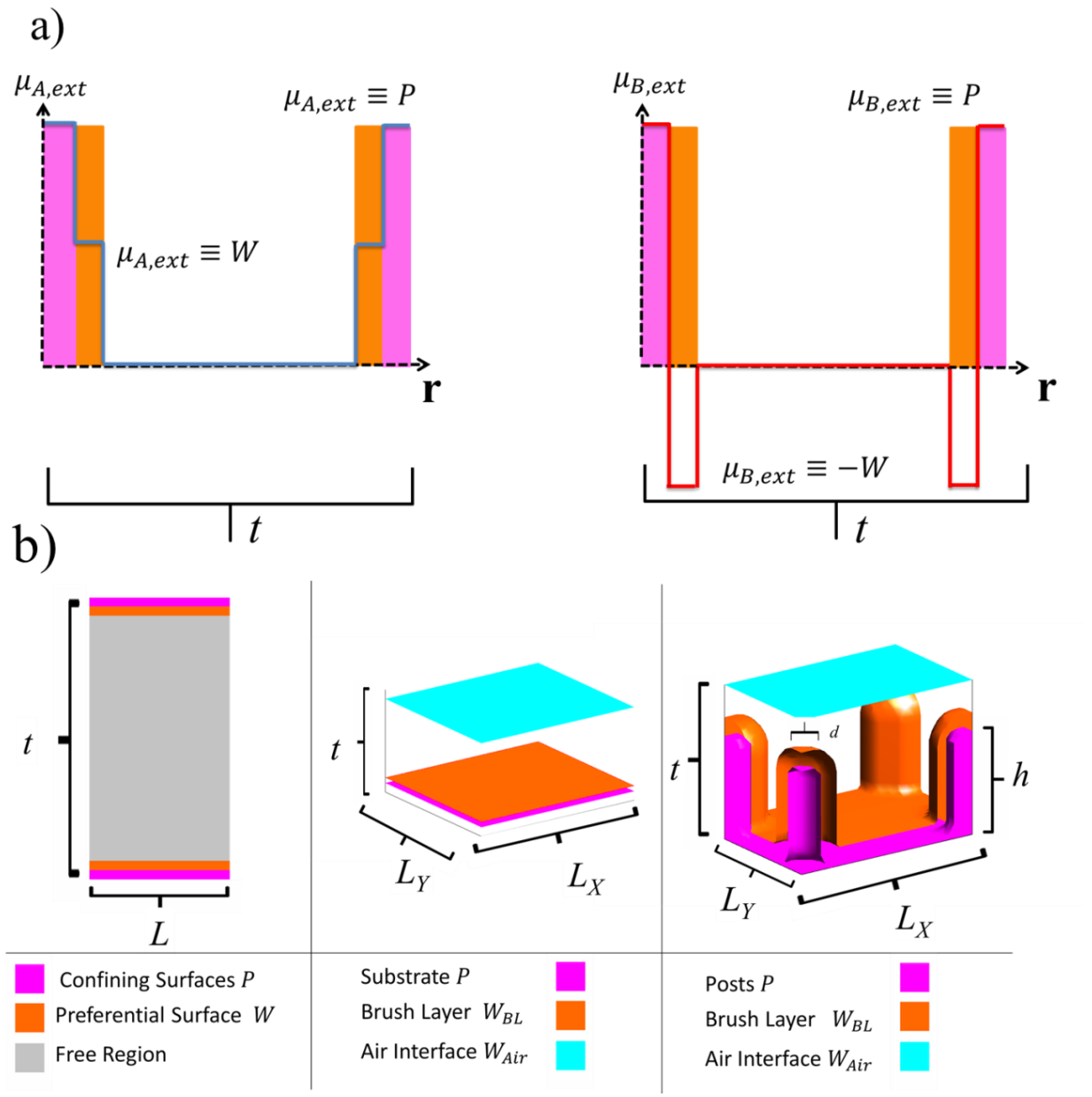

Figure 2-2: a) Diagram showing how the external field boundary conditions $\mu_{A,ext}$ (left) and $\mu_{B,ext}$ (right) were set for the A block and the B block across a one-dimensional cross section of a unit cell for the 2D thin film case. The external field values as a function of position **r** (in the through-thickness direction) for the case where both surfaces are preferential to the same block, in this case the B block. b) Schematic layout of the unit cells used in the simulation studies. Left: 2D unit cell used for BCPs confined between two impenetrable surfaces with a variable attractive surface affinity controlled by *W*. Middle: 3D unit cell used for thin film BCPs confined between an air interface and a brush layer on a hard substrate surface. The air interface surface energy is described by W_{Air} and the brush layer surface energy by $W_{BL.}$ Right: A 3D unit cell used for BCPs confined by a rectangular array of posts with variable post diameter *d* and height *h*.

2.5.2 Thin Film Boundary Conditions

For BCPs confined between two surfaces or a film of fixed thickness in 2D, unit cells with a height equal to the film thickness t and widths a multiple of L_0 with periodic boundary conditions along the in-plane direction were used. The chemical affinity of the top (air interface) and bottom (substrate interface) are controlled with W parameters W_{Air} and W_{SI} respectively. These parameters can be varied between being fully preferential to one block and being neutral depending on their magnitude. For a fully preferential surface as an example, $W \sim -\chi N$ for the minority A block and $W \sim \chi N$ for the majority B block. A completely neutral surface thus has $W = 0$ for both blocks. Since χ is related to the surface energies as $\chi \sim \gamma^2$, the magnitude of $W \sim \gamma^2$. The top and bottom boundaries represented impenetrable barriers for the BCP by having P set to a large value. Examples of studies using such boundary conditions for lamellar and cylindriccal BCP systems have been reported previously [91–93].

To model morphologies of BCPs thin films in 3D unit cells, a similar approach with 2D is used with in-plane dimensions L_X and L_Y both being some multiple of L_0 and the Z-direction being constrained to thickness t. This thickness is generally chosen to be commensurate with the formation of a monolayer of minority component features in the unit cell when the system has fully preferential surfaces. Surface energy differences between the air interface and the substrate interface are modeled using the same specific field constraint boundary conditions as in the 2D case just over a plane of the simulation box. If one polymer block has a much lower air surface energy than the other block as is the case of polydimethylsiloxane (PDMS) compared to PS, the top of the simulation cell has boundary conditions set to be preferential to the block corresponding to PDMS. If the polymers that are to be modeled have approximately neutral air affinity, then the field constraints are set to have W equal to 0. The substrate is modeled similarly depending on what types of polymer brushes are being modeled on the surface. Using the appropriate boundary conditions for the interfaces is important as the neutrality verses the preferentiality of the surfaces to the different substrates greatly affects the orientation of the morphologies observed.

In general, the total field for the two polymer species are given as $\mu_A = \Omega_+ + \Omega_-$ and $\mu_B = \Omega_+ - \Omega_-$ in the free regions, $\mu_A = \mu_{A,ext} = W$ and $\mu_B = \mu_{B,ext} = -W$ in the brush layer or air interface regions with the value of W changing appropriately for the type of feature modeled, and $\mu_A = \mu_{A,ext} = P$ and $\mu_B = \mu_{B,ext} = P$ in the substrate as schematically shown in Figure 2.2.b for the 2D and 3D thin film cases. Schematic details of how the fields are constrained for modeling thin films are shown in Figure 2.3 along with example results of modeling 2D thin films of dots and lines.

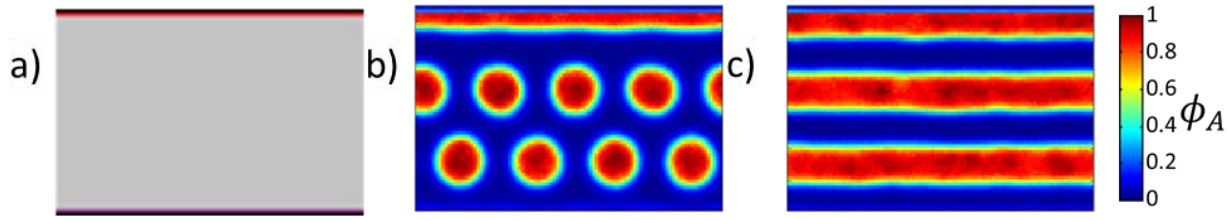

Figure 2-3: 2D schematics for SCFT boundary conditions and simulation results for those boundary conditions modeling thin films. ϕ_A density color map is on the right where A is the minority block. a) Confined boundary conditions to model thin films; grey area has no field constraints, red top area is preferential to the A block, purple bottom area is neutral to both blocks, and black area is a potential barrier to both blocks. e) SCFT results for thin films where f_A = 0.33, χN = 18.0, L_X = $4L_0$, and L_Y = $2.67L_0$. c) SCFT results for thin films where f_A = 0.50, χN = 18.0, L_X = $4L_0$, and L_Y = $2.67L_0$.

2.5.3 Chemical Boundary Conditions

Chemical patterning such as self-assembled monolayers, polymer brush layers, and surface energy differences created through EBL induced oxidation, are all modeled on the assumption the effect of such patterning allows for a range of interaction energies from fully preferential to one block to neutral preferentiality. In the context of SCFT for AB systems, regions in the simulation space can have their Ω_- constrained to a fixed value that if positive will preferentially attract the B block and thus repel the A block and vice versa for negative values. Ω_- is set to a value of 0 to model neutral surfaces. These constraints are all regulated by the W parameter discussed earlier now with the location where this parameter is fixed to be variable through the simulation cell (not just at the top and bottom interfaces). Schematic details of how the fields are constrained for modeling chemical

patterning are shown in Figure 2.4 along with example results of modeling 2D chemical patterning of dots and lines.

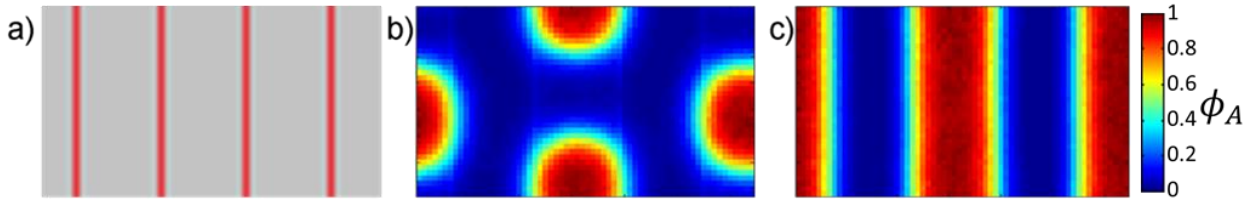

Figure 2-4: 2D schematics for SCFT boundary conditions and simulation results for those boundary conditions modeling chemical templating. ϕ_A density color map is on the right where A is the minority block. a) Periodic stripe boundary conditions to model chemical patterning used in experiment; grey area has no field constraints and red area is preferential to the A block with stripe period $P_S = 0.25L_X$. b) SCFT results of dots patterned by periodic stripes where $f_A = 0.30$, $\chi N = 21.0$, $L_X = 1.77L_0$, and $L_Y = L_0$. c) SCFT results of lines patterned by periodic stripes where $f_A = 0.50$, $\chi N = 21.0$, $L_X = 1.75L_0$, and $L_Y = L_0$.

2.5.4 Topographic Boundary Conditions

In the case of graphoepitaxy or topographical boundary conditions such as arrays of posts studied in this thesis, the posts represent a constraint where the density of the polymer must be zero. This is enforced through the external fields similar to how the thin film boundary conditions make sure the BCP density goes to zero at the box boundaries. In the region constrained by such features, $\mu_A = \mu_B = P$ where P is selected to be a large number to compress the polymer out of that region of the simulation cell while not so large numerical instabilities are introduced.

One should note that the Fokker-Planck equation is similar to the Schrödinger equation of quantum mechanics, thus the external field constraints can be thought of as the infinitely repulsive walls of the infinite potential well problem for the post constraints and as attractive wells for the brush layer or surface chemistry constraints. These strongly repulsive potentials are thus placed at the site of the posts. The wells and repulsive humps modeled by the W parameter represent whatever brush layer or surface chemistry exists around the post features. These external post features were shown schematically in Figure 2.2. The large values in the post features prevent polymer density from evolving in those regions and the well areas allow that particular block to wet and occupy that region of the simulation cell more than the other block.

For BCPs confined by regular lattices of posts, the posts were placed in the unit cell with periodicity L_X in the X-direction and L_Y in the Y-direction and the diameter d and height h of the posts can be varied as long as it is less than the fixed film thickness t. The dimensions are chosen to correspond to the experimental arrays of posts with similar dimensions and post spacings that are functionalized with various surface chemistries. 2D schematic of how these boundary conditions are applied for a hexagonal array of posts are shown in Figure 2.5[49].

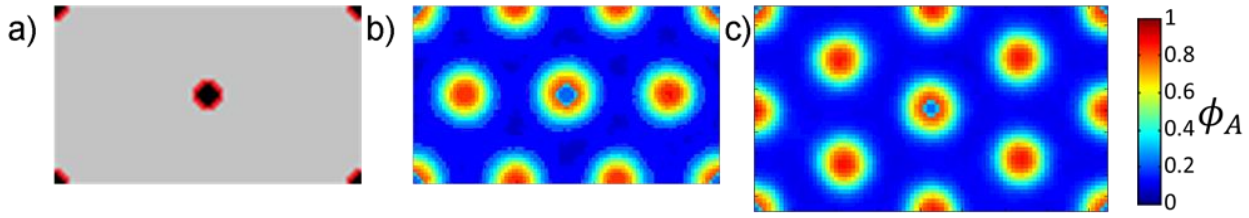

Figure 2-5: 2D schematics for SCFT boundary conditions and simulation results for those boundary conditions modeling topographical templating. ϕ_A density color map is on the right where A is the minority block. a) Hexagonal post array boundary conditions to model topographical posts used in experiment; grey area has no field constraints, red area is preferential to the A block, and black area is a potential barrier to both blocks. b) SCFT results for hexagonal post array where f_A = 0.25, χN = 18.0, L_X = $3L_0$, and L_Y = $1.73L_0$. c) SCFT results for hexagonal post array where f_A = 0.25, χN = 18.0, L_X = $3.46L_0$, and L_Y = $2L_0$.

Between 2D and 3D topographical templating boundary conditions, a few fundamental issues need to be addressed. For posts, in 2D only radius and post period effects can be investigated; in 3D post height, tilt angle, and height variable radii can all be investigated. Similarly for trenches, trench depth and gradient can be investigated in 3D versus in 2D only the spacing distance inside the trench can be investigated. A schematic of how boundary conditions are implemented in the case of a rectangular grid of posts in 3D and representative 3D results using various 3D topographical boundary conditions are shown in Figure 2.6[56–58,61].

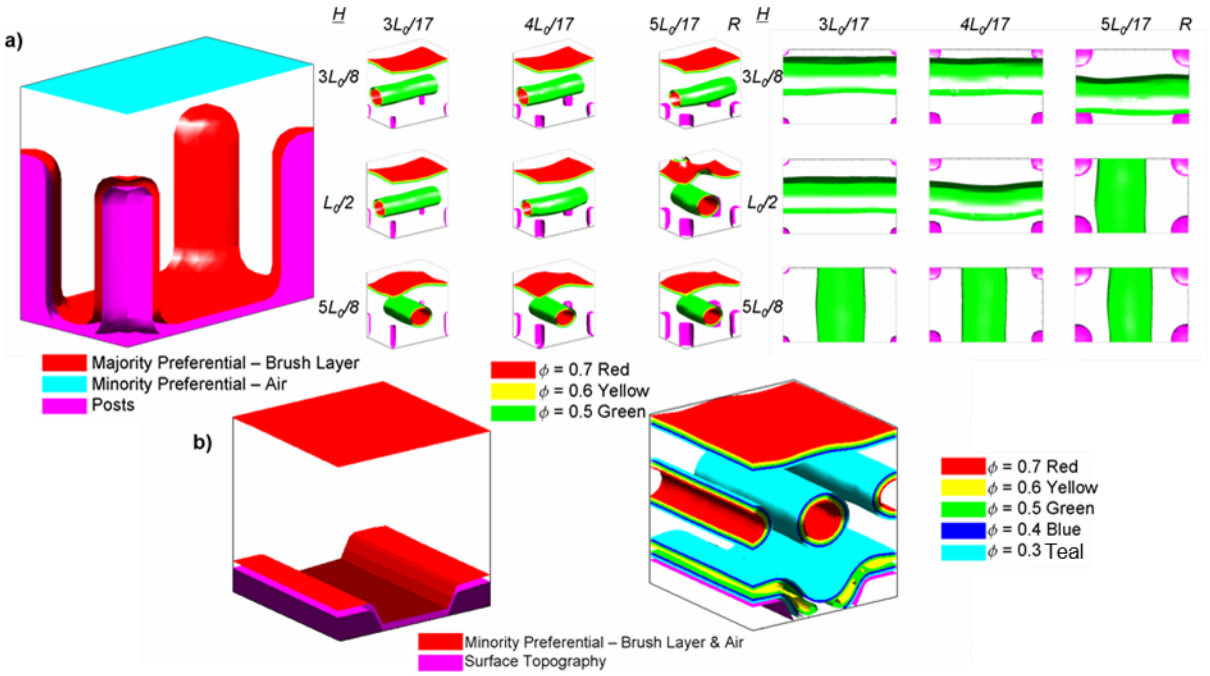

Figure 2-6: 3D schematics for SCFT boundary conditions and simulation results for those boundary conditions modeling surface topography and interfaces. Surfaces of constant density ϕ for the minority block are color coded as shown. a) Left: Rectangular post array unit cell boundary condition schematic showing regions constrained to model posts, substrate, brush layer, and air interface. Middle: Representative simulation results varying post height H and post radius R for a rectangular post array with f = 0.36, χN = 28.0, and dimensions L_X = L_0, L_Y = 1.5L_0, and L_Z = 1.5L_0. Simulations show the orientation of the templated cylinders change depending on the height and radius of the post. Right: Top-down view of the post dimension study simulations. b) Left: Trench topography unit cell boundary condition schematic showing regions constrained to model the trench surface topography, brush layer, and air interface which in this case has the same polymer preference as the brush layer. Right: Simulation result for trench boundary conditions with f = 0.31, χN = 18.0, and dimensions L_X = L_Y = L_Z = 2L_0. Simulation shows the effect of hierarchical templating using trench surface topography with twice the period of the templated BCP[61].

2.6 Summary

All the necessary methodology and theory for numerically implementing SCFT simulations has been presented in this chapter. Having these different equations and methodology, an outline for the basic progress of the simulations is presented. The algorithm goal of finding Ω^* first starts with a random or guess field configuration. The Fokker-Planck equations are solved for q at that initial state configuration for each distinct chain type. The densities for

each component are then calculated as well as the total single chain partition function Q_{Tot} and H. The fields are then updated based on these calculated values through the relaxation scheme used. These new fields are then used and the process is iterated several thousand times until H reaches an approximately constant value. Since Gaussian noise is introduced in the complex Langevin dynamics of the relaxation scheme, there is the possibility the system can escape energy wells that are not too deep, so caution should always be taken when to stop the simulations in case a metastable solution is encountered. The methods as presented do not handle situations where not equilibrium structures form due to processes such as shear aligning or concentration gradient flow thus dynamical schemes need to be implemented if such systems are to be investigated. However, the methods are well adapted for thin film systems with periodic boundary conditions and variously shaped topographical features with blends of solvents and other polymer species. Thus with these methods in place, the focus of the next chapter will look at applying these simulation methods to finding the equilibrium solutions of BCPs under well controlled SVA conditions. Then various simulation studies of thin films and topographically templated BCP systems will be examined in the rest of the thesis.

Chapter 3

Modeling Solvent Vapor Annealing Systems

3.1 Introduction

A large range of BCP thin film morphologies can be produced using solvent vapor annealing (SVA) that are different from bulk equilibrium morphologies[59]. Experimentally these morphologies are controlled by varying the flow rate of different solvent vapors and an inert gas in a control flow system or using a closed or open atmosphere of solvent vapor with controlled vapor pressures[44,59]. The experimental variables such as the swelling ratio (the swollen film thickness divided by the initial film thickness) of the films and the solvent vapor selective ratios are correlated to SCFT simulation parameters such as film thickness, effective χ parameters, and volume fractions of different components. By comparing the resulting morphologies in simulation and experiment with these various parameters, a framework for predicting the range of morphologies available under different solvent vapor conditions is produced to allow precise dimension and morphology control for lithographic applications.

SVA is an important method for achieving BCP thin film self-assembly since high χ BCPs are difficult to thermal anneal due to kinetic issues and the ordering of such χ systems is of great interest since they can theoretically form feature of size ≈ 5 nm[3,10–12,62]. Additionally, SVA allows for control on the morphology formed in systems by changing the effective volume fraction of a given BCP by varying the SVA control parameters allowing for a natural cylinder forming BCP to form spheres and lamellae structures[41]. These morphologies with their periodicity and feature sizes that normally only depend on the χ, N, and f of the BCP[40,41,94] in SVA additionally depend on the effective swelling of the two blocks with solvent selectivity. These effects on the normal control parameters will be discussed in detail in this chapter.

As a comparison with SVA, thermal annealing can lead to microphase separation and formation of equilibrium motphologies[4,95]. In these thermal annealing experiments, film thickness and substrate chemistry can be used to control the orientation and type of these morphologies to some extent[96]. Due to the simplicity of implementing thermal annealing, PS-PMMA has become a leading BCP for nanolithographic applications with a relatively low ODT temperatures such as $T_{ODT} = 200°C$ for a lamellae $f = 0.5$ molecular weight 29 kg/mol[10,97]. Since PS and PMMA have similar surface energies at normal annealing temperatures, the morphologies formed in thin film readily forms perpendicular to the substrate[10,12]. The χ for this system though is relatively low (room temperature $\chi \cong 0.06$)[98] thus reaching very small feature sizes is limited in this system. Thus higher χ BCPs are desirable to reach lower feature sizes, but T_{ODT} increases greatly with χ. As an example, a 29 kg/mol BCP with $\chi = 0.26$ would have a theoretical $T_{ODT} > 2000°C$ assuming $\chi \cong \frac{\alpha}{T}$, which would be well above the degradation temperature of ~450°C[99,100].

To get these high χ BCPs to self-assemble into desired morphologies at relevant temperature ranges, SVA can be used[44,45,68,101–110]. Assembly kinetics is much improved in SVA due to the solvent molecules plasticizing the BCP film. This solvent incorporation increases the free volume for polymer diffusion and decreases T_g[111]. In determining the appropriate solvents to use for a given BCP system, a first order consideration is taken using Hildebrand solubility parameters δ. In nonpolar materials δ indicates solubility very well with a difference in solubility parameters less than 2.5 $[MPa]^{1/2}$ indicating miscibility between polymer and solvent[112]. Flexibility and conformation of the BCP chains also affect the ability of a polymer to absorb solvent through the unwinding energy of polymer-polymer segmental contacts[113]. By measuring the film thickness *in situ* through an optical technique such as UV spectral reflectometry, the amount of solvent absorbed during SVA can be monitored to know when the system reaches equilibrium[114].

In the presence of solvent vapor, many effects on the BCP occur such as increase in volume, increase in diffusivity, decrease in effective χ such that $\chi_{eff} \cong \chi(1 - \phi_{sol})^{\alpha}$ where α is a constant close to 1 at low swelling ratios and increase toward 1.3 to 1.6 for higher swelling ratios[87,115–117], change in the relative surface energies of the blocks at the free

surface, and change in effective f that is a function of the solvent selectivity between the two blocks. Additionally, reversibility between morphologies can be controlled and morphologies changed repeatedly using different SVA conditions[44,118]. Thus a wide range of morphologies with differing periodicities can be examined using SVA[44,119–121]. The surface energy control from the solvents used can mitigate preferential wetting of one block favoring in-plane orientations of microdomains. Since high χ BCPs usually have large differences in surface energies, this effect is important if perpendicular morphologies with respect to the substrate are desired as then neutral solvent free surface environments would be desired coupled with a neutral substrate. Alternatively, such perpendicular structures can be produced using thick films with controlled directional quenching of solvent from the system which leads to a discussion on the different stages of SVA.

SVA occurs in three main stages. These stages are swelling, annealing, and quenching. In general swelling and quenching are mutually exclusive while annealing can occur during the swelling and quenching stages. For purposes of modeling, if the quench step is relatively fast or done in such a way that the annealing conditions from the fully swollen step do not vary much while solvent is removed from the system, the final state of the system can simply be considered a collapsed form of an equilibrated structure accounting for the presence of the solvent on the simulation parameters at the fully swollen film thickness. These situations will be the main focus of study for the SCFT simulations performed. Future work that accounts for slower quenching rates or thicker films where concentration gradients matter in the kinetic pathways to access the final BCP morphology will be discussed in Chapter 7.

Two main approaches to SVA have been used. The simplest experimental system uses a chamber containing a reservoir of liquid solvent or mixed solvents where the BCP film is placed above such that the evaporation of the solvent creates a solvent vapor atmosphere above the sample[120]. PS-PDMS morphology tunability has been studied using such systems with liquid mixtures of toluene and heptane[44]; poly(2-vinylpyridine)-PDMS has been studied similarly showing a greater tunability using a variety of solvent mixtures[122]. Although these reservoir systems have shown great success in using SVA to control BCP morphologies, independently controlling the partial vapor pressures of the

solvents is difficult. The other approach of SVA, using a continuous flow system, allows the simultaneous mixing, reacting, and flow of the solvents[59,123,124] thus creating the desired saturated vapor stream for the SVA. Vapor concentration is thus easily controlled[96,125] and the effect of solvent vapor pressure as well as deswelling rate has been investigated in how they affect the morphology and orientation of the features in the BCP film with one study using a combinatorial microfluidic approach[45]. A separate N_2 gas stream can be varied to control the solvent vapor pressures by dilution of the vapor stream[68,126]. In the results of this chapter, a systematic study of such control over the vapor stream will be presented.

In this chapter, the effects of flow rates of toluene and heptane vapor with a diluent N_2 gas on the thin film morphologies of PS-PDMS bulk cylindrical forming BCPs are examined. Mappings of these morphologies as a function of vapor pressure and swelling ratio are performed. Comparisons with SCFT simulations that use either implicit or explicit solvent modeling are performed to better understand how the control variables affect the BCP morphologies. Modeling SVA has been limited due to the initial black box nature of the processes, but as more experimental data has been gleaned a better theoretical framework has developed in understanding exactly what goes on during various kinds of SVA[87,117,127,128]. By examining these recent experimental studies and theoretical ideas, a general framework for understanding the nature of SVA control variables on BCP morphology is obtained and used for improving the modeling of these systems under a variety of additional boundary conditions.

3.2 Experimental Methods and Results

For experimental study, a number average molecular weight 45.5 kg/mol of PS-PDMS ($f = 0.32$ from Polymer Source, Inc. P7517-SDMS,) was used due to the polymer forming cylindrical morphologies in the bulk. Kevin Gotrik and Brent Keller designed the flow control SVA system and performed these experiments. The measured natural periodicity of this BCP is $L_0 \cong 35$ nm, although this exact value varies with SVA conditions. For comparing thin film swelling, a PDMS homopolymer of molecular weight 1390 kg/mol (100 000 cSt Dow Corning 200 fluid) and a PS homopolymer of molecular weight 1350 kg/mol PS (Polymer Source, Inc. P620-S) were used. Since lower molecular weight

homopolymers tend to dewet quickly on the time scale of minutes, higher molecular weight homopolymers were used since dewetting takes longer with increased molecular weight and the swelling interested in these studies are uniform film swelling before dewetting occurs. The control flow SVA setup had three independently controlled vapor streams which were saturated toluene, saturated heptane, and nitrogen. In a reservoir system, the solvents would have been mixed in the liquid state and vapor pressure was controlled using a small leak in the chamber which differs in this control flow setup[44].

Polymer thin films are spun cast onto the substrate using appropriate solvents for the polymer type. This substrate was functionalized using a PDMS brush for the BCP thin films that improves the kinetics of self-assembly and creates a preferential layer of PDMS on the substrate to encourage the formation of in-plane morphologies. Using a range of solvent mixing ratios and vapor pressures, BCP samples were annealed with their film thickness as a function of time being tracked by spectral reflectometry. Using a measurement of the changes in the UV absorption peaks of toluene, steady state solvent atmosphere conditions were reached after 15 minutes[129]; film annealing at 25 ± 1°C lasted approximately one hour. After 30 minutes most microphase separation had completed with correlation lengths increasing as the annealing time was increased towards one hour. Film quenching and thus morphology preservation occurred spraying the system with N_2 removing the solvent and deswelling the system in under 1 second, qualitatively measured by the change in color of the film. Reactive ion etching of the films then allowed the samples to be imaged using scanning electron microscopy by removing the PS matrix and oxidizing the PDMS features.

Here the experimental procedures are given in minute detail. Spin casting of PS-PDMS thin films of initial thickness $D_0 \cong 38$ nm and PDMS thin films of initial thickness $D_0 \cong 70$ nm was performed onto $1\text{ cm} \times 1\text{ cm}$ silicon wafers. These wafers were functionalized beforehand using a 0.8 kg/mol hydroxyl-terminated PDMS brush by spinning a solution of the polymer onto the substrate and heating for 14 hours at 170°C then rinsing with toluene to remove unreacted brush. Spin casting of PS thin films of initial thickness $D_0 \cong 70$ nm were performed on prime silicon wafers. The spin cast thin films were placed in the control flow annealing chamber and their thicknesses recorded *in situ*

using UV spectral reflectometry. Due to gradients in film thickness from spin casting, only central uniform regions on the samples were analyzed. Various combinations of flow rates for toluene, heptane, and N_2 were tested. Steady state solvent atmosphere conditions were reached 15 minutes after starting solvent and gas flow. Following 1 hour of solvent flow, rebaselining of the reflectometer was performed to account for the solvent atmosphere presence due to absorption peaks of toluene in the UV range. After rebaselining the reflectometer the polymer swollen thickness was recorded. After about 30 minutes, steady state equilibrium morphologies of the BCPs were reached as indicated by polymer swollen film thickness reaching a steady state. Further annealing helped improve long range ordering in the films as long as the film did not begin to dewet. Reactive ion etching of the films to remove any surface layer of PDMS that may have formed and the PS matrix was performed using a quick 5 second CF_4 etch for removal of any surface layer PDMS and a longer 22 second O_2 etch for removal of the PS matrix. Both plasma etches were performed with power 90 W and pressure 10 mTorr.

In the SVA, Airgas, Inc. 99.9997% purity N_2 gas with backpressure 200 kPa provided the gas flow for three MKS Inc. M100B high precision mass flow controllers (MFCs). These flow controllers were rated to control the flow rates within 1% of a set point for a range of 0 to 10 sccm. Custom solvent glass bubblers were used with two flow lines for toluene and heptane solvents from VWR >99.9% purity. The chambers were positioned in the flow line after the MFCs to prevent solvent degradation in the MFCs. Quarter inch outer diameter fluorinated ethylene propylene tubing was used for gas and solvent flow between the MFCs, bubblers, and annealing chamber. This tubing was chosen due to high resistance to absorption of toluene and heptane. Small diameter syringes were used to introduce the solvent into the annealing chamber preventing solvent backflow into the different flow lines. In addition to the solvent flow lines, N_2 gas was flowed through a separate third line for vapor pressure control. The glass annealing chamber was made with volume $\cong 80$ cm^3 with ports for solvent inflow and outflow. A quartz plate was made to cover and seal the chamber allowing for *in situ* measuring of film thickness using a Filmetrics, Inc. F20-UV spectral reflectometer with wavelength range 250-1500 nm. Tight sealing of the quartz plate with solvent vapor interaction minimization was accomplished using a Markez Inc.,

Z1210 perfluoroelastomer O-ring. The liquid solvents used in the SVA were kept at room temperature to minimize thermal gradient effects with the flowing of solvent vapor. Such thermal gradients could cause undesirable condensation of solvent vapor in the flow lines or onto the polymer sample unless the sample or flow lines are at least the same temperature as the solvent vapor.

Partial vapor pressures in the system are directly proportional to the flow rates used in the control flow system. Since the partial pressures in the reservoir system are much higher than the control flow system, a conclusion could be made the reservoir system is better than the control flow system. However, for lower molecular weights BCPs these higher vapor pressures tend to cause dewetting of the thin films and thus the control flow system is better for such systems since it can easily reach these lower vapor pressures more controllably.

An important parameter from experiment needed to correlate simulation parameters with experimental parameters is the swelling ratio $S_R = D/D_0$ where D is the swollen film thickness and D_0 is the as cast film thickness. For a homopolymer thin film and single species solvent atmosphere, the partial pressure p of the solvent is related to S_R via the solvent-homopolymer χ_{sp} via the relationship

$$\ln[p/p^*] = \chi_{sp} S_R^{-2} + \ln[1 - S_R^{-1}] + (1 - N^{-1}) S_R^{-1}$$

where p^* is the total vapor pressure[114]. Partial pressures of the solvents can be calculated from the flow rates of the solvents and the nitrogen[59]. This relationship gives the theoretical limit for the swelling of the homopolymers under each solvent. Since the actual partial pressures will be lower in practice in the control flow system, this relationship can be used to predict the highest possible swelling for the BCP system although a true relationship for the BCP system plus two solvents will in general be more complicated.

To better gauge the range of possible S_R for the system of PS-PDMS with toluene and heptane, various experiments for the swelling behavior were carried out as shown in Figure 3.1. Swelling behavior for both homopolymers of PS and PDMS as well as the diBCP were characterized by measuring S_R as a function of the mole fraction of toluene $\boldsymbol{y_{tol}}$ in the toluene and heptane vapor with no addition of N_2 gas and various solvent vapor flow rates

for one hour as shown in Figure 3.1. Heptane swelled the PDMS homopolymer greatly with $S_R \cong 3$ for pure heptane while PS swelled very little with heptane. Toluene vapor was less selective in swelling the two homopolymers as $S_R \cong 2.2$ for PS and $S_R \cong 1.8$ for PDMS. Toluene and PDMS have a large difference in Hildebrand solubility parameters δ and thus one would expect toluene to not swell PDMS much, but since PDMS is highly flexible due to a $T_g \cong -125°C$ at room temperature, more solvent was able to incorporate into the thin film. For the PS-PDMS BCP, S_R fell somewhere between the values for the homopolymers but followed PS more closely due to the fact the BCP was majority block PS. In general, S_R increased with partial pressure with maxima for PDMS homopolymer at $\boldsymbol{y_{tol}} < 0.2$ and for PS homopolymer and PS-PDMS BCP at $\boldsymbol{y_{tol}} > 0.7$. As expected from the nonideal nature of the liquid mixture, the maximum S_R for the polymer films in the control flow system was less than those achievable in the reservoir system.

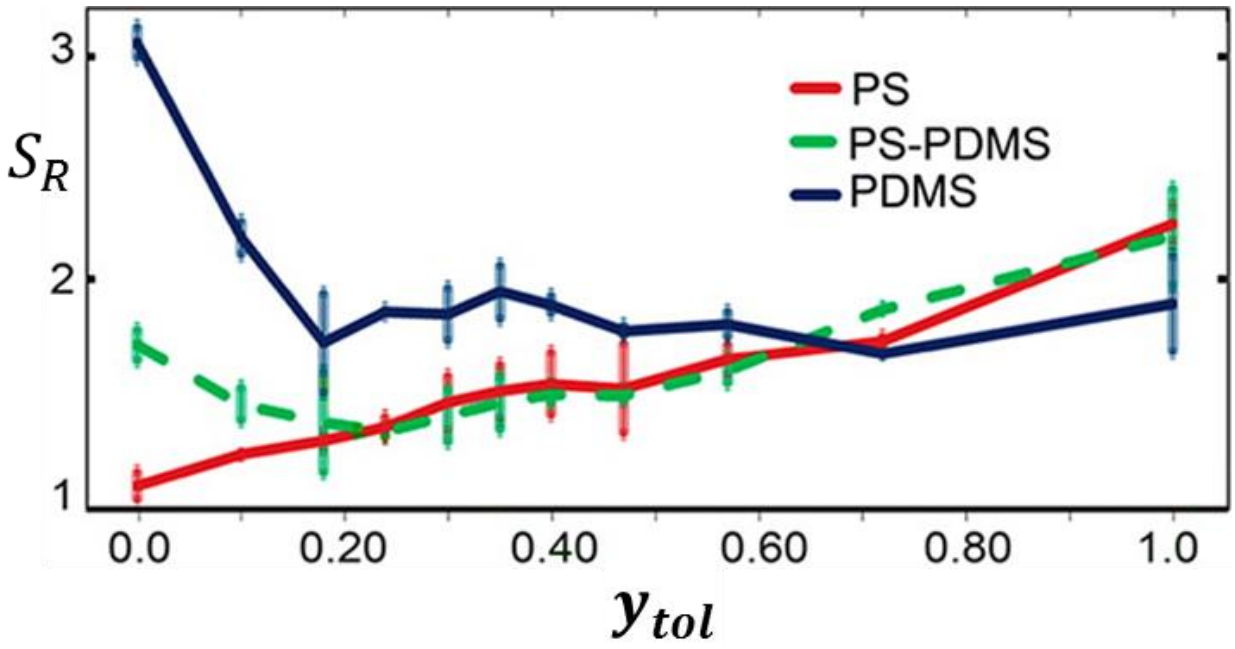

Figure 3-1: S_R=D/D_0 plotted as a function $\boldsymbol{y_{tol}}$ for PS homopolymer (red), PDMS homopolymer (blue), and PS-PDMS BCP (green)[59].

Once annealed, thin film BCP samples were reactive ion etched to remove PS matrix and leave the PDMS microdomains. Scanning electron micrographs of these etched morphologies for initial thicknesses $D_0 \cong 1.0L_0$ and $1.5L_0$ are shown in Figure 3.2 for a variety of annealing conditions. These different morphologies will later be compared to

simulations using various parameter correlations to model the effective thicknesses and solvent incorporation under the different conditions tested experimentally.

Transitions of morphologies from discontinuous in-plane $\approx 10\,\mu$m lateral dimension lamellae to perforated lamellae to in-plane cylinders with decreasing period and width occurred in the high vapor pressure regime for $D_0 = 38$ nm $\cong L_0$ with increasing $\boldsymbol{y_{tol}}$. Changing morphologies between cylinders and perforated lamellae has been observed in other studies as well using reservoir SVA systems[44]. Additionally, the low vapor pressure regime allowed access to micellar and disordered structures not observed in reservoir annealing. There were also regions where multiple morphologies coexisted on the same sample such as in-plane cylinders and lamellae.

For $D_0 \cong 1.5L_0$, the morphological transitions observed in the $D_0 \cong L_0$ films were different and in some cases suppressed. Lamellae no longer formed as readily, perforated lamellae did not form at all, and a much wider range of vapor pressures showed cylindrical morphologies. A few unique morphologies were observed over a small range of vapor pressures. As shown in Figure 3.2.f, a nonperiodic bicontinuous phase was observed. As shown in Figure 3.2.h a two-phase voided film was observed that was due likely to the aggregation of solvent in the PDMS in the film and the subsequent removal creating the voids. As shown in Figure 3.2.e, perpendicular to the substrate PDMS cylinders were observed for $\boldsymbol{y_{tol}} > 0.4$ at low vapor pressures due to the film thickness incommensurability and reduction in surface energy difference from the solvent atmosphere being more neutral at these conditions[128].

These perpendicular to the substrate cylinders having an aspect ratio of $\cong 1.1$ were confirmed by using cross sectional scanning electron micrographs[59]. Both in-plane cylinders and perpendicular to the substrate cylinders coexisted at various intermediate vapor pressures with increasing vapor pressure suppressing the formation of perpendicular to the substrate cylinders. The solvent atmosphere being neutral in the vapor pressure range where perpendicular to the substrate cylinders were observed was tested by not etching a sample with CF_4 initially that traditionally was done to remove any PDMS surface layer that was present in samples where the atmospheric conditions favored the formation of PDMS wetting layer. In this case, the same morphology was observed

indicating the solvent atmosphere conditions do indeed create a more neutral condition helping promote the formation of the perpendicular to the substrate cylinders. The perpendicular to the substrate cylinders packed in a hexagonal close-packed fashion with long range order correlations over 500 nm. This contrasts what is observed in micellar feature formation at low vapor pressures where there is little long range order and uniformity between the micelles.

Osmotic rupture was observed to varying degrees when PDMS swelled greatly and PS swelled little with interior voids being observed in the PDMS as shown in Figure 3.2.g. Such voids in PS-PDMS has been observed in other studies[130] although in these previous cases the films were completely submerged in a PDMS selective solvent. In the high heptane vapor pressure regime, two-phase regions were observed with these voids caused by the rapid removal of solvent when quenching as shown in Figure 3.2.h. All of these observed morphologies show that the control flow system allows for self-assembly of a much wider range of morphologies than the reservoir system with the perpendicular to the substrate cylinders being one of the most interesting structures for nanolithography applications.

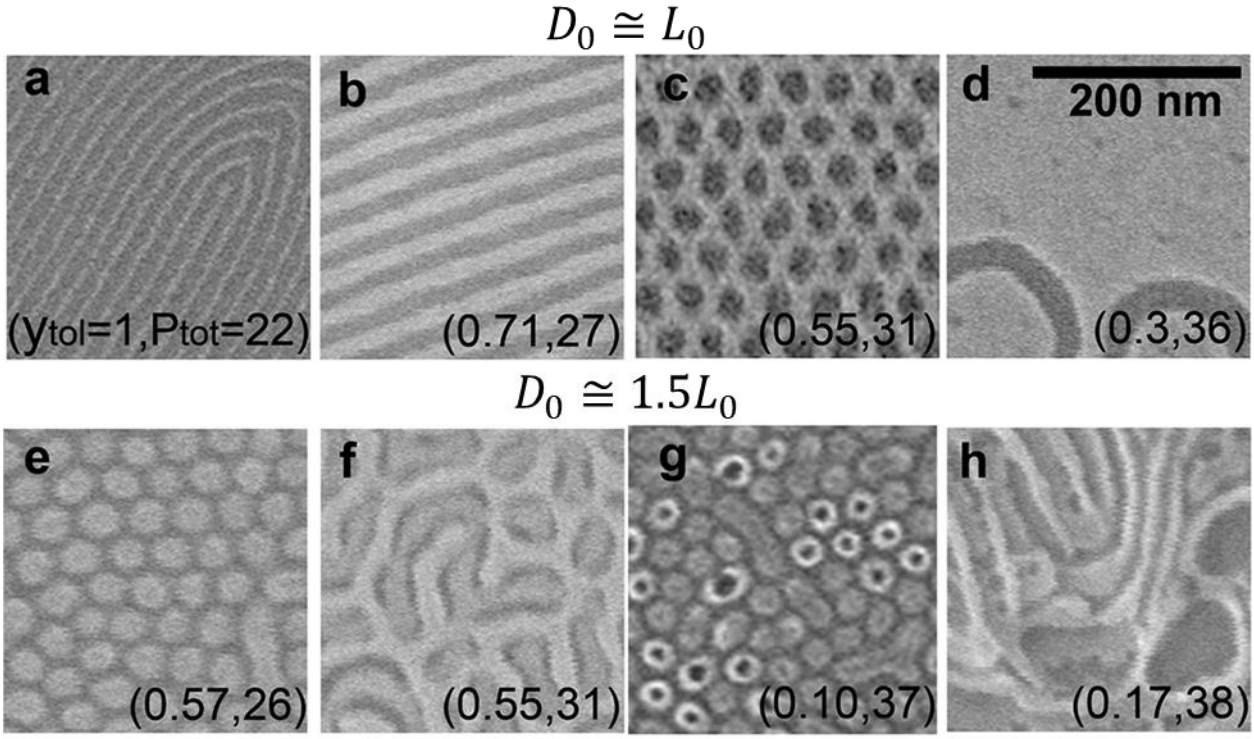

Figure 3-2: Various morphologies observed in PS-PDMS system solvent annealed by toluene and heptane vapor with $D_0 \cong 1.0L_0$ and $1.5L_0$ (total vapor pressure P_{tot} [Torr] and fraction of toluene $\boldsymbol{y_{tol}}$ in vapor are labeled in each image): (a,b) different width in-plane cylinders; (c) perforated lamellae; (d) limited width lamellae; (e) perpendicular to the substrate cylinders; (f) bicontinuous morphology; (g,h) solvent induced void two-phase morphologies[59].

3.3 Implicit Modeling

In modeling SVA, there are several simplifying assumptions that can be made to make modeling such systems approximately equivalent to a BCP melt with no solvent under thermal annealing conditions. These assumptions amount to introducing an effective Flory-Huggins parameter χ_{eff} between the two blocks for diBCPs and effective volume fraction f_{eff} of minority block and solvents that selectively swell the minority block domains; the resulting system is thus treated as an equivalent BCP melt. Such assumptions are valid either when the amount of solvent incorporated into the system is small or the solvents do not phase separate from the BCP. Such an approach is known as implicit modeling since the effects of the solvents on the final BCP film morphology are modeled using effective parameters as opposed to explicitly accounting for the solvent species in the system. For

thin film systems that do not go above the ODT due to solvent incorporation, these assumptions are generally valid and thus such assumptions should hold for high χ systems like that of PS-PDMS. The assumptions start to break down if the system goes into a disordered state while swollen or if swelling is so fast the system cannot equilibrate while swelling. For such cases kinetic effects will be important and dynamical simulation methods in future work can examine such systems as later discussed in Chapter 7.

The effective value for χ is primarily determined through the consideration of how much the solvents swell the BCP thin film. The main assumption here in the case of toluene and heptane swelling PS-PDMS is that the solvents selectively swell the blocks such that the volume fraction occupied by the solvent ϕ_{sol} is related to one minus the inverse of the swelling ratio S_R such that $\chi_{eff} \cong \chi(1-\phi_{sol})^{\alpha} = \chi S_R^{-\alpha}$. The exponent α varies with concentration and is essentially a fit parameter to determine what χ_{eff} yields the morphologies with solvent that most closely fit with the dry BCP morphologies. The experimental films in this thesis have S_R ranging from $\cong$ 1.5 to $\cong$ 3.0 meaning χ_{eff} ranges from $2\chi/3^{\alpha}$ to $\chi/3^{\alpha}$. α is usually close to 1 for low swelling ratios (the dilute regime) and recent evidence suggests values between 1.3 to 1.6 are better fits at higher S_R[117,127].

Accounting for the effective volume fraction f_{eff} is less straight forward than χ_{eff} due to an inability to know exactly how much of each selective solvent is present in each block of the BCP. To get a potential range of where the effective swollen volume fraction is, two extreme cases of swelling are considered and then a composite model developed from the previous experimental data is compared with these extreme cases. From the experimental swelling studies[59], toluene was found to be neutral or slightly preferential to PS and heptane very preferential to PDMS. Thus for the first case considered, the assumption is made that 50% of the toluene that swells the film goes into the PDMS domains and 50% of the toluene goes into the PS domains with heptane only swelling the PDMS domains. This 50% split assumption is irrespective of PDMS volume fraction. However, when both solvents are present in the BCP the presence of each solvent may influence the swelling behavior of the other solvent. This may influence the more neutral solvent toluene to be more selective to the PS since the heptane is very selective to the

PDMS and thus will limit toluene uptake in PDMS. Thus for the second case considered, we assume that toluene only swells the PS matrix and that heptane only swells the PDMS minority. We can thus define the effective volume fraction for the first case as

$$f_{eff1} = f_{PDMS}S_R^{-1} + \left(f_{hept} + \frac{f_{tol}}{2}\right)(1 - S_R^{-1})$$

and for the second case as

$$f_{eff2} = f_{PDMS}S_R^{-1} + f_{hept}(1 - S_R^{-1})$$

where f_{PDMS} is the bulk volume fraction of PDMS, f_{hept} is the fraction of solvent that is heptane in the film, and f_{tol} is the fraction of solvent that is toluene in the film. By these definitions, $f_{hept} + f_{tol} = 1$ since these equations assume there is some kind of solvent present in the film and distributes the amount to either toluene or heptane. A more general form for predicting the effective fraction of minority phase in the swollen film is

$$f_{eff3} = f_{PDMS}S_R^{-1} + \alpha(f_{tol}, f_{hept})(1 - S_R^{-1})$$

where $\alpha(f_{tol}, f_{hept})$ is a selectivity function that accounts for the nonideal and nonlinear behavior of the solvent mixing between heptane and toluene[131].

In order to develop a best fit model for $\alpha(f_{tol}, f_{hept})$, f_{eff} for PDMS needs to be estimated. The simplest model to estimate the effective swollen fractions in the BCP goes as follows. The dry film volume fraction is defined as $f_{PDMS} = \frac{V_{PDMS}}{V_0}$ where V_0 is the initial volume of the thin film and V_{PDMS} is the volume of PDMS in the dry film. The effective volume fraction of PDMS in the swollen film is thus $f_{eff} = \frac{(V_{PDMS}+V_{sol})}{V_S}$ where V_S is the swollen film volume and V_{sol} is the volume of solvent present only in the PDMS features. Dividing the second equation by the first yields the following relationship: $f_{eff} = f_{PDMS}\left(\frac{V_{PDMS}+V_{sol}}{V_{PDMS}}\right)\frac{V_0}{V_S}$. The expression is further simplified noting that $\frac{V_0}{V_S} = S_{R,BCP}^{-1}$, the inverse swelling ratio for the BCP thin film, and $\frac{V_{PDMS}+V_{sol}}{V_{PDMS}} \cong S_{R,PDMS}$, the swelling ratio of PDMS homopolymer. Using the swelling data for the PS homopolymer, PDMS homopolymer, and PS-PDMS homopolymer, a best fit of this data yields

$\alpha(f_{tol}, f_{hept}) = \beta_{tol}(f_{tol})f_{tol} + \beta_{hept}(f_{tol})f_{hept}$ where $\beta_{hept}(f_{tol})$ and $\beta_{tol}(f_{tol})$ are best fit functions to the swelling data from Figure 3.1. The values of these two fit functions are shown in Figure 3.3. Note that in fitting the data the assumption is made that $\boldsymbol{y_{tol}} \cong f_{tol}$ which is valid assuming equilibrium had been reached. Notice that $\beta_{hept}$is close to 1 over most of the range while $\beta_{tol}$is close to 0 until pure toluene is reached where the value increases to $\cong 0.25$ implying toluene does not incorporate into the PDMS much when heptane is present but does incorporate slightly when no heptane is present. This implies that the toluene is more selective to PS than previously assumed. Thus for most of the range of solvent ratios the two solvents are essentially completely selective.

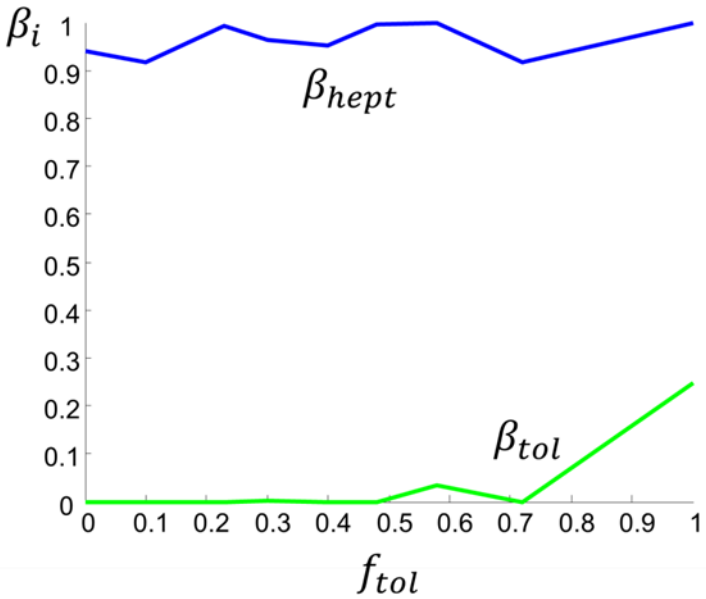

Figure 3-3: Plots of β parameters fitted using swelling data from Figure 3.1. β_{hept} in blue was close to 1 for all f_{tol} suggesting heptane is almost completely selective to PDMS while β_{tol} was close to 0 for most values of f_{tol} except in the high f_{tol} regime suggesting that toluene only swells PDMS for nearly pure toluene solvent mixtures and is purely selective to the PS domains when more heptane is mixed into the system.

Theoretical comparison plots for fixed values of S_R and two f_{PDMS} ($f_{PDMS} = 0.33$ for 45.5 kg/mol PS-PDMS and $f_{PDMS} = 0.41$ for 75 kg/mol PS-PDMS) for f_{eff1}, f_{eff2}, and f_{eff3} as a function of f_{tol} are shown in Figure 3.4. From this data, f_{eff3} should theoretically be

the best fit for the experimental system, and thus implicit solvent annealing studies should try to use values closer to the predicted f_{eff3} to best correlate with experimental results. Additionally, f_{eff1} and f_{eff2} give theoretical limits to the range of values the effective volume fraction should approach with the largest values of f_{tol} correlating better with f_{eff1} and low to highly moderate values of f_{tol} closer to f_{eff2}.

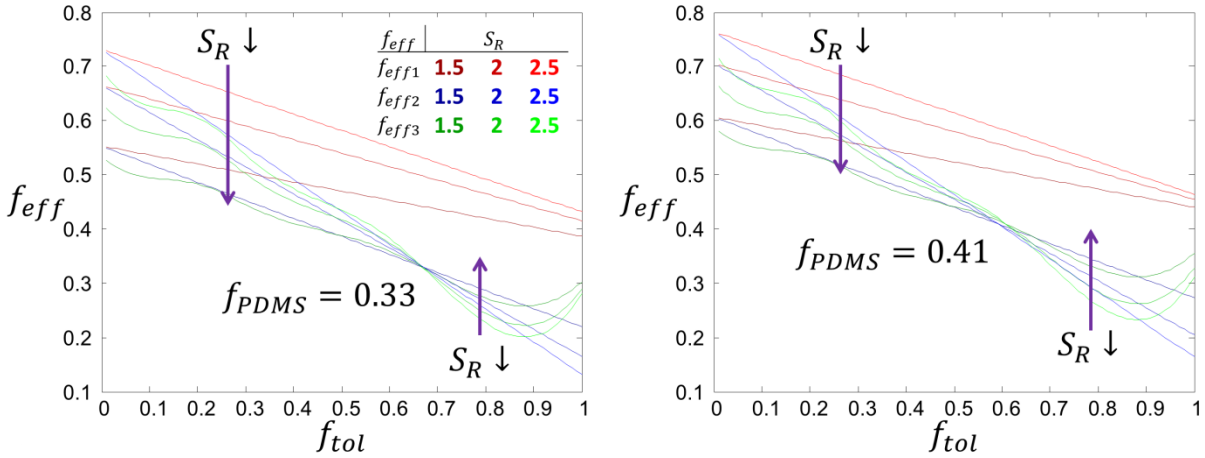

Figure 3-4: Plots of f_{eff} using three different models for f_{PDMS} = 0.33 (left) and f_{PDMS} = 0.41 (right) for three values of S_R = 1.5, 2, and 2.5. f_{eff1} shown in shades of red assumes toluene is always neutral in swelling both blocks and heptane is fully preferential to PDMS. In general f_{eff1} increases with increasing S_R since heptane always incorporates more than toluene into the PDMS. f_{eff2} shown in shades of blue assumes toluene is completely preferential to PS and heptane completely preferential to PDMS. f_{eff3} shown in shades of green was found using swelling data from Figure 3.1 assuming the homopolymer and BCP swelling data could be used to infer f_{eff}. f_{eff3} matches closely with f_{eff2} for moderate to low values of f_{tol} and then increases slightly for high values of f_{tol} but never quite reaches the limit of f_{eff1}.

As an example comparison study of implicitly modeled SVA, the morphologies observed experimentally and through implicit simulations for modeling PS-PDMS 75 kg/mol with $f_{PDMS} = 0.41$ were compared. A table of these compared results are shown in Table 3.1 with appropriate S_R and annealing conditions. The assumption is made here that the mixed vapor ratio is approximately the same in the film as in the atmosphere around the film due to equilibrium being reached. The expected equilibrium morphology using implicit modeling as a function of swollen film thickness are shown in Figures 3.5 for pure toluene for $f_{eff} = 0.25$, $S_R = 1.5$ with spheres, 5:1 toluene to heptane for $f_{eff} = 0.35$,

$S_R = 2$ with cylinders, 3:1 toluene to heptane for $f_{eff} = 0.411$, $S_R = 2$ with perforated lamellae, and 2.5:1 or 1.5:1 for $f_{eff} = 0.45$, $S_R = 2$ with in-plane lamellae.

Toluene to Heptane	f_{tol}	f_{hept}	S_R	f_{eff1}	f_{eff2}	f_{eff3}	Observed Morphology
1:0	1	0	2.5	0.466	0.166	0.313	Spheres
10:1	10/11	1/11	2.5	0.493	0.221	0.308	Spheres
5:1	5/6	1/6	1.5	0.468	0.330	0.354	Cylinders
4:1	4/5	1/5	2.0	0.506	0.306	0.327	Cylinders/Perforated Lamellae
3:1	3/4	1/4	2.2	0.528	0.323	0.323	Perforated Lamellae
2.5:1	5/7	2/7	1.5	0.488	0.369	0.361	Cylinders/Lamellae
1.5:1	3/5	2/5	1.3	0.478	0.409	0.411	Perforated Lamellae/Lamellae

Table 3-1: Comparison of effective volume fractions with observed experimental morphologies.

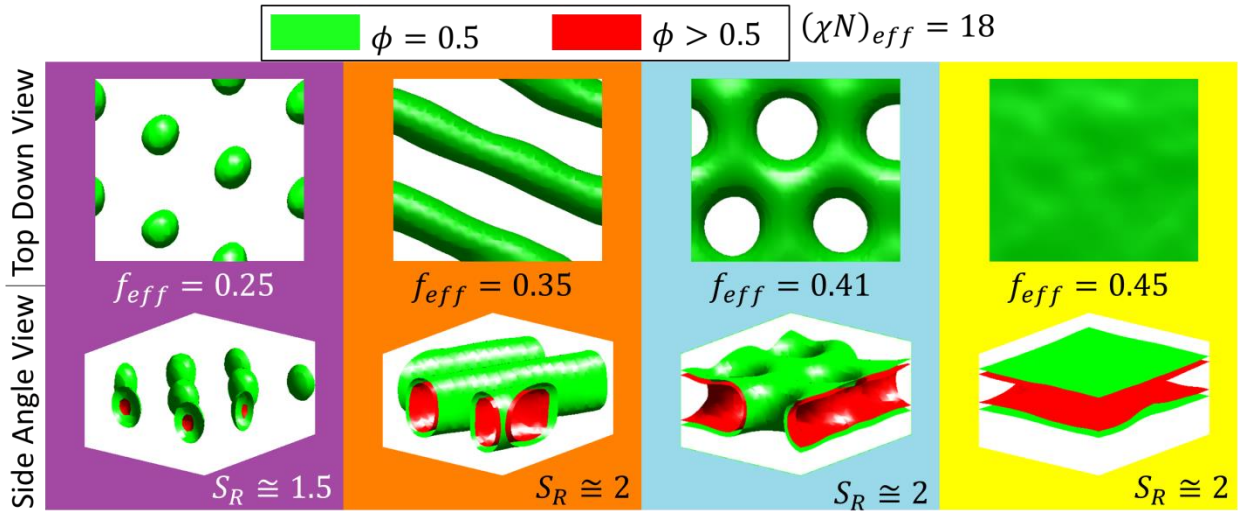

Figure 3-5: Different monolayer equilibrium morphologies found using implicit solvent annealing SCFT simulations based on PS-PDMS 75 kg/mol f_{PDMS} = 0.41 experimental system. ϕ = 0.5 isosurfaces for the PDMS are plotted in green and boundary surfaces showing the region where ϕ increases above 0.5 are plotted in red. In-plane x and y simulation cell dimensions were chosen to be around 2 to 3 lamellar L_0 lengths but not exactly commensurate as to not bias the morphologies formed. Scans over many thicknesses were done to find where the first monolayer equilibrium morphology had a local energy minima with respect to film thickness. S_R is approximately the multiple of the lamellaer L_0 where these structures had such an energy minima with respect to thickness. From left to right: Spheres at conditions corresponding to high toluene vapor, cylinders corresponding to 5:1 toluene to heptane, perforated lamellae corresponding to 3:1 toluene to heptane, and lamellae corresponding to 1.5:1 toluene to heptane.

One other parameter that has an effective value in the simulations is N, the degree of polymerization. In modeling the polymer chain, the chain is broken up into N_s statistical

segments for numerically solving the Fokker-Plank equation. The more N_s segments used the more accurate the SCFT solutions become. However, for computational efficiency only $\approx$100 such segments are used in practice since computation time scales with N_s. Additionally, N_s should not be larger than the experimental value of N since the system would be coarse grained with more segments than contained in the real chain. Thus in practice the N_s and thus N used in the simulation is normally a fraction of the experimental N and should be accounted in the values inputted in the effective simulation parameters. Practically when modeling a given diBCP system chain length is chosen based on R_g or L_0 and thus feature sizes and periods correspond through these parameters rather than the degree of polymerization itself. Only in blend systems will variations in N for each chain matter explicitly, but for single chain component systems everything normalizes to either the R_g or L_0 of that chain for experimental comparison purposes.

3.4 Explicit Modeling

Modeling solvent explicitly in SCFT simulations amounts to having an additional partition function [53–55]. Using such an approach is necessary when there are large quantities of solvent present in the system. As previously discussed in Section 2.2.3, this monotonic fluid partition function Q_{sol} is simply given as

$$Q_{sol} = \int d\vec{\mathbf{r}} e^{\Omega_{sol}(\vec{\mathbf{r}})}$$

For AB diBCP systems with solvents that are purely selective to the A and B block, the formalism using the total H for the two distinct chemical species is given as

$$H[\Omega_+, \Omega_-] = C\left(\int d\vec{\mathbf{r}}\left((2f-1)\,\Omega_- + \frac{\Omega_-^2}{(\chi N)_{eff}} - \Omega_+\right) - V\sum\nolimits_{i=BCP,solA,solB} \ln(Q_i)\right).$$

This model is excellent for the PS-PDMS system with toluene and heptane as shown in Section 3.3 since heptane is almost purely selective to PDMS and toluene is mostly purely selective to PS except when the toluene concentration is near pure. For these systems, the normalized densities ϕ_A and ϕ_B are calculated for the A or PDMS block and B or PS block using the$q$ propagator functions solved from the Fokker-Planck equation such that:

$$\phi_A(\vec{\mathbf{r}}) = \frac{\rho_A(\vec{\mathbf{r}})}{\rho_0} = \frac{1}{Q}\int_0^{f_{PDMS}} ds q^{\dagger}(\vec{\mathbf{r}}, 1-s, \boldsymbol{\mu})\, q(\vec{\mathbf{r}}, s, \boldsymbol{\mu})$$

and

$$\phi_B(\vec{\mathbf{r}}) = \frac{\rho_B(\vec{\mathbf{r}})}{\rho_0} = \frac{1}{Q}\int_{f_{PDMS}}^{1} ds q^{\dagger}(\vec{\mathbf{r}}, 1-s, \boldsymbol{\mu})\, q(\vec{\mathbf{r}}, s, \boldsymbol{\mu})$$

For the solvents, the normalized density ϕ_{solA} for heptane and ϕ_{solB} for toluene is given as

$$\phi_{solA}(\vec{\mathbf{r}}) = \frac{e^{\Omega_A(\vec{r})}}{Q_{solA}} f_{solA} \text{ and } \phi_{solB}(\vec{\mathbf{r}}) = \frac{e^{\Omega_B(\vec{r})}}{Q_{solB}} f_{solB}$$

where f_{solA} and f_{solB} are the explicit volume fractions of each solvent present and thus are two additional parameters to be considered in addition to the diBCP f_{PDMS} and χN of the system. Here Ω_A and Ω_B are defined from the set of chemical potential fields $\boldsymbol{\mu}$ as

$$\boldsymbol{\mu} = \begin{cases} \Omega_A = \Omega_+ + \Omega_- & s < f_{PDMS} \\ \Omega_B = \Omega_+ - \Omega_- & s \geq f_{PDMS} \end{cases}$$

In this model an effective χN parameter $(\chi N)_{eff}$ must be defined and is treated the same as in the implicit modeling case. To get around using such effective parameters, each solvent would need to be treated as its own species. In such a system starting with an AB diBCP, each solvent added to the system would introduce additional χ parameters for the new solvent interacting with each block and other solvent already in the system. In general this means for a p species system, there are $\sum_{i=1}^{p}(i-1) = \frac{(p^2-p)}{2}$ Flory-Huggins interaction parameters. Thus for a diBCP with a single independent solvent there would be three independent χ parameters, six for a diBCP with two independent solvents, ten for a diBCP with three independent solvents, etc. Additionally, each solvent has an independent volume fraction parameter. Thus, the degrees of freedom in exploring systems explicitly can become quite immense even for only two solvents added to the system. In this thesis only explicit consideration of AB systems for PS-PDMS with toluene and heptane were explored, but future outlook on considering p species solvent and BCP blends will be discussed in Chapter 7.

3.5 Explicit Model Results and Experimental Comparison

To gauge how the phase behavior varies as a function of solvent volume fraction, simulations were performed where the volume fraction of a diBCP was kept constant and the volume fraction of A and B selective solvents were varied using a large 2D simulation unit cell of size N_x by $N_y \cong 4L_0$ by $4L_0$, $(\chi N)_{eff} = 28$, and $f_A = 0.4$. The values of f_{solA} and f_{solB} were varied from 0 to 0.60 with the constraint that $f_{solA} + f_{solB} \leq 0.60$. Here the incompressibility constraint implies the sum of the fractions of solvent and fraction of BCP f_{BCP} must be 1, or $f_{BCP} + f_{solA} + f_{solB} = 1$. Thus if f_{BCP} is needed it is readily calculable.

The results of these simulations are shown in Figure 3.6. For small values of f_{solA} and f_{solB} the effect of adding the solvent is simply to change the effective morphology of the system if the solvent volume were considered to be the corresponding polymer species and thus similar results are expected if the appropriate effective parameters were used in an implicit simulation. This process can be seen schematically in Figure 3.6 where the morphologies observed for the pure BCP are compared with those of adding $f_{solB} = 0.15$ and $f_{solB} = 0.45$. Here the effect of increasing the fraction of B selective solvent was to push the system into hexagonally close-packed structures before becoming more isolated micelle-like structures due to the large quantity of B solvent. As seen in the overall morphology observation diagram, too much solvent eventually pushes the system above the ODT and leads to either homogeneous or local inhomogenous mixing of the BCP. Only in the lower right corner region where the total solvent fraction has not extended too much over $f_{sol} = 0.2$ does the system appear to exhibit behavior analogous to pure BCP systems. This implies for 2D systems implicit annealing modeling can work within a range of $f_{eff} = f_{PDMS} \pm 0.2$. 3D thin film systems require more attention and will be discussed in more depth in chapter 4, however a specific study related to the 45 kg/mol PS-PDMS system will be discussed briefly here.

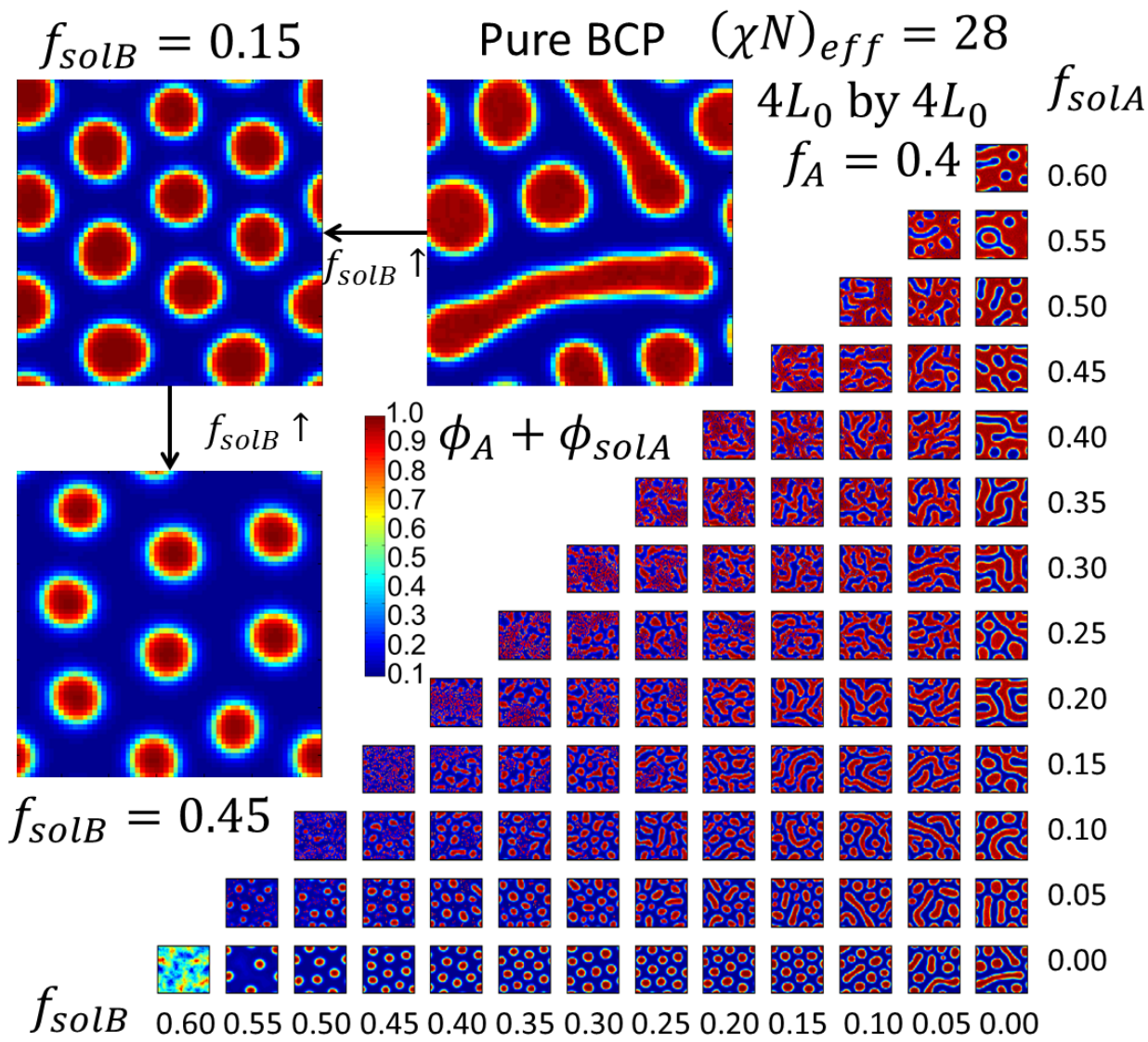

Figure 3-6: Observed morphologies using explicit solvent annealing for a 2D BCP system with both A and B selective solvents. Select morphologies are examined for comparison.

Using these explicit solvent incorporation simulations, a systematic study on the effect of adding solvents to a cylindrical thin morphology was performed. Two selective solvents were used to model the selectivity of toluene and heptane in the experimental PS-PDMS system and find potential equilibrium morphologies under the appropriate solvent annealing conditions. A complex Langevin dynamics relaxation scheme[53–55] was used to evolve a seeded in-plane cylindrical structure for reduction in computation time since most

of the structures should be cylindrical based on the base volume fraction of the BCP. This seeding biases the final morphology to have similar orientations for the cylinders.

For this system, $(\chi N)_{eff} = 18.0$ based on the following logic. For PS-PDMS, χ at room temperature is estimated to be between 0.11[132] and 0.26[118] based on different studies. For the molecular weight of the PS-PDMS used, $N \cong 485$ in terms of chemical repeat units. The coarse graining used in the simulation was $N_S = 175$ thus decreasing the effective N by a factor of 2.8. As discussed in implicit modeling section, χ_{eff} decreases proportionately with the amount of solvent in the simulation and so a value in the midrange of these potential effective values for the expected solvent incorporation was chosen to reach the value of 18[115,116]. A more detailed study could try to systematically change χ_{eff} as a function of the incorporated solvent fraction, but since trends in morphology evolution were of interest such variations in the χ_{eff} parameter were reserved for later studies. The solvent incorporation here was modeled explicitly using various amounts of A and B selective solvent fractions. The overall copolymer volume for different swelling ratios was held constant since this should not change in real swelling experiments, thus the swelling ratio dictates the total amount of solvent added in the system.

Since toluene swells both blocks at high concentration, in the model the actual corresponding fractions of solvents can be thought to be partitioned between the two solvents. The A solvent is thus mostly heptane with some toluene and the B solvent is completely toluene in the model. These simulation results are shown in Figure 3.7. An initial simulation with no solvent incorporated was performed in a periodically bound unit cell with in-plane dimensions $3L_0$ by $2\sqrt{3}L_0$ and f = 0.32 to verify that the equilibrium morphology of the unmodified thin film was indeed cylinders as expected at the initial monolayer commensurate thickness of $D_0 = 1.7L_0$ for the assumed case that the top and bottom surface layers were PDMS preferential. These in-plane dimensions were chosen to be commensurate with hexagonally close-packed structures that might evolve from the system under different solvent annealing conditions. Having verified the cylindrical morphology was the equilibrium structure for the system with no solvent, the chemical

potential fields of that structure were seeded into simulation cells with increased thickness and the additional thickness volume having the fraction of solvent added to the system corresponding to the change in film thickness for various ratios of the selective solvent. These now solvated simulation unit cells were relaxed using complex Langevin steepest descent dynamics and the new structures verified as potential modified equilibrium structures due to the presence of the solvent. For each case the relaxation was done multiple times to ensure metastable structures were not being encountered.

The precise method of inducing swelling involved increasing the unit cell grid size in the *z*-direction by a discrete amount, usually one or two grid points at a time in that direction. Defining the amount of selective solvents present as S_A and S_B the ratio added defined as $\frac{S_A}{S_A+S_B}$ was systematically varied between 50% to 100%. At the time these simulations were performed toluene was assumed to be completely neutral preference to the two blocks, although this now appears to only hold when only toluene is present. However, the basic idea here is that the 50% ratio is closer to pure toluene and the 100% ratio is closer to pure heptane. For characterizing morphologies observed, any connections forming between the original seeded cylindrical structures constituted as perforated lamellae. Similarly, lamellae were defined when the entire in-plane cylinders connected.

Increasing the solvent selectivity toward the minority block resulted in a transition from thinner cylinders to thicker cylinders to perforated lamellae to in-plane lamellae. Compared with experimental results, these transitions agree qualitatively as the same sequence of morphological transitions are observed by increasing the ratio of heptane solvent in the system. Additionally, higher vapor pressures in the experiment showed cylinders were more prominent due to the higher swelling ratios at these higher vapor pressures meaning more heptane would be necessary in these regions to proportionally push the morphologies into the lamellae regime. From the experimental results in Figure 3.2.b, the experimental results do show cylindrical morphologies at these higher swelling ratios. All these comparisons show these simulations correspond well with what is observed experimentally. As has been suggested for thin film systems with high χ values that are swollen below their ODT, most of the morphological transitions that occur happen

during the film swelling and equilibration period in the solvent once swollen and little essential morphological change occurs during the quenching step[108]. Other recent studies using *in situ* GiSAXS suggests similar results[117] and thus effects due to quenching can be neglected since the films studied here are only a few monolayers thick at most and are not swollen above their ODT such that the solvent would quench the BCP self-assembly during swelling but instead mediates the ordering. Perpendicular to the substrate cylinders were not observed in these particular simulations since the surface chemistry was fixed as PDMS preferential which would theoretically change in the real system as solvent ratios were changed as well as the solvent ratios needed for such structures not being examined.

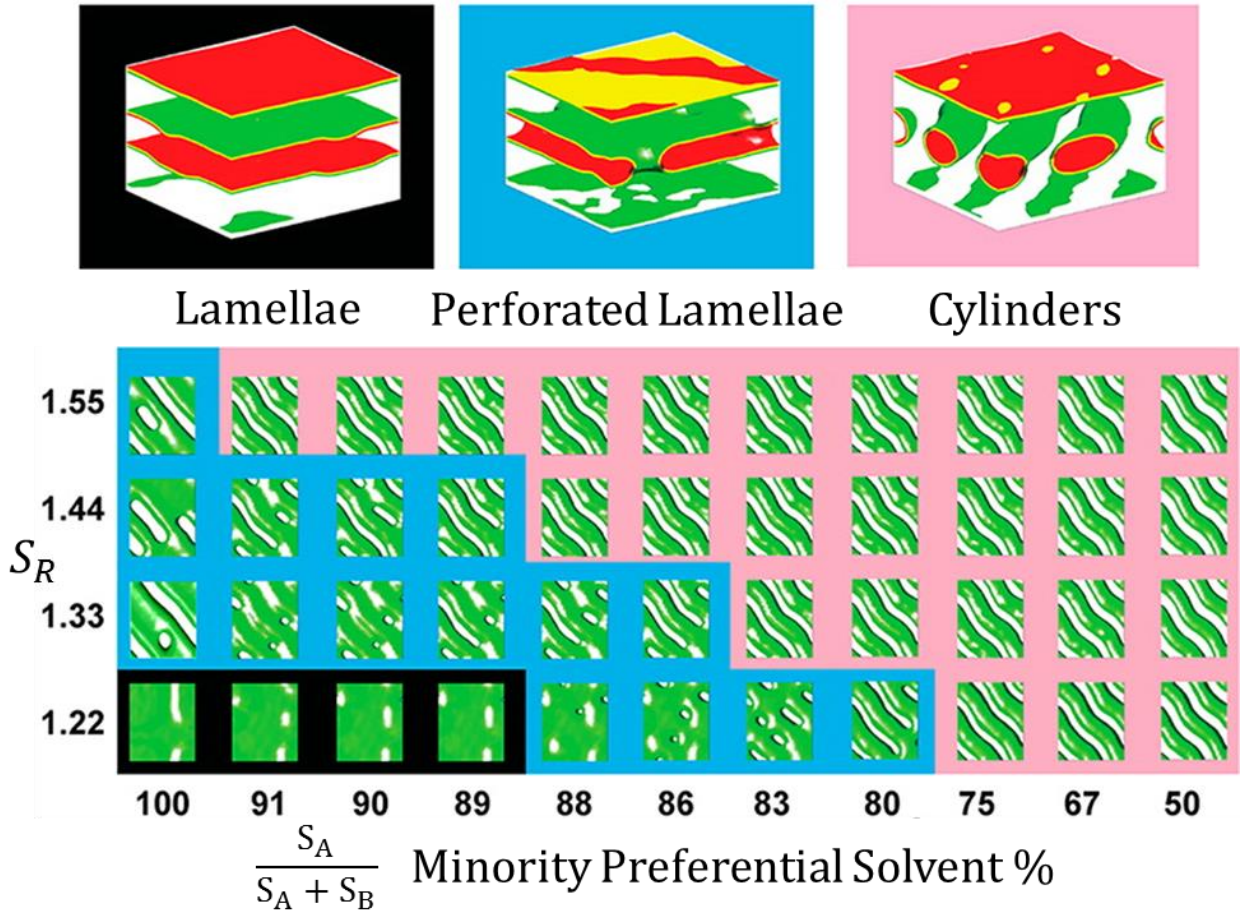

Figure 3-7: Simulation results using explicit solvent modeling SCFT of a cylindrical forming BCP with block selective solvents in different ratios and different swelling ratios $S_R = D/D_0$. Isosurfaces of total PDMS selective solvent and PDMS density are plotted in green for ϕ = 0.5 with yellow being ϕ = 0.6 and red being $\phi \geq 0.7$. Separated cylindrical morphologies are color coded pink, perforated lamellae morphologies color coded blue, and in-plane lamellae black[59].

3.6 Summary

Control flow SVA and reservoir SVA can both be well modeled and characterized through both implicit and explicit solvent annealing simulations. For the thin film systems of PS-PDMS examined in the rest of this thesis, both implicit and explicit simulations were used to model thin film systems and implicit simulations with effective parameters were used to model topographical DSA thin film BCP systems based on the assumption the morphologies in these systems are dominated by topography commensuration effects. Experimentally, the control flow SVA method shows great potential in accessing a wide control parameter space not easily accessible without synthesis of new BCPs in the case of thermal annealing or by carefully making each individual chamber for the reservoir systems. This method is advantageous for simulation comparison studies since the vapor pressures reached are not strictly reachable in the reservoir system and thus mapping simulation parameters with the experimental control parameters of vapor pressures, solvent ratios, and swelling ratios becomes a more systematic process. Many different morphologies are accessible from the same BCP using this method as well such as perpendicular to the substrate cylinders which has not been observed for reservoir systems with PS-PDMS.

Low molecular weight BCPs need lower vapor pressures to self-assemble properly using this system which is easier to control than in the reservoir based systems such that dewetting does not occur. All the qualitative morphological transitions observed experimentally are captured in the SCFT simulations and more quantitative comparisons are possible as fine details are introduced in the explicit modeling for effects like quenching that are being considered by recent studies. The quenching process is definitely important in many systems, thus future work will look at applying dynamical models to investigate how nonequilibrium morphologies can form with different quench pathways. SVA is definitely one of the key ways of accessing the periods, morphologies, and critical dimensions necessary for enabling the next generation of nanolithography, and thus modeling these systems are extremely necessary. These systems and models are very adaptable for other more complex systems such as additional solvent inclusion, blended

systems, nanoparticle inclusion, etc. and such complexities will be elucidated in the studies of topographical DSA systems in Chapter 5. Before examining such complexities, key issues in modeling thin film boundary conditions will be examined first in the next chapter.

Chapter 4

Modeling Thin Film Boundary Conditions

4.1 Introduction

In modeling BCPs directed self-assembly (DSA), understanding the equilibrium phase behavior of BCPs in the thin film state is important due to the majority of DSA currently being possible only using templates that are part of a substrate that cannot extend very far into the BCP material. Although bulk 3D DSA would be an interesting endeavor with many potential applications, current technological limitations make creating such 3D templates for the BCPs difficult both in fabrication and analyzing resulting morphologies[133]. Thus understanding DSA of thin film BCPs is the starting foundation to enable such future endeavors. In this chapter, thin films of usually no more than two layers of BCP features will be examined. Before adding topographical boundary conditions, the general effects of top and bottom surface chemistry with pure thin film boundary conditions need to be established; by doing so an understanding of how film thickness and surface preferentiality plays a role in determining the natural thin film morphologies of BCP systems is developed. With these trends determined in the model, understanding the effects of topographical boundary conditions in the next chapter will be made easier.

In order to fully understand thin film morphological behavior, full 3D simulations are necessary to capture the effects of surface and substrate energy effects on the morphology in addition to allowing for periodic boundary conditions to account for the natural periodicity of the BCPs in the thin film plane direction. 2D simulations can still be useful in elucidating information either in thickness cross-sections to examine thickness commensuration effects as well as surface energy effects or planar cross-sections to try to gain information on the planar periodicity of the structures. However, in general these

effects are coupled in determining the final equilibrium morphologies and ultimately 3D simulations are necessary for capturing all the physics of the thin films.

In this chapter several studies both in 2D and 3D will be examined of a variety of conditions to get a better understanding of how thin film BCP self-assembly is affected by various annealing conditions and substrate chemistry. Discussion on how comparisons with experiments should be carried out will be presented as well as some example experimental results. The simulations reveal general trends in morphology dependence on the key control parameters of surface energies γ, film thickness t, f_{eff}, and $(\chi N)_{eff}$ so that DSA studies can be done in a more systematic way with the understanding of the base morphologies in a given set of conditions. All these effects gained in modeling thin films allow for a better framework of understanding BCP DSA.

4.2 Thin Film Studies

Simulation approaches have become invaluable in studying the microphase segregation behavior of BCPs confined on flat surfaces, in cylindrical pores, and in spherical pores, with such systems having been explored extensively[67,134–142]. These results predict that complex morphologies such as helical cylinders in cylindrical pores or concentric spherical shells in spherical pores can form spontaneously[134,143–145], as well a wide range of morphologies produced under tunable boundary conditions[146–152]. The thin film state of BCPs is analogous to the flat surface confinement except that the top surface is actually a free surface. However, prior experimental studies have shown the primary effect of having a free surface is that the BCP can form hole and island structures when not deposited at a commensurate film thickness[153–155] and thus the equilibrium phase behavior of confined flat films at commensurate thicknesses correspond to the thin film phase behavior examined in this chapter.

There has been considerable work on the microphase separation of BCP thin films under topographical boundary conditions[2,8,10,12,24,61], including the effects of arrays of nanoscale posts on a cylindrical-morphology BCP[28,49,56–58,60]. This latter work has revealed the importance of commensurability between the BCP equilibrium period and the post period, and the effect of the substrate chemistry, i.e. whether the substrate surface is

attractive to the majority or minority block of the BCP. Focus on these nanoscale post arrays and other topographical post conditions will be discussed in depth in Chapter 5.

Before examining the effects of surface topography on BCP thin films, general thin film behavior due to film thickness t commensuration and surface energy γ effects will be considered. SCFT simulations of microphase separation of BCPs are presented in a variety of cases for these thin film effects. Self-assembly of thin films of lamellar and cylindrical morphology BCPs on smooth substrates with different chemical affinity are described. Understanding the behavior of these features on a pure substrate is important for later comparing with the self-assembly of a cylindrical morphology BCPs templated on a substrate patterned with an array of posts with a range of height h and diameter d.

SCFT provides a method to test the effects of χ, the segmental Flory-Huggins parameter, N, the degree of polymerization, and f, the volume fraction of the minority block, on the equilibrium morphologies of BCP systems both computationally efficiently and without *a priori* knowledge of the exact equilibrium structures[53–55]. Additionally, the effects of surface energies and topographical boundaries can be incorporated by setting appropriate boundary conditions[49]. The inclusion of local surface energy and topographical features is important in designing templates to generate complex patterns for nanolithography applications[6,17,156,157].

Here, different confinement boundary condition cases are examined. The first case of 2D confined thin film lamellae systems with symmetric surface preferentiality were performed to ensure the model used was consistent with previous results in addition to examining a finer range of surface preferentiality. These 2D simulations use effective parameters and thus can be considered as models of either thermal annealing or implicit solvent annealing. For 3D confined thin film systems, simulations were performed to examine asymmetric strong surface preferentiality cases and symmetric strong preferentiality cases in addition to confirming the optimal thickness necessary for a monolayer of features for post confined systems discussed in Chapter 5. For these various 3D thin film cases, implicit solvent annealing conditions for cylindrical bulk and gyroid-bulk forming BCPs are examined and compared with their bulk morphologies. Additionally, some simulations using explicit solvent added to thin films to demonstrate the effect of

swelling on ordering of the system are examined for a variety of volume fractions, film thicknesses, and surface energies.

4.2.1 Simulation Results in 2D – Lamellae

The following set of simulations was performed to determine how much an effect the surface chemistry, W, had on whether the morphology formed was completely parallel to the surface morphology, a mixed morphology, or perpendicular to the substrate morphology. Previous simulation studies using Monte Carlo simulations have been performed, so these simulations serve to gauge the effectiveness of the SCFT simulations in modeling thin film BCP systems[135]. For systems confined between two surfaces, the reduced thickness t/L_0 was varied from 0.50 to 3.00 and the top and bottom surface affinity was varied from $W = -10.0$ to 10.0 where W is the constrained value of the exchange field Ω_- as previously discussed in Chapter 2 Section 2.5. Here L_0 is defined as the unit cell length where the minimum free energy point for a seeded simulation of a single repeat of lamellae was constrained to retain that morphology by constraining the density fields while the unit cell lengths was varied. The schematic for the boundary conditions of this system was shown in Figure 2.2.b on the left. In these simulations, $f = 0.5$ and $\chi N = 18.0$ (corresponding to PS-PDMS with $\chi = 0.224$ at room temperature[158], effective $N = 80$, molecular weight 7.1 kg/mol and $L_0 \cong 8.7$ nm). Note that recent studies suggest the actual χ of PS-PDMS may be as low as 0.14 at room temperature[132] compared to the previously assumed value of 0.224, but the simulations studied here were done before these studies took place and thus used the previous values. This is of little consequence to the simulation studies though as they should be applicable to any potential real BCP with these same parameters.

The morphologies included lamellae perpendicular to the surface ($\perp$), T-junction lamellae (T), T-junction lamellae mixed with lamellae parallel to the surface (PT), and parallel lamellae (Pn) with the total number of PS and PDMS layers varying from $n = 2$ to 7. In multiple simulation runs, some conditions yielded either parallel or perpendicular morphologies ($\perp$P) where these two orientations were approximately degenerate in their free energy. Similarly, both T-junction and perpendicular structures were observed for

other sets of conditions. These morphologies are all shown in Figure 4.1. The morphological phase diagram in terms of reduced thickness t/L_0 and W using the background color coding from Figure 4.1 is shown in Figure 4.2; the lowest energy configuration over multiple simulations were used for this phase diagram in cases where more than one morphology was predicted. Due to the symmetry of the lamellar BCP, this phase diagram is symmetric between the PS and PDMS blocks as effects due to monomer Kuhn size differences were not addressed at the coarse graining used.

For highly preferential surfaces with $W > 5.0$, lamellae parallel to the surface were almost always observed with the number of distinct layers n increasing as a function of the thickness of the film. In general for the highly preferential regime, when t/L_0 is approximately an integer value (i.e. the polymer is commensurate with the constrained thickness) n is odd ($t/L_0 = 1.0$ corresponds to $n = 3$, $t/L_0 = 2.0$ corresponds to $n = 5$, and $t/L_0 = 3.0$ corresponds to $n = 7$) with the block forming the top and bottom layers matching the preferential boundary condition surface.

When the film thickness was incommensurate with L_0 (e.g. $t/L_0 = 1.5$) there is a competition between perpendicular lamellae and either highly strained in-plane lamellae where both surfaces are in contact with the preferential block (n is odd) or low-strain in-plane lamellae where one surface is in contact with a layer of the non-preferential block (n is even). For $t/L_0 = 0.5$ and $W > 5.0$, perpendicular lamellae were observed but in-plane lamellae with $n = 2$ occurred at slightly higher incommensurate thicknesses in which a polymer layer was in contact with an unfavorable surface. At $t/L_0 = 1.5$, in-plane lamellae with $n = 4$ formed. However, at $t/L_0 = 2.5$ the larger number of layers was better able to accommodate the strain, and odd-n configurations ($n = 5$ and 7) occurred instead of $n = 6$.

For less preferential surfaces with $W < 5.0$, a variation between perpendicular, parallel, and T-junction lamellae was observed. When the films were incommensurate with t/L_0 close to half integers, perpendicular structures dominated the energy landscape whereas parallel lamellae were observed more commonly when close to commensuration. T-junctions occurred at $t/L_0 > 2.0$ between half integer and integer values of the reduced thickness for the low preferentiality values. Throughout the phase diagram there were multiple metastable regions observed where the energies of perpendicular, lamellae,

and/or T-junctions were approximately degenerate. For neutral surface boundary conditions, lamellae perpendicular to the surface were almost always observed.

The formation of the morphologies in the different regions on the phase diagram is explained in terms of a competition between minimizing the strain energy and the surface energy of the polymers. Since the surface energy is about the same for both polymers at low W values, perpendicularly oriented lamellae are more favorable with little strain. For highly preferential substrates the surface energy reduction can give a lower total energy for in-plane lamellae, even if this leads to a through-thickness strain when the thickness is incommensurate.

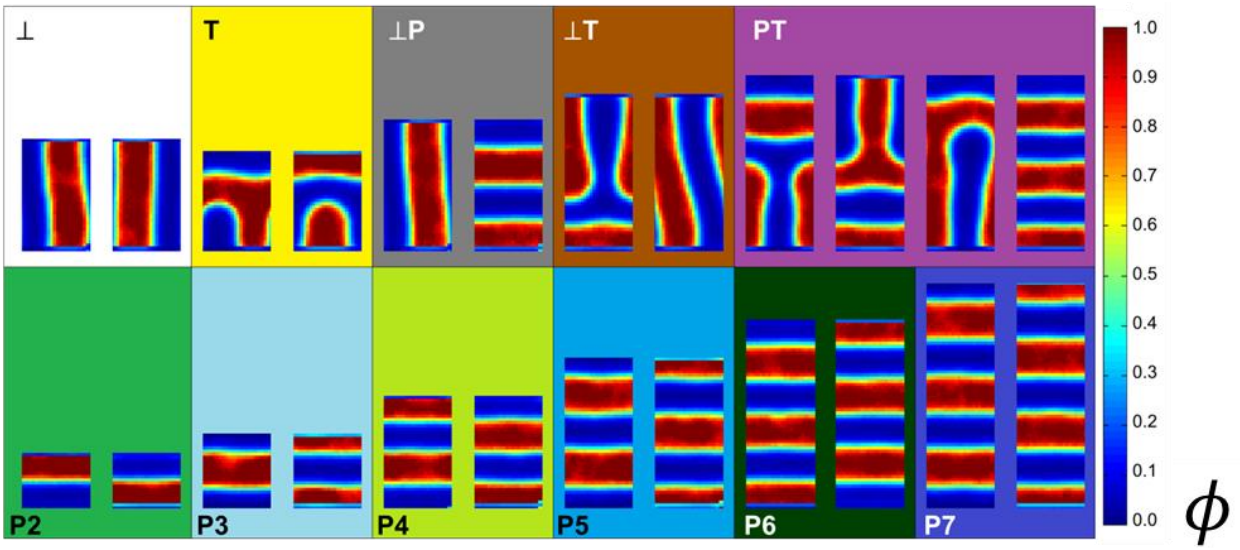

Figure 4-1: Representative lamellar morphologies observed in 2D thin films. (⊥) Perpendicular. (T) T-junction. (⊥P) Metastable perpendicular/parallel. (⊥T) Metastable perpendicular/T-junction. (PT) Metastable parallel/T-junction. (P2) n = 2 parallel. (P3) n = 3 parallel. (P4) n = 4 parallel. (P5) n = 5 parallel. (P6) n = 6 parallel. (P7) n = 7 parallel. ϕ represents the density of one of the blocks.

The trends in the observations of these simulations generally agree with previous work on lamellar systems that used Monte Carlo-based simulations[67,91,135–141,159,160] as well as with experimental work that examined the case of neutral and highly preferential surfaces[148]. Neutral surfaces favored perpendicular lamellae while preferential surfaces favored parallel lamellae. When t/L_0 was commensurate with the number of half layers of lamellae, parallel lamellae formed even for small preferential surface energy values. The reduced thickness values where the number of half layers was observed for the strong

preferential regime agree with previous studies[149]. $W = 10$ or -10, representing highly preferential surfaces, produced parallel lamellae except for thin incommensurate films[55,141].

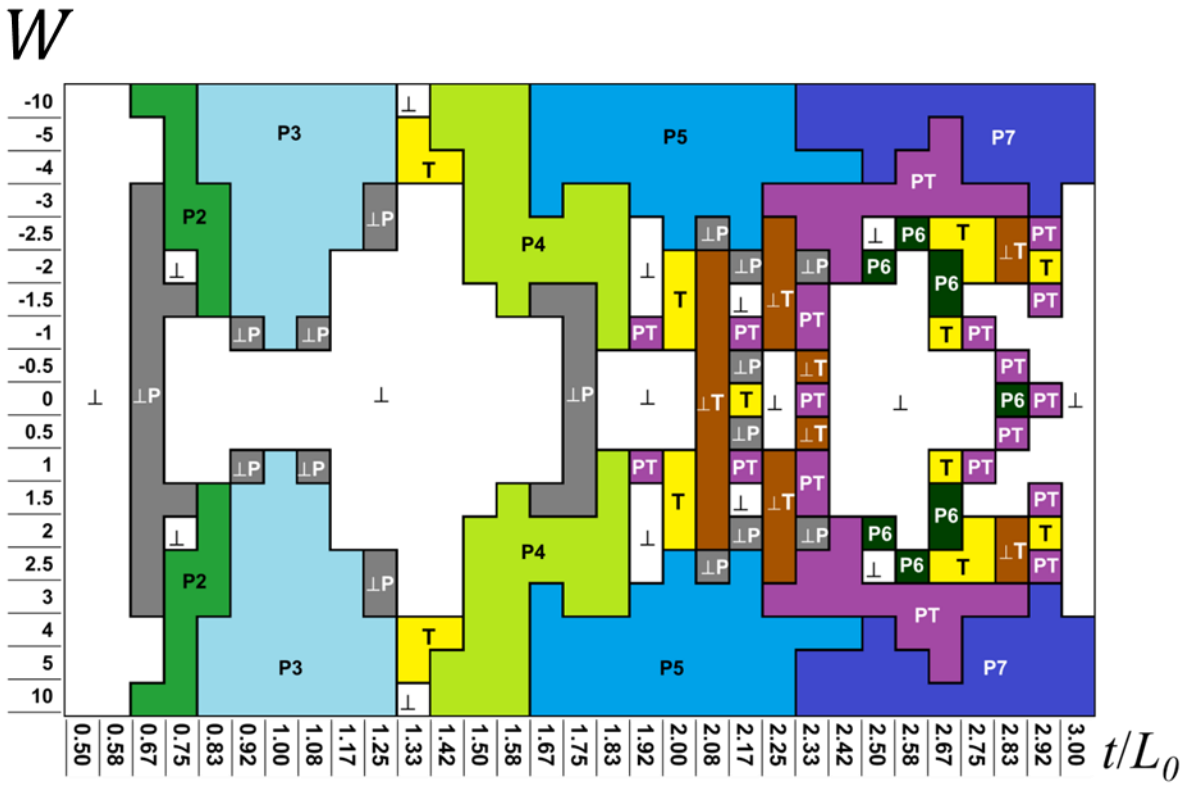

Figure 4-2: 2D SCFT simulation phase diagram of morphologies observed at specified W surface field values and reduced thickness t/L_0 for lamellar BCP confined between two surfaces. The axis scale in W is not linear.

4.2.2 Simulation Results in 3D – Cylinders

The previous 2D results show general trends of morphological behavior for a variety of surface energy conditions possible in the thin film state. In order to apply the model to real systems of cylinder forming BCPs, 3D simulations are necessary. For these simulations strongly preferential surface energies corresponding to those in the 2D lamellae of $|W| = 10$ are performed as experimental systems of interest are known to have strongly selective air and substrate boundary conditions due to brush layers being used and high χ values leading to high surface energy differences in the polymers. Similar studies in confined systems have previously been performed[152], and thus the simulations

here are compared with those results and ensure the simulations agree with previous work before considering topographical features.

For 3D thin film simulations, unit cell boundary conditions were used similar to those depicted in Figure 2.2.b in the middle. Unit cell dimensions L_Y and L_X were chosen to be large enough to allow all expected morphologies to form but small enough that the structures did not exhibit local defects. Additionally, the dimensions were picked to be approximately commensurate with a hexagonal lattice symmetry morphology as such morphologies are common in BCP systems and extra strain from in-plane incommensurability was not desired in obtaining these equilibrium morphologies. This constraint can be relaxed if the bias of commensuration is not desired and a later study will use such an effect. Thus the values assigned to the in-plane dimensions were L_Y by $L_X = 2.0\sqrt{3}L_0$ by $3.0L_0$.

The in-plane dimensions were defined in terms of the equilibrium period L_0 of a lamellar polymer, $f = 0.5$, in the limit $\chi N = 10.5$ (the order-disorder transition value) for N = 125. (For PS-PDMS this corresponds to $L_0 \cong 9.9$ nm). This choice of L_0 was made to maintain a consistent unit cell size when comparing different simulations in which χ was changed, because the equilibrium period varies slowly with χ. The air surface was preferential to the minority block to model a PS-PDMS BCP with PDMS the minority block as previous studies have shown PDMS to always be the surface wetting layer when thermal annealing was performed[118,161]. PDMS has a lower surface energy of $\gamma_{PDMS-Air} = 19.9\frac{m\mathrm{N}}{\mathrm{m}}$ compared to PS $\gamma_{PS-Air} = 40.7\frac{m\mathrm{N}}{\mathrm{m}}$ under normal atmospheric conditions[115]. The substrate surface affinity was either strongly preferential to PDMS or PS to model the effects of brush layers.

Results for self-assembly of films on smooth substrates are described. $W_{BL} = -10.0$ was chosen to represent a PDMS substrate brush and $W_{BL} = +10.0$ for a PS brush. These values are characteristic of the strongly preferential regime observed in the 2D lamellae simulations. $W_{Air} = -10.0$ was chosen to represent the segregation of PDMS at the air interface because PDMS has a lower surface energy and forms a surface layer under normal atmospheric conditions[118,161,162]. The issue of PDMS surface layer wetting will be

reexamined during experimental comparison. The reduced thickness t/L_0 was varied from 0.90 to 2.70 to examine both monolayers and bilayers of cylinders. $f = 0.32$ and $L_0 \cong 9.9$ nm (at the ODT limit), and χN was varied between 12.0 to 30.0 in incremental steps to examine the effect of annealing conditions, because solvent or thermal annealing lower the effective χ[115,116]. An increasing χ can model evaporation of solvent to some degree, though this would need to be coupled with changing film thickness and effective volume fractions for a complete model of solvent evaporation. By starting at a low value of $\chi N = 12.0$ and incrementally equilibrating at higher χN, metastable structures were less likely to form at higher χN, and led to a faster simulation time since the Langevin field relaxation scheme step magnitude is inversely proportional to χN for the exchange field. As a result, simulations with larger χN and random seeding converged slowly and tended to be trapped in metastable structures. The drawback of seeding the simulation with a prior morphology is that the seed morphology may be trapped even if it is not the lowest energy configuration. However, multiple examples of morphology transitions upon raising χN were observed, e.g. both spheres and perpendicular cylinders transitioned to in-plane cylinders upon increasing χN. If there was doubt about which morphology was the most stable, the energies were compared.

The morphologies observed included hexagonally packed spheres (S) or bilayer spheres (DS), monolayer in-plane cylinders (C), perpendicular out-of-plane cylinders (PC), double layers of close-packed in-plane cylinders (DC), and mesh structures (MC) and are shown in Figure 4.3. The morphological phase diagram versus reduced thickness $\frac{t}{L_0}$ and χN is shown in Figure 4.4 for $W_{BL} = +10.0$ (substrate attractive to the PS block) and in Figure 4.5 for $W_{BL} = -10.0$ (substrate attractive to the PDMS block) using the color coding from Figure 4.3.

In the simulations for the PS brush substrate, at around $t = 1.5L_0$ monolayer cylinder structures C were most stable and least strained in the vertical direction. Double layer structures DC were more stable at $t \cong 2.5L_0$ ($2.3, 2.5$ and $2.7L_0$). For the PDMS brush substrate, C formed around $t = 2.0L_0$ for C. The commensurate thickness can be understood by considering the presence of a half layer of PDMS in contact with each PDMS

preferential surface. Therefore the commensurate C structure is expected at $t = 1.5L_0$ for the PS brush substrate (1 monolayer of cylinders plus a half surface layer of PDMS) and $t = 2.0L_0$ for the PDMS brush substrate (1 monolayer of cylinders plus 2 half layers of PDMS). These results agree qualitatively with past experimental and theoretical studies of BCP thin films confined between two surfaces[67,128,136,163–168].

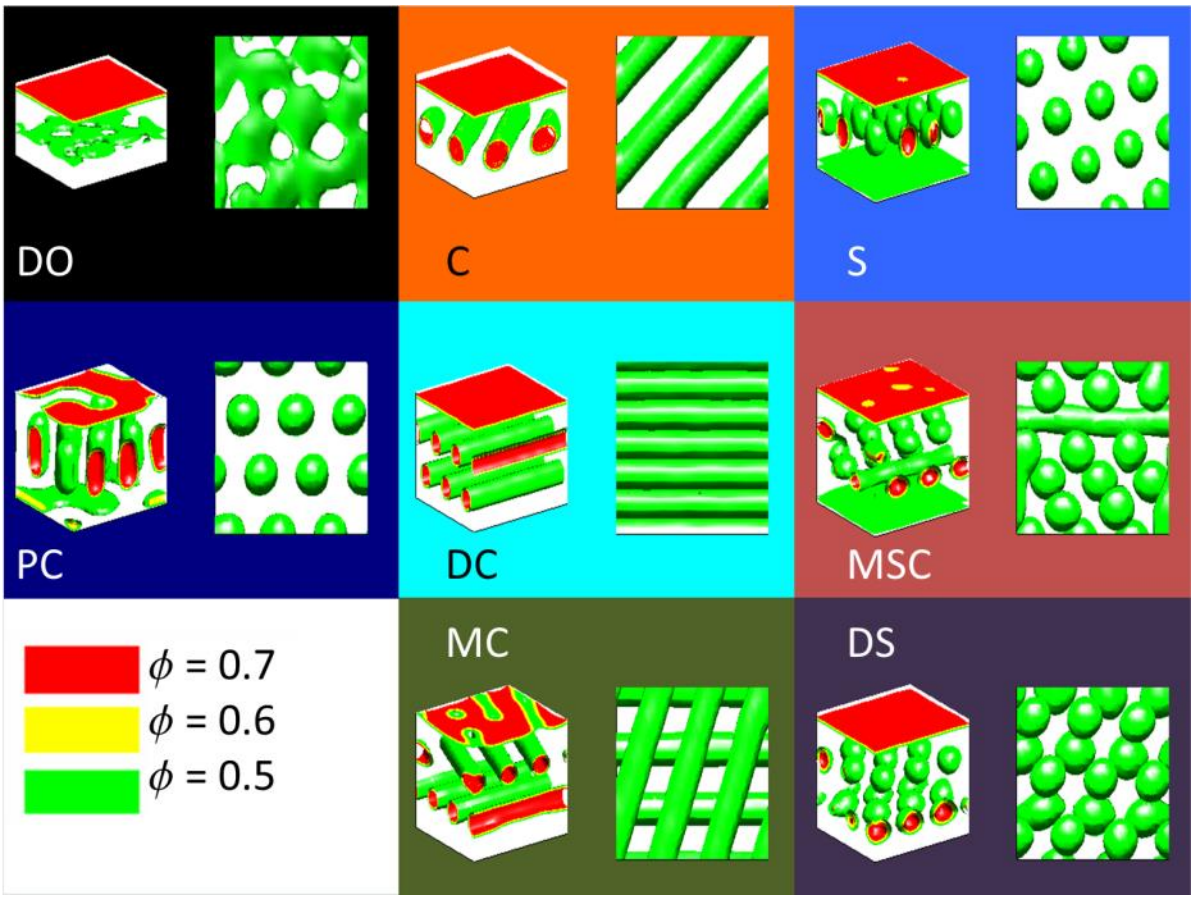

Figure 4-3: Representative morphologies observed in 3D SCFT simulations of cylindrical BCP thin films with substrate attractive to the PS block. (DO) Surface layers with possible disordered internal structure (the internal structure did not always have 50% density surfaces). (C) Single layer cylinders. (S) Single layer spheres. (PC) Internal perpendicular cylinders. (DC) Double layer hexagonally close-packed cylinders. (MSC) Mixed cylinders and spheres. (MC) Double layer mesh grid cylinders. (DS) Double layer spheres. ϕ represents the density of the PDMS block.

Interestingly, the double layer cylinder structures for the PS brush substrate were always DC, hexagonally close-packed (i.e. cylinders in each layer were parallel) whereas the double layer observed in the PDMS brush substrate case consisted of a mesh grid of cylinders (MC). Meshes of cylinders were also observed in prior simulation studies[152],

although those studies only considered confinement where both surfaces were PS preferential thus the commensurate thicknesses were smaller. We expect the mesh formation is a result of incommensurability in thickness rather than being determined by the substrate brush layers since this previous study found similar behavior for the PS preferential case. The meshes occurred only at the highest thickness studied here ($t = 2.7L_0$) and it is possible that DC might form at a more commensurate thickness such as $3L_0$ as the double cylinders were observed to be more stable for the commensurate $2.5L_0$ for the asymmetric surface preferentiality case in this study and $2.0L_0$ for the PS preferential case in other studies.

For incommensurate thicknesses, $t = 2.0L_0$ for the PS brush substrate and $t = 2.5L_0$ for the PDMS brush substrate, PC was observed, consisting of ellipsoidal cylinders perpendicular to the substrate. The boundaries between the different structures were generally independent of χN except at small χN, where spherical morphologies S and DS became more common. This follows the trend seen in a bulk BCP where the spherical morphology persists to higher f at lower χN. At $\chi N = 12$, or for $t < L_0$ no spheres or cylinders were observed, only surface layers.

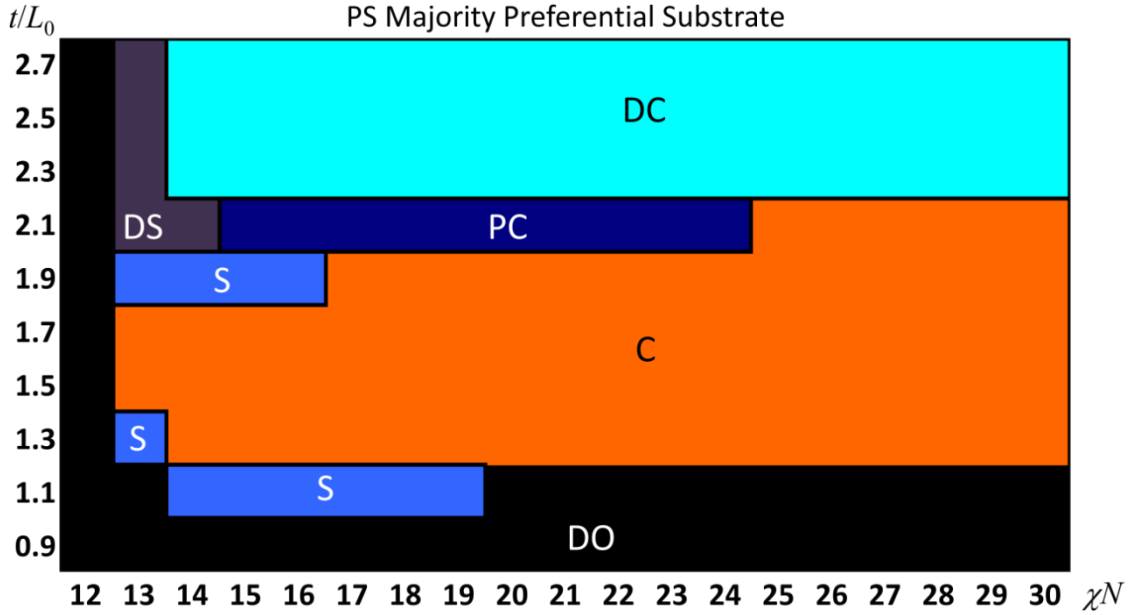

Figure 4-4: 3D SCFT simulation phase diagram of morphologies vs. reduced film thicknesses t/L_0 and χN for a bulk cylindrical BCP, f = 0.32, in a 3D cell of dimensions t by $2.0\sqrt{3}L_0$ by $3.0L_0$. The top (air) surface is preferential to the PDMS block with W_{Air} = -10.0 and the bottom (substrate) surface is preferential to the PS block with W_{BL} = +10.0.

For the thin film cylinder simulations with a PDMS brush layer, the results follow the same general trends observed for the PS brush layer except the structures occur at $\cong 0.5L_0$ thicker unit cells due to the need for an additional half layer of PDMS to wet the bottom of the simulation unit cell. The notable difference from the PS brush layer phase diagram is the occurrence of double layer mesh cylinders rather than a hexagonally close-packed double layer of cylinders.

Free energy plots as a function of reduced thickness t/L_0 and χN for the PS brush and the PDMS brush cases are shown in Figure 4.6. Especially for the strong segregation regime (high χN), the free energy difference between the morphologies is large enough to show where the phase transitions between disordered internal structure, monolayers of cylinders, and double layers of cylinders occur. Each of these regions for the cylinder phase cases are centered around their respective commensurate thicknesses (i.e. $t = 1.5L_0$ for monolayers with PS brush, $t = 2.5L_0$ for double layers with PS brush, and $t = 2.0L_0$ for monolayers with PDMS brush).

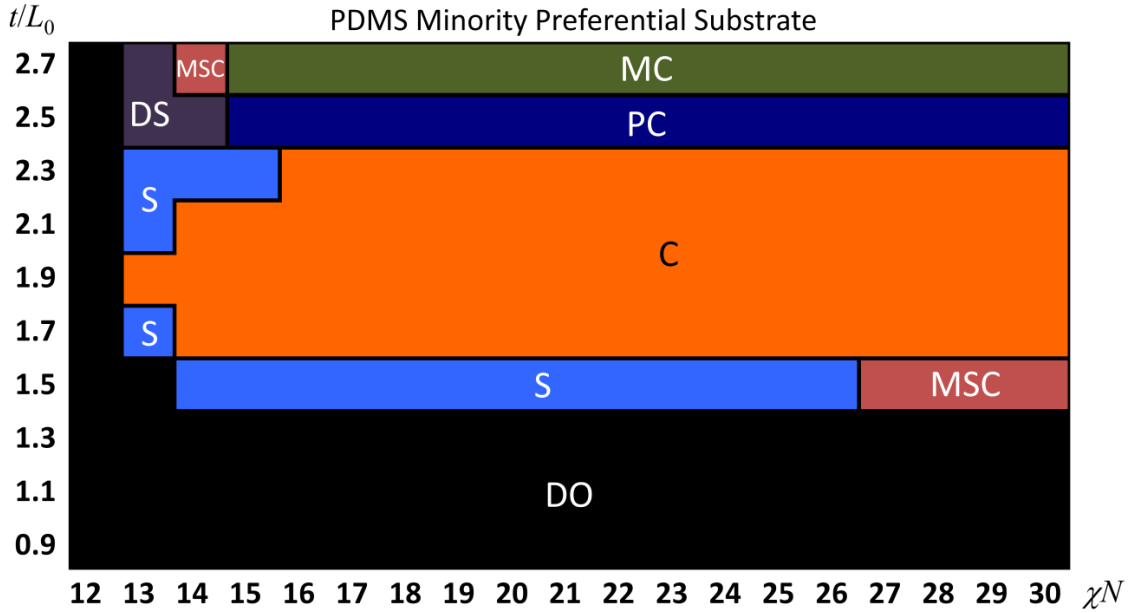

Figure 4-5: 3D SCFT simulation phase diagram of morphologies observed at specified reduced film thicknesses t/L_0 and χN for a cylindrical BCP, f = 0.32, in a cell of dimensions t by $2.0\sqrt{3}L_0$ by $3.0L_0$. The top surface is preferential to the PDMS block and the bottom surface to the PDMS block with W_{BL} = -10.0.

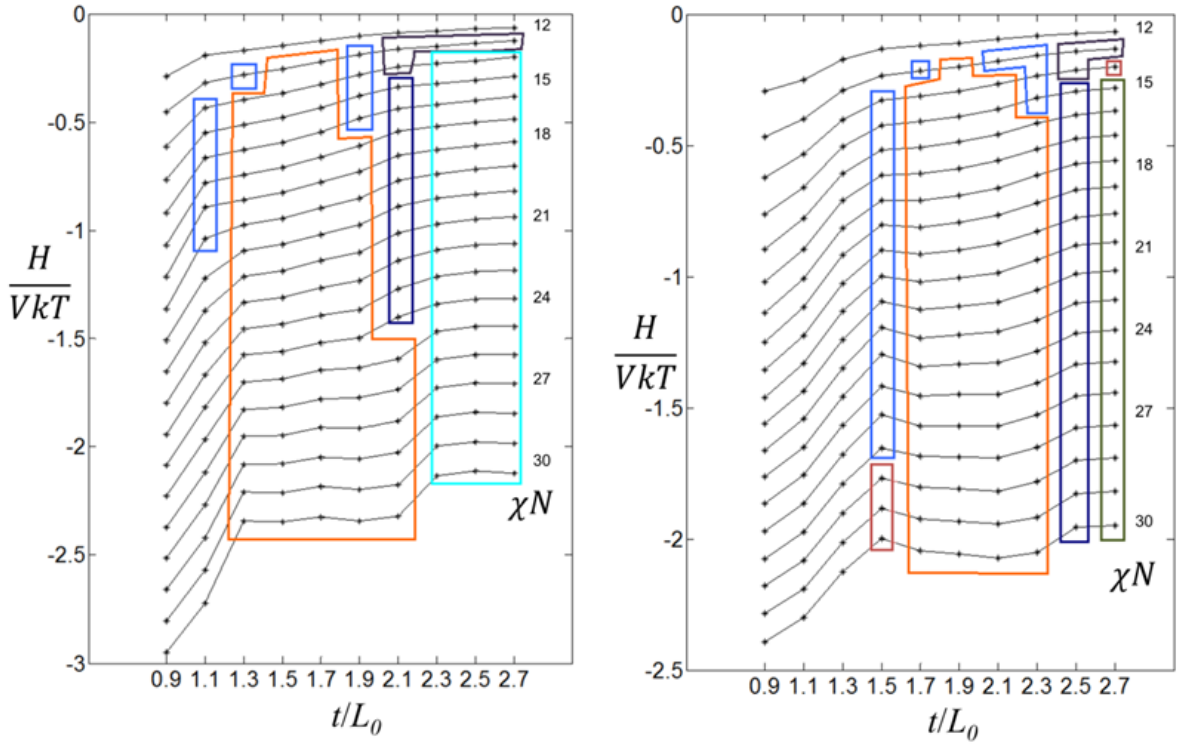

Figure 4-6: Normalized free energy H/VkT (normalized by grid volume V and thermal energy kT) plotted versus specified reduced film thicknesses t/L_0 and χN for a cylindrical BCP, f = 0.32, in a cell of dimensions t by $2.0\sqrt{3}L_0$ by $3.0L_0$. Left: The top surface is preferential to the PDMS block and the bottom surface to the PS block with W_{BL} = +10.0. Right: Top and bottom surfaces are preferential to PDMS block with W_{BL} = -10.0. The free energy curves are given for different χN and phase morphology regions are identified using the color code from Figure 4.3.

4.2.3 Simulation Results in 3D – Bulk Gyroid

To better gauge general trends in thin film morphology as a function of volume fraction, thin film simulations based on effective volume fractions of a solvent annealed bulk gyroid BCP were performed. These simulations were previously discussed with the main results in Chapter 3 with those main results being shown in Figure 3.8. Here comparisons with the bulk morphology results and full phase diagram as a function of film thickness at a fixed χN are shown and discussed.

3D SCFT simulations were performed to assess how the thickness of a film of a bulk-gyroid BCP affected the morphology. Periodic boundary conditions were used and the equilibrium morphologies were modeled at a range of thicknesses by using a complex

Langevin field relaxation scheme to find the density and chemical potential field configuration that minimized the free energy of the system. In the simulations, bulk equilibrium structures were first calculated for volume fraction $f = 0.41$ using fully periodic boundary conditions within a cubic unit cell with various edge lengths, and looking at three values of $(\chi N)_{eff} = 14, 18, \text{and } 30$, possible equilibrium structures were screened. Observed structures included square packed cylinders, hexagonally packed cylinders, cubic gyroid, and double gyroid, depending on the unit cell size. These different potential bulk morphologies are shown in Figure 4.7. To compare the equilibrium nature of these morphologies, free energy curves for the dominant morphologies were calculated over the range of edge lengths by holding the density fields constant. Cylinders had the lowest free energy at lower χN while the gyroid became the favored structure as χN was increased. Thus a $(\chi N)_{eff}$ value of 18 was chosen for the thin film simulations to model a bulk gyroid.

The value of $(\chi N)_{eff}$ is lower than the predicted lower limit value of 119 for the 75 kg/mol experimental system for two reasons. First, the swelling by a factor of ~2 during solvent annealing lowers χ as solvent is incorporated and the effective fraction occupied by the BCP is reduced. Thus the χ selected here represents an effective χ based on considerations of solvent annealing effectively lowering the actual χ value by a factor of ~½ due to the film swelling. Second, the coarse-graining of the model reduces the value of N since the simulation treats the 848 chemical monomers in the chain as 125 Kuhn segments. Thus the N for χN in the simulations should be $\frac{125}{N_{DOP}}$ less than for the experimental system, where $N_{DOP} = 848$. This scaling results in a lower effective χN that is best found by trying different simulation χN values. Based on comparing the equilibrium morphologies of the known bulk, $(\chi N)_{eff} = 18$ was chosen as the best fit parameter which is much less than the lower limit expected value of 119 using $N_{DOP} = 848$ and $\chi = 0.14$.

For bulk simulations, periodic boundary conditions were considered in all 3 directions with $N_x = N_y = N_z = 16$. To gauge the natural periodicities of the morphologies in the bulk, a length L in units of R_g was assigned to the to the x, y, and z sides of the unit cell and varied from $2.43R_g$ to $7.30R_g$. The simulations were then performed over this

range of assigned box lengths and the resulting morphologies were categorized. The dominant morphologies found then had free energy curves computed by taking the density field solutions from the side length simulations, calculating equilibrated energies by holding those density fields constant, and finding the corresponding chemical potentials under the different conditions. These calculations were done for four observed structures: square packed cylinders, hexagonally packed cylinders, cubic gyroid, and double gyroid, for three different values of χN. The resulting energy curves are shown in Figures 4.8, 4.9, and 4.10. From this analysis, the natural period of the hexagonal cylinder phase was found to be $5.27R_g$ and this was used as L_0 in order to provide a length scale for the thin film simulations.

To calculate morphologies of thin films, rectangular unit cells were used with periodic boundary conditions and $(\chi N)_{eff} = 18$. The cell dimensions are expressed in terms of the equilibrium spacing L_0 of the hexagonal cylinders observed in bulk simulations, which was $\sim 5.27R_g$ with R_g the radius of gyration. In-plane dimensions of the unit cell were chosen to be $1.85L_0$ wide and $1.62L_0$ long (i.e. incommensurate with L_0 to not bias in-plane morphologies) and the unit cell thickness was varied from less than $0.5L_0$ up to $1.5L_0$. Boundary conditions for the top and bottom surfaces were preferential to the majority block to avoid the formation of minority wetting layers (In the case of minority-preferential top and bottom surfaces, half layers of PDMS lamellae form as wetting layers at the top and bottom).

As the film thickness was increased, the morphology transitioned from in-plane spheres and cylinders to perforated lamellae, then lamellae, perforated lamellae, cylinders, bicontinuous cylinders, two layers of perforated lamellae and double layer lamellae. In general, the free energy decreased with increasing thickness until the transition between one and two layers of microdomains was reached. Around this transition region there was a local free energy minimum representing perforated lamellae and cylinders.

Additional simulations were done for higher and lower volume fractions f corresponding to selective solvent annealing conditions, which change the volume fraction. An effective volume fraction of 0.25 favored spheres, an effective volume fraction of 0.35

favored cylinders near the energy minimum, and an effective volume fraction of 0.45 favored lamellae.

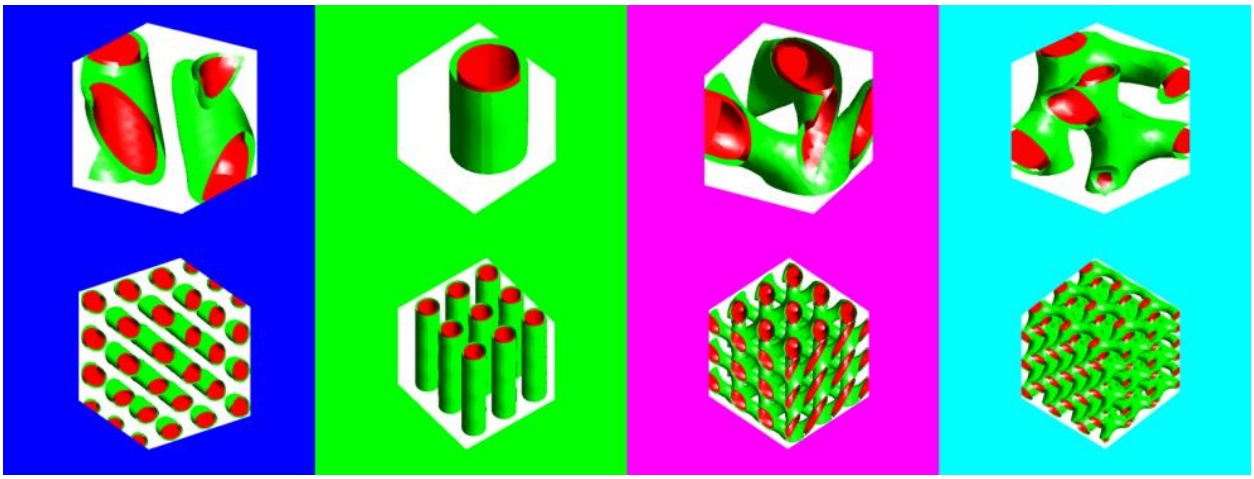

Figure 4-7: Simulated SCFT equilibrium structures of the nanostructures formed in the bulk state. Green surfaces are where the polymer density ϕ = 0.5 and red areas are where the density is minority rich (ϕ > 0.5). Top row shows a single unit cell from the SCFT calculations and bottom row shows 3 units cells by 3 unit cells of the structure. From left to right the structures are hexagonally packed cylinders (blue), square packed cylinders (green), cubic gyroid (magenta), and double gyroid (teal).

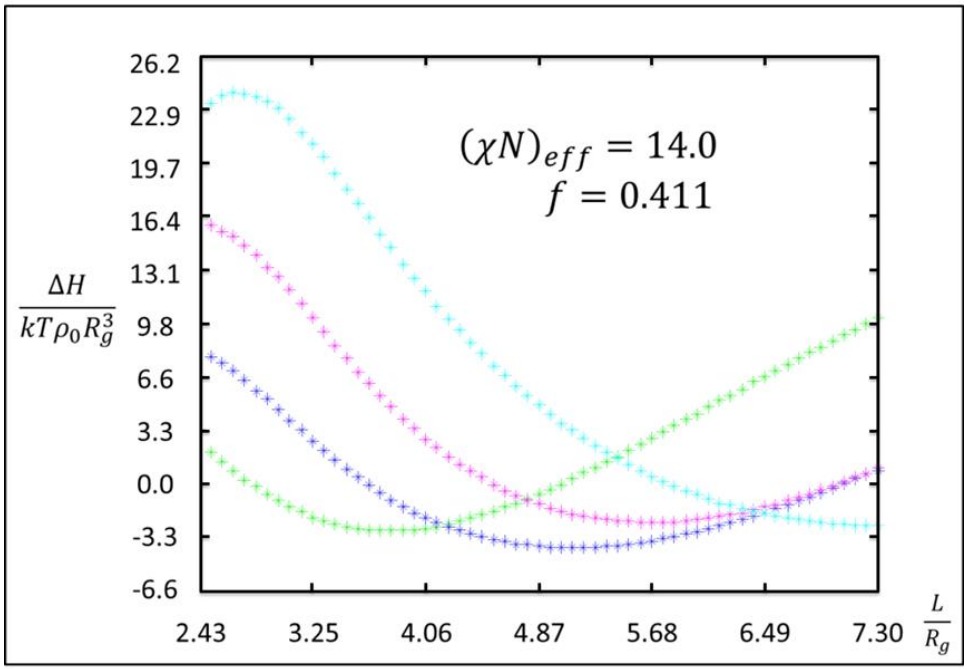

Figure 4-8: Normalized free energy differences of simulated SCFT equilibrium structures formed in the bulk state versus normalized unit cell box sidewall length for χN = 14.0 and f = 0.411. Curve color coding corresponds to colors around structures in Figure 4.7.

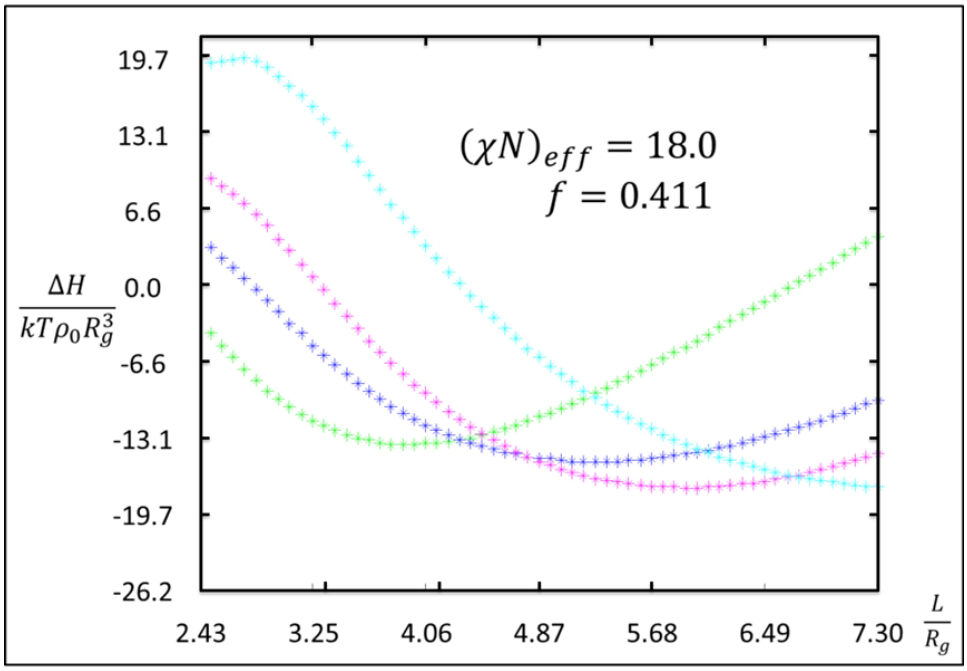

Figure 4-9: Normalized free energy differences of simulated SCFT equilibrium structures formed in the bulk state versus normalized unit cell box sidewall length for χN = 18.0. Curve color coding corresponds to colors around structures in Figure 4.7.

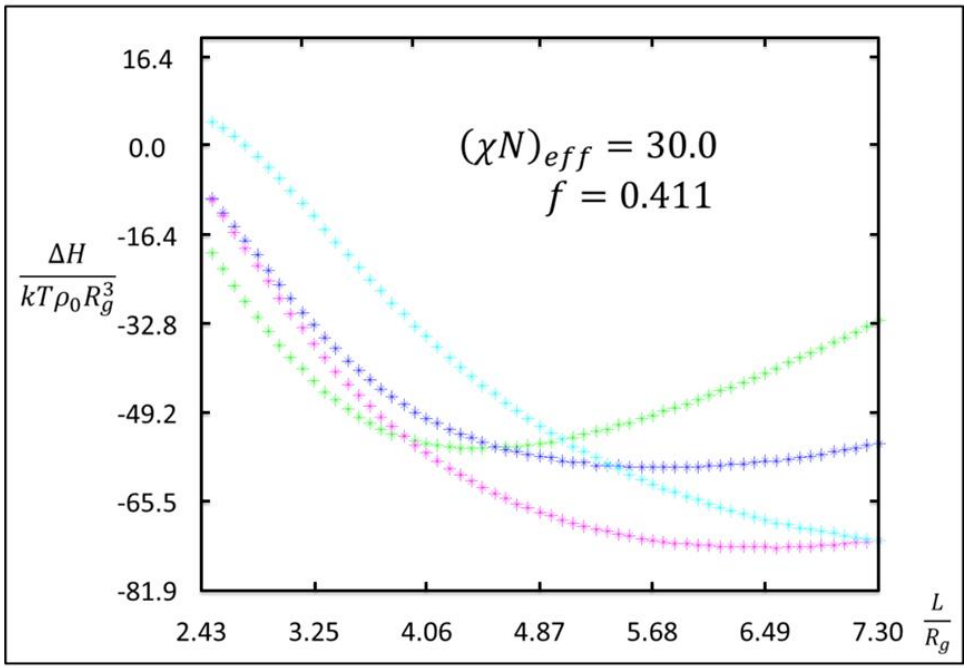

Figure 4-10: Normalized free energy differences of simulated SCFT equilibrium structures formed in the bulk state versus normalized unit cell box sidewall length for χN = 30.0. Curve color coding corresponds to colors around structures in Figure 4.7.

For the thin film simulations, periodic boundary conditions were only considered in the x and y directions and hard wall boundary conditions with a preferential surface layer were considered at the top and bottom surfaces in the z direction with the number of grid points $N_x = 32, N_y = 28,$ and $N_z = 18$. The x and y dimension lengths were chosen to be both larger than a single cylinder period and such that the diagonal distance in the unit cell was also a non-integer spacing. These non-commensurate dimensions were chosen to avoid biasing the morphologies formed in the system, because commensurate structures in-plane would have a lower free energy than strained structures. The approach of using a very large cell size to avoid commensurability issues was not practical for covering a wide parameter space. t, the film thickness or z direction length, was then varied from $1.62R_g$ to $8.11R_g$ for $\chi N = 18.0$.

In the thin film simulations, four different volume fractions were explored to compare the effect of selective swelling of the two blocks in addition to the film thickness with $f = 025, 0.35, 0.41,$ and 0.45. The phase diagrams with thickness are shown in Figures 4.11, 4.12, 4.13, and 4.14 for the respective volume fractions. The normalized free energy plots versus thickness of these morphologies are shown in Figures 4.15, 4.16, 4.17, and 4.18 for the respective volume fractions.

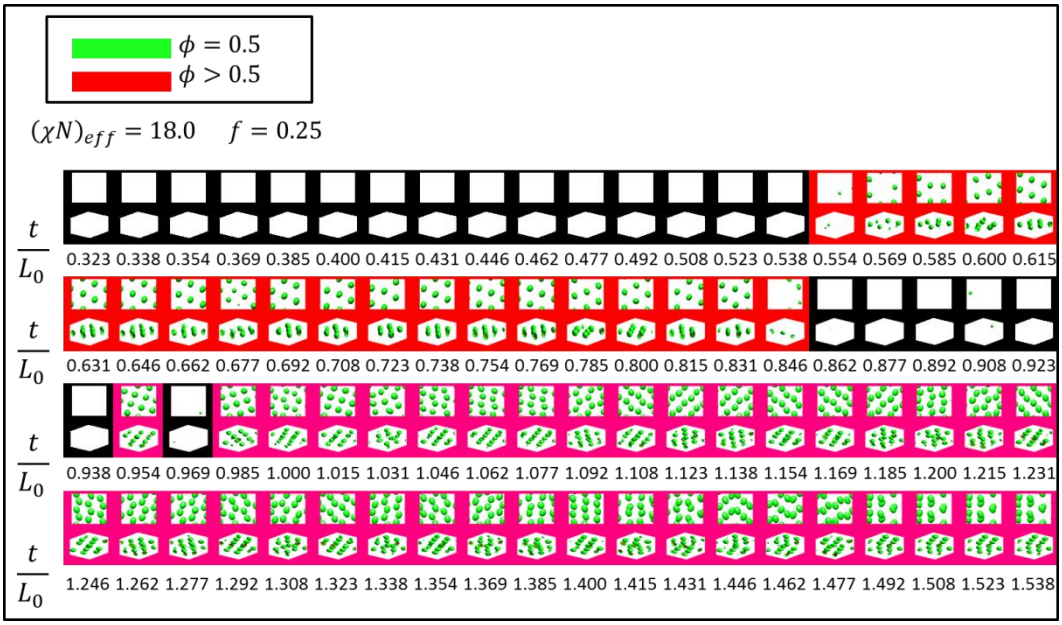

Figure 4-11: Simulated SCFT equilibrium structures of the nanostructures formed in the thin film state with differing normalized thickness t/L_0 for f = 0.25. L_0 is the period of bulk cylinders equal to 5.27 R_g. Structures include spheres and double layers of spheres.

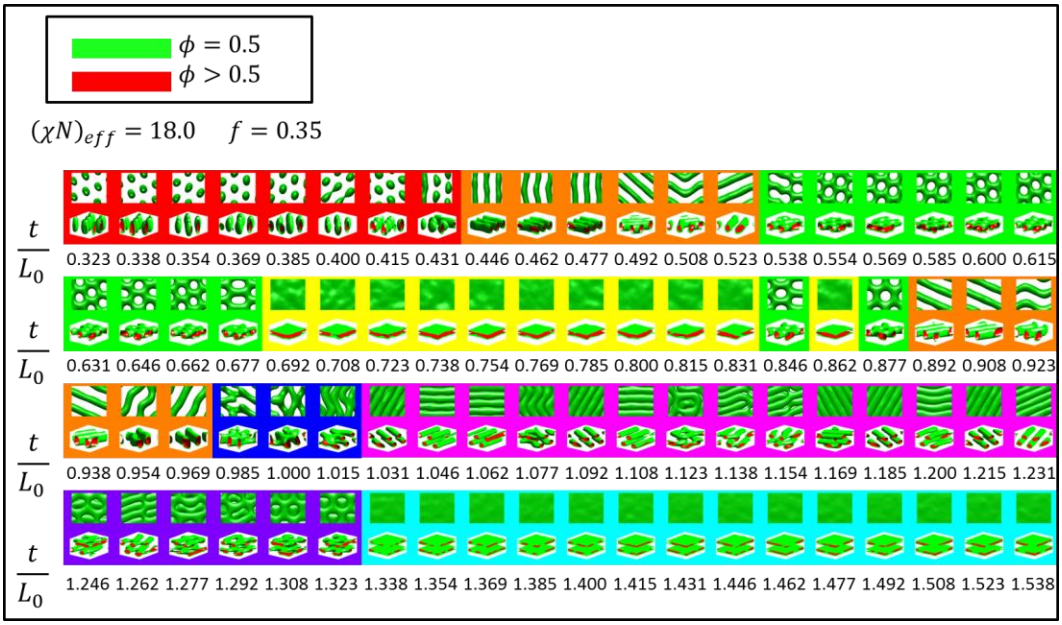

Figure 4-12: Simulated SCFT equilibrium structures of the nanostructures formed in the thin film state with differing normalized thickness t/L_0 for f = 0.35. L_0 is the period of bulk cylinders equal to 5.27 R_g. Structures include spheres, perforated lamellae, cylinders, lamellae, and double layered structures.

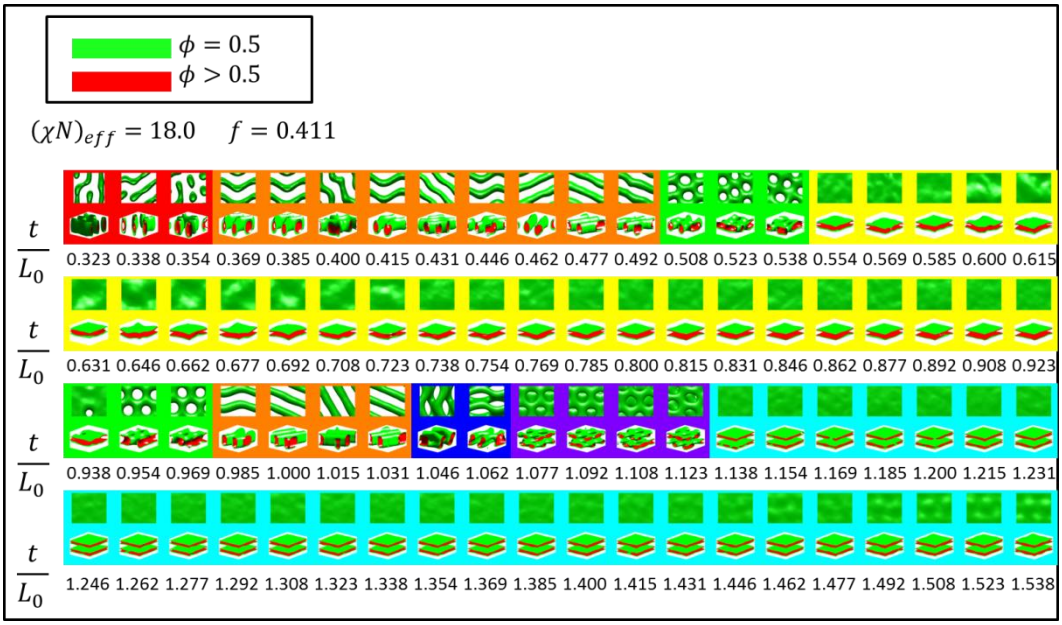

Figure 4-13: Simulated SCFT equilibrium structures of the nanostructures formed in bulk and in thin films with differing normalized thickness t/L_0 for f = 0.411. Structures include perforated lamellae, cylinders, lamellae, and double layered structures.

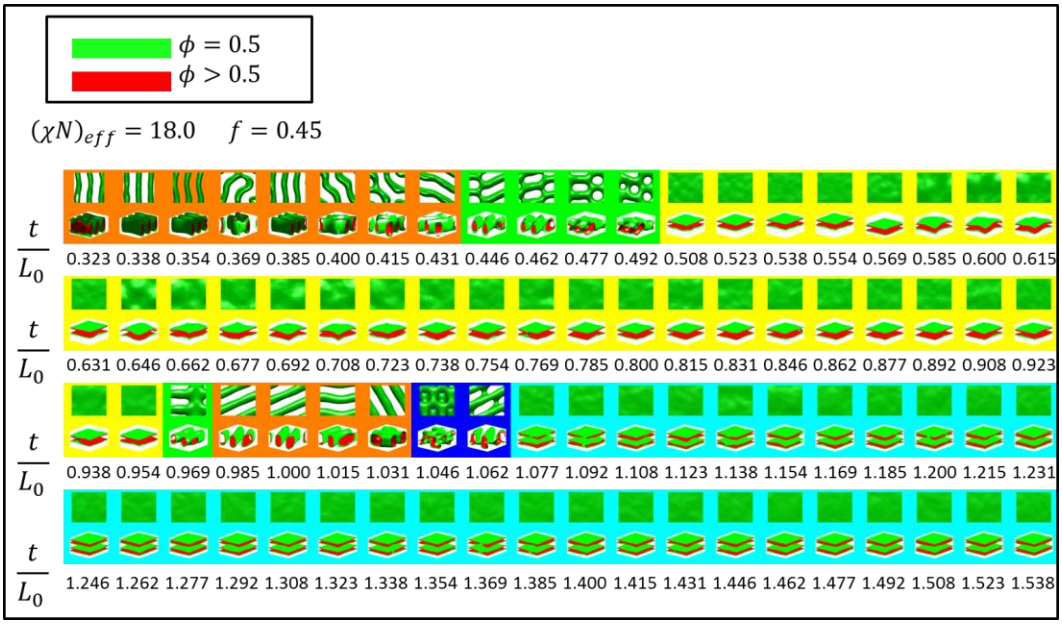

Figure 4-14: Simulated SCFT equilibrium structures of the nanostructures formed in the thin film state with differing normalized thickness t/L_0 for f = 0.45. Structures include perforated lamellae, cylinders, lamellae, and double layered structures.

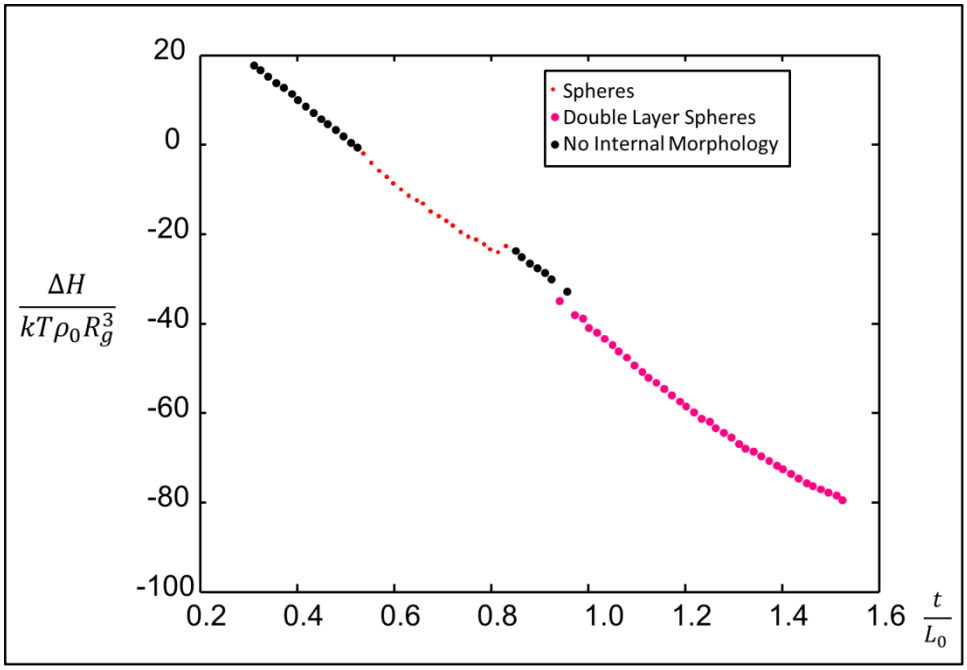

Figure 4-15: Normalized free energy difference ΔH of the simulated thin film structures from a disordered state for f = 0.25 versus normalized film thickness. Different structures are color coded using the colors of Figure 4.11. k is the Boltzmann constant, T the temperature, ρ_0 is the monomer density, and R_g the radius of gyration.

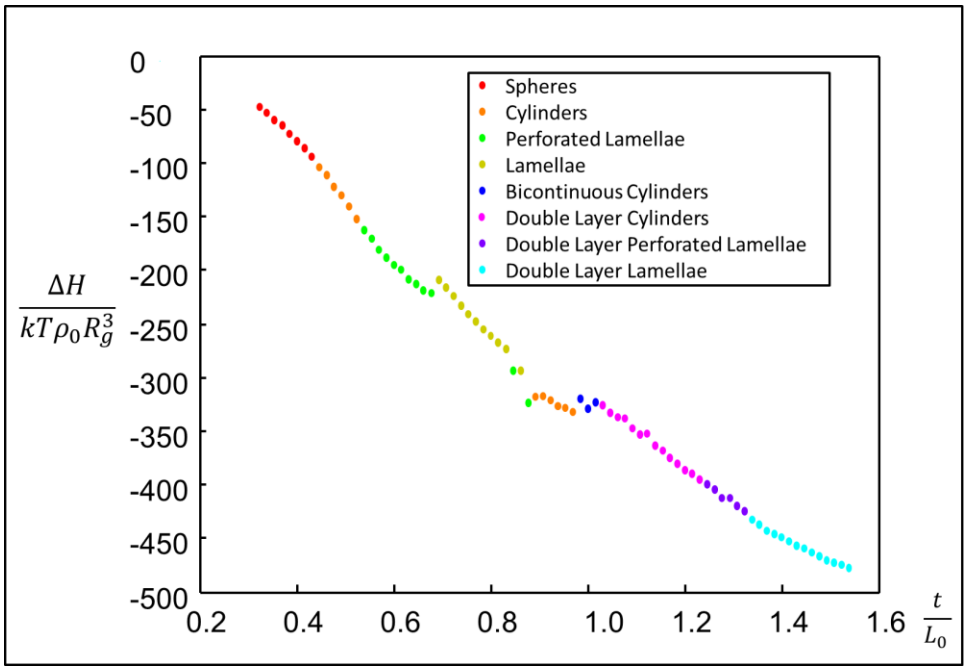

Figure 4-16: Normalized free energy difference ΔH of the simulated thin film structures from a disordered state for f = 0.35 versus normalized film thickness. Different observed structures are color coded using the colors of Figure 4.12.

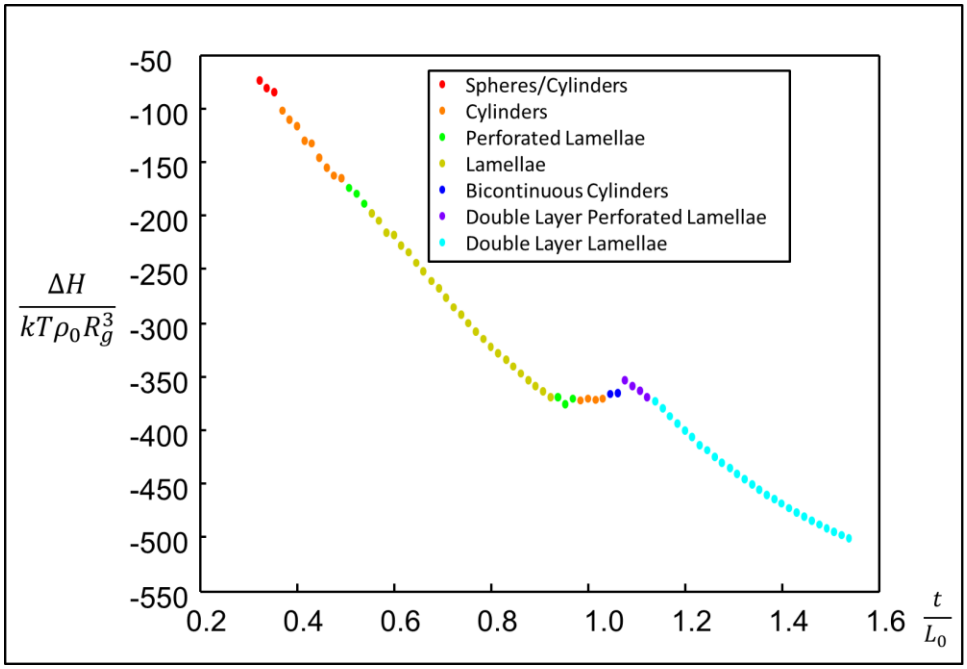

Figure 4-17: Normalized free energy difference ΔH of the simulated thin film structures from a disordered state for f = 0.411 versus normalized film thickness. Different structures are color coded using the colors of Figure 4.13.

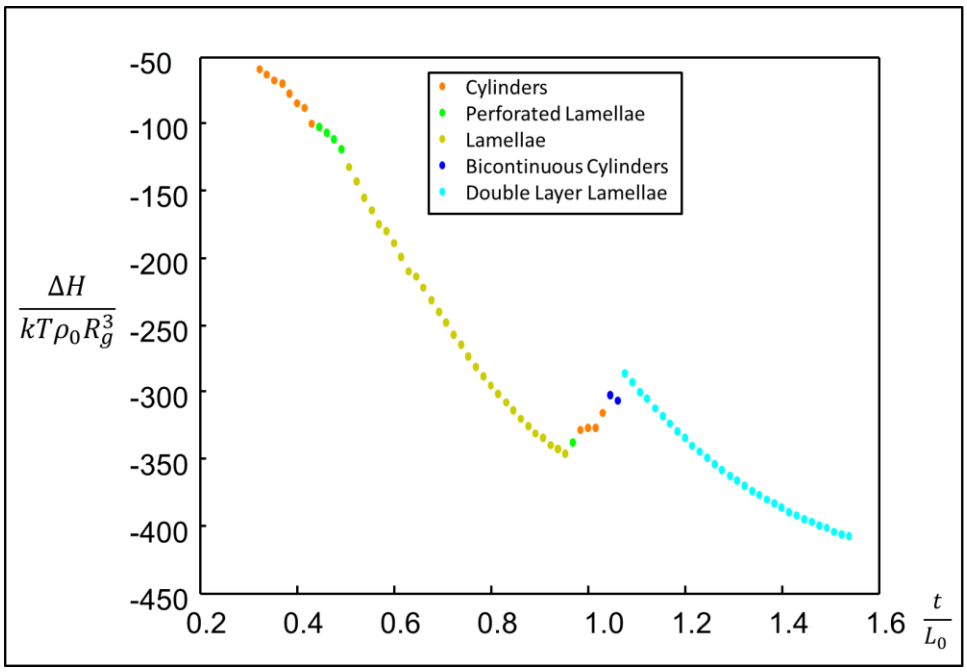

Figure 4-18: Normalized free energy difference ΔH of the simulated thin film structures from a disordered state for f = 0.45 versus normalized film thickness. Different observed structures are color coded using the colors of Figure 4.14.

4.2.4 Simulation Results in 3D – Volume Fraction Effects

In addition to simulations for the previously considered bulk gyroid case, several general simulations were performed using a range of volume fractions $f_{PDMS} = 0.3$ to 0.5 for a fixed effective $\chi N = 14$ to better understand how the effective f in thin films affects the morphology. All of these were performed on the same size grid of N_X by N_Y by $N_Z =$ 34 by 20 by 16 points. The dimensions were chosen to bias the formation of in-plane hexagonally packed structures commensurate with the cylindrical L_0 chosen. The effective box lengths are thus $2\sqrt{3}L_0$ by $2L_0$ by $1.6L_0$. First, bulk simulations were performed over this range of volume fractions to ensure that the canonical morphologies observed in BCPs were found. Consistent with previous studies transitions from spheres to cylinders to gyroid to mixed lamellae states due to incommensuration with the lamellae unit cell were found as shown in Figure 4.19.

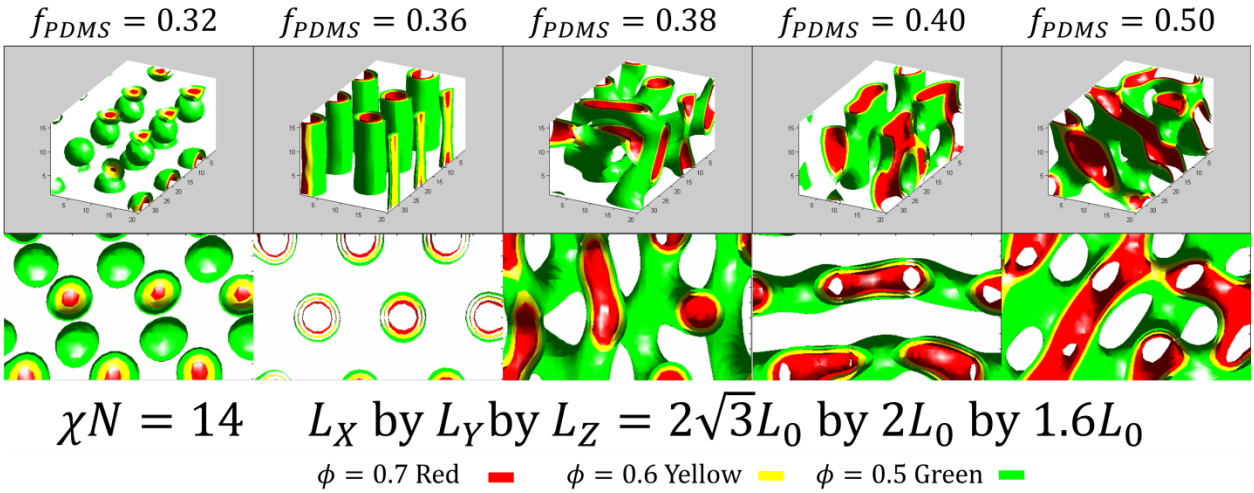

Figure 4-19: Bulk simulation results for a range of f_{PDMS} fractions. 3D side view on top and top-down view on bottom. From left to right: Hexagonally close-packed spheres, hexagonally close-packed cylinders, strained gyroid, perforated lamellae, mixed lamellae.

Having these bulk simulation results, a variety of thin film boundary conditions were examined across various volume fractions as well as attempts at explicit simulated solvent annealing using a quasi-static state assumption. These quasi-static simulations will be explored in more depth in the next section. These thin film boundary conditions are the

same as previously discussed with $W_{Air} \equiv W_{Top}$ and $W_{BL} \equiv W_{Bot}$. In cases where the top and bottom surface conditions were the same, this parameter is just defined as W.

The first set of simulations used neutral surface conditions on both the top and bottom surface such that $W = 0$. Additionally, two extra simulations were done for each volume fraction by increasing the film thickness by 2 grid points and adding the equivalent volume fraction of solvent into the system as a quasi-static way of simulating a controlled solvent anneal to that swelling ratio. Equal amounts of PDMS and PS selective solvent were incorporated in each case. The initial film thickness in all cases is $\sim 1.5L_0$. The morphology results for a variety of starting volume fractions are shown in Figure 4.20.

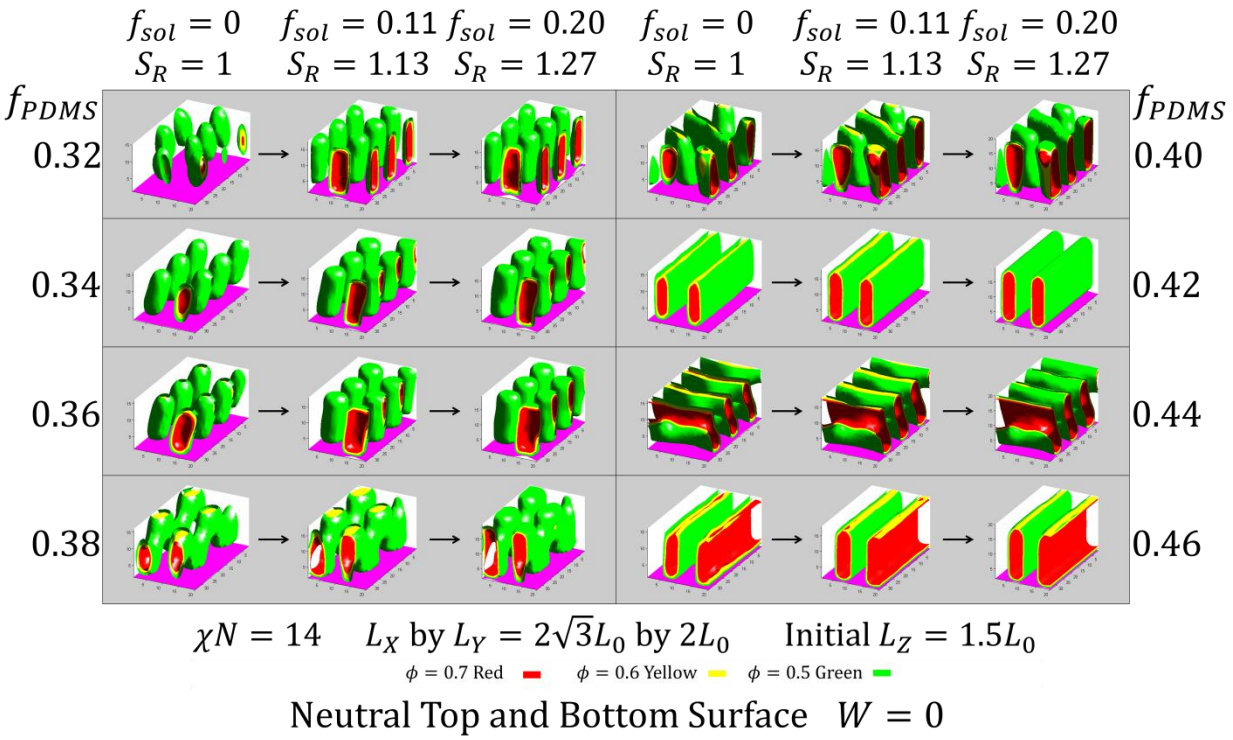

Figure 4-20: Thin film simulation results with quasi-static solvent annealing performed with neutral top and bottom surface conditions. From top left to bottom left: Increasing initial volume fraction started with elongated spheres or perpendicular to the substrate cylinders that were enriched upon adding solvent to the simulation cell. At f_{PDMS} = 0.38, what appears to be slices of perforated lamellae perpendicular to the substrate formed. From top right to bottom right: Perpendicular to the substrate lamellae with some defects in some cases formed. Adding solvent tended to anneal out the defects.

4.2.5 Simulation Results in 3D – Quasi-Static Solvent Vapor Annealing

To better understand whether quenching during SVA of monolayer thin films has a large impact on the final observed morphological state of a solvent annealed BCP thin film, quasi-static SCFT simulations were performed. Explicit solvent in the simulations was removed after being added in incremental steps during which the system was equilibrated using the complex Langevin steepest descent dynamics, and then on a final quenching step all solvent removed and the fields relaxed. Such a method allows kinetically trapped structures to form that would not otherwise form from starting from an unbiased random initial field configuration.

These simulations used a top and bottom surface preferential to the minority PDMS. All morphologies of interest in these simulations formed as in-plane morphologies between two surface layers of PDMS. The simulated quasi-static solvent annealing simulations were performed with both PDMS and PS selective solvents in equal proportions. A final simulation taking the results of the thickest solvent incorporated simulation had the internal fields taken and equilibrated under no solvent conditions to have an effective quench simulation to see how much removing the solvent affected the in-plane morphologies. Generally the morphologies did not change much, though there was some in-plane relaxation when quenching indicating that using such quenching simulations is not necessary for in-plane morphologies as those expected in monolayer of PS-PDMS systems. Results of these simulations are shown in Figure 4.21.

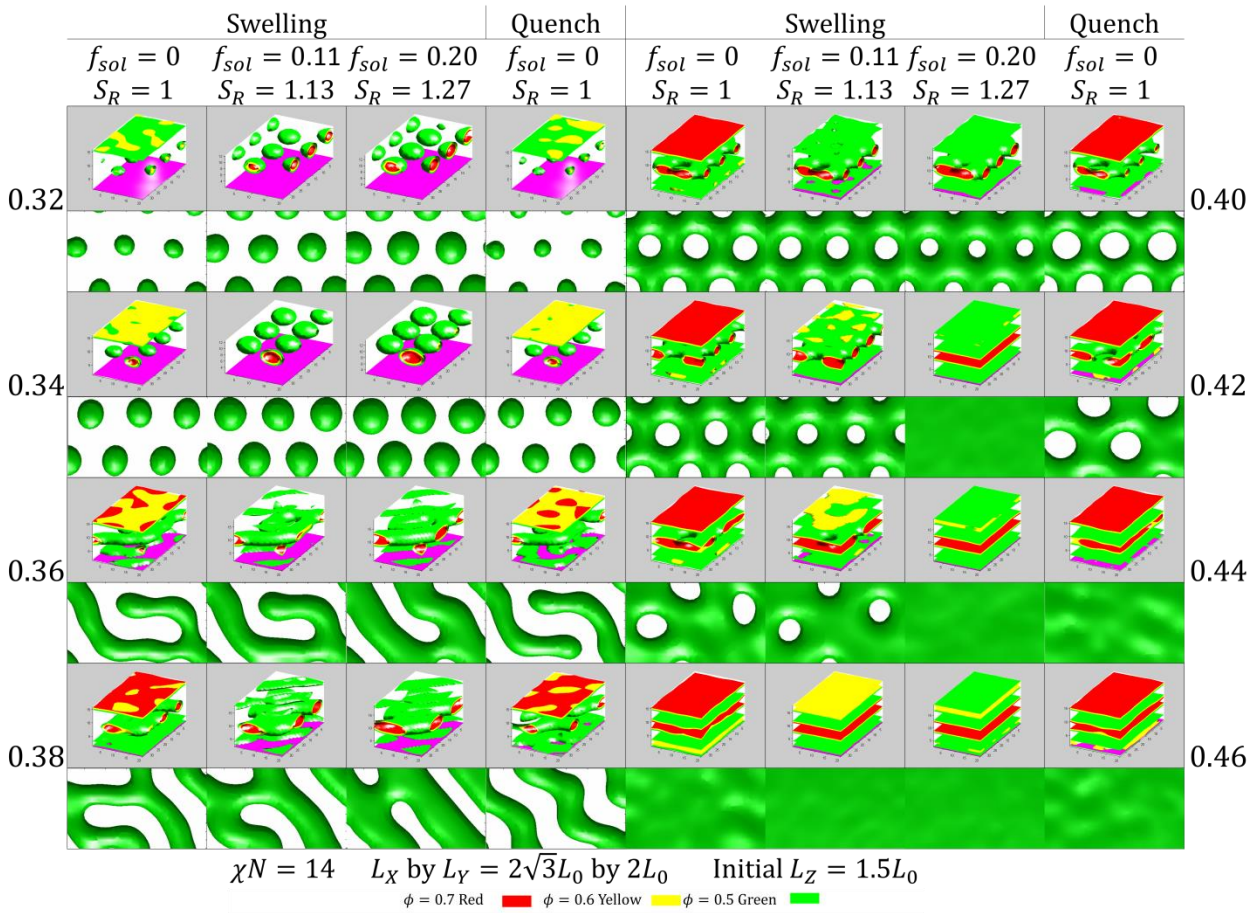

Figure 4-21: Thin film simulation results with quasi-static solvent annealing and quenching performed for PDMS preferential surfaces. From top left to bottom left: For f_{PDMS} = 0.32 and 0.34 hexagonally close-packed spheres formed, got larger upon swelling, and then collapsed back to about their original size upon quenching. For f_{PDMS} = 0.36 and 0.38, cylinders with defects formed with some of these defects annealing out upon quenching. Swelling served only to make cylindrical domains larger. From top right to bottom right: For f_{PDMS} = 0.40 and 0.42, perforated lamellae formed initially and upon swelling, with the perforations connecting for the larger volume fraction during swelling and then reappearing upon quenching with different hole sizes and period. For larger f_{PDMS}, only in-plane lamellae were observed that were simply enriched upon swelling and contracted upon quenching.

In addition to the PDMS preferential surface case, simulations with a PS preferential bottom and PDMS preferential top were performed using similar methods. The results of these simulations are shown in Figure 4.22. In all of these thin film simulations, general

trends that are observed in experiment occurred. Comparison of these trends will be discussed in the next section.

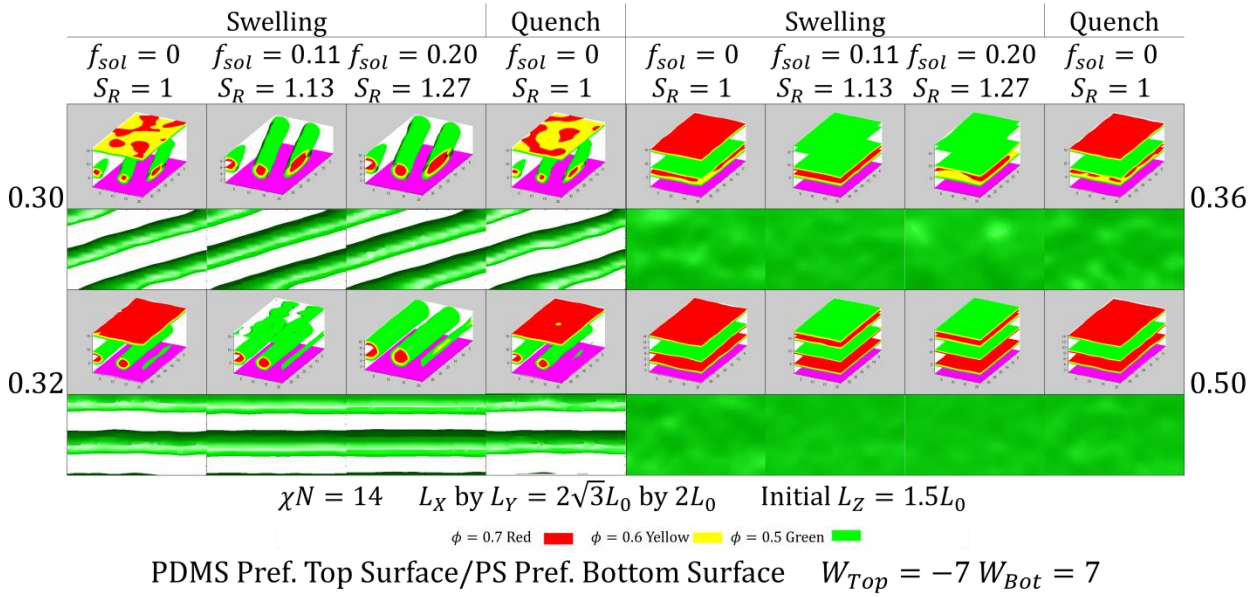

Figure 4-22: Thin film simulation results with quasi-static solvent annealing and quenching performed for a PS bottom preferential surface with a top surface preferential to PDMS. Left: In-plane cylinders formed at lower volume fractions and did not show much difference in swelling and quenching behavior other than cylinder size changing. Right: Larger volume fractions for this system tended to only yield in-plane lamellae. In general the addition of the PS surface layer affected the commensuration of in-plane structures making spheres inaccessible at these conditions.

4.2.6 Experimental Results and Comparison

In comparing the 3D thin film simulation results with experimental results, several factors need to be considered. Firstly, in the solvent annealing experiments the thin film morphology most of interest is that of the swollen film at an equilibrium swelling ratio. Thus when examining scanning electron micrographs care needs to be taken to realize these morphologies may have changed upon quenching the sample. Ideally the quenching only collapses the sample structures perpendicular to the substrate, but due to the effective volume fraction changes there will likely be some shrinkage of PDMS features in-plane as well (and thus growth of PS matrix around these features). When etching the sample for imaging, care needs to be performed whether there was a PDMS surface layer or not and if the etching also has damaged any of the underlying PDMS features to make sure the actual

internal morphology is being compared. Ideally the parameters modeled will be approximately equal to the effective parameters of the system under the solvent annealing conditions, but because of the inherent nonequilibrium process competing with the microphase segregation of the BCP and solvent mixture such as dewetting, defects or kinetically trapped morphologies are all possible in forming in the thin films. This is why the best simulation approach when not trying to account for such kinetic effects is to do ranges of parameters including χ_{eff} and f_{eff}. Additionally, the interplay between the final film thickness as measured and constrained in the simulation as well as surface energies accounting for brush layers or due to solvent environments changing those conditions are difficult to model exactly and thus ranges of those parameters should ideally be considered as well.

Since there are limited resources in performing simulations, only a finite number of parameters can be explored for a given system in a given amount of time, thus trends are the best indicator of the model working. Thus in comparing the previous results, trends observed in experiment are compared. For the case of the bulk-gyroid PS-PDMS of molecular weight 75.5 kg/mol, morphologies observed as a function of various solvent ratios are shown in Figure 4.23. Comparing these with the expected equilibrium morphologies at the appropriate effective volume fraction, the general morphology observed at those conditions were also observed. Since these trends appear to hold over a variety of conditions, the model can be adjusted to account for various effective parameters when topographical features are added to the system and these results will be explored in Chapter 5.

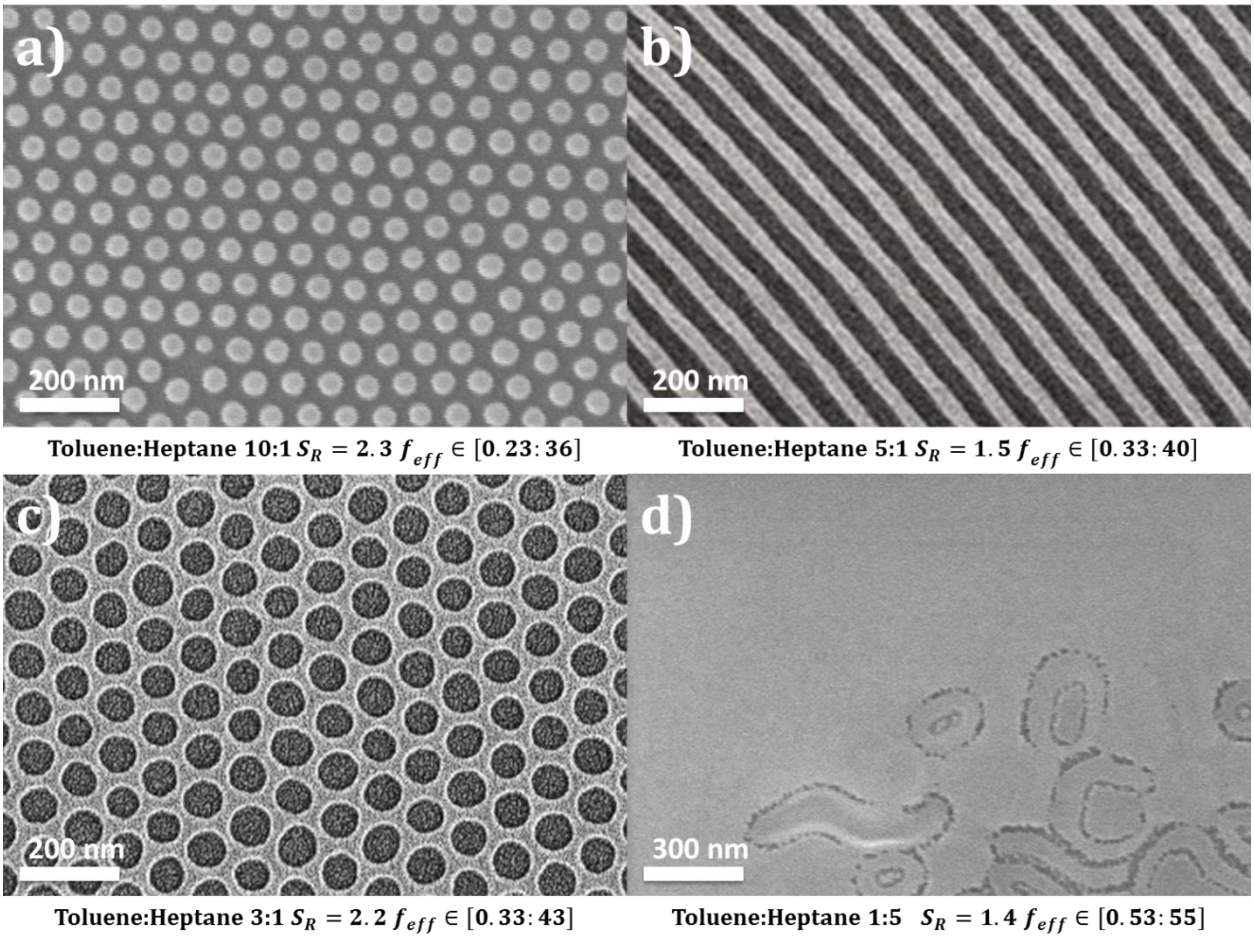

Figure 4-23: Experimental thin film morphology results for a 75.5 kg/mol PS-PDMS BCP with bulk volume fraction f_{PDMS} = 0.415 as a function of swelling ratio S_R and selective solvent ratio of toluene:heptane. The range of f_{eff} here is calculated using f_{eff1} as the lower limit of the range and f_{eff3} with the maximum value of β_{tol} for the upper limit of the range. These ranges are by no means an absolute range of where the morphology will be observed but are at a minimum a good reference for where the structure should be possible in the simulations. a) Spheres are observed at a ratio of toluene to heptane of 10:1 and S_R = 2.3. This best correlates to simulations with t = 2.3L_0 and $f_{eff} \in$ [0.23:0.36]. b) Cylinders are observed at a ratio of toluene to heptane of 5:1 and S_R = 1.5. This best correlates to simulations with t = 1.5L_0 and $f_{eff} \in$ [0.33:0.40]. c) Perforated lamellae are observed at a ratio of toluene to heptane of 3:1 and S_R = 2.2. This best correlates to simulations with t = 2.2L_0 and $f_{eff} \in$ [0.33:0.43]. a) Lamellae are observed at a ratio of toluene to heptane of 1:5 and S_R = 1.4. This best correlates to simulations with t = 1.4L_0 and $f_{eff} \in$ [0.53:0.55][169].

4.3 Summary

Modeling thin films of BCPs requires the exploration of a great deal of parameter space and thus general trends and correlations between observed experimental morphologies and simulation results are the best way to compare whether the model is capturing the appropriate physics of the real system. A variety of surface energy boundary conditions and film thicknesses can be examined, thus once a particular system of interest is defined with the parameters the fine tuning of the simulation for effective χ_{eff} and f_{eff} can be performed to zone into the best experimental parameters and be used to predict what morphologies are expected from a given experimental system.

From the studies examined, the following general principles are deducted for guiding simulations with topographical features. $|W| \geq 5$ generally correspond to fully preferential wetting conditions and thus a value of $|W| = 10$ will be suitable for modeling brush layers and interfaces in the systems of interest. Monolayer features appear commensurate at expected thicknesses based on consideration of appropriate half layers of wetting surfaces, thus these corresponding values are easily transferable to 3D DSA simulations. The effects of volume fraction of the morphology in thin films is well enough understood from these simulations to make sure either bulk thin film cylindrical or spherical BCPs are being considered in the appropriate DSA applications. Additionally, quasi-static quenching studies demonstrate quenching essentially keeps the swollen film morphology for the in-plane morphologies that will be considered in the DSA applications and thus explicitly modeling quenching in such systems is not necessary.

Having a given thin film system model working, adding topographical features or local chemical templates is the next step in modeling DSA. Modeling such features will utilize all the methods previously discussed with thin films. The next chapter will examine various kinds of DSA templates that have been studied and how parameters already discussed in modeling thin films play a role in those systems.

Chapter 5

Modeling Directed Self-Assembly Systems

5.1 Introduction

Directed self-assembly (DSA) of thin film BCPs requires the use of topographical or chemical templates of a variety of geometries and spatial placement to either locally or globally template the BCP. Many examples of BCP DSA have been demonstrated including the formation of dot patterns[2,10,23], complex line patterns[1,6,12], and aperiodic patterns[17,170]. In all these cases the BCP self-assembly is guided by either topographical features[1,2] or altered surface chemistry[6,10,12,23]. In doing this, structures that form are a modification of the normal thin film morphology. This simply can be an enhancement of long range order in the normal thin film morphology or this can form locally confined morphologies different than the untemplated morphology. With such a wide parameter space of templates possible, the theoretical parameter space in modeling these features is immense as well. To unify modeling such a wide variety of systems, basic principles of what constitutes template versus BCP in the system need to be established to both simplify this parameter space as well as have a consistent way of modeling topography and surface chemistry.

In the context of the SCFT simulations, these template constraints amount to masking either the local pressure fields for topography or exchange fields for chemical surface modification. This formulism allows for the design of many potential template geometries using simple rules with the SCFT constraints. The general way of implementing these constraints were previously discussed in Chapter 2. In this chapter, several kinds of templates that have been experimentally tested will be compared with SCFT modeling results. Hierarchically templated samples where a previous BCP was converted into a topographical template are discussed to show how simple commensurate line patterns can

perform DSA. Films patterned by arrays of hydrogen silsesquioxane (HSQ) posts produced using electron beam lithography (EBL)[31] are examined in depth for both hexagonal and rectangular symmetry arrays with a great deal of comparison between experiment and modeling. Cylindrical forming BCPs patterned with lines of HSQ are examined as well for achieving an effective doubling of template features. Additionally, results of BCPs confined to square and circular hole templates produced in a similar manner to the HSQ posts are presented and discussed. These very specific examples all serve to set the stage for a general form of DSA with arbitrary template placement to be discussed in the context of inverse design in Chapter 6.

5.2 Hierarchical Template Studies

As previously discussed, the size dimensions and variety of the features formed from BCP self-assembly are comparable and in some cases better than traditional photolithgraphy[40,41] making BCP self-assembly have many uses in nanolithography[11,16,20,171–177], nano-scale array formation[178,179], and photonic crystal formation[180]. Since BCP DSA requires templates on the same size dimensions as the BCPs themselves to induce long range order and good alignment[16,20,27,44,118,181–185], one potential avenue of the resulting BCP pattern is to template another BCP, something known as hierarchical templating where a higher molecular weight BCP is used to make a template for a commensurate lower molecular weight BCP[61].

Such hierarchical methods are important for lower molecular weight and thus very small feature sizes where producing initial templates for such systems is difficult to begin. There are similar methods using chemical templating of line patterns[24,186], but in those cases the same principle applies that an initial BCP self-assembly annealing step must be performed. PS-PDMS is one such BCP that has great potential use in these kinds of applications due to silicon in the PDMS block making that block very etch selective to reactive ion etching processes[20,175] as well as itself oxidizing and hardening during the etch process, in addition to having a high χ parameter and being able to form sub-10 nm feature sizes[44,118,181,182]. Here different base molecular weight BCPs are used under different solvent annealing conditions to modify feature size and effective period. Commensurability

with the hierarchical BCP template is demonstrated and SCFT simulations are used for comparing with the 3D BCP structure.

5.2.1 Simulation Results in 3D

SCFT simulations[53–55] were used to simulate the internal 3D structure of cylinders of a lower molecular weight 16 kg/mol PS-PDMS (denoted SD16, $f_{PDMS} \cong 0.31$, PDI $\cong 1.08$) annealed on an oxidized template of a higher molecular weight 45.5 kg/mol PS-PDMS cylinder pattern (denoted SD45, $f_{PDMS} \cong 0.32$, PDI $\cong 1.15$). These simulations capture the internal morphology of the SD16 cylinders prior to reactive ion etching under the assumptions made in the model. Based on the results of the simulation, the SD16 cylinders formed parallel over the underlying template from the hardened and collapsed SD45 cylinder features that were modeled using hard mask constraints in the simulation as shown in Figure 5.1.

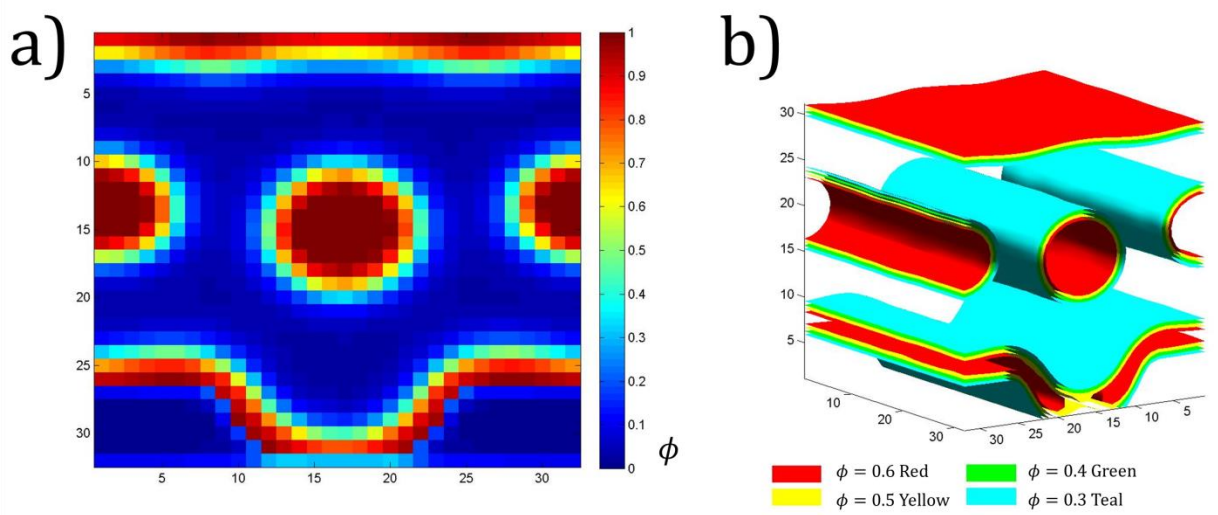

Figure 5-1: a) 2D simulation result of cross-section cylindrical features being templated by the underlying topography representing hardened PDMS from the higher molecular weight BCP SD45. b) 3D simulation result of system in a) with different noted colors representing constant PDMS density isosurfaces[61].

In these simulations, the system was modeled using unit cells with the underlying topography of the oxidized SD45 having $\mu_A = \mu_B = P$ with $|P| = 20$ in normalized simulation units. This value is based the value required to achieved the effective total density of the BCP in topographically constrained regions to be less than 10%. This kind of

topographical constraint model was first used by Mickiewicz et al[49] and will be discussed more in depth later when examining hexagonal arrays of topographical posts. Right outside the region masked by the oxidized topography, the chemical potential fields were constrained to model the PDMS brush layer on the surface and the assumption the top air surface was more preferential to PDMS was made such that $\mu_A = -\mu_B = W = -10$ to have preferential wetting of the A minority block representing PDMS in the simulation. These unit cells are thus similar to the thin film conditions discussed in the previous chapter but now with the added topography constraints.

To best match the experimental parameters $f_{PDMS} = 0.3125$, $\chi_{eff} = 0.104$, and $N_S = 53$ where this N_S denotes the number of statistical repeat monomers used for coarse graining the chain in the simulation (less than the actual $N_{DOP} = 173$). The effective χN was thus 18 for these simulations. Initially cross-sectional 2D simulations were performed to determine thickness at which a monolayer of cylindrical features formed. The result of a 2D simulation at the commensurate thickness is shown in Figure 5.1.a where the plotted polymer density represents the PDMS in the SD16 and the dark blue topography at the bottom represents the hardened SD45 features. One of the cross-sectional cylinders formed over the trench and another over the mesa formed from the hardened SD45 cylinders. These simulations were run multiple times and for enough iterations to ensure the structures found were energy minimum structures.

Using the results from the 2D simulations, an N_X by N_Y by $N_Z = 32$ by 32 by 32 3D unit cell was constructed such that the length along the N_Y direction was ≈ 34 nm. To expedite these 3D calculations due to long computation times for the 3D cells, the simulations were seeded with the expected structure using the results from the 2D simulations and allowed to equilibrate using steepest descent relaxation. The resulting density fields as isosurfaces contours of equal PDMS volume fraction are shown in Figure 5.1.b. There is a slight height difference observed in the simulations with the cylinder above the trench dipping slightly into the trench and the overall size of the trench cylinder being slightly larger than the mesa cylinders.

5.2.2 Experimental Results and Comparison

In the experiments that inspired the simulations of the previous section, Jeong Gon Son performed all experiments with the assistance of Kevin Gotrik[61]. A schematic diagram of the main steps in the experimental process is shown in Figure 5.2. The initial template was fabricated by solvent annealing an initially ≈ 40 nm thick SD45 film for 12 hours in a toluene heptane saturated vapor chamber at room temperature on a PDMS brush functionalized substrate with 4 μm wide by 40 nm deep trenches made with photolithography and reactive ion etching as schematically shown in Figure 5.2.a. A quick CF_4 plasma followed by a longer ≈ 20 s oxygen plasma reactive ion etch was used to remove any potential PDMS surface layer and then the internal PS matrix while oxidizing the remaining PDMS features as shown in Figure 5.2.b.

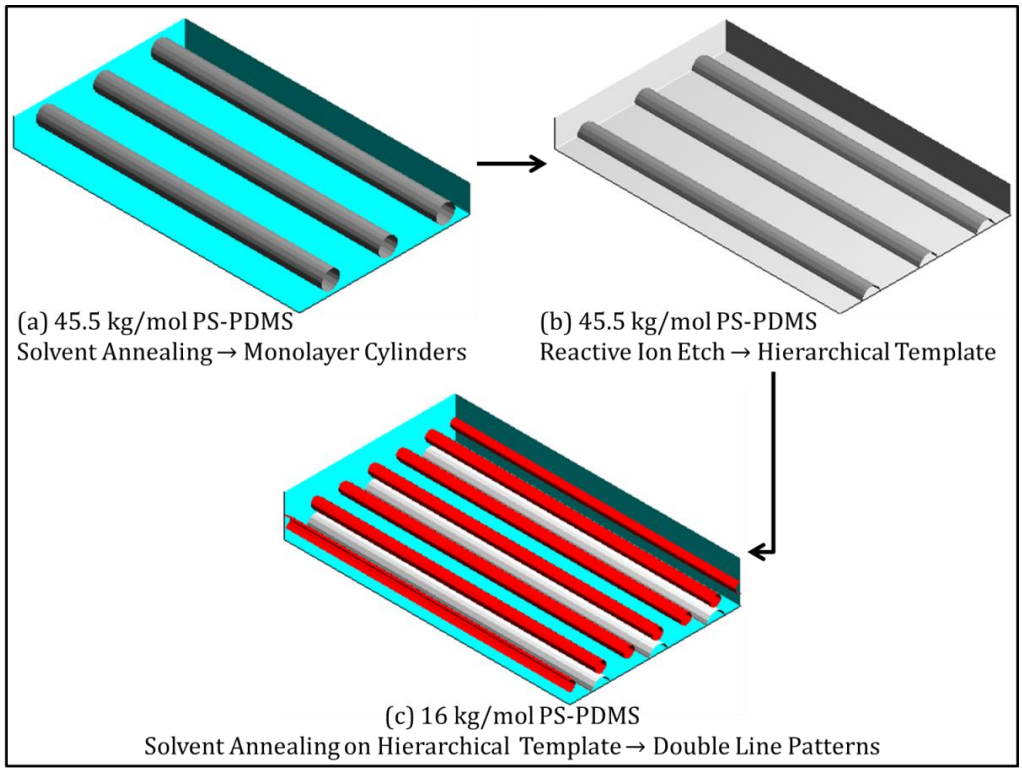

Figure 5-2: Schematic diagram of the major steps in the hierarchical DSA using SD45 to template SD16. (a) A monolayer of PDMS cylinders (grey) self-assembles during solvent annealing on a PDMS functionalized substrate (teal) using SD45. (b) SD45 monolayer cylinder film is reactive ion etched to remove PS and leave oxidized silicon features from the PDMS lines on the silica substrate (grey). (c) Using SD16 on template formed from SD45 line patterns, a double templated set of PDMS cylinders (red) self-assembles over the SD45 line template (light grey) functionalized with PDMS brush (teal).

At a volume ratio of 5 to 1 toluene to heptane, in-plane cylinders of pitch 35 nm and width 15 nm formed[44] and were used as the topographical template for patterning the SD16 as shown in Figure 5.2.c. Other morphologies formed by changing the solvent vapor ratios, but for simulation purposes only the cylinder morphology was of interest here and the effects of changing solvent volume fractions and thus the effective volume fraction of the internal morphology of the film were discussed previously in Chapter 3 and 4. Similar procedures were done with the SD16 except the solvents chosen were annealing were different due to the lower molecular weight BCP needing different vapor pressures to form similar morphologies without dewetting. Using acetone solvent vapor, in-plane cylinders with a 17.8 nm pitch ($\approx \frac{1}{2} L_{0,SD45}$) were formed upon annealing[182]. Using other solvents, other morphologies such as close-packed spheres formed which is attributable to the selective swelling behavior of different solvents as previously discussed[121,187].

For the hierarchical template experiment, the resulting oxidized patterns for the SD45 was functionalized with a PDMS brush layer. SD16 was spun cast onto this functionalized template and annealed with the same annealing conditions where the in-plane cylinders were observed. The primary advantage gained in this hierarchical method is that the long range order of the cylinders templated by the SD45 template is better than just on the trench substrate. After etching away any potential PDMS surface layer and the PS matrix of the SD16, the hierarchical patterns were observed using scanning electron microscopy (SEM) and atomic force microscopy (AFM) as shown in Figure 5.3. Since the period of the SD45 was almost exactly twice that of the SD16, the patterns that formed were commensurate and were confirmed to be the lowest energy structure from the SCFT simulations as multiple simulations performed converged to this structure using the steepest descent relaxation scheme. Additionally, the height difference between cylinders above the trench and above the SD45 line mesas was $\approx$ 1.5 nm as measured by AFM.

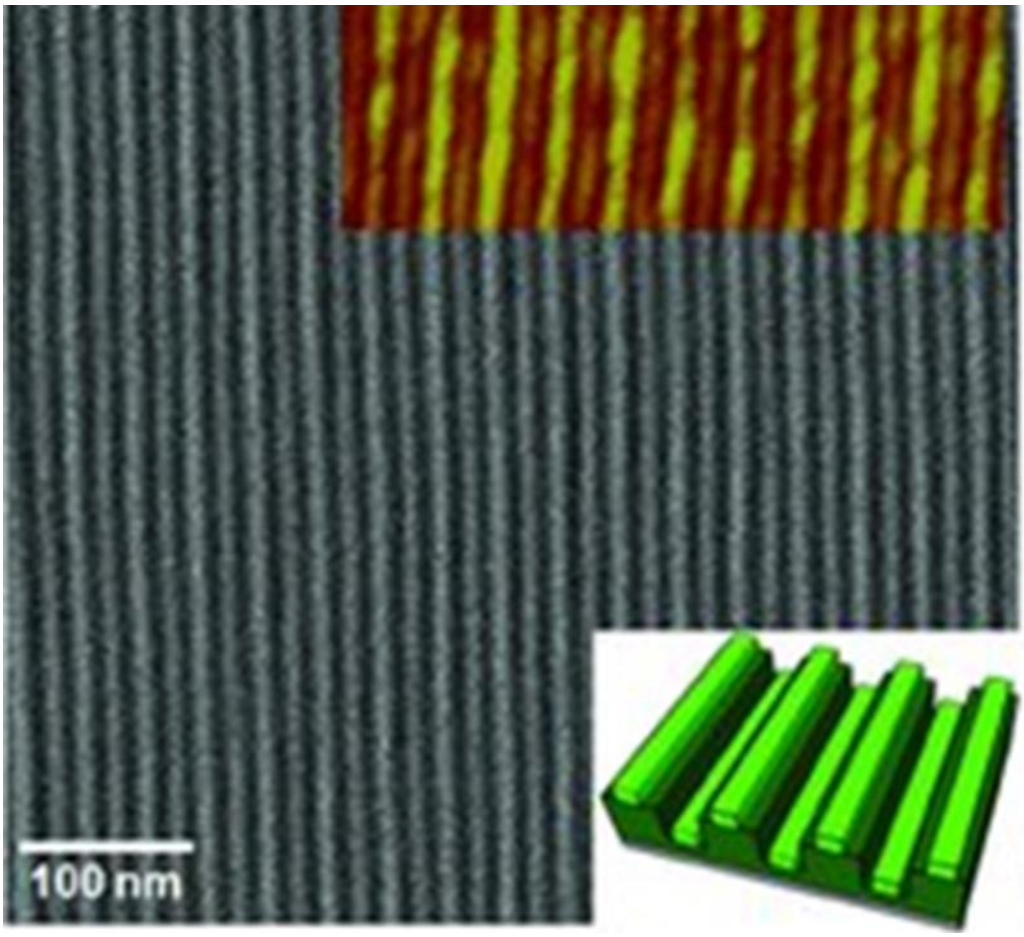

Figure 5-3: SEM image of the results of SD16 cylinder patterns hierarchically templated by SD45 cylinder patterns with the template period twice that of the templated SD16. Upper right inset: AFM image of pattern. Lower right inset: Schematic image of pattern[61].

Previous studies suggest that due to the commensuration of the SD16 cylinders with the underlying topography, the cylinders align parallel to the hardened SD45 pattern because the bending energy of the cylinders to go against the underlying topography would require too much distortion in the polymer chains compared to simply aligning with the commensurate direction[188], though this likely would change with incommensurate patterns or rough surfaces such that perpendicular to the surface cylinders would be more preferential or even cylinders perpendicular to the underlying topography[176,189]. However, in this particular case the directionality and commensuration of the topography leads to specific alignment and long range ordering of the DSA guided SD16 cylinders[44,118].

Overall, these results demonstrate that topography produced from BCPs can be used to template additional BCPs and that the SCFT modeling can be applied in such situations

by considering the underlying template formed from the first BCP carefully. This process is analogous to double templating methods in traditional photolithography[190] with the benefits of the small sub-10 nm feature sizes accessible using BCPs. Commensurability of the templates was the key parameter in ensuring the underlying structure formed as designed, and will be seen to be one of the most important parameters involved in the next few sections on DSA simulations with more complex topographical constraints.

5.3 Hexagonal Post Array Studies

BCP with two species (diBCPs) generally have hexagonal close-packed symmetries in their cylindrical or spherical morphologies in the thin film. Thus one DSA system of interest consists of diBCP films templated by topography with hexagonal symmetries. In the simulations and corresponding experimental studies that follow, both spherical and cylindrical forming BCPs are subjected to topographical constraints with these kinds of symmetries. In most cases the post template features are functionalized with a brush of the minority PDMS, although in a few select cases a majority PS brush is used. Simulations with PDMS brush conditions templating mainly spherical forming PS-PDMS will be discussed first and some discussion of PS brush functionalized arrays templating cylinder forming PS-PDMS will be discussed afterwards. The chief objective in these studies is to make the underlying close-packed structures have better long range order, but in general other interesting phenomenon is observed for a variety of templates besides the simple underlying untemplated morphologies.

In the majority of these studies, the main variable in the simulation is the vector spacing of the hexagonal array of posts and the resulting equilibrium morphologies under changes in these distances between posts in different directions as schematically shown in Figure 5.4. When the post array is a true hexagonal lattice, this is simply characterized by a single variable L_{post}. In general the x and y-directions can be decoupled such that the unit cell is no longer truly hexagonal but a centered rectangular lattice with nonprimitive lattice lengths L_x and L_y, however for the studies that follow only strictly hexagonal post arrays were considered so everything will be a function of L_{post}.

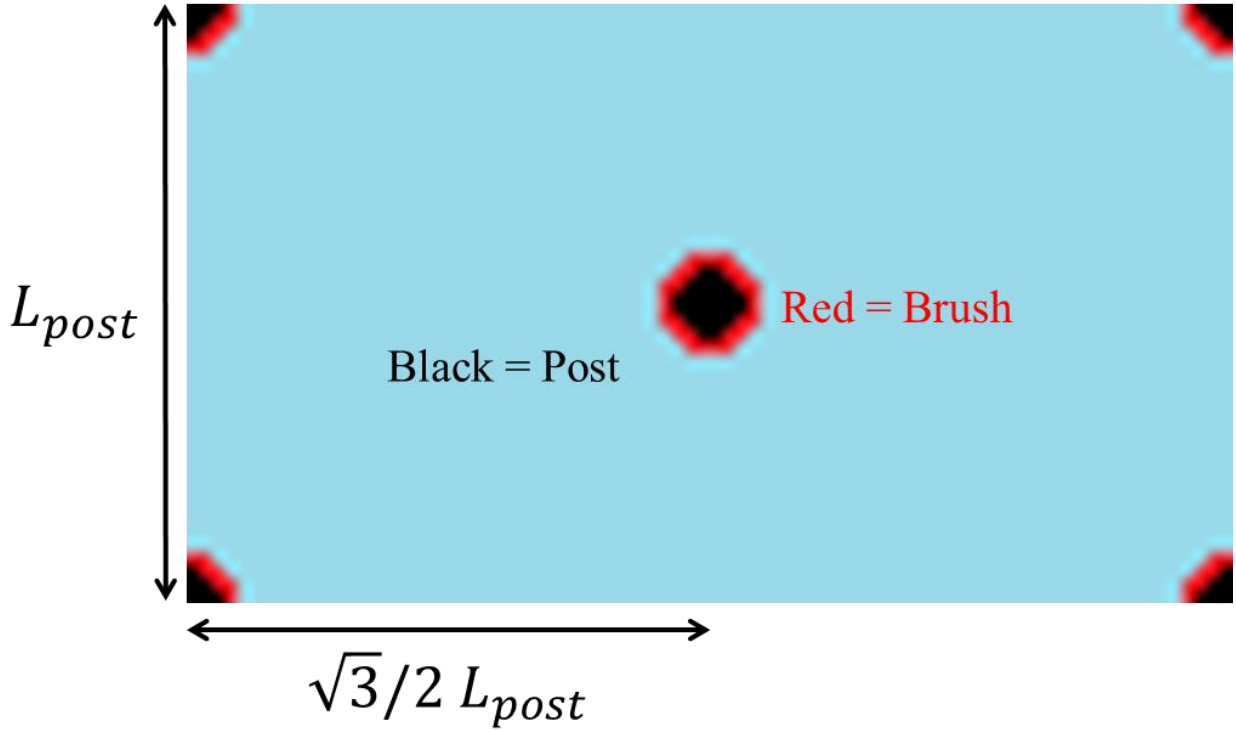

Figure 5-4: Schematic layout of the simulation unit cells for 2D hexagonal post arrays. Black area is where the posts are modeled and red area is where PDMS brush is modeled. The rest of the unit cell is unconstrained. Post size was varied in the simulation[49].

When near commensuration of a close-packed structure in the case of spheres or a commensurate direction for cylinders, a single dominate structure forms for multiple simulations. When away from commensuration, mixed or aperiodic states tend to form. Such structure formation is corroborated by free energy analysis. Additional factors are found to play a role in the formation of the structures such as post size dimensions including post diameter and height in 3D simulations. Both 2D and 3D simulations are examined to try to decouple these effects realizing the 3D simulations when optimized portray a better view of reality. Other factors such as f and χN affect the morphologies that form as expected from the thin film studies discussed previously. In general these studies show for a fixed set of f and χN corresponding to a fixed polymer and solvent annealing conditions, there is a wide parameter space available to explore simply from the possible post commensurations and size effects and thus a large engineering space for many potential structures for a variety of applications.

5.3.1 Simulation Results in 2D – Minority Block Preferential Posts

A variety of hexagonal based templates were modeled using SCFT in 2D for a variety of post spacing distances. These simulations were done in collaboration with Rafal Mickiewicz[49]. Field constraints used to model the posts were such that $\mu_A = \mu_B = P$ with $|P| = 20$ in the regions defined by the posts to ensure the internal polymer density in those regions were close to 0 and $\mu_A = -\mu_B = W = -10$ right around the posts to model the effects of a PDMS brush layer. The effective χN and f were varied in the simulations to try to best capture corresponding cross-sectional effective volume fraction parameters and the effective χ parameter of the corresponding PS-PDMS experimental system. For the system explored this corresponded to $(\chi N)_{eff} = 18$. In general the 2D f should roughly correspond to the observed area fraction in experiments so that effective features compared are as similar as possible, though in general full 3D simulations are necessary to capture the full details of the experimental morphologies. 2D simulations however allow great insight into overall physics of the morphologies formed while being computationally less expensive. Unit cells with N_x by $N_y = 84$ by 48 grid points were used with periodic boundary conditions and topographical post boundary conditions as shown in Figure 5.4.

For the initial set of simulations, $f = 0.25$ to try to best match the observed area fraction of a sphere forming PS-PDMS BCP. For this set of simulations, a variety of post lattice spaces keeping hexagonal symmetry were examined such that the ratio of the closest post spacing L_{post} to the natural period of the polymer L_0 was the parameter that was varied. Various dot patterns arrangements were observed as shown in Figure 5.5.

The observation that the underlying post lattice vectors makes an angle θ with the basis vectors of the PDMS dot patterns allows for characterization of the observed patterns as a function of L_{post}/L_0. The same observation was made experimentally in another study[2]. The lattice types are denoted by indices $\langle i\, j \rangle$ such that the post lattice vector $\vec{r}_{ij} = L_0(i\hat{a}_1 + j\hat{a}_2)$ where $\hat{a}_1$ and $\hat{a}_2$ are the PDMS dot pattern lattice vectors. For a given PDMS dot pattern, one can determine the i and j pair that satisfies this vector relationship. Previously in Chapter 1 in Section 1.3.1, a free energy model was given for this system. Using that model, the corresponding BCP PDMS dot pattern lattice that has the lowest

energy as a function of normalized post spacing L_{post}/L_0 is obtained and the results of these predictions are shown in Figure 5.6. Multiple simulations were run for the same L_{post}/L_0 but with different initial conditions, and in general converged to the same underlying BCP lattice except when the system was far from commensuration where disordered lattices were observed. There were also defective lattices observed in which case the underlying lattice was observed to be consistent between simulations but there were local defects in a given simulation. Overall these observations of the transition between different BCP lattices as a function L_{post}/L_0 were consistent with the previous experimental results and the free energy model.

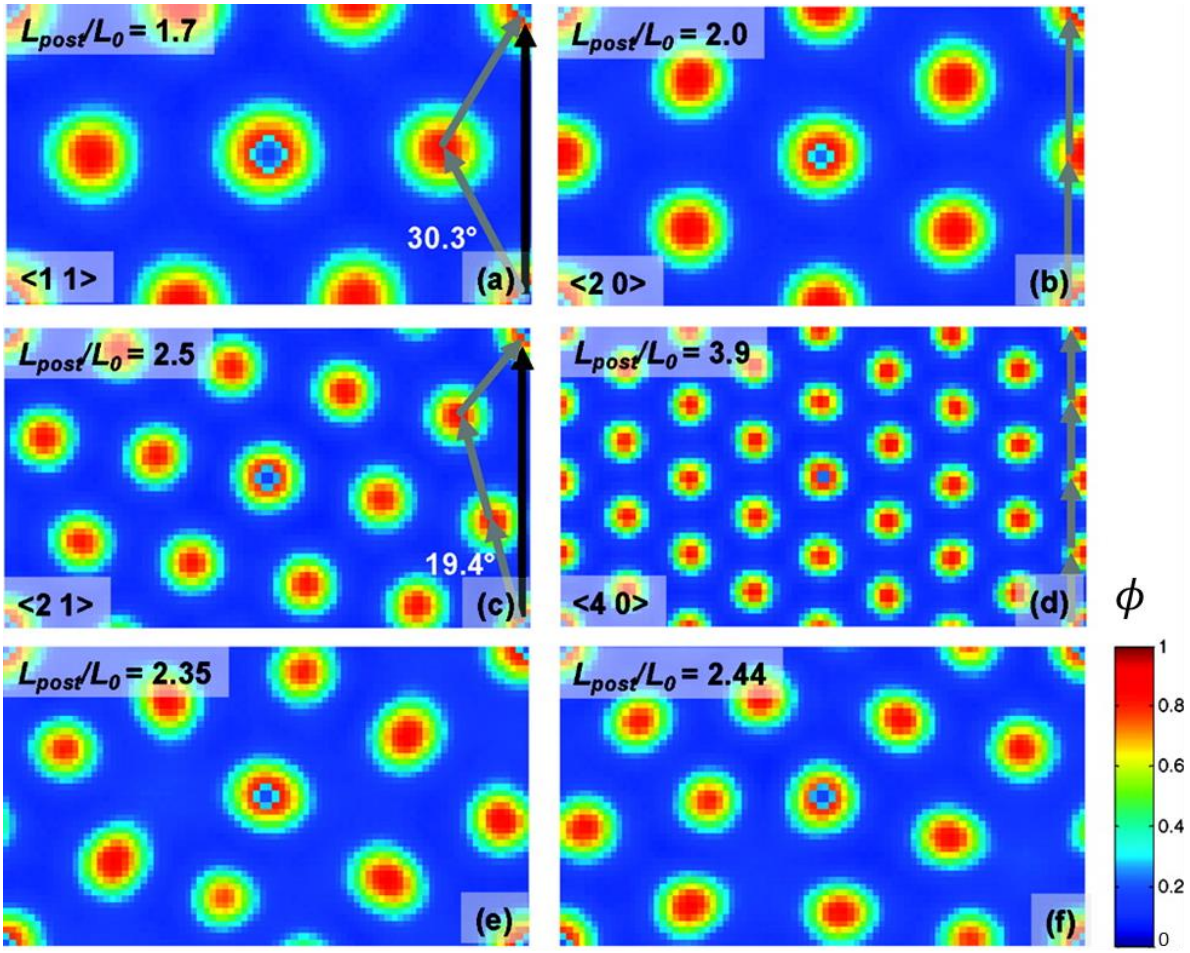

Figure 5-5: Simulation results for various L_{post}/L_0 values. (a) L_{post}/L_0 = 1.7 yielded an ordered BCP lattice with $\langle i\ j \rangle$ = $\langle 1\ 1 \rangle$, (b) L_{post}/L_0 = 2.0 yielded an ordered BCP lattice with $\langle i\ j \rangle$ = $\langle 2\ 0 \rangle$, (c) L_{post}/L_0 = 2.5 yielded an ordered BCP lattice with $\langle i\ j \rangle$ = $\langle 2\ 1 \rangle$, (d) L_{post}/L_0 = 3.9 yielded an ordered BCP lattice with $\langle i\ j \rangle$ = $\langle 4\ 0 \rangle$, (e) L_{post}/L_0 = 2.35 yielded a disordered BCP lattice, and (f) L_{post}/L_0 = 2.4 yielded a disordered BCP lattice[49].

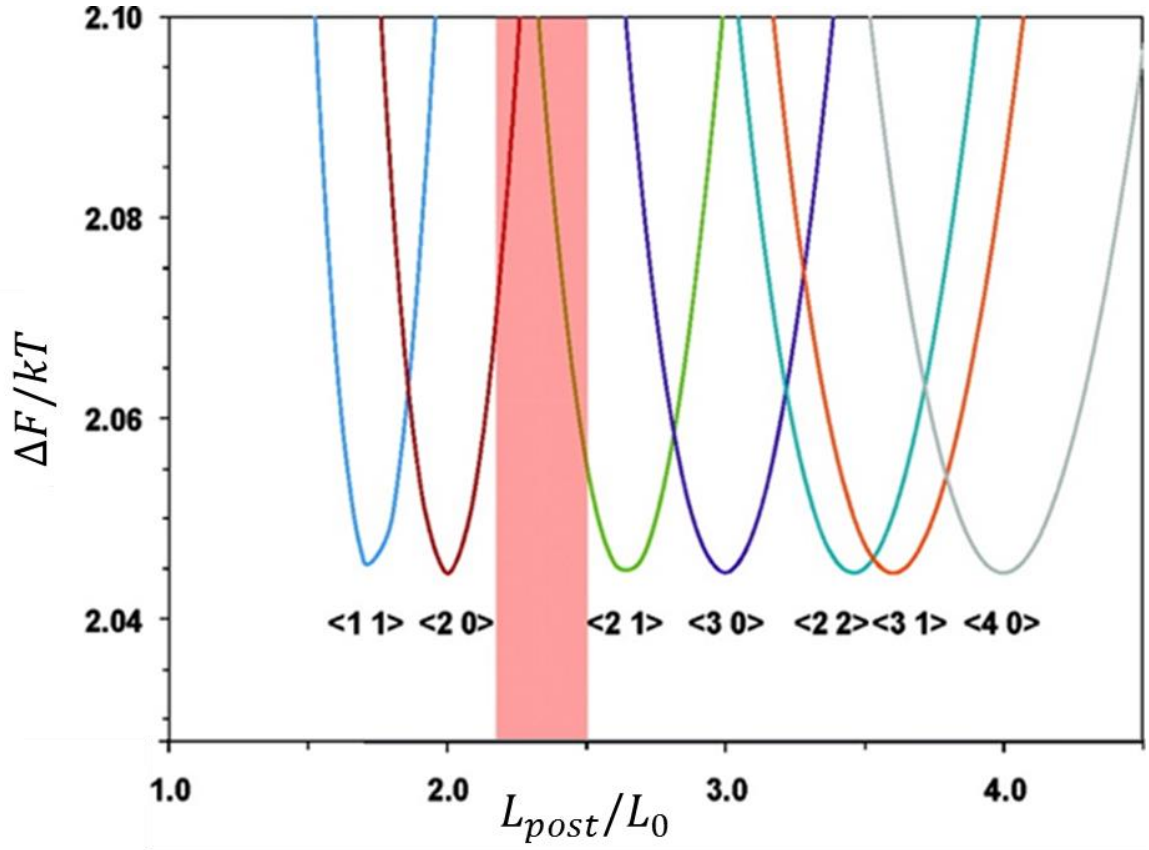

Figure 5-6: Free energy curves for different BCP PDMS dot lattices plotted versus L_{post}/L_0. At a given L_{post}/L_0, the curve with the lowest free energy should theoretically be the observed BCP lattice for that post spacing. In general those lattices were observed in the simulations at those post spacing distances. Near where curves intersect, disordered lattices were generally observed[49].

From these results, commensurability of the template post array with the targeted BCP PDMS dot pattern is very important for pattern design purposes. Although a range of L_{post}/L_0 may result in the same underlying template, that template will have strain in the system if not exactly commensurate. By plotting the actual observed polymer period L in a lattice normalized by the untemplated period L_0, a measure of the strain in the system is possible. Values of this ratio, L/L_0, are plotted as a function of L_{post}/L_0 in Figure 5.7. From the plot, tensile strains as high as 10% are observed before lattice orientation changes to accommodate the strain in the system and lower the free energy. Additionally, compressive strain in the lattice is harder to stabilize compared to tensile strain. Other work has shown similar strain levels achievable in lamellar systems[12,69] in addition to the observation of

tensile strain being more easily accommodated in lamellar studies with flat plates[191] and spherical domains on a patterned substrate[23]. Defective lattices were observed for very high strain values in addition to ordered lattices with local defects. At these transition regions corresponding to where the free energy curves of different structures meet, mixed lattices are expected experimentally with small grain sizes. In the simulations due to periodic boundary conditions, metastable disordered structures are instead observed. These results show in general that if a perfectly ordered lattice is desired, the lattice needs to be as close to the commensurate spacing as possible or just slightly strained in tension since compression is not favored.

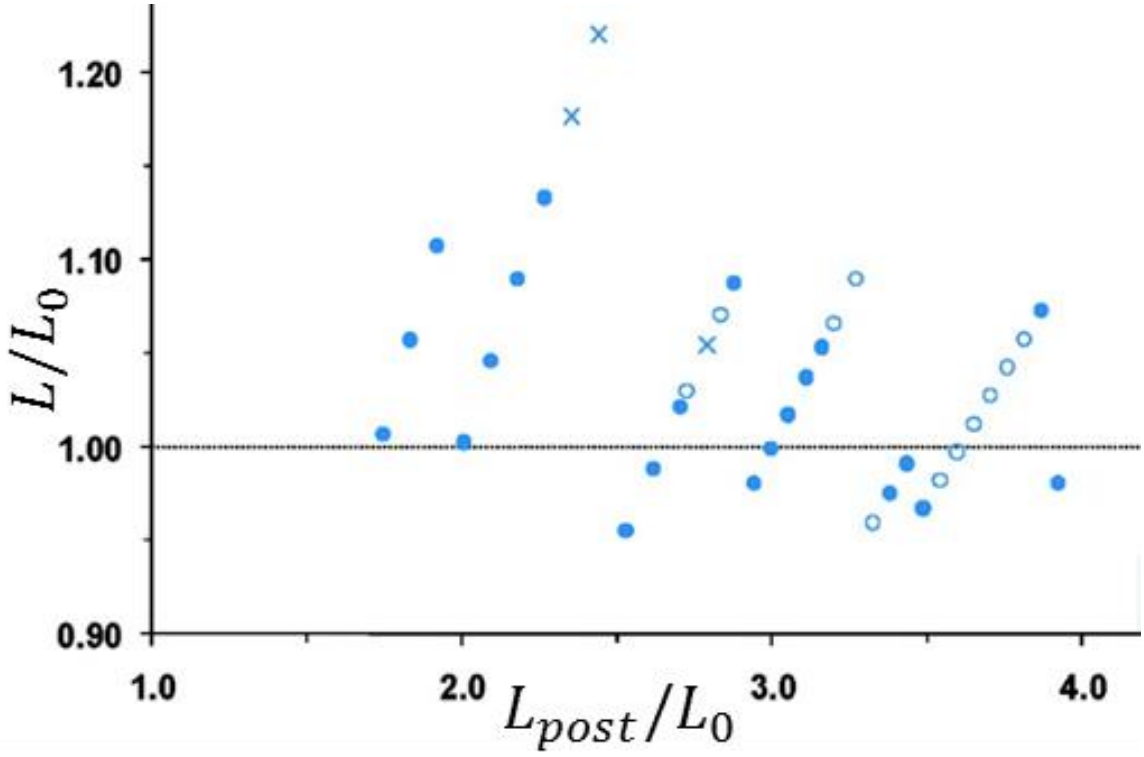

Figure 5-7: Plot of the effective strain L/L_0 versus normalized post spacing L_{post}/L_0. Blue dots correspond to ordered BCP lattices, blue circles to ordered BCP lattices with local defects, and blue 'x's to disordered structures[49].

To further explore hexagonal templates, simulations for fixed L_{post}/L_0 while varying either volume fraction f or post diameter size were performed. Results for varying post diameter are shown in Figure 5.8 and for varying f are shown in Figure 5.9. In the case of varying post diameter, $L_{post}/L_0 = 2$ where the $\langle 2\ 0 \rangle$ lattice was observed in the other

simulations. The post diameter D normalized by post lattice spacing L_{post} was varied across the range $D/L_{post} \in [0.04,0.33]$. For D/L_{post} less than 0.17, the ⟨2 0⟩ lattice always formed. Increasing D/L_{post} led to distortion of the microdomains until around $D/L_{post} = 0.23 \pm 0.02$ where the coordination of microdomains around a post became higher than six. At $D/L_{post} = 0.29$, the system transition to a ⟨1 1⟩ lattice due to the space between posts being reduced so much that the formation of the ⟨2 0⟩ would be highly strained.

In the case of varying volume fraction, $f \in [0.30,0.50]$ with a fixed post spacing of $L_{post}/L_0 = 2.18$ and fixed diameter of $D/L_{post} = 0.08$. Initially the effect of increasing volume fraction serves only to increase the size of the dots while retaining the ⟨2 0⟩ lattice. As f increases above 0.37, the dots begin to connect as a transition to a lamellar like morphology occurs. These transitional structures tend to have poor order due to the lamellae having competing symmetry directions in which to align. At $f = 0.50$, a full lamellar morphology is expected but due to high attraction potentials in the model and competition between alignment directions in the six fold post symmetry a metastable honeycomb structure was rather observed as shown in Figure 5.9.f. Weakening the attractive strength of the brush layer to $W = -5$ leads to better aligned lamellae but still with a defect as shown in Figure 5.9.g. Other studies showed well aligned lamellae using SCFT with two fold symmetry post arrays to enforce the direction of the lamellae[1].

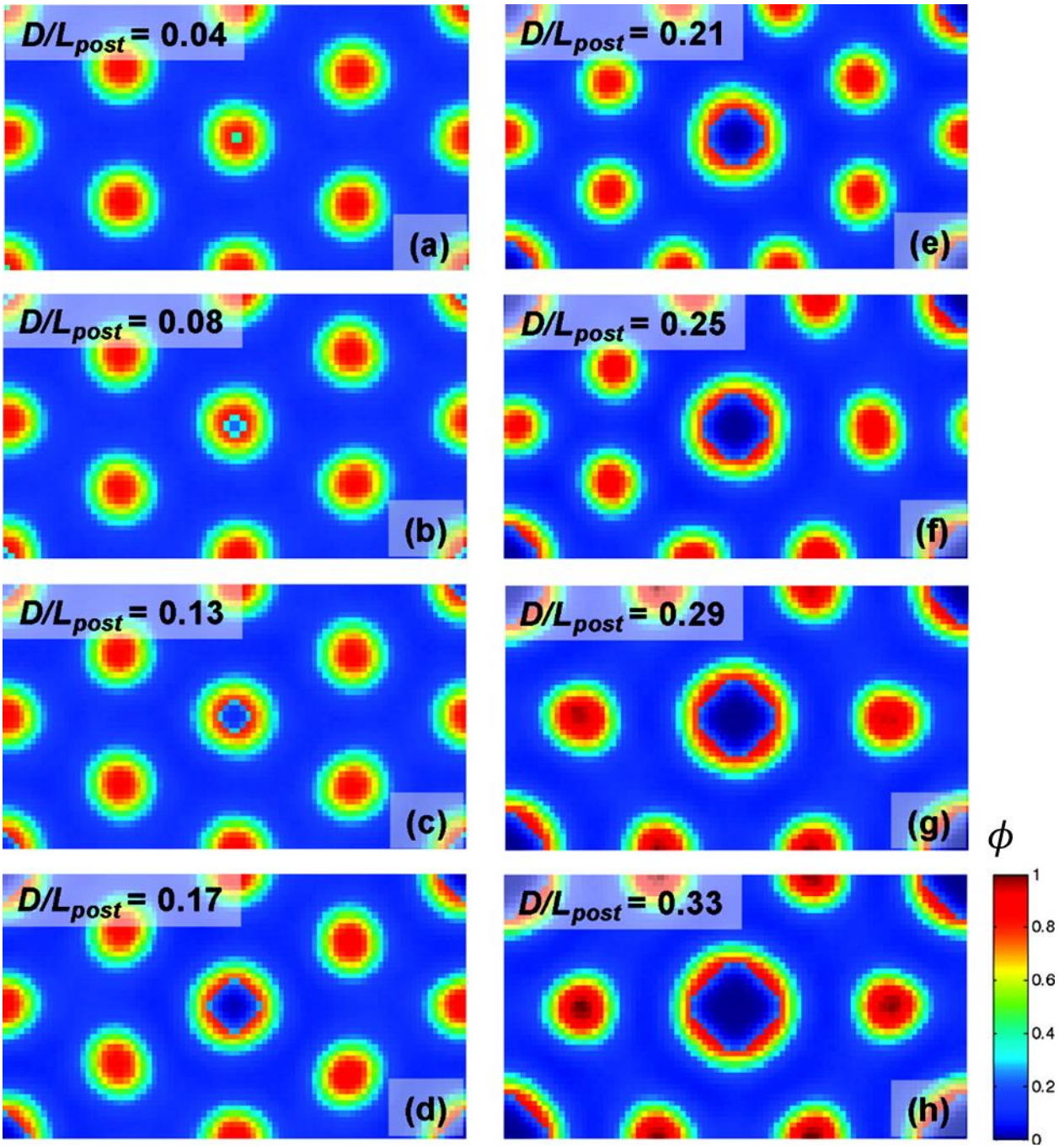

Figure 5-8: Simulations results as a function of D/L_{post}. (a) D/L_{post} = 0.04 had a ⟨2 0⟩ lattice form. (b) D/L_{post} = 0.08 had a ⟨2 0⟩ lattice form. (c) D/L_{post} = 0.13 had a ⟨2 0⟩ lattice form. (d) D/L_{post} = 0.17 had a ⟨2 0⟩ lattice form with some distortion. (e) D/L_{post} = 0.21 had a mixed lattice with increasing coordination around the post. (f) D/L_{post} = 0.25 had a disordered lattice. (g) D/L_{post} = 0.29 had a ⟨1 1⟩ lattice form. (h) D/L_{post} = 0.33 had a ⟨1 1⟩ lattice form[49].

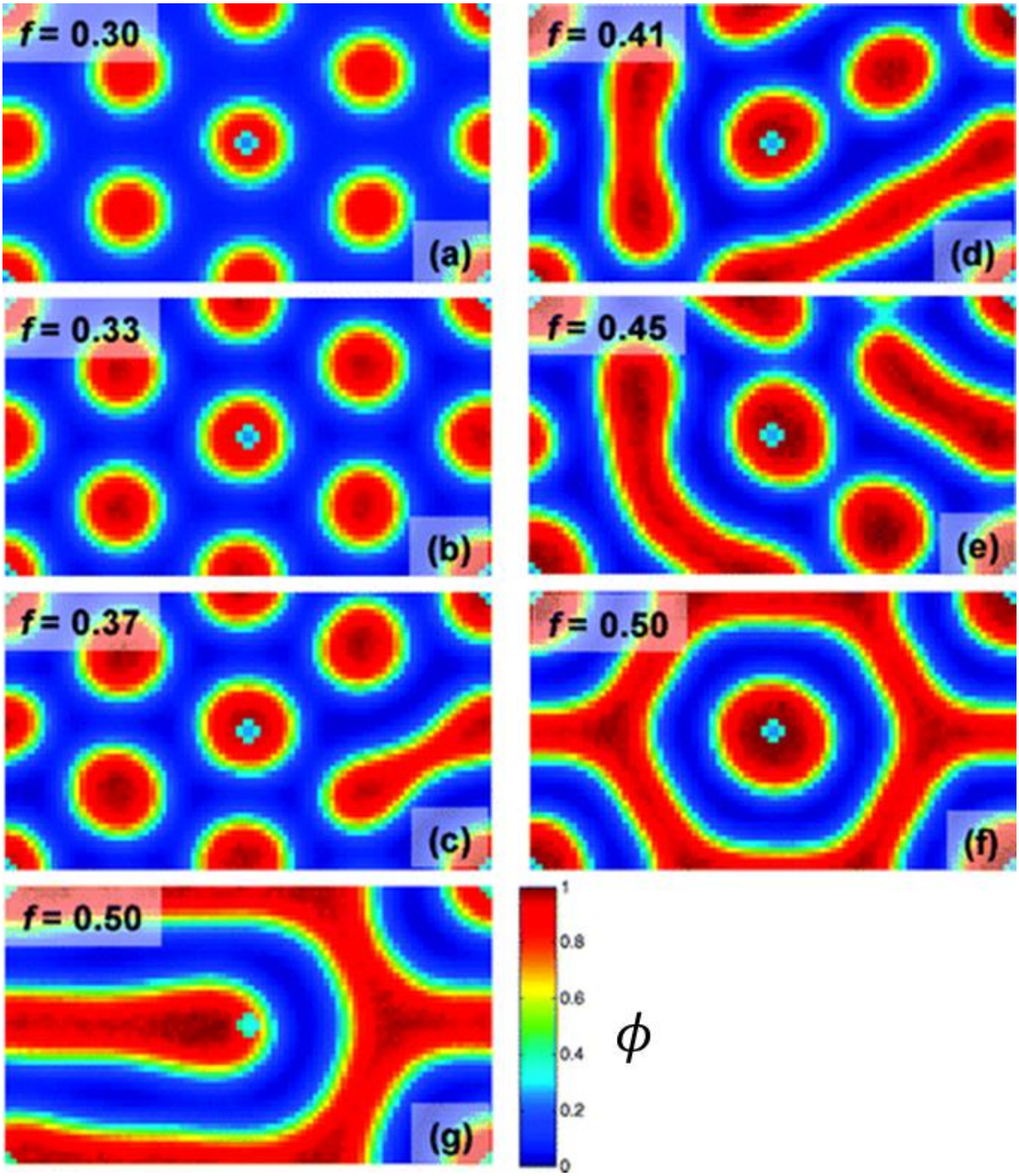

Figure 5-9: Simulations results as a function of f for fixed L_{post} and D. (a) f = 0.30 had a ⟨2 0⟩ lattice form. (b) f = 0.33 had a ⟨2 0⟩ lattice form. (c) f = 0.37 had a ⟨2 0⟩ lattice form with a defect connection between dots. (d) f = 0.41 had elongated disordered structures. (e) f = 0.45 had elongated disordered structures. (f) f = 0.50 had a metastable lamellar honey comb structure form. (g) f = 0.50 with W = -5 had horizontal lamellae form with a defect due to the degeneracy of mixed states imposed by the six fold symmetry of the lattice[49].

5.3.2 Simulation Results in 3D – Minority Block Preferential Posts

For the case of a hexagonal lattice with PDMS brush, 3D simulations were performed to examine how the spheres templated by the hexagonal post arrays changed with film thickness. In these simulations $f = 0.25$, $L_{post}/L_0 = 2.0$, and N_z was set to either 36 or 48 grid points representing either 1.5 or 2.0 L_0 thick films, both in the range of observed commensurate thicknesses in experiment[192]. The bottom surface was preferential to PDMS to represent the PDMS brush layer and the top surface was left neutral. Results for the two thicknesses are shown in Figure 5.10 and for both thicknesses a distorted ⟨2 0⟩ lattice of spheres forms between the post features. The posts in these simulations went through the whole thin film thickness meaning the corresponding experimental film would have a thickness greater than the height of the posts. Later simulations will relax this constraint and look at post height directly in addition to changing post diameter such that the posts are not as tall as the film thickness. Since the bottom surface is preferential to PDMS and top surface is neutral, a commensurate thick film occurs when the thickness is $1.5L_0$. Thus the elongation in the $z-$direction observed for the $2.0L_0$ thick film is due to the film being strained in that direction. These results agree well with what is expected experimentally in the actual films in terms of thickness of features.

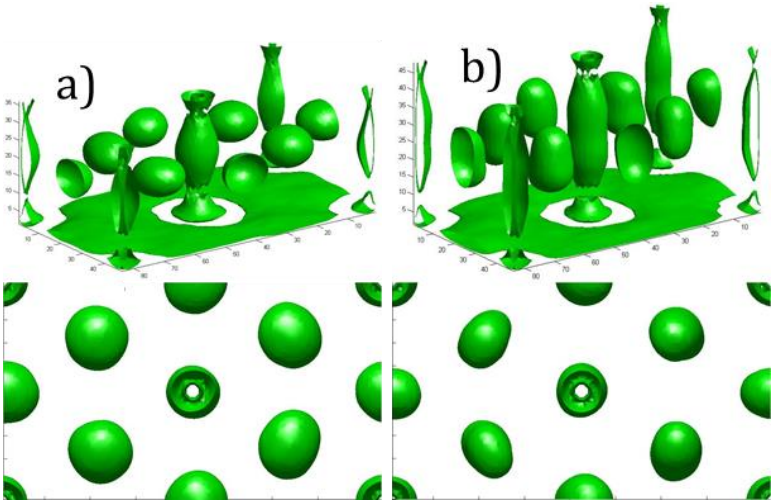

Figure 5-10: 3D simulations for L_{post}/L_0 = 2.0 and f = 0.5 with constant density isosurfaces ϕ = 0.5 plotted green. Top images are 3D side angle views and bottom images are top-down cut through views with the brush layer removed for clarity. (a) Thickness of 1.5 L_0 shows ⟨2 0⟩ lattice with slightly distorted spheres. (b) Thickness of $2.0L_0$ shows ⟨2 0⟩ lattice with distorted spheres elongated in the z-direction[49].

5.3.3 Experimental Results and Comparison – Minority Block Preferential Posts

Overall the SCFT results as well as free energy analytical model predictions agreed with the BCP PDMS dot array patterns types as a function of L_{post}/L_0 observed using HSQ EBL patterned hexagonal arrays of posts[31] functionalized with PDMS brush in the experiments done by Ion Bita and colleagues[2]. In those experiments, the post pattern had a diameter of approximately 15 nm and height of 30 nm and the PS-PDMS had a volume fraction $f_{PDMS} = 0.165$ (smaller than the values used in simulation since area fraction was being matched for the 2D simulations) and $L_0 = 40$ nm. After coating the substrates with the PS-PDMS, the samples were thermally annealed at a temperature of 200℃ and the resulting thin film morphology was observed to be monolayers of spheres at the film thicknesses used.

As shown in the SEM image in Figure 5.11, the darker grey PDMS dots or spheres formed between the lighter white HSQ posts. In this particular case, the lattice that formed was a $\langle 1\ 1 \rangle$ for $L_{post} = \sqrt{3}L_0$. Experimentally L_{post}/L_0 was varied from 1.5 to 5.0. When incommensurate, the observed BCP period was strained to a value of L as previously discussed in the context of the calculated strain in the simulations. The ratio of the post period to strained BCP period $L_{post}/L = \sqrt{i^2 + j^2 + ij}$ where i and j are the integer coefficients of the BCP lattice vectors as previously discussed. The angle that the BCP lattice vector makes with the post lattice vector is given as $\Theta = \cos^{-1}\left((2i + j)/(2\sqrt{i^2 + j^2 + ij})\right)$. In Figure 5.11, the displayed angle θ is related to the other angle Θ as $\theta = \pi - 2\Theta$. Since the post diameter was constant in the experiment, the range of post diameter to post spacing ratio varied from $D/L_{post} \in [0.075, 0.250]$ meaning that only for the smallest L_{post} distances is there concern for the post size straining the lattice as observed in the simulations where the post diameter was varied since the simulations showed such distortion due to post size occurring for diameters greater than $0.21L_{post}$. Thus the simulation parameters are well correlated with the experimental parameters across the whole parameter space of L_{post}/L_0.

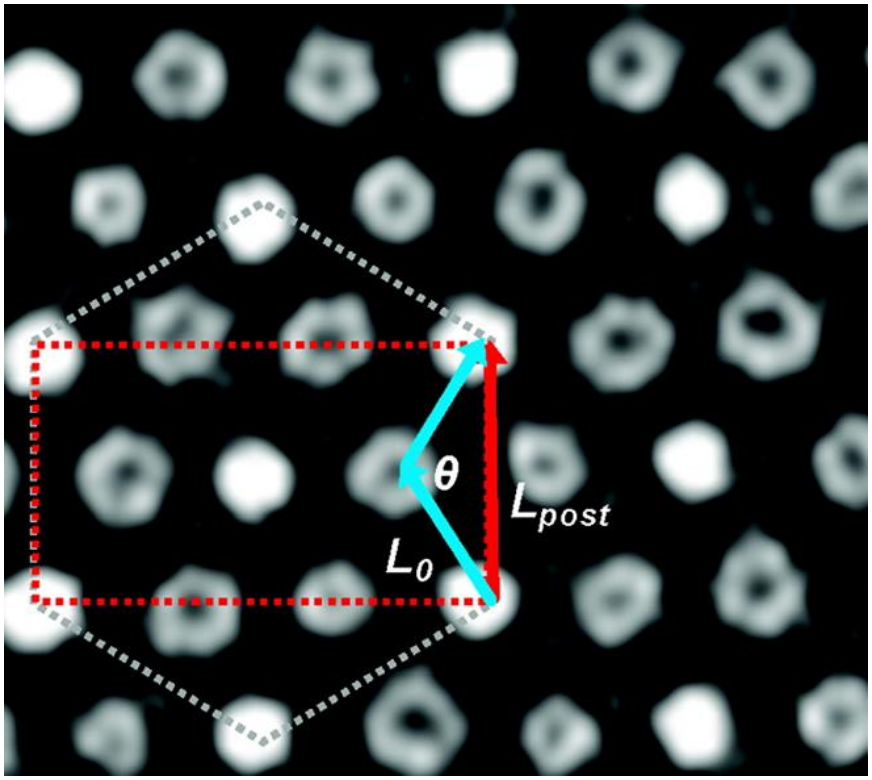

Figure 5-11: SEM image showing a DSA templated array of PDMS spheres (grey) by an HSQ post lattice (white) with $L_{post}/L_0=\sqrt{3}$ resulting in the BCP lattice having a ⟨1 1⟩ lattice orientation. The angle θ shown is 120° and the post lattice vector is shown in red and BCP lattice vector in teal. The result agrees with the SCFT simulations for the same post lattice parameters[49].

As an additional study, an intentional defect was imposed on a lattice with $L_{post}/L_0 = \sqrt{3}$. For this defect study, a post was chosen to have the six surrounding posts be moved away from the center post by a 1.15 factor increase in distance in all six directions. The resulting post distance shift left a spacing of $2.0L_0$ between the shifted posts and the center posts. As shown in Figure 5.12.a, the experimental result gave a ⟨1 1⟩ BCP lattice everywhere as expected except right around the defect region where a ⟨2 0⟩ lattice rotated 30° relative to the ⟨1 1⟩ instead formed. The boundary between the two lattices contained spheres with coordination symmetries that were 5-fold and 7-fold as shown in the Voronoi diagram in Figure 5.12.b. Large 2D SCFT simulations with multiple unit cells were performed to compare with these results on a N_x by $N_y = 114$ by 110 grid points (total size $4L_{post}$ by $3\sqrt{3}L_{post}$ or 4 by $3 = 12$ unit cells). As shown in Figure 5.12.c, the results agree well with the experiment. Additionally, a simulation was performed where

the central post in the defect area was shifted by $\approx 0.08L_0$ horizontally. The shift resulted in the BCP lattice shown in Figure 5.12.d in the defect region realigning back to the ⟨1 1⟩ orientation showing that relatively small changes in the spacing of the post template can drastically affect the resulting BCP lattice.

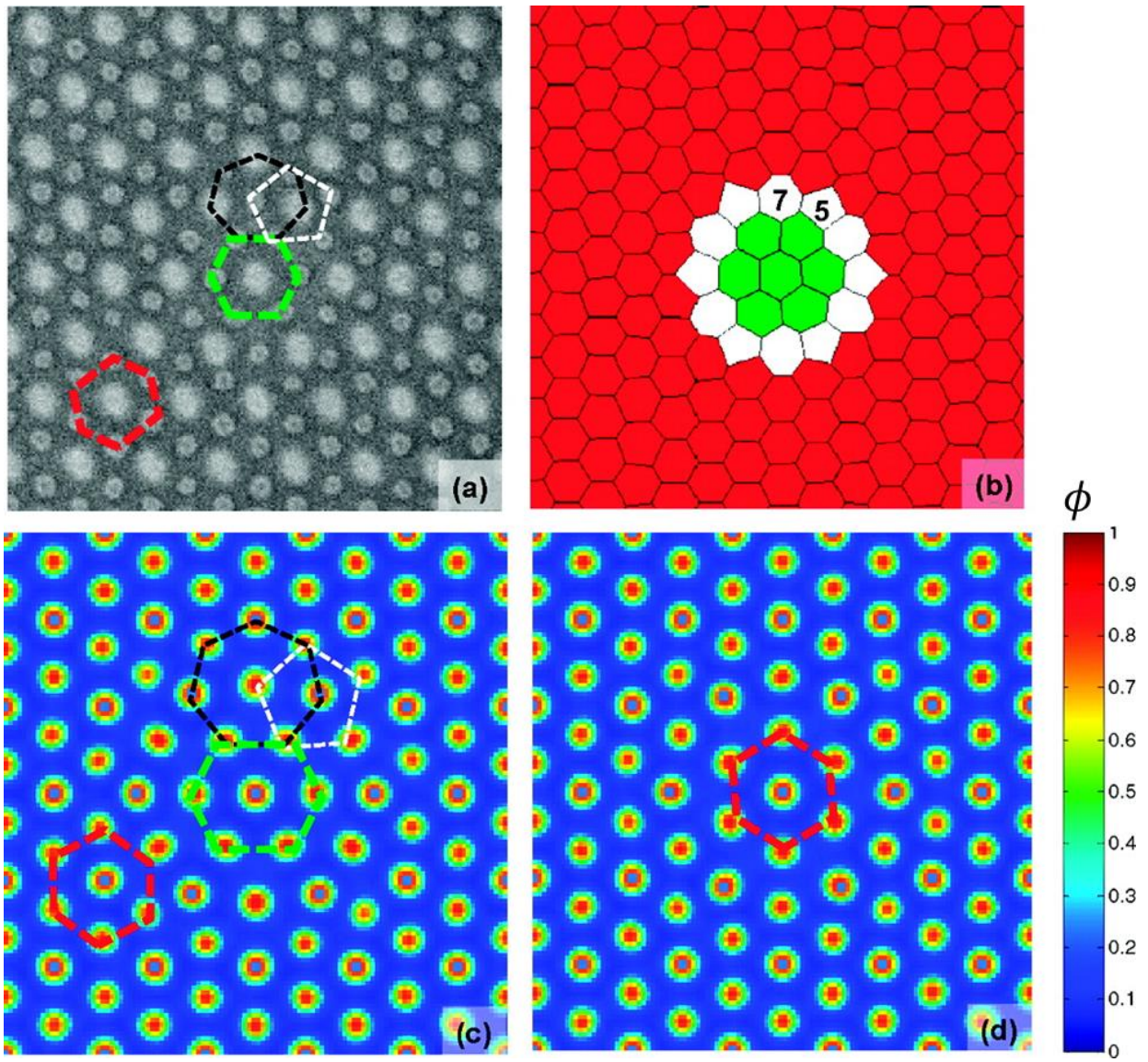

Figure 5-12: Results of studying the effect of intentional defects on the local BCP lattice formation through both experiments and simulations. (a) Experimental result of intentional defect study where red color shows ⟨1 1⟩ region, green color shows ⟨2 0⟩ region, white color shows 5-fold symmetry defect, and black color 7-fold symmetry defect. (b) Voronoi diagram of the experimental results in (a) with same color coding. (c) SCFT result showing the same result as in (a) with same color coding representing different regions. (d) SCFT result where defect region center post was shifted slightly allowing for the BCP lattice to adjust and form a ⟨1 1⟩ lattice everywhere and anneal out the defected region[49].

5.3.4 Simulation Results in 3D – Majority Block Preferential Posts

Hexagonal arrays of posts were used to template a cylinder forming PS-PDMS BCP with PS brush functionalization on the posts and substrate. Such a system was of interest because at the right commensuration of post diameter D_{post} and post spacing distance L_{post} a perforated lamellae structure formed and was stabilized by the posts that would normally be metastable under normal annealing conditions[193]. The observation that the size of the holes in the perforations are tunable as a function of D and L_{post} was also a key influence in the simulation studies[60]. The holes in the perforated lamellae structure has hexagonal symmetry and thus the posts in this templating functionalized with the majority block PS act as fixed regions of PS where the holes of the perforated lamellae form. Thus this templating can be thought of as inverted structure of the spheres that were previously templated with PDMS preferential posts.

A schematic diagram of the 3D unit cell used in these simulations is shown in Figure 5.13. The purple regions designate where the posts were located that were modeled by constraining the fields according to the constraint $\mu_A = \mu_B = P$ with $|P| = 20$ as before. Similarly, the yellow regions representing the brush layer were modeled under a majority block exchange field constraint such that $\mu_A = -\mu_B = W_{BL} = 10$. The teal top region was had the exchange field constraint $\mu_A = -\mu_B = W_{Air} = -10$ to model an assumed preferential wetting of PDMS on the top surface of the film. Periodic boundary conditions were applied in the x and y −directions. In the simulations $(\chi N)_{eff} = 28.0$ for effective solvent annealing conditions and $f = 0.32$ which is close to the expected volume fraction of the PS-PDMS at experimental solvent annealing conditions. Steepest descent complex Langevin dynamics was used to drive the system from random initial field conditions to saddle point equilibrium structures. The unit cell box size was N_x by N_y by N_z varied from 28 by 48 by 22 to 38 by 68 by 22 for different L_{post} spacing distances. The film thickness corresponds to a $T \approx 1.8L_0$ thick film which is in the range of observed swollen thicknesses experimentally. The volume of a single grid point is approximately $(2.9\text{ nm})^3$ based on the observed experimental period of ≈ 35 nm. The posts had a constant height of $h_{post} \approx L_0$ and a diameter with explored range $D_{post}/L_0 \in [0.39,1.20]$. Note that the coarse graining

used to model the post features resulted in the posts looking like squares rotated by 45°, so the diameter as reported is an effective diameter calculated as $D_{post} = s\sqrt{2/\pi}$, where s is the diagonal length along the square. This effective diameter is necessary to properly compare the post diameters to circular posts used in experiment and the formula here is based on equating the area of a square post with a circular post. The post spacing $L_{post} = P_x$ with $P_y = \sqrt{3}P_x$ was varied with range $P_x/L_0 \in [2.33,3.33]$.

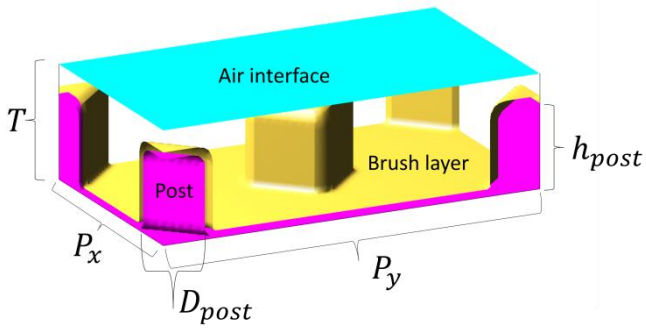

Figure 5-13: Hexagonal post array unit cell 3D unit cell field boundary conditions schematic used in the SCFT simulations. The regions constrained for the posts and substrate are purple, for the PS brush layer are yellow, and for the PDMS preferential air interface are teal[60].

In the simulations, the main goal was to find at what combinations of D_{post} and P_x the perforated lamellae structure was the equilibrium solution to the SCFT conditions. An example result of this perforated lamellae structure is shown in Figure 5.14 using the same simulation result concatenated together for clarity in displaying the structure. The conditions this particular structure was observed were $P_x = 2.67L_0$ and $D_{post} = 0.80L_0$.

Simulations were performed at a variety of combinations of D_{post} and P_x to determine where the perforated lamellae structure was stable and a large sampling of these results are shown in Figure 5.15 along with other structures that formed at other commensurations. Eight different combinations of D_{post} and P_x resulted in the perforated lamellae structure, six of which are shown in Figure 5.15. Additional simulations not shown were performed at D_{post} =1.07 and $P_x = 3.00L_0$ as well as $D_{post} = 1.20$ and $P_x = 3.16L_0$ with these resulting in the formation of the perforated lamellae structure. However, these two results were outside of the range of experimental parameters tested, but are still instructive in understanding how the phenomenon of the stabilization of perforated

lamellae occurs and will be discussed more in depth in the next section. Additionally at four combinations of D_{post} and P_x, a structure with half the unit cell having the perforated lamellae structure but the other half having a defect hole connection was observed. These results were used in comparing hole sizes with experimental results even though they are strictly not the perforated lamellae structure and are noted as such in the experimental comparison section.

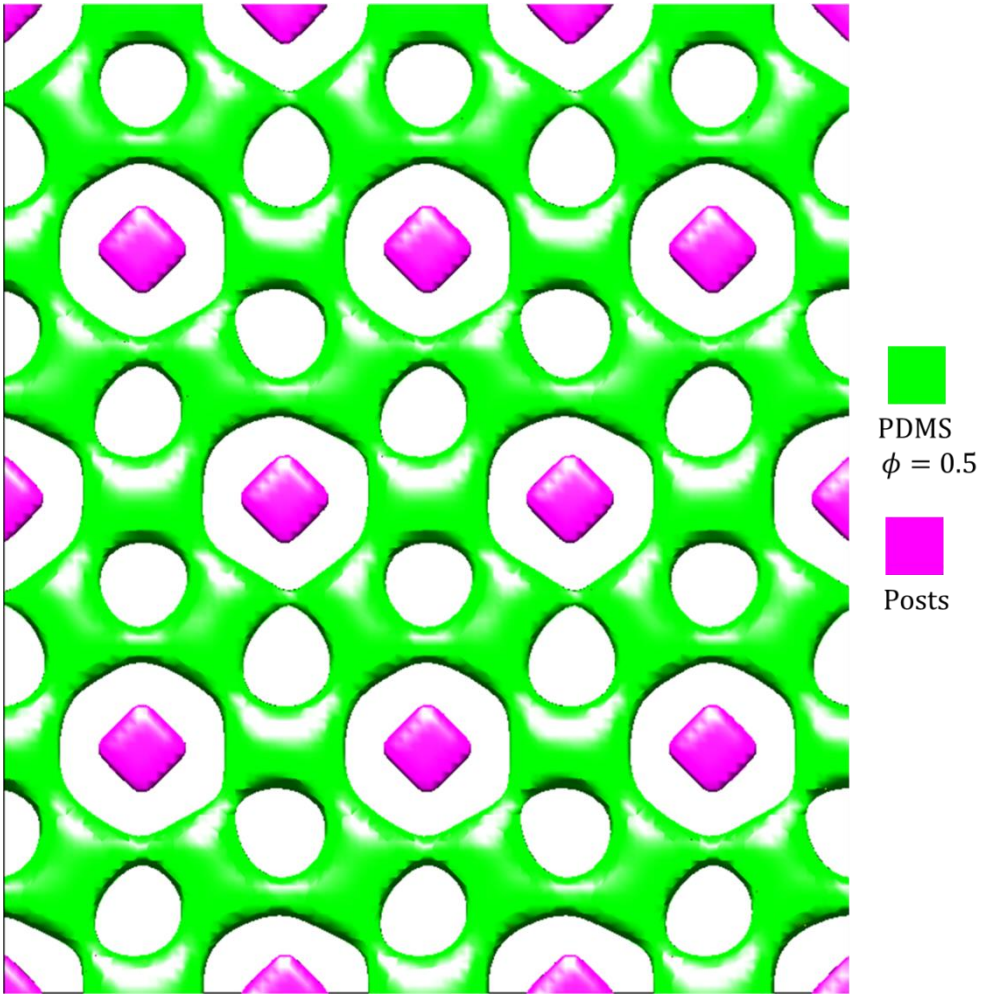

Figure 5-14: Top-down cut through view showing the desired perforated lamellae structure stabilized at certain combinations of P_x and D_{post}. Posts are colored purple and ϕ = 0.5 density cross-sections showing where the PDMS domains start are green[60].

The general trend observed in these simulations is that as D_{post} increases, the relative P_x must also be increased in order to maintain the stability of the perforated lamellae structure. In terms of commensuration, this means the key parameter at

stabilizing the structure is the spacing between posts or effective $P_x - D_{post}$ and in the next section will be shown to be $\sim 2L_0$ for the region where the perforated lamellae structure is stabilized (corresponding to the commensuration of two effective cylinder domains joining in the regions between the holes around the closest posts). This is analogous to the PDMS spheres forming a ⟨1 1⟩ lattice but now with holes in a perforated lamellae structure due to the polymer symmetry inversion from the majority PS posts being used.

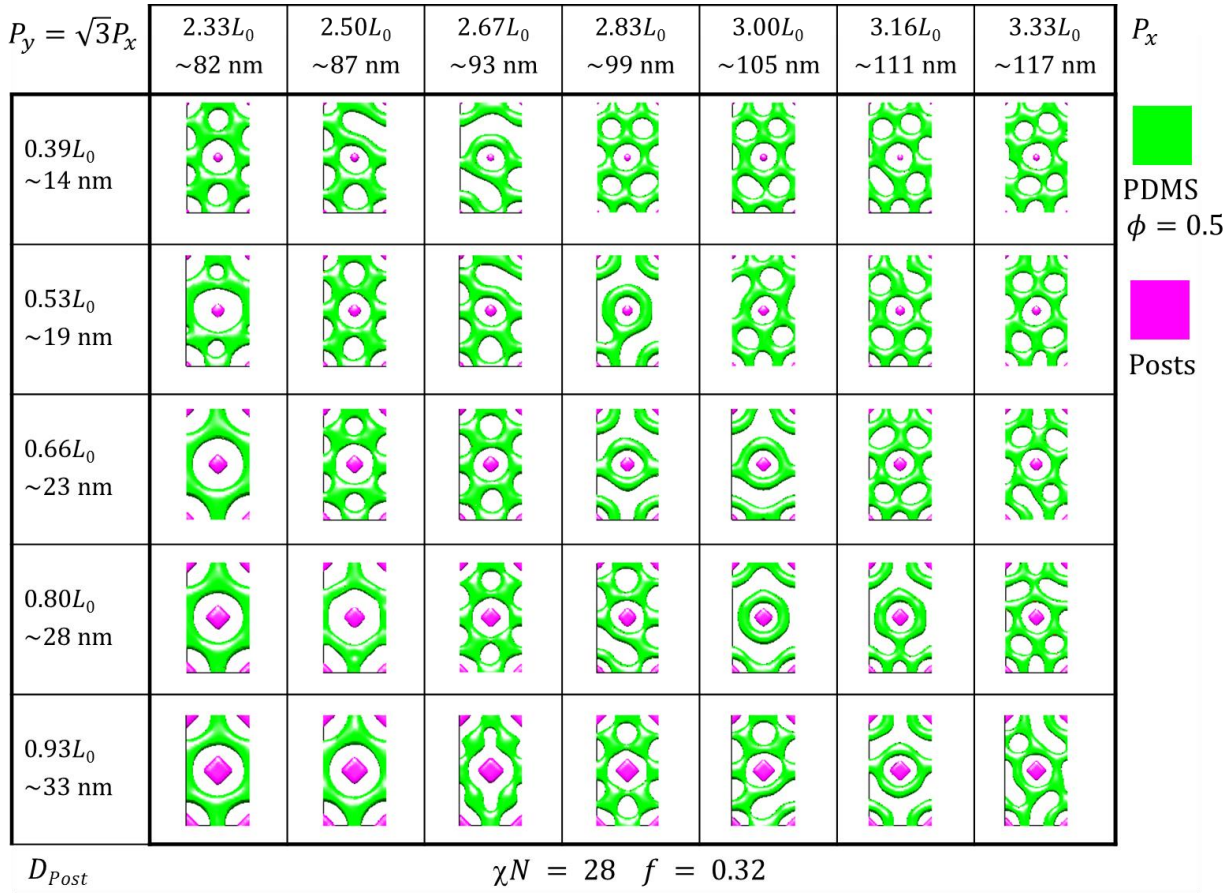

Figure 5-15: Simulation results as a function of D_{post} and P_x. Plots are top-down cut through views of the internal structure in the simulations with posts colored purple and PDMS domains at the ϕ = 0.5 boundary colored green. The perforated lamellae structure was observed at $D_{post} = 0.39L_0$ and $P_x = 2.33L_0$, $D_{post} = 0.53L_0$ and $P_x = 2.50L_0$, $D_{post} = 0.66L_0$ and $P_x = 2.50L_0$, $D_{post} = 0.66L_0$ and $P_x = 2.67L_0$, $D_{post} = 0.80L_0$ and $P_x = 2.67L_0$, and $D_{post} = 0.93L_0$ and $P_x = 2.83L_0$. A defect structure of a half way formed perforated lamellae structure was observed at $D_{post} = 0.39L_0$ and $P_x = 2.50L_0$, $D_{post} = 0.53L_0$ and $P_x = 2.67L_0$, $D_{post} = 0.80L_0$ and $P_x = 2.83L_0$, and $D_{post} = 0.93L_0$ and $P_x = 3.00L_0$. Not shown are two perforated lamellae results at $D_{post} = 1.07L_0$ and $P_x = 3.00L_0$ as well as $D_{post} = 1.20L_0$ and $P_x = 3.16L_0$ as not all P_x were tested for these D_{post} and they were outside the experiment test range of post diameters[60].

5.3.5 Experimental Results and Comparison – Majority Block Preferential Posts

In the experiments performed by Amir Tavakkoli K.G. with the assistance of Sam Nicaise and Kevin Gotrik, both HSQ and poly(methyl methacrylate) (PMMA) posts were used in the hexagonal post array DSA template for the 45.5 kg/mol cylinder forming PS-PDMS BCP. The purpose of using PMMA to make posts was because the cross-linked PMMA is etched away during the oxygen plasma reactive ion etching step used to remove the PS matrix and thus leaves the sample with a mesh grid of holes for the perforated lamellae morphology rather than a perforated lamellae with HSQ posts in some of the holes. The samples were prepared as previous thin films noting that they were annealed using a solvent anneal with a solvent ratio of 5 to 1 toluene to heptane. Thus the simulations consist of implicit parameters for modeling the system. An experimental SEM image result with HSQ posts for sample corresponding to the $D_{post} = 0.80L_0$ and $P_x = 2.67L_0$ simulation is shown in Figure 5.16. Another experimental result for the same conditions but using PMMA posts that were etched away before imaging using a plasma reactive ion etch is shown in Figure 5.17.

As can be seen in these experimental results as well as the SCFT simulation results, the size of the perforated lamellae holes varies whether the hole is between the posts (a generated hole) or if the hole is around a post (a post hole). To quantify this behavior, plots of hole diameter for both kinds of holes were plotted versus both post diameter D_{post} and post pitch P_x for both the simulation results that gave the perforated lamellae structure as well as the results with half structure and the experimental results where the perforated lamellae was observed. These two plots are shown in Figure 5.18. In general, the generated hole did not vary much with D_{post} and P_x while the post hole diameter increased linearly with both variables. This can be understood in terms of the strain on the polymers required to keep the perforated lamellae structure stable in that the generated holes have no internal source to relieve strain and thus are limited in the size range they can form while the hole around the posts can grow larger with both the diameter of the posts filling the space inside the hole. The linear trend with post pitch is just a consequence of the region where the perforated lamellae structure is stable being a linear function of the post

diameter such that the post hole size growing with post pitch is still a consequence of the larger posts filling the space inside the hole.

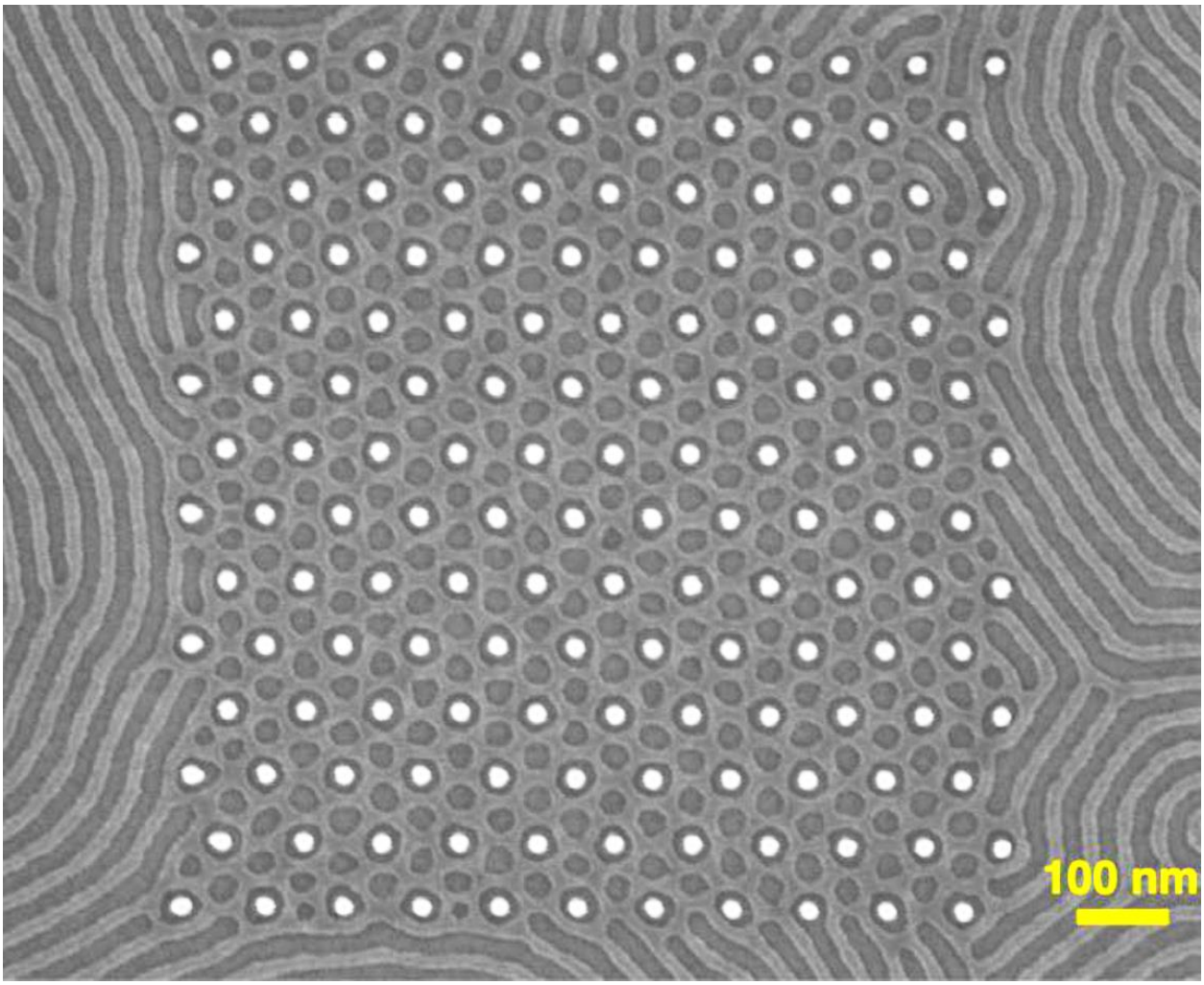

Figure 5-16: SEM image showing the resulting perforated lamellae morphology with HSQ posts for a sample corresponding to $D_{post} = 0.80L_0$ and $P_x = 2.67L_0$[60].

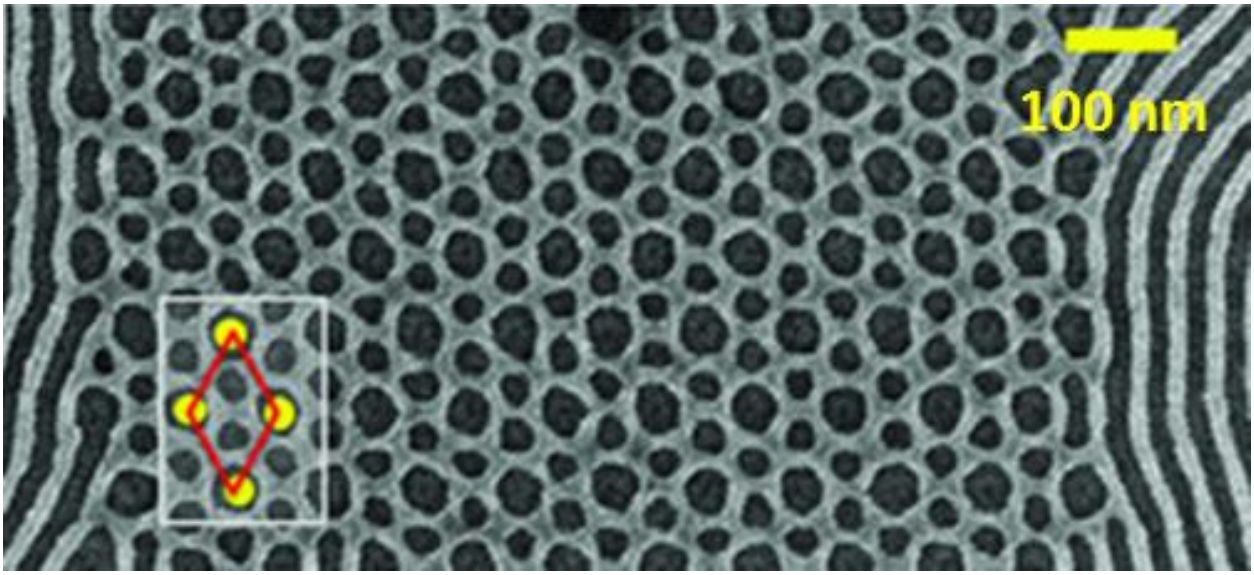

Figure 5-17: SEM image showing the resulting perforated lamellae morphology with PMMA posts that were removed for a sample corresponding to D_{post} = 0.80L_0 and P_x = 2.67L_0. The inset with overlaid yellow circles and red diamond show where the posts were before etching for a single unit cell with the diamond sides representing the distance P_x between posts[60].

One other key parameter of interest is the interpost spacing, $P_x - D_{post}$. This value is plotted as a function of post pitch P_x along with a plot of D_{post} as a function of P_x in Figure 5.19. In general the interpost spacing is constant with $P_x - D_{post} \cong 2L_0$ suggesting that the main stabilizing effect of the perforated lamellae structure is the interpost spacing being commensurate with the effective conversion of two lines of cylinders into a set of perforated lamellae. Thus the structure is stabilized by the normal cylinders making junctions at the proper points by through chain stretching. The presence of the posts in the system allows for such stretching of the chains and thus when the proper interpost spacing range is achieved the perforated lamellae structure that is normally metastable is able to form spontaneously[193]. Since the difference in P_x and D_{post} needs to be constant for the perforated lamellae structure to form, the linear relationship between the two is expected as they both need to increase proportionately in order to keep their difference approximately equal.

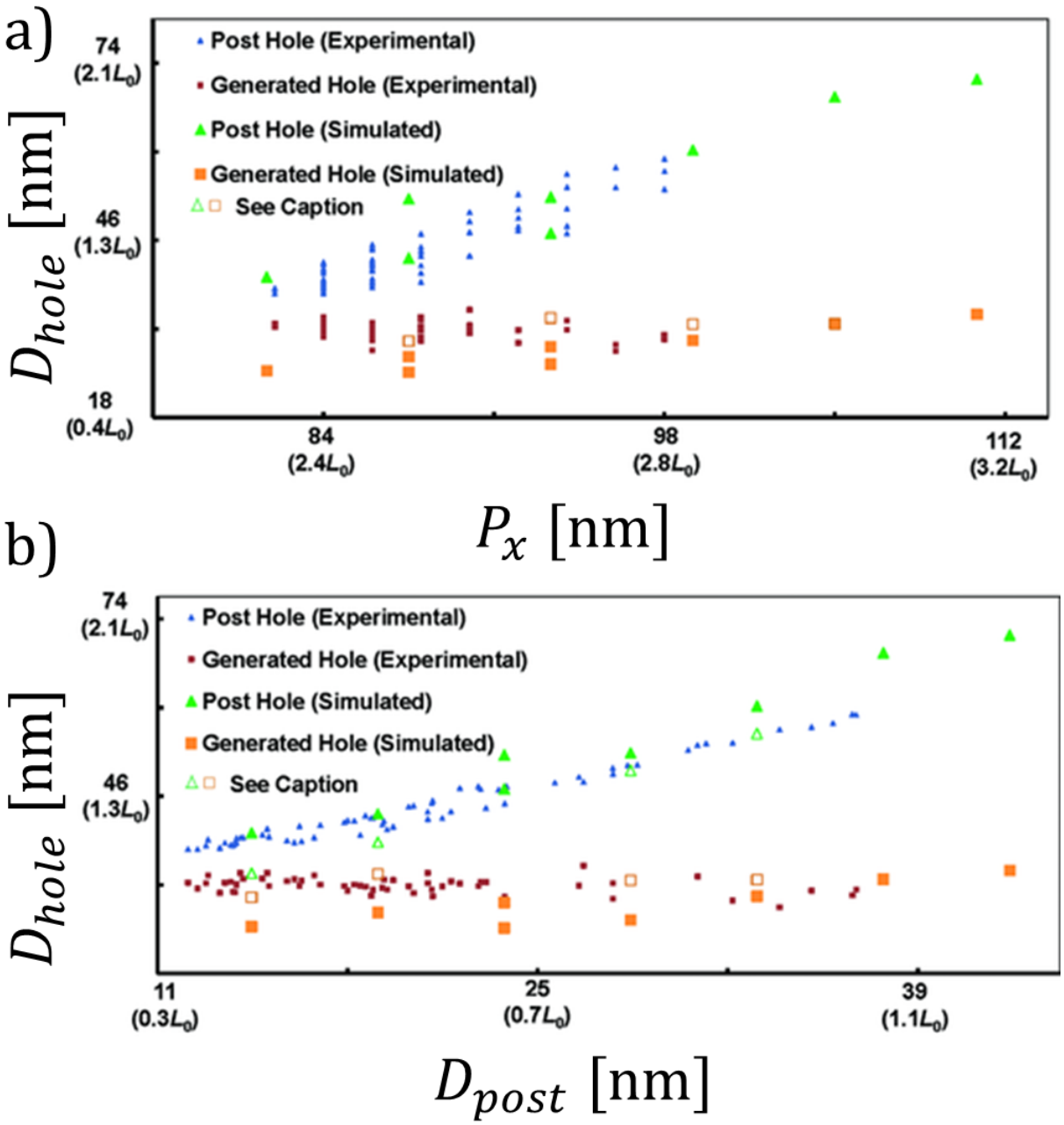

Figure 5-18: Plots of the measured hole diameters D_{hole} for both generated (blue and green triangles) and post (red and orange squares) holes as a function of post pitch P_x in a) and post diameter D_{post} in b). Open points are where defect structures were observed in the simulations. Multiple points at the same post pitch in a) had different post diameters and multiple points at the same post diameter in b) had different post pitches. The generated holes had a fairly constant size while the post holes increased linearly with both variables. This linear relationship is most likely strongly dependent on D_{post} more so than P_x as there is evidence the P_x values where the perforated lamellae structure is stabilized itself is a linear function of D_{post}[60].

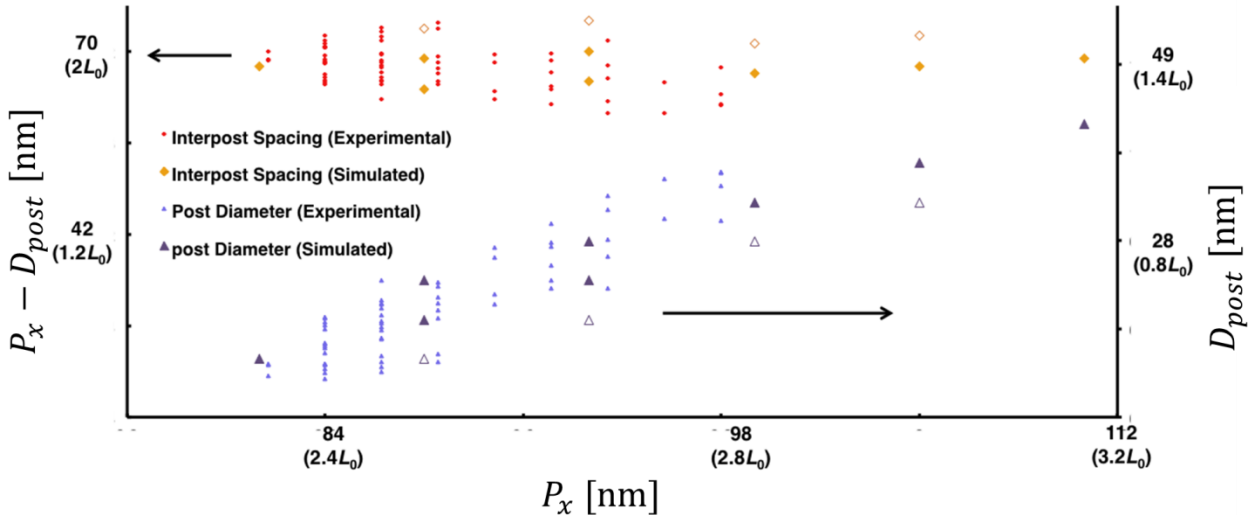

Figure 5-19: Plots of the post diameter (blue and purple triangles) and P_x - D_{post} interpost spacing (red and orange diamonds) as a function of post pitch P_x. Open points are where defect structures were observed in the simulations. Multiple points at the same post pitch had different post diameters. The linear relationship between post diameter and post pitch and the approximately constant value of interpost spacing suggests that the perforated lamellae structure is stabilized around this commensuration of the interpost spacing and thus post diameter and pitch should be linear since they need to increase proportionately together in order to keep a constant interpost spacing[60].

5.4 Rectangular Post Array Studies

In the previous section, post arrays with hexagonal symmetry were examined since diBCPs naturally form hexagonally close-packed features and thus using DSA templates with that same inherent symmetry allows for great control over the close-packed structures that can be formed as evidenced by the arrays of dots and hole made depending on the brush conditions used. However, many applications require square and rectangular symmetry features rather than hexagonal symmetry[194]. In order to obtain such structures that do not naturally form in diBCPs, the templates used in the BCP DSA must be conditioned in a way that can overcome the natural tendency of the BCPs to form hexagonal symmetry structures. Methods such as blending[174] and confining[21,57] can do this, and alternatively the use of ABC triblocks[195,196] can be used to create square symmetry patterns.

In this section, several studies using a rectangular symmetry lattice with high confinement of the BCPs will be examined to gain insight in what is required to produce

BCP structures with rectangular symmetry structures. First both 2D and 3D studies of monolayer features with high confinement by PS functionalized square and rectangular post lattices are examined and the morphologies possible as a function of lattice spacing mapped out using SCFT and compared with experimental results. Next, the effects of post height and diameter with both PS and PDMS functionalized posts are examined in 3D SCFT simulations to gauge how these parameters affect the commensuration of the cylinders or eventually to create confined structures. Finally, double layer feature formation under rectangular symmetry structures will be examined and the interplay between the confining effect on the bottom layer of features versus nonconfinement of the top layer of features will be examined.

5.4.1 Simulation Results in 2D – Majority Block Preferential Posts

2D simulations were performed where the main variable of interest was the post pitches or spacing distances in the x and $y-$directions, P_x and P_y respectively. Since there is an expected symmetry of morphologies formed about the $P_x = P_y$ axis, the choice is made that $P_y < P_x$ for simplicity. Unlike the previously discussed hexagonal array simulations were there was a single independent post spacing variable L_{post}, here the rectangular symmetry of the post lattice results in two independent parameters P_x and P_y. The periodically bound 2D unit cell used is schematically shown in Figure 5.20. In these topographical post simulations and all those that follow, the field constraints are just like those presented previously for the hexagonal array simulations with $\mu_A = \mu_B = P$ with $|P| = 20$ to ensure the total density inside the posts is close to 0 and the brush layer is modeled with conditions $\mu_A = -\mu_B = W_{BL} = 10$ to model PS or majority attractive brush layers and the opposite sign for PDMS brush.

The corresponding experimental systems used solvent annealing to reach equilibrium structures, thus effective parameters $(\chi N)_{eff} = 30.0$ was chosen based on appearing to give the best corresponding results with the experimental system of 45.5 kg/mol PS-PDMS solvent annealed in a 5 to 1 toluene to heptane atmosphere[57]. The effective $N \cong 250$. For simplicity, the volume fraction was assumed to be approximately that of the BCP volume fraction $f_{PDMS} = 0.32$ for both 2D and 3D simulations. This assumption likely resulted in

discrepancies observed in the 2D simulations since a better approach in 2D simulations would be to use an effective area fraction parameter corresponding to the area fraction observed experimentally such as was done in the hexagonal array templated spheres[49]. Still, several 2D simulations corresponded well with experimental results and thus there appears to be a range where the effective volume fraction is robust in making such comparisons.

All these simulations were performed starting from random initial field conditions and evolved to a saddle point equilibrium solution using steepest descent complex Langevin dynamics. Several simulations were performed to ensure the lowest energy structure was observed and not a metastable structure. The main variable of interest, the post spacing distances P_x and P_y each varied from values of $0.7L_0$ to $1.3L_0$ corresponding to a variance of grid points from 22 to 42. Additionally, several simulations were done with $P_x = P_y$ or square symmetry all the way up to values of $2.0L_0$. Post diameter D_{post} was fixed at a constant value of $0.4L_0$ corresponding roughly to $\approx$ 14 nm diameter as the experimentally observed L_0 in the corresponding experiments was $L_0 \cong$ 35 nm.

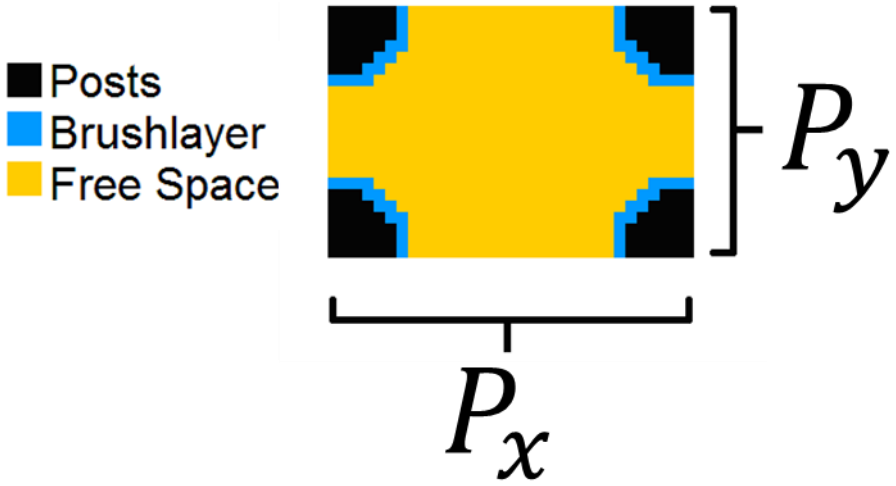

Figure 5-20: Schematic of unit cells used in SCFT simulations. Black area is where the fields are constrained to prohibit the polymers from evolving in the simulation to model the posts. Blue area is where the fields are constrained to be attractive to the majority block (PS) and repulsive to the minority block (PDMS) to model the PS brush layers used in experiment. Orange area is the free space where the polymer chemical potential fields evolve during the simulation and thus where the polymer density develops and phase separates into distinct ordered structure morphologies.

Four different key morphologies were observed in the simulations and are shown in Figure 5.21. When $P_x = L_0$ and $P_y < L_0$, confined cylindrical morphologies were observed as shown in Figure 5.21.a. When $P_y = L_0$ and $P_x > L_0$, cylinders with an undulation of bulge in the center were observed as shown in Figure 5.21.b. When $P_x = P_y$ and the post spacing values were near or less than L_0, confined spherical morphologies were observed as shown in Figure 5.21.c. When $P_x = P_y$ and the post spacing values were close to $\sqrt{2}L_0$ meaning the diagonal distance was $\sqrt{P_x^2 + P_y^2} \cong 2L_0$, elliptical structures were observed with degenerate alignment along one of the two axes with angle 45° relative to the P_x or P_y axis as shown in Figure 5.21.d. All four of these morphologies were observed experimentally for the modeled PS-PDMS system at similar ranges of post spacing commensurations.

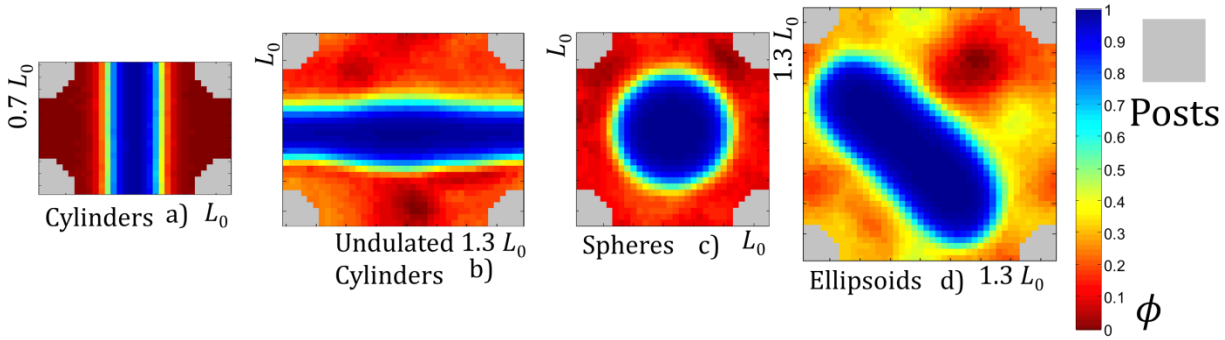

Figure 5-21: 2D SCFT simulation results of morphologies observed as a function of post spacing distances P_x and P_y. Since the posts here are modeled with a PS preferential brush, the PDMS density was colored blue as opposed to the traditional red for PDMS rich regions so the posts were distinguishable from the PS matrix. The posts were further colored a separate grey color for further distinction. a) Cylinders that are constrained by P_x and are not commensurate with P_y. b) Cylinders that are commensurate with P_y globally in the middle regions and bulge or undulate while constrained between the posts in the other region and are not commensurate with P_x. c) Spheres that are constrained by the posts when $P_x = P_y$. d) Ellipsoids that are commensurate with a 45° rotation of the post lattice for $P_x = P_y \cong \sqrt{2}L_0$.

In addition to the $f = 0.32$ simulations, simulations of a spherically confined BCP with a square post array were performed as similar experiments were performed with a lower molecular weight 16 kg/mol $f_{PDMS} = 0.165$ sphere forming PS-PDMS BCP. A comparison of a bulk 2D simulation with periodic boundary conditions with a simulation containing square post symmetry boundary conditions is shown in Figure 5.22. The main effect of the square post array is to constrain the normal hexagonal close-packed lattice

into forming a square lattice at the commensuration chosen due to the PS functionalized posts disallowing the normal hexagonal close-packing of the spheres. This effect is analogous to what happens in the cylinder case where at the small confinement lengths of $P_x = P_y \cong L_0$ or smaller, the cylinders cannot form together and spheres are instead observed between the posts.

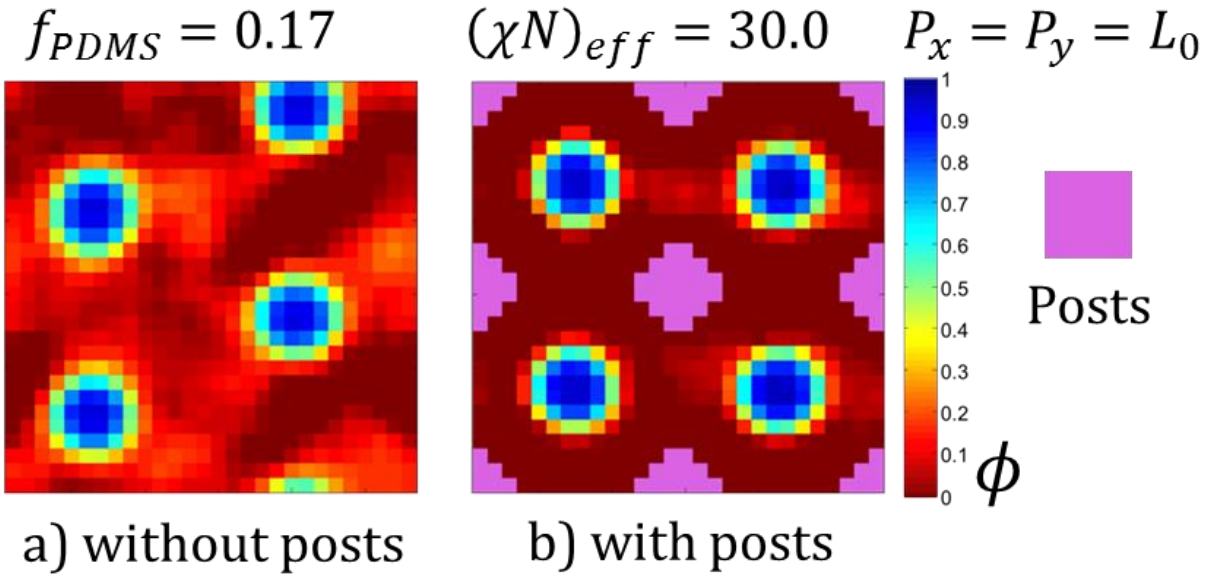

Figure 5-22: 2D SCFT simulations of PDMS spheres (blue) in PS matrix (red) for f_{PDMS} = 0.17 and $(\chi N)_{eff}$ = 30.0 in a unit cell of dimensions $2.0L_0$ by $2.0L_0$. a) Bulk simulation of PDMS spheres with periodic boundary conditions. The spheres formed a strained hexagonally close-packed array due to the unit cell constraint not being commensurate with the equilibrium structure. The expected equilibrium morphology for these conditions is thus a hexagonally close-packed array of spheres. b) Simulation of PDMS spheres in a square post template lattice (purple). Spheres are constrained to form a square lattice with the same period as the post period $P_x = P_y = L_0$.

For simulations with $P_x = P_y \geq \sqrt{2}L_0$ for the $f = 0.32$ case, the 2D simulations performed showed little correlation with the structures observed experimentally. Rather than forming confined bicontinuous cylindrical structures, confined structures with multiple spheres for a given unit cell were observed. The likely reason for this discrepancy was the volume fraction chosen being too small compared to the effective area fraction for proper comparison of 2D simulations with the top-down cross sections of the 3D morphologies in the experiments. Rather than trying to scan 2D simulations of various

higher volume fractions to find the best effective area fraction that corresponded best with experimental results, 3D simulations were performed with monolayer thicknesses at the corresponding real volume fraction of $f = 0.32$. These results will be discussed in the next section.

5.4.2 Simulation Results in 3D – Majority Block Preferential Posts

For all 3D simulations in this section, unit cells as schematically depicted in Figure 5.23 were used. The values of P_x and P_y were varied from $0.71L_0$ to $2.00L_0$ which corresponds to a change in number of grid points of 10 to 28 in each direction. The thickness $t = 1.5L_0$ corresponding to 22 grid points was chosen to account for the formation of a PDMS surface layer in addition to the monolayer of features and corresponds to the swollen film thickness observed in experiments. The height of the posts was set to $\approx L_0$ corresponding to 14 grid points which is slightly taller than the observed 30 nm HSQ film thickness in experiments but roughly close in value. The post diameter was set to match the maximum experimental value with $D_{post} = 0.7L_0$ corresponding to ≈ 25 nm. $(\chi N)_{eff} = 30.0$ and $f = 0.32$ to try to best model the solvent annealing conditions.

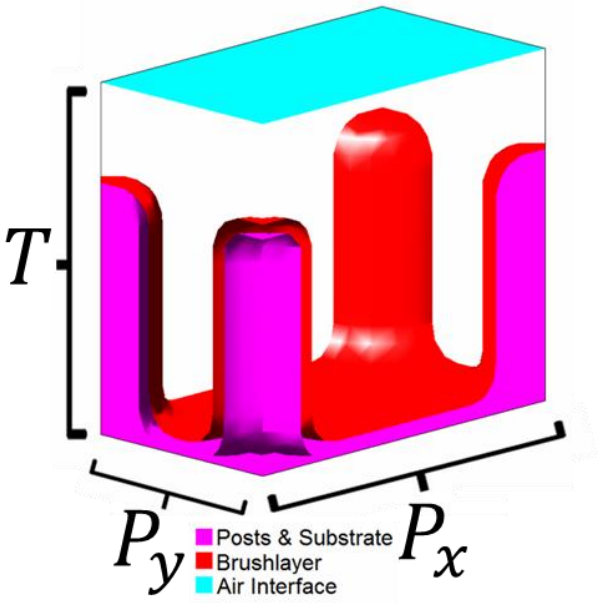

Figure 5-23: Schematic of the in-plane periodically bound unit cell used in simulations for rectangular symmetry post array constraints. Posts and substrate are colored purple, brush layer area is colored red, and air interface is colored teal. Key dimensions are labeled[56,57].

Over the range of post spacing distances tested, seven distinct morphologies were observed as shown in Figure 5.24. In general the phase diagram of these morphologies shown in Figure 5.24.a showed the same trends and transitions as the experimental results that will be discussed in the next section. The morphologies observed included cylinders, spheres, ellipsoids, square symmetry perforated lamellae with no generated hole (PL1), square symmetry perforated lamellae with a generate hole (PL2), double cylinders per post unit cell, and for the smallest confinements only a surface wetting layer with no internal morphology all shown in Figure 5.24.b. An additional simulation at a post spacing distance of $P_x = P_y = 2.29$ was performed to examine the effects of larger pitches. In this case a degenerate state between double cylinders and PL2 was observed.

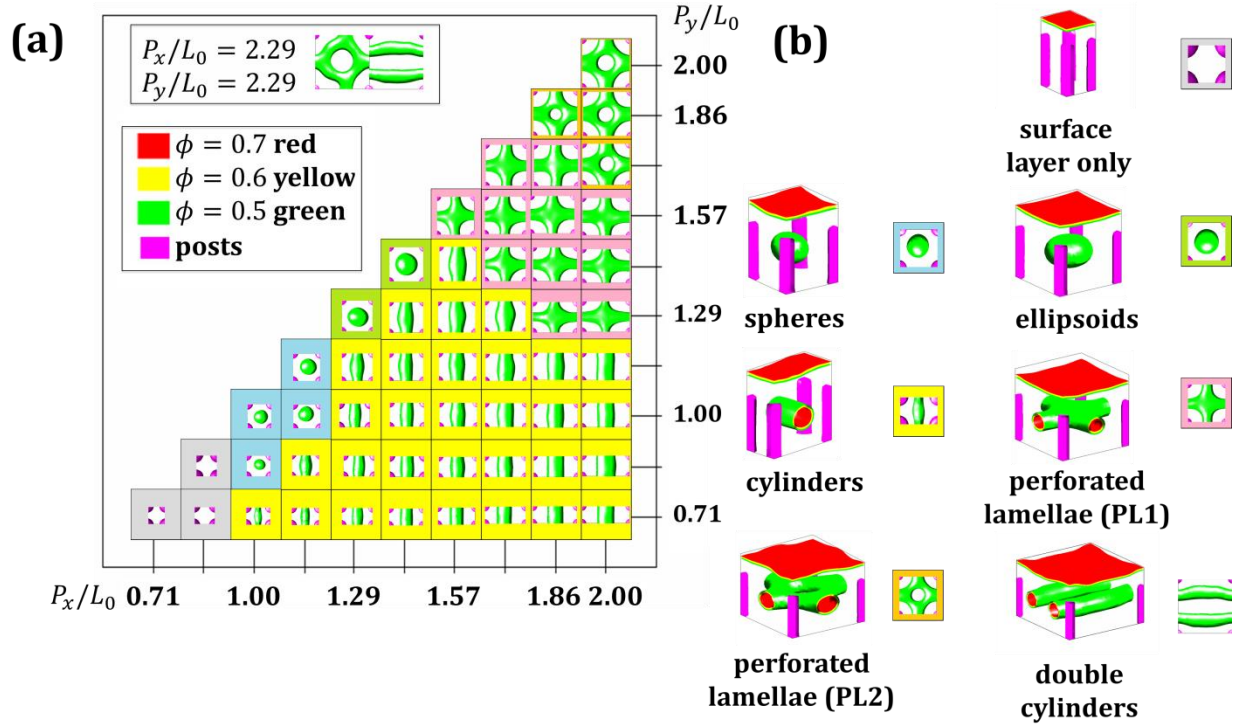

Figure 5-24: (a) Phase diagram of the 3D SCFT simulation results for PS-PDMS cylinders confined by a rectangular array of posts as a function of P_x and P_y. Additional simulation results with two metastable solutions for P_x = P_y = $2.29L_0$ are shown in the inset of the phase diagram. (b) 3D side angle views and top-down views with color coding corresponding to the phase diagram in (a) of the different constrained morphologies observed as a function of P_x and P_y for the rectangular post array boundary conditions. Morphologies types observed are labeled in the figure[57].

Before comparing these simulation results with experimental results, the following issues should be addressed. The experimental system only has a finite region where posts are on the sample surrounded by untemplated cylinders meaning edge effects may play a role in the observed experimental morphology and such effects are not considered in the periodically bound simulations. In the experiment, the film thickness is not constrained as in the simulation so local film thickness fluctuations in the experiment can affect the local morphology. The solvent annealing may also not reach a true equilibrium structure but may reach a kinetically trapped structure which the simulation may not find since a steepest descent method is used to reach saddle point equilibrium structures that may not be the kinetically trapped structures in the experiment. The next section will look at how experimental studies compare with these simulation results.

5.4.3 Experimental Results and Comparison – Majority Block Preferential Posts

Experiments were performed by Amir Tavakkoli K.G. with the help of Kevin Gotrik[57]. Rectangular arrays of HSQ posts were fabricated using EBL and the samples functionalized with a low molecular weight PS brush. PS-PDMS thin films were spun cast to appropriate thicknesses to reach a swollen commensurate thickness $t \cong 1.5L_0$ during solvent annealing in a solvent environment with selective solvent toluene and heptane with ratios of 5 to 1 toluene to heptane. The arrays of PS functionalized brush allowed for the local control of the BCP morphology that formed during the annealing with the potential for multiple morphologies on the same substrate and for the case of square symmetry arrays of commensurate spacing led to a doubling of the areal density of surface features in the square array.

The range of morphologies observed experimentally as a function of post spacing distances P_x and P_y are shown in Figure 5.25. All of these morphologies match those observed in the simulations in the appropriate P_x and P_y range except for a couple of cases. Experimentally P_x and P_y were varied from $0.5L_0$ to $2.5L_0$, a slightly larger range than tested in the simulations. In the case of cylinders oriented parallel to the larger period axis when $P_y < L_0$ and $P_x > L_0$, the 3D model showed that state to be higher energy than

aligning with the smaller period axis. As will be seen the next section, this discrepancy is likely due to the simulation post diameter being slightly larger than the experimental post diameter for these cases as reducing the diameter results in the undulated cylinder morphology. Whereas the simulation fixed the post diameter to a value $D_{post} = 0.7L_0$, experimental post diameters varied from $0.28L_0$ to $0.7L_0$ due to variance in EBL writing conditions and thus the interplay between post diameter and post pitch should be taken into account to fully understand what morphologies form at different conditions as was previously shown with the interpost spacing distance being a key variable in getting the hexagonal perforated lamellae morphology for a hexagonal array of posts[60]. The 2D simulations in this region did show undulated cylinders as in experiment, but as discussed before the effective volume fraction was smaller than the expected area fraction from experiment; thus the results having smaller line patterns from the lower effective area fraction was the most likely reason the undulated cylinders were the lower energy state in the model at those conditions and thus the post diameter might play an effect as that effective fraction increases.

The other discrepancy occurred where mixed superstructure morphologies were observed experimentally as shown in Figure 5.25.e. Two reasons for not observing such states in the simulation are possible. Firstly only a single unit cell was modeled meaning for a given simulation only one confined morphological feature would be observed. The possibility exists that these mixed states are due to the energy between the two morphologies being approximately degenerate; such testing was performed in simulations using a double unit cell seeding one half with an ellipsoid and the other half a cylinder and observing the state was metastable at best corroborating such a possibility. For $P_x = L_0$ and $P_y \cong 1.5L_0$, the superstructure simulation energy was only 0.034% higher than a pure cylinder state implying the energy difference between the states may be low enough for the states to coexist. The other possibility is that since the post lattice in experiment is finite, kinetic effects of how the features form may bias the formation of such superstructures. Thus these structures are not a true equilibrium morphology and thus not comparable with the model. The existence of such mixed state morphologies is of future work interest as

previous studies have required multiple steps to obtain such mixed morphologies[197,198] as opposed to the single annealing step used in these experiments.

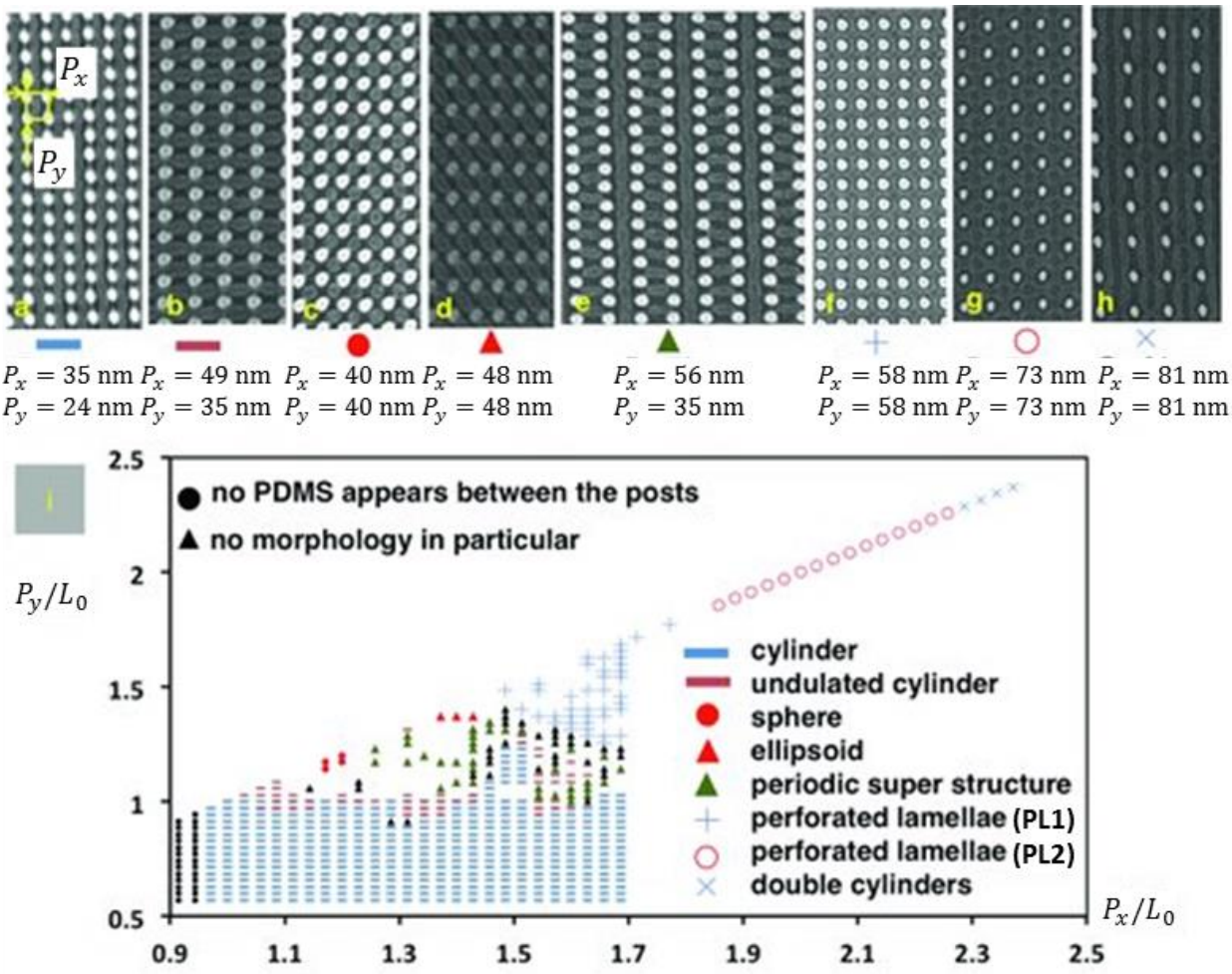

Figure 5-25: SEM images of the different morphologies observed in the experiments as a function of P_x and P_y. a) Constrained cylinders. b) Commensurate undulated cylinders. c) Confined spheres. d) Confined ellipsoids. e) Mixed superstructures of ellipsoids and cylinders. f) PL1. g) PL2. h) Double cylinders mixed with PL2 (corresponds to simulation result at $P_x = P_y = 2.29L_0$) i) Phase diagram with each data point corresponding to a sample where more than 70% of the observed templated region exhibited the corresponding morphology with the symbols in the inset legend[57].

Overall the general trends of where morphologies occurred as a function of post pitch agreed between experiments and SCFT simulations. The few discrepancies appear to mainly be due to post size effects interplaying with post period and optimization of effective χN and f used for the appropriate solvent annealing conditions. The other possible sources of discrepancy come from metastable phases competing or kinetic effects

not captured in the model. In the next section, the effect of post height and diameter will be examined for three post spacing distance cases in the simulations.

5.4.4 Simulation Results in 3D – Majority Block Preferential Posts – Post Height and Diameter Effects

To explore the effects of post height and diameter on the microdomain morphology of rectangular post array templated BCPs, the same boundary conditions shown in Figure 5.23 were used with two modifications. These modifications were allowing the post height h_{post} and post diameter D_{post} to vary. In the simulations that follow, the reduced post diameter D_{post}/L_0 was varied from 0.125 to 0.875 and the reduced post height h_{post}/L_0 from 0.125 to 1.250. Two effective values of χN were examined, $\chi N = 28.0$ ($\chi_{eff} = 0.224$ and effective N = 125 corresponding to an 11.7 kg/mol molecular weight for PS-PDMS based on known measurements of $\chi_{PS-PDMS}$ at the time the simulations were performed[118]) and χN = 14.0 ($\chi_{eff} = 0.112$ and N = 125). Without posts these conditions yielded a monolayer of cylinders. The volume fraction $f = 0.36$ was higher than the thin film cylinder study to ensure cylinder formation at $\chi N = 14.0$. The theoretical equilibrium periods in real units are $l_0 \cong 11.7$ nm for $\chi N = 28.0$ and $l_0 \cong 10.4$ nm for $\chi N = 14.0$. The normalized post dimensions and cell size were based on $L_0 \cong 9.9$ nm, the equilibrium period calculated at the ODT for $f = 0.5$, and were the same for each simulation. Although having a fixed cell size simplifies comparison between the results, it does lead to a different effective strain as χN varies which will change the commensurability conditions. The effective strain $\varepsilon = \frac{L_0 - l_0}{l_0}$ is $\varepsilon \cong -0.048$ for χN = 14.0 (the negative sign indicating compression) which is modest, but for $\chi N = 28.0$ $\varepsilon \cong -0.154$. Experimentally, microdomain thin film arrays accommodate from 10-45% strain depending on the number of layers before commensurability is lost and changes in the number of layers occurs[149,191]. The posts themselves have a finite diameter which further reduces the interpost volume.

Three fixed post spacing periods were used for these simulations with $P_x = P_y = L_0$, $P_x = 1.5L_0$ and $P_y = L_0$, and $P_x = P_y = 1.5L_0$ which in the previous sections with fixed post dimensions corresponded to spheres, cylinders, and the boundary between elllipsoids and

perforated lamellae PL1, respectively. The simulations varying the post dimensions generated a rich array of morphologies shown in Figure 5.26 including cylinders oriented along the nominally unstrained direction (CC), or the strained direction (EC), undulating (UC) cylinders, diagonally oriented cylinders (GC), perforated lamellae (PL), and spheres (S), which could be connected to a surface layer (SS). CC describes cylinders oriented perpendicular to the L_0 dimension of the unit cell, with period L_0. EC describes cylinders oriented perpendicular to the $1.5L_0$ dimension of the unit cell, with period $1.5L_0$. Both CC and EC could exist in the L_0 by $1.5L_0$ cell, but EC was not an option in the L_0 by L_0 cell. For GC, which only formed in the $1.5L_0$ by $1.5L_0$ cell, the period was $1.5L_0/\sqrt{2} = 1.06L_0 \cong L_0$.

The morphological phase diagrams as a function of h_{post}/L_0 and D_{post}/L_0 for $\chi N = 14.0$ are shown in Figure 5.27 and for $\chi N = 28.0$ are shown in Figure 5.28 each using the color coding from Figure 5.26.

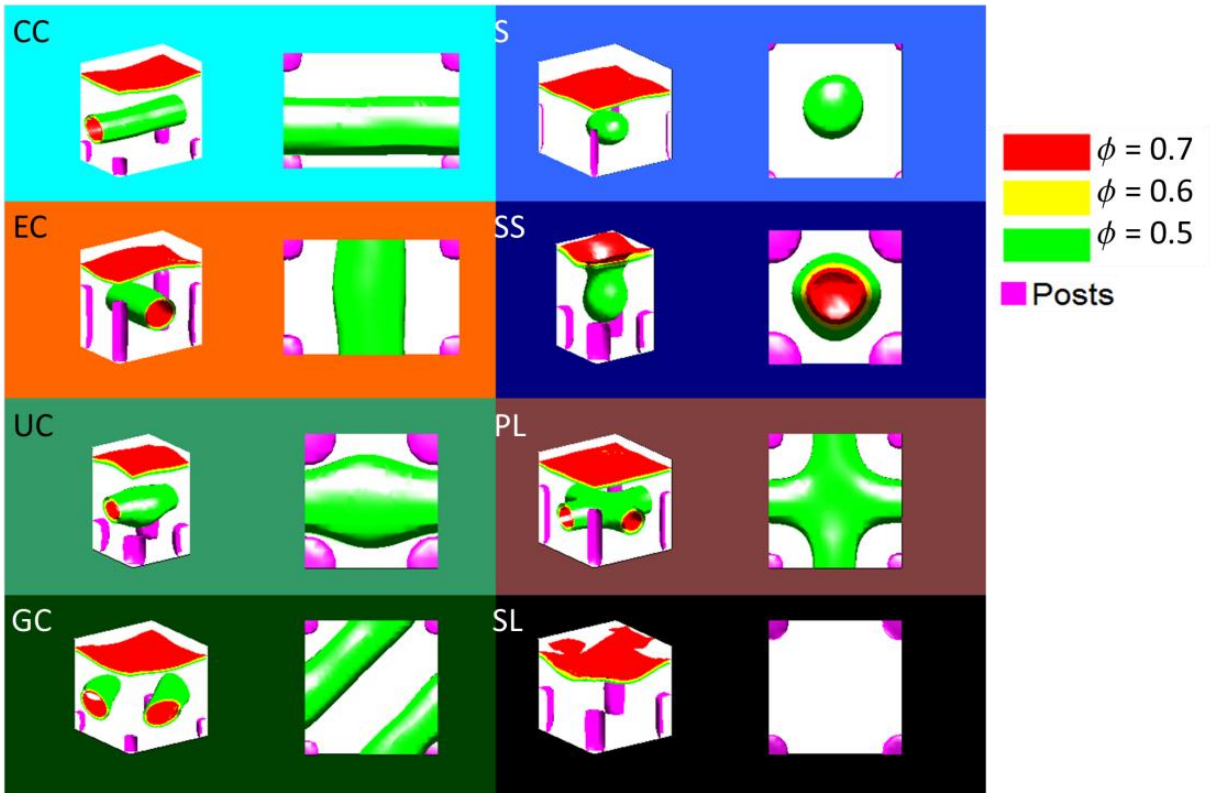

Figure 5-26: Representative morphologies observed in 3D SCFT simulations of cylindrical BCP thin films with confinement in a periodic rectangular array of posts with varying diameters and heights. CC) Cylinders with period L_0. EC) Cylinders with period $1.5L_0$. UC) Undulated cylinders. GC) Diagonally oriented cylinders. S) Spheres. SS) Spheres connected to surface layer. PL) Perforated lamellae. SL) Surface layer only with no internal structure.

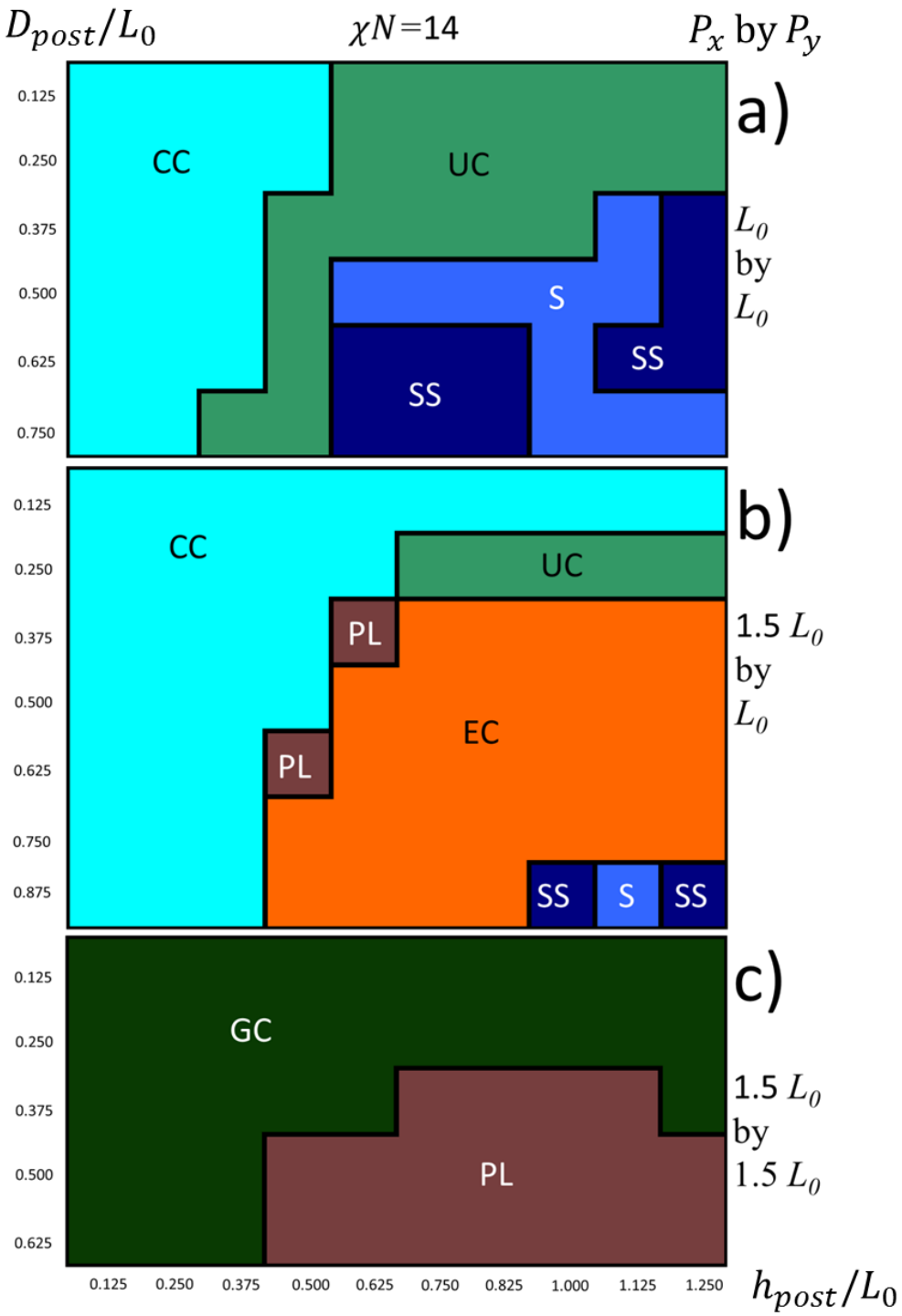

Figure 5-27: 3D SCFT simulation phase diagrams of morphologies observed vs. reduced post diameter D_{post}/L_0 and reduced post height h_{post}/L_0 for a cylindrical BCP in a rectangular periodic post array with χN = 14.0. a) Post periods P_x by P_y = L_0 by L_0. b) Post periods P_x by P_y =1.5L_0 by L_0. c) Post periods P_x by P_y =1.5L_0 by 1.5L_0.

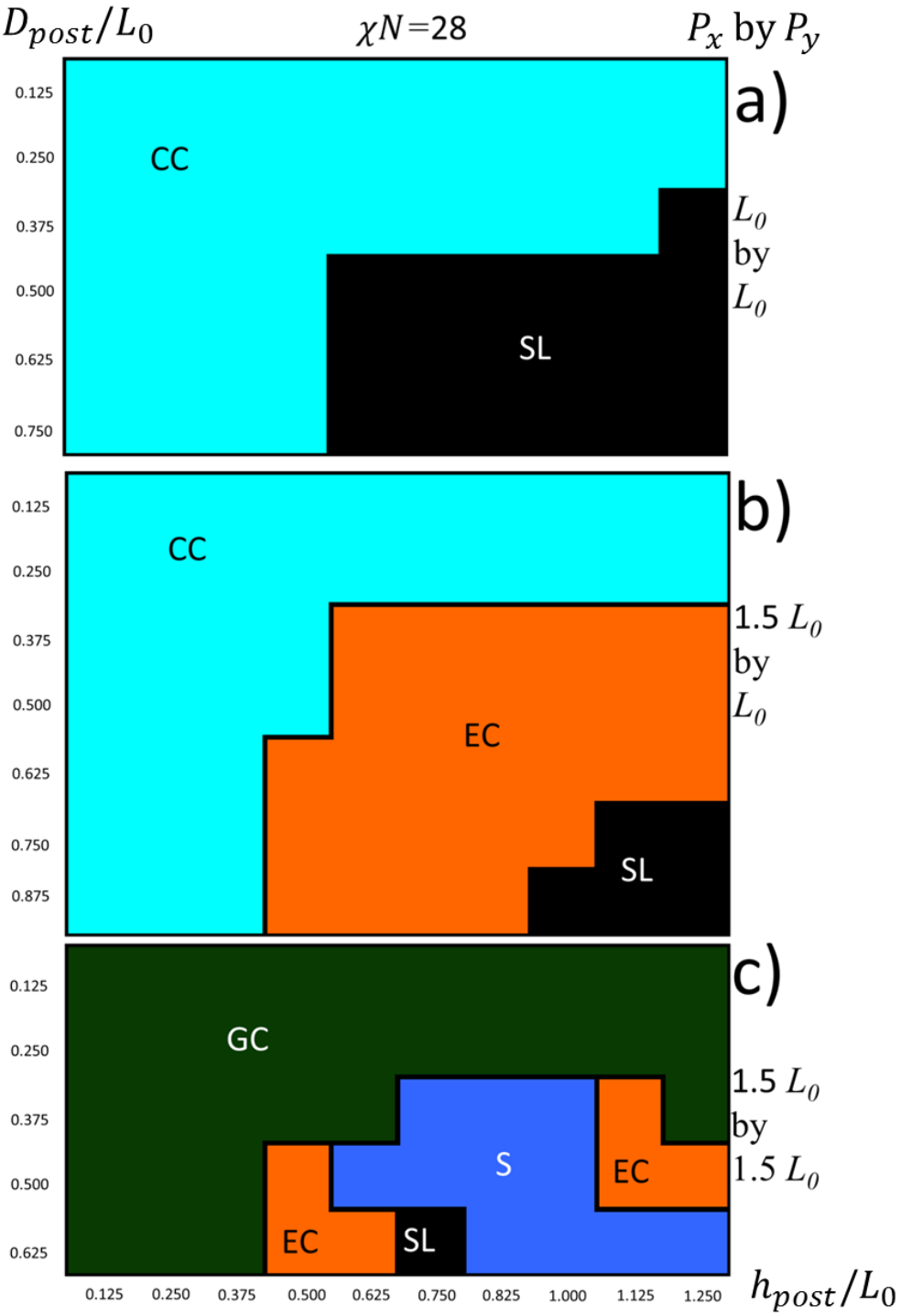

Figure 5-28: 3D SCFT simulation phase diagrams of morphologies observed vs. reduced post diameter D_{post}/L_0 and reduced post height h_{post}/L_0 for a cylindrical BCP in a rectangular periodic post array with χN = 28.0. a) Post periods P_x by P_y = L_0 by L_0. b) Post periods P_x by P_y =1.5L_0 by L_0. c) Post periods P_x by P_y =1.5L_0 by 1.5L_0.

As can be seen in the phase diagrams, for $P_x = L_0$, $P_y = L_0$ and $\chi N = 28.0$, CC was observed for posts with $D_{post}/L_0 \leq 0.375$ and $h_{post}/L_0 \leq 0.5$ and SL for larger posts. For the same unit cell with $\chi N = 14.0$, for $h_{posts}/L_0 \leq 0.375$ CC was observed while for taller posts with $D_{post}/L_0 \leq 0.375$ UC was observed. For larger posts for $\chi N = 14.0$, either S or SS was observed.

For $P_x = 1.5L_0$, $P_y = L_0$ and $\chi N = 28.0$, CC was observed for posts with $D_{posts}/L_0 \leq 0.25$ and $h_{posts}/L_0 \leq 0.375$, EC for posts with $0.375 \leq D_{posts}/L_0 \leq 0.625$ and $0.5 \leq h_{posts}/L_0 \leq 1.00$, and SL for larger posts. For the same unit cell with $\chi N = 14.0$, for $h_{posts}/L_0 \leq 0.375$ and $D_{posts}/L_0 = 0.125$, CC was observed. For $D_{posts}/L_0 = 0.25$ and $h_{posts}/L_0 \geq 0.75$, UC was observed. For larger posts for this χN, EC was mostly observed with a few transition regions with PL and S for the tallest and widest posts.

For the $P_x = 1.5L_0$ by $P_y = 1.5L_0$ case and $\chi N = 28.0$, GC were observed for posts with $D_{posts}/L_0 \leq 0.25$ and $h_{posts}/L_0 \leq 0.375$ and EC for $h_{posts}/L_0 = 0.5$ and $D_{posts}/L_0 \geq 0.5$ and $h_{posts}/L_0 \geq 1.125$ and $D_{posts}/L_0 = 0.5$. S was generally observed for the other larger posts. For the same unit cell with $\chi N = 14.0$, for $h_{posts}/L_0 \leq 0.375$ and $D_{posts}/L_0 \leq 0.25$ GC was observed and for larger posts PL were observed.

As a general observation, when the posts were short they had little perturbing effect on the morphology and commensurate in plane cylinders were observed, CC or GC, having period L_0 or $1.06L_0$, respectively. As the post height and diameter increased the polymer was confined within the spaces between and above the posts. In the higher $\chi N = 28.0$ simulations, this reoriented the cylinders into the EC configuration, and eventually produced SL, surface layers with no internal structure, or spheres S for the largest cell. The lower $\chi N = 14.0$ simulations more commonly yielded non-bulk structures (PL, UC and S) and did not show SL morphologies. This is partly due to the lower interface energy which meant that additional interface area incurred a lower energy penalty.

The results in the previous section had a fixed post diameter of $0.7L_0$ and fixed post height of $1.0L_0$ and showed spheres for the L_0 by L_0 case, constrained cylinders for the $1.5L_0$ by L_0 case, and perforated lamellae for the $1.5L_0$ by $1.5L_0$ case[57]. These same results were observed for the $\chi N = 14.0$ case in these simulations at these post dimensions. In the

previous study, the polymer modeled was effective χN = 30.0 with the larger effective molecular weight of $N \cong 250$ and had a slightly lower volume fraction f = 0.32, so a direct comparison cannot be made with these results alone, but the fact that the same results were observed here in the predicted regions for approximately half the effective χN demonstrates the results obey the same trends in the polymer phase space. These results demonstrate that by starting from these points on the phase diagram, other morphologies can be reached by simply changing the post dimensions based on the trends of the confinement effects similar to how changing the post spacing itself allowed other morphologies to form. Thus the entire morphological parameter space is governed by a combination of these parameters and coupled together by interpost spacing distances.

5.4.5 Simulation Results in 3D and Experimental Comparison – Minority Block Preferential Posts – Post Height Effects

As the previous section showed, the height of the post is a key parameter in determining the morphology formed in a DSA BCP by arrays of posts. In the following simulation study, only the height of the post was changed to show that for a given desired commensurate morphology the range of post heights where that morphology forms needs to be determined for optimal production of that morphology. In the system studied here, the posts were made preferential to PDMS rather than PS to examine commensuration of cylinders going around the post template features[56]. The unit cells modeled are the same as shown in Figure 5.23 but with the brush layer constraint being that for PDMS attraction. The grid size was fixed as N_x by N_y by $N_z = 24$ by 16 by 20 corresponding to 48 nm by 32 nm by 40 nm thin film unit cell with a rectangular array of posts. $(\chi N)_{eff} = 14.0$, $N_S = 69$ statistical monomers, and $f = 0.33$ were chosen to model a 16 kg/mol cylinder forming PS-PDMS under implicit solvent annealing conditions. The natural period of the polymer was $L_0 \cong 18$ nm corresponding to 9 grid points in the simulation. Thus the film thickness is a little above $2L_0$ close to that required for a monolayer of features with PDMS wetting conditions on the top and bottom surface and corresponds to the swollen film thickness encountered during solvent annealing. Simulations were run from initial conditions until an equilibrium saddle point solution was obtained.

As shown in Figure 5.29, three different post heights corresponding to $h_{post} = 12, 19, \text{and } 27$ nm were examined in the SCFT simulations. These correspond to experimental results performed by Jae-Byum Chang and Jeong Gon Son for the modeled BCP system shown in Figure 5.30[56]. For the $h_{post} = 12 \text{ nm} = 0.67L_0$ case, a perforated lamellae like structure formed because of the periodic boundary conditions and the competition of orientation of the cylinders in either direction with such short posts. When compared with the experimental results, no long range ordered structure was observed experimentally since the short posts were unable to template cylinders into a preferentially commensurate direction and rather unoriented cylinders formed. This observation is analogous to the case of the honey comb structure observed in the 2D hexagonal array simulations were multiple commensurate directions resulted in a metastable composite structure[49].

For the $h_{post} = 19 \text{ nm} = 1.06L_0$ case, cylinders that were commensurate with underlying lattice formed with bulges around the posts. This corresponded very well with the experimental observations where the same commensurate cylinders were observed experimentally. For the $h_{post} = 27 \text{ nm} = 1.5L_0$ case, the posts were so tall that they simply had a layer of PDMS form around them and the cylinders between the posts formed confined undulating cylindrical structures analogous to those observed in the PS functionalized post case when the cylinders were confined between a commensurate and noncommensurate set of post periods. Similar observations were made experimentally. One other interesting feature the PDMS functionalized posts had over the PS functionalized posts was the effective diameter of the posts after etching increased in the PDMS case. For the taller posts, the layer of PDMS that surrounded the posts was not etched away as the PS that forms around the posts in the PS preferential case, thus the taller posts appear larger in the experimental SEMs than the shorter posts where the PDMS goes through the posts in-plane rather than over and around them out-of-plane as observed in the SCFT simulations.

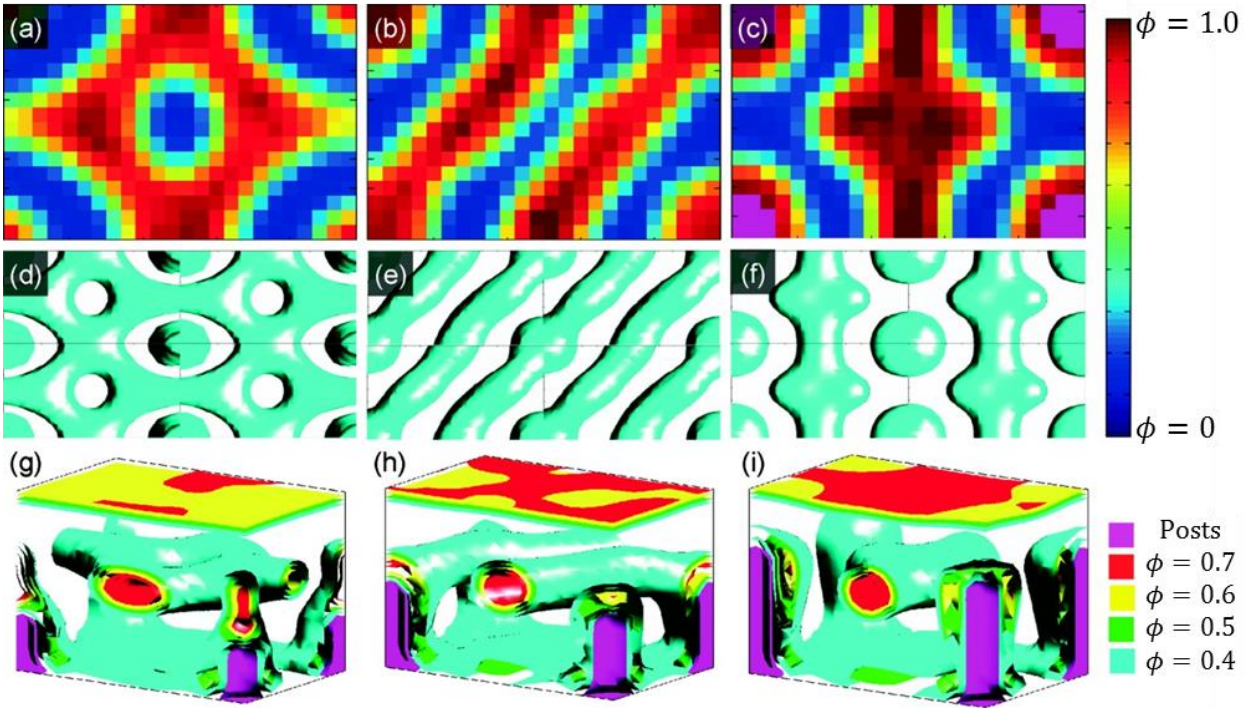

Figure 5-29: SCFT simulation results from changing the height of the posts in a unit cell with PDMS preferential rectangular post array boundary conditions. Simulation parameters are $(\chi N)_{eff}$ = 14.0 and f = 0.33 for the 16 kg/mol PS-PDMS. (a-c) 2D cut-through view halfway up unit cell for (a) h_{post} = 12 nm. (b) h_{post} = 19 nm. (c) h_{post} = 27 nm. (d-f) View looking top-down without wetting surfaces of four unit cells (two by two) concatenated together for (d) h_{post} = 12 nm. (e) h_{post} = 19 nm. (f) h_{post} = 27 nm. (g-i) View looking from a side angle at a single unit cell for (g) h_{post} = 12 nm. (h) h_{post} = 19 nm. (i) h_{post} = 27 nm[56].

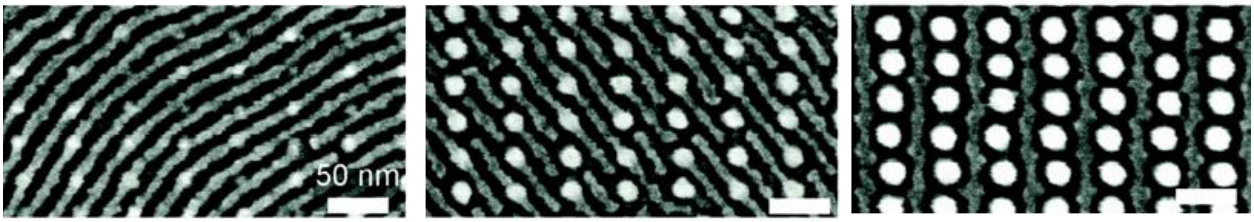

Figure 5-30: SEM images showing the oxidized PDMS microdomains that remained after reactive ion etching away any PDMS surface layer and all PS matrix after solvent annealing the samples templated with HSQ posts of various heights. P_x = 48 nm and P_y = 32 nm. Disconnections in the cylinders were due to the samples being over etched. From left to right: h_{post} = 12 nm, h_{post} = 19 nm, and h_{post} = 27 nm[56].

5.4.6 Simulation Results in 3D – Majority Block Preferential Posts – Double Layers of Minority Features

The effects of post height, diameter, and pitch on the morphology of DSA templated BCP thin films with monolayers of features were all examined in the previous sections. In this section, the principles learned in the previous studies are applied to thin films with double layers of features. In these systems, the post DSA effects are decoupled between the two layers such that the bottom layer of features is generally under confinement from the posts and the top layer is simply influenced by the very top features of the posts and get templated through commensuration effects. These decoupled effects lead to morphologies that have a mesh patterns when viewed top-down at the right commensurations[58].

Simulations for these double layer systems used the same unit cell boundary conditions as shown in Figure 5.23 used in the other rectangular post array studies. PS preferential posts were chosen to compare with experiments performed by Amir Tavakkoli K.G. with the assistance of Kevin Gotrik. Simulation parameters were chosen to model the implicit solvent annealing of a 45.5 kg/mol PS-PDMS cylinder forming BCP in a 5 to 1 toluene to heptane atmosphere such that $(\chi N)_{eff} = 30.0$ and $f = 0.32$. Since varying all possible combinations of post diameters, heights, post pitches, and film thicknesses is impractical, a set of simulations were performed to find the most optimal double layer film thickness, post diameter, and post height that resulted in a particular experimentally known morphology. These parameters were chosen to be fixed since the main parameter varied in the experiments was the post pitches P_x and P_y. Based on the experimental images, the posts had a diameter approximately 21 nm or $0.6L_0$. The maximum height of the posts based on the initial HSQ film thickness was 38 nm or $1.09L_0$ (measured by ellipsometry) and decreased to 34 nm or $0.97L_0$ after exposure and salty development. These values give a good initial range to vary the post dimensions around to find the optimal simulation parameters for best quantitative comparison of the morphologies observed in the simulation with experiment.

The experimental morphology to be matched is shown in Figure 5.31 and occurred when P_x was less than $2.00L_0$ and $P_y = 1.00L_0$. In the simulations, P_x was set to $1.71L_0$ and

P_y was set to $1.00L_0$. D_{post} was varied from $0.29L_0$ to $0.86L_0$ (thus including the observed experimental diameter of $0.6L_0$) and h_{post} was varied from $0.57L_0$ to $1.00L_0$ (thus including the observed experimental height of $0.97L_0$) in the simulations. Two film thicknesses were chosen based on the experimentally measured swollen film thickness of $t \cong 2.5L_0$ (measured by UV-Vis spectral reflectometery) and the predicted commensuration of a double layer features plus the top and bottom wetting layers giving $t = 3.00L_0$. For the $t = 3.00L_0$ case, the h_{post} range examined was increased to $1.14L_0$ to $2.14L_0$ since the thicker films were expected to require taller posts to get the mesh structure. By simulating saddle point solutions over this range of parameters, the top-down morphology was compared with what is expected to be observed for the mesh grid structure and the matching morphology with the smallest D_{post} and h_{post} closest to the experimental values were chosen to perform further simulations varying P_x and P_y. The results of these simulations are shown in phase diagrams in Figure 5.32 for $t = 2.50L_0$ and Figure 5.33 for $t = 3.00L_0$. From these results, the best set of parameters that yielded the mesh structure were $t = 3.00L_0$, $h_{post} = 1.71L_0$, and $D_{post} = 0.71L_0$ so these values were used for further simulations with P_x and P_y being varied.

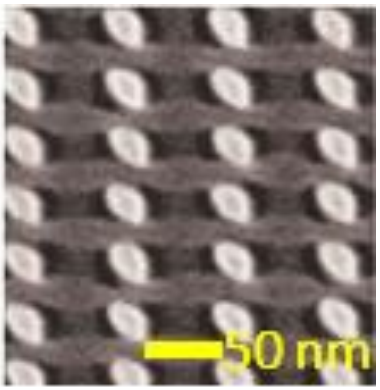

Figure 5-31: Mesh grid morphology observed in experiments with P_x = $1.71L_0$ and P_y = $1.00L_0$. Whiter areas are HSQ posts and light grey areas oxidized PDMS cylinders[58].

Based on these results, there were multiple combinations of post height, diameter, and film thickness that gave the mesh grid structure. As will be discussed later in Chapter 7 with direct experimental work comparison, assumptions about the thickness and surface preferentiality may not be exactly correct, and thus even more combinations of these

parameters are expected to produce the mesh grid structure. However, the results found using the conditions chosen based on the smallest h_{post} and D_{post} conditions show general trend agreement with morphologies observed experimentally and thus overall give good correspondence in understanding why the different morphology combinations form at different commensurations of the posts. Some of these observed structures may additionally be metastable as will be examined later in terms of connections between layers. Additionally at these high swollen film thicknesses, implicit solvent annealing modeling may begin to break down at the high concentrations of solvent vapor incorporated thus future studies should likely try to account for such effects. Even with these caveats, the results do appear to agree with the general trends in morphological phase behavior observed experimentally as will be discussed in the next section.

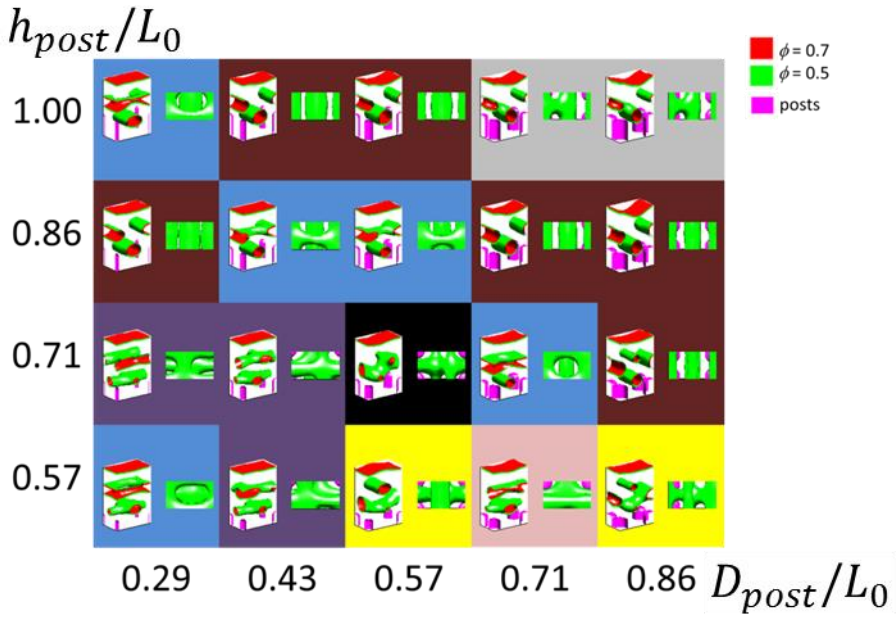

Figure 5-32: Simulation results for a thickness of t = 2.50L_0 with fixed P_x = 1.71L_0 and P_y = 1.00L_0 varying D_{post} and h_{post}. In each result box, the left image is a side angle view of the 3D PDMS density isosurfaces (green for ϕ = 0.5 and red for ϕ = 0.7) with posts colored purple and the right image is a top-down cut through surface view. Different morphology types observed are color coded based on the top-down view as follows: (light blue) Perforated lamellae over confined cylinders. (crimson red) Hexagonal close-packed cylinders. (grey) Hexagonal close-packed cylinders with connection defect. (dark purple) Parallel top and bottom commensurate cylindrical type structure with possible defects. (yellow) Inverted mesh grid structure. (pink) Almost a mesh grid structure with bottom feature being perforated lamellae. (black) Monolayer defective cylinder structure[58].

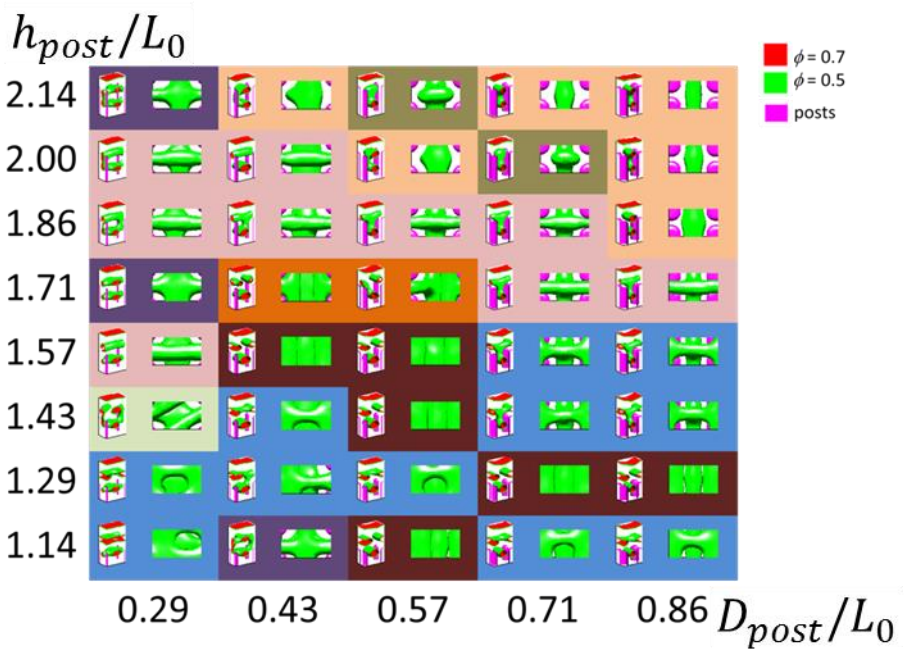

Figure 5-33: Simulation results for a thickness of t = 3.00L_0 with fixed P_x = 1.71L_0 and P_y = 1.00L_0 varying D_{post} and h_{post}. In each result box, the left image is a side angle view of the 3D PDMS density isosurfaces (green for ϕ = 0.5 and red for ϕ = 0.7) with posts colored purple and the right image is a top-down cut through surface view. Different morphology types observed are color coded based on the top-down view as follows: (light blue) Perforated lamellae over confined cylinders. (crimson red) Hexagonal close-packed cylinders. (light grey) Diagonal cylinders over perforated lamellae. (beige) Hexagonal close-packed cylinders with connection defect. (dark purple) Parallel top and bottom commensurate cylindrical type structure with possible defects. (pink) Mesh grid structure as observed from top-down view. (cream) Overlapping confined cylinders in both layers. (old gold) Connected sphere over confined cylinder[58].

Having determined an optimal film thickness and post parameters, $t = 3.00L_0$, $D_{post} = 0.71L_0$, and $h_{post} = 1.71L_0$, simulations were performed varying P_x and P_y. Since these 3D simulation cells were very large, computation time was on the order of a couple of weeks to reach saddle point solutions. Thus only a focused set of simulations was performed for the case of $P_y = L_0$ with P_x being varied from L_0 to $3.00L_0$ and a range of simulations with $P_x = P_y$ were performed varying value from $0.86L_0$ up to $1.57L_0$. The key morphologies observed are shown in Figure 5.34. These morphologies that agreed with the trends of the experimental parameters included hexagonally close-packed double layer cylinders when P_x was commensurate with $2L_0$ as shown in Figure 5.34.a. Mesh grid structures with one confined cylinder and two confined cylinders were seen at conditions

with $P_y = L_0$ and $P_x < 2L_0$ and $P_y < 3L_0$ respectively as shown in Figure 5.34.b and Figure 5.34.c respectively. These mesh grid structures were also observed for certain boundary conditions for BCPs confined between two flat walls with strongly preferential to one block surface boundary conditions in simulations, though not as controllable in terms of directionallity[152]. Diagonal cylinders over spheres were predicted at square lattice conditions with $P_x = P_y \leq \sqrt{2}L_0$ as shown in Figure 5.34.d and diagonal cylinders over perforated lamellae PL1 for square lattice conditions with $P_x = P_y > \sqrt{2}L_0$.

The simulation results using initially random field conditions usually resulted in mesh grid structures where the top and bottom features had a connection. There was some experimental evidence to suggest the top and bottom layers might be connected, but the possibility these connections are merely metastable defects also exists. To test this possibility, a simulation for the case of $P_x = 1.71L_0$ and $P_y = 1.00L_0$ were seeded with a set of fields representing a mesh grid structure without a connection. As shown in Figure 5.35, once the system reached a saddle point solution that still had no connections, the energy of the system was degenerate with that of the system with a connection. The energy difference between the two states is quite small, being within 0.15% of each other. This implies such connections are real potential energetically favorable defects in the system and thus should be considered when preparing samples for post processing applications such as pattern transfer. This connection issue will be examined further in Chapter 7 in terms of direct experimental measurement work.

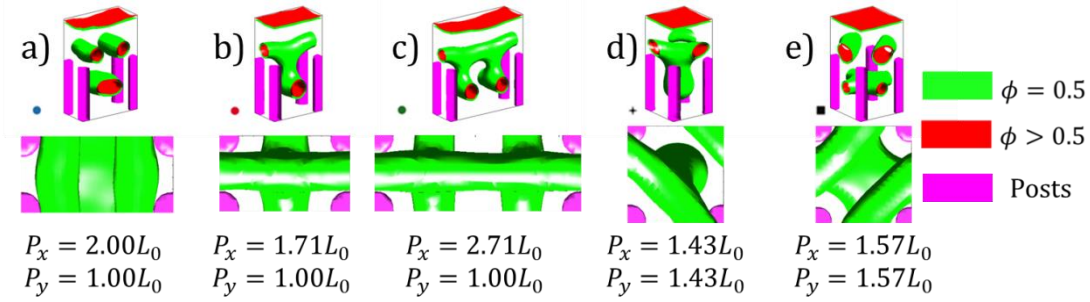

Figure 5-34: Key simulation results that were observed experimentally at different P_x and P_y values with side view on top and top-down cut through surface view on bottom. Colored symbols correspond to symbols in experimental phase diagram in Figure 5.36. a) Hexagonal close-packed cylinders commensurate with P_x direction. b) Mesh grid structure. c) Double bottom confined cylinder mesh grid structure. d) Diagonal cylinders over a sphere. e) Diagonal cylinders over perforated lamellae PL1[58].

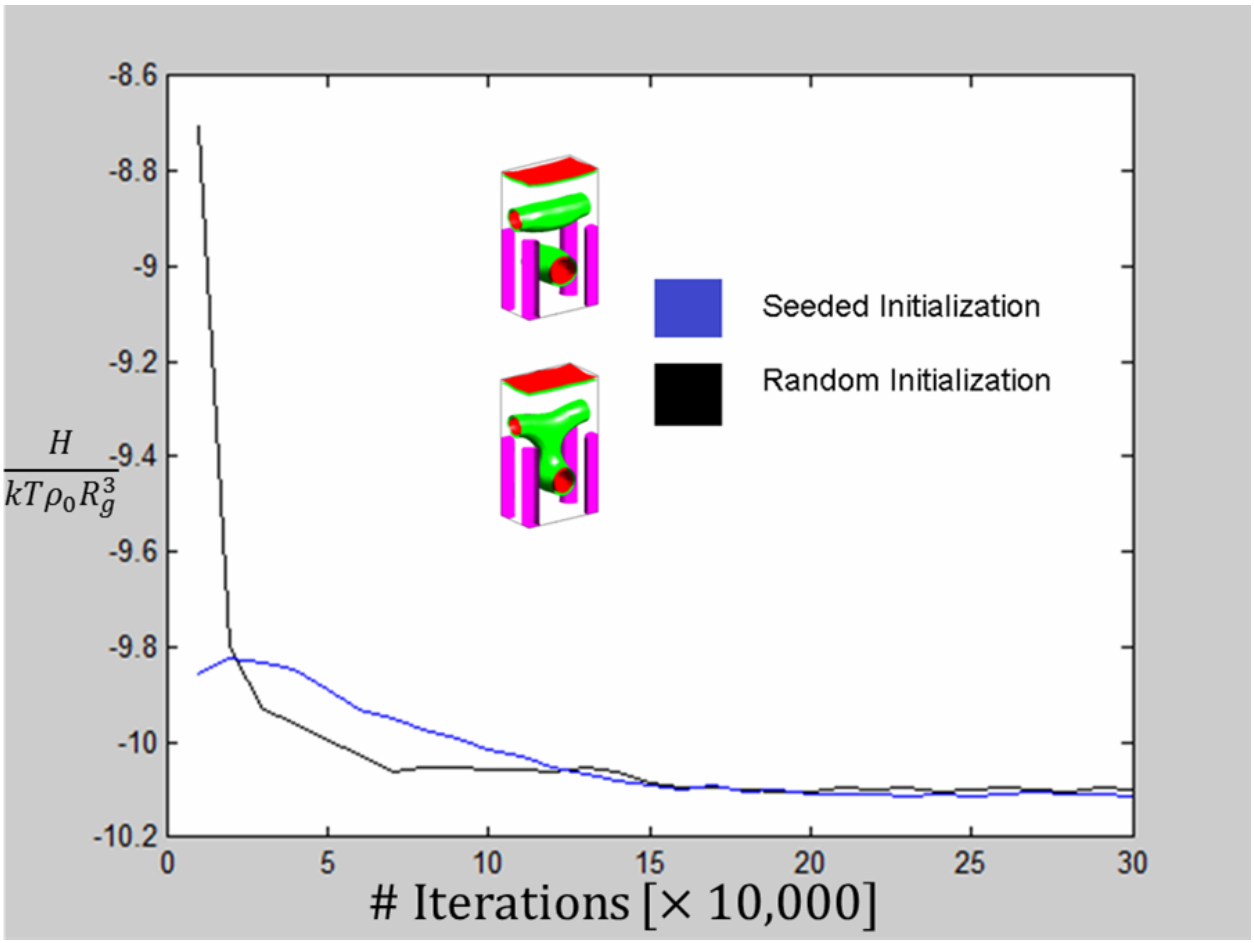

Figure 5-35: Plot of the normalized free energy Hamiltonian $H/kT\rho_0 R_g{}^3$ (where k is Boltzmann's constant, T is the temperature, ρ_0 is the monomer density, and R_g is the radius of gyration) as a function of number of simulation iterations. Energy levels of the simulation reached a saddle point solution around 200,000 iterations. P_x = 1.71L_0 and P_y = 1.00L_0. Inset: Density fields isosurfaces 3D side views at 300,000 iterations are shown for the seeded mesh grid without a connection (energy curve in blue) on top and mesh grid structure with connection (energy curve in black) on bottom. The two structures energy levels are degenerate within the error of the simulation implying they are both potential equilibrium solutions to the SCFT saddle point condition[58].

5.4.7 Experimental Results and Comparison – Majority Block Preferential Posts – Double Layers of Minority Features

In the double layer rectangular post layer experiments done by Amir Tavakkoli K.G. and Kevin Gotrik, P_x and P_y were varied over a range of values from 0.5L_0 up to almost 3.00L_0 (corresponding to 18 nm to almost 105 nm). Various morphologies with different combinations of top and bottom layer structures were observed as a function of P_x and P_y

depending upon various commensuration effects and SEM images of the etched morphologies are shown in Figure 5.36 along with a phase diagram of where the structures were observed experimentally. In the simulation parameters explored, the P_x commensurate hexagonally close-packed double layer of cylinders in Figure 5.36.A, mesh grid structure in Figure 5.36.C, double bottom confined cylinder mesh grid structure in Figure 5.36.E, diagonal cylinders over spheres in Figure 5.36.H, and diagonal cylinders over perforated lamellae in Figure 5.36.I were all observed in the same commensurate regions in the simulation as experiment. Other structures observed in the experiment were not observed in simulation because the simulations were limited in the range of P_x and P_y explored due to computation time constraints. Additionally, simulations did not show superstructure results since only single unit cells were considered and as previously discussed for monolayer simulations these structures are either a combination of metastable phases near phase transition boundaries or have kinetically trapped structures not accounted for in the model.

The phase diagram of all experimentally observed structures shown in Figure 5.36.L has all the different observed states plotted as an appropriate colored symbol from Figures 5.36.A through 5.36.I in the P_x and P_y phase space. The colored bands in the phase diagram represent commensuration regions with different directions (x, y, or diagonal directions) with a band of $\pm$9% strain. The strain amount of 9% was chosen based on other experimental evidence suggesting BCPs being able to accommodate strain from topographical features up to these amounts[6,17,149,191]. The transitions between different morphologies appear to correspond well with these different bands implying that the morphologies observed are mainly influenced by commensuration effects in the two layers.

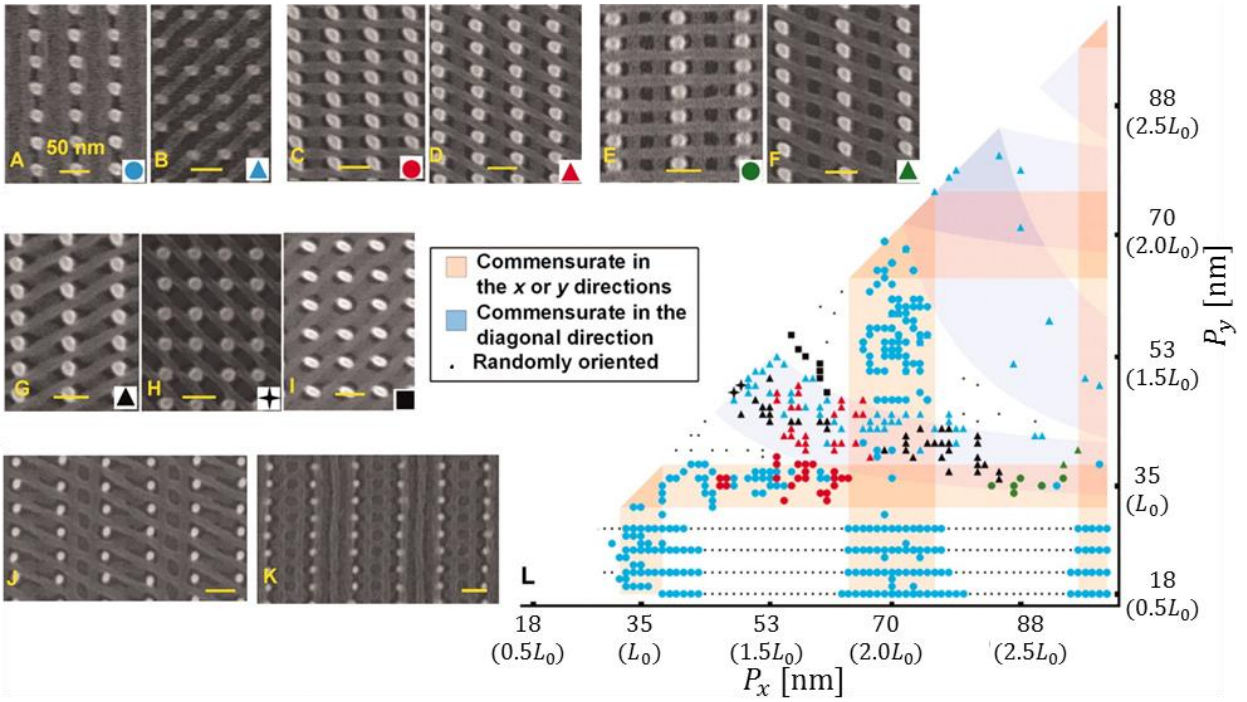

Figure 5-36: Experimental results for double layer structures templated by a rectangular post array lattice with various P_x and P_y dimensions. Left are SEM images of various structures observed at different P_x and P_y values. White structures are HSQ posts and grey structures are oxidized PDMS features. Middle is a legend for the commensuration bands and randomly oriented observed cylinders in the phase diagram on the right. A) Parallel to *y*-direction commensurate with P_x cylinders. B) Cylinders commensurate in diagonal directions in both layers. C) Mesh grid structure with one bottom layer confined cylinder. D) Diagonal top layer mesh grid structure with one bottom layer confined cylinder. E) Mesh grid structure with two bottom layer confined cylinders. F) Diagonal top layer mesh grid structure with two bottom layer confined cylinders. G) Diagonal top layer cylinders over ellipsoids. H) Diagonal top layer cylinders over spheres. I) Diagonal top layer cylinders over perforated lamellae. J) Superstructure combination of diagonal top layer cylinders over ellipsoids or two confined cylinders. K) Superstructure of perforated lamellae or parallel to *y*-direction commensurate with P_x cylinders. L) Phase diagram of where structures in (A-I) occurred with corresponding symbols from (A-I) as well as randomly oriented cylinder structures denoted by black dots[58].

5.5 Line Doubling Studies

In the previous sections, the ability of HSQ post templates to double the number of areal features when used to perform BCP DSA was demonstrated for hexagonal arrays of posts templating spheres where commensurate post lattices allowed for the increase in number of dots in a top-down dot pattern of templated spheres and similarly for spheres and

cylinders templated by square symmetry arrays of posts[49,57]. In a similar manner, by patterning lines of HSQ rather than posts and increasing the distance between these line patterns, BCPs can be templated by such line patterns resulting in a doubling of the density of features or higher multiplying for large enough distances. Simulation results for such systems will be examined in this section with some experimental comparison.

5.5.1 Simulation Results

To study the effects of HSQ lines templating BCP cylinders, a simulation unit cell was used as shown in Figure 5.37. In the simulations, the top air interface was made to model a PDMS selective wetting air interface condition, the brush layer was modeled with a PS preferential field, and the substrate and template was modeled with large pressure field constraints. The numerical values of these field constraints are all the same as used in the HSQ post simulations. In all simulations, implicit solvent annealing conditions with an effective $\chi N = 30.0$ and $f = 0.33$ were used to model conditions of a 5 to 1 toluene to heptane vapor atmosphere of a 45.5 kg/mol cylinder forming PS-PDMS BCP. Simulations were performed on 3D grids with N_x by N_y by $N_z = 12$ by 16 by 42 to 64 by 16 by 42 corresponding to L_x by L_y by $t = 0.43L_0$ by $0.57L_0$ by $1.5L_0$ to $2.29L_0$ by $0.57L_0$ by $1.5L_0$. The height of the template was L_0. For the initial set of simulations, defects in the $y-$direction were undesirable since only doubling of cylindrical features were of interest initially and having large L_y dimensions would lead to potential periodic defects in that direction. Such defects are important in transition regions and are studied separately using a larger commensurate $L_y = L_0$. These initial simulations were all started from random initial field conditions.

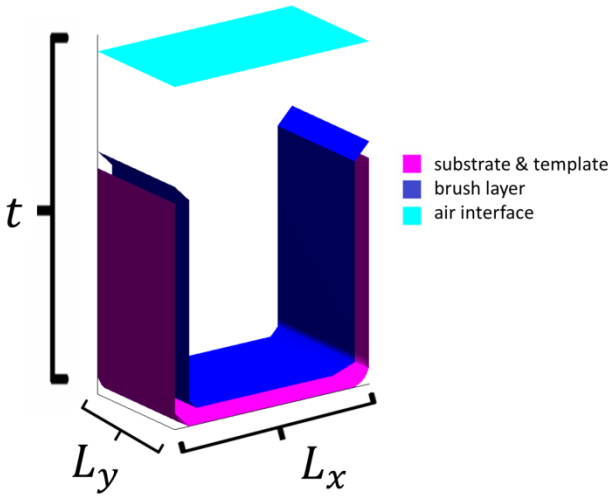

Figure 5-37: 3D unit cell schematic used in simulations. Purple area is where the fields are constrained to prevent the polymer density from evolving to model the HSQ line templates and bottom substrate. Dark blue area is where the fields are constrained to be attractive to the majority block (PS) and repulsive to the minority block (PDMS) to model the PS brush layers used in experiment. Light blue area where the fields are constrained to be attractive to the minority block (PDMS) to model the air interface wetting behavior of the PDMS observed in experiment. Boundary conditions are periodic in the L_x and L_y directions. L_x was varied from $0.43L_0$ up to $2.29L_0$ in the simulations and t was kept constant at a film thickness of $1.5L_0$.

The results of the simulations spanning the L_x range of $0.43L_0$ to $2.29L_0$ are shown in Figure 5.38. Three distinct dominant morphological regions are observed. Besides the one data point at $L_x = 0.43L_0$ where only the surface PDMS layer formed and there was no internal cylinder morphology between the template, either a single cylinder, a cylinder under larger in-plane tension in the L_x direction, or two cylinders formed as L_x/L_0 was increased. These distinct regions correspond to L_x/L_0 ranges of [0.50,1.00], [1.14,1.64], and [1.71,2.29], respectively. To better gauge the transition between a single cylinder and two cylinders, simulations were performed for $L_x/L_0 = 1.50$ to 1.71 with an increased $L_y = L_0$ (28 grid points) and were seeded with a single cylinder structure with a hole defect. After the simulation reached a saddle point solution, the morphologies observed in Figure 5.39 were observed where the hole annealed in the $L_x/L_0 = 1.50$ case but did not in the others.

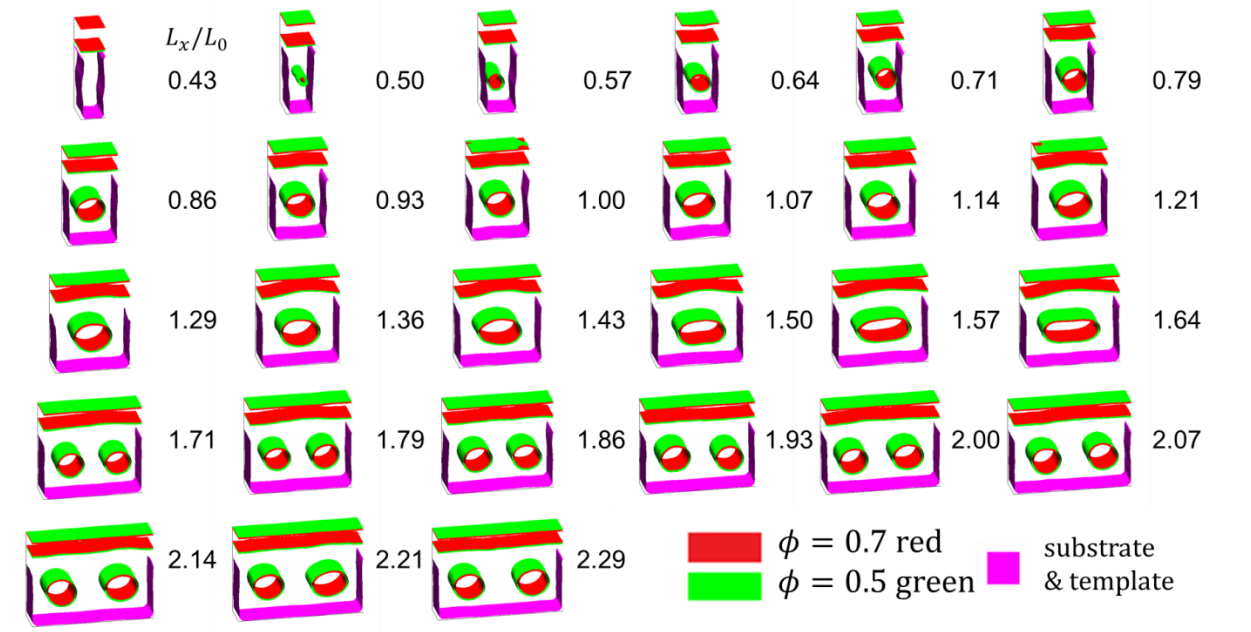

Figure 5-38: 3D SCFT simulations of f_{PDMS} = 0.33 and χN = 30.0 cylindrical forming PS-PDMS polymer between line templates of varying width L_x and height L_0. Green area is the ϕ = 0.5 and red area the ϕ = 0.7 normalized PDMS density surfaces. Purple area is substrate and template. As L_x/L_0 is increased from 0.43 to 2.29, the simulations show a transition from no cylinders present (0.43) to a single cylinder present (0.50 to 1.00) to strained cylinders in the L_x direction (1.14 to 1.64) to two cylinders forming (1.71 to 2.29).

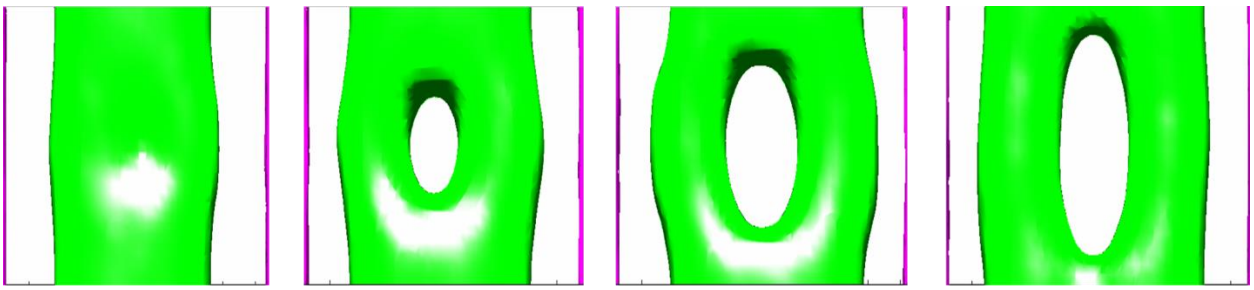

Figure 5-39: Top-down view of 3D SCFT simulations of f_{PDMS} = 0.33 and χN = 30.0 cylindrical forming PS-PDMS polymer between line templates of varying normalized width L_x/L_0 1.50 to 1.71 for the one and two cylinders transition region observed in experiment. Simulations were seeded with cylinders with a hole defect to see how hole defect size changes with increasing line width. For L_x/L_0 = 1.50 the hole annealed out of the structure to form a single strained cylinder and for other simulations the hole increased in size with increasing line width.

Based on the results of these simulations, there is a clear transition region where one and two cylinders are metastable based on the seeded hole size growing as L_x/L_0 increased. To better gauge this transition region, the engineering strain in the L_x direction

was calculated as $d_{cyl}/d_0 - 1$ by taking the measured L_x direction cylinder diameter d_{cyl} relative to the equilibrium cylinder diameter d_0. d_0 was measured as 14 grid points or $0.5L_0$. A plot of these strain calculations with SCFT measurement error of 1 grid point or $L_0/28$ is shown in Figure 5.40 as a function of L_x/L_0.

A couple of calculation anomalies in the compressive region for one cylinder need to be pointed out. For the $L_x = 0.43L_0$ point, there was no cylinder between the posts, so $d_{cyl} \equiv 0$ meaning the strain is -1 by virtue of the absence of a cylinder. For some of the other supposedly compressed cylinders, the cylinders themselves are completely circular with no apparent compression in the thickness direction more so implying they simply have less total PDMS rather than really being under compression, so these compression values are more of an artifact of the cylinders simply being overall smaller than the equilibrium cylinder size. For the cylinders under tension, they definitely do stretch in the L_x direction resulting in an ellipsoidal cross-section behavior as observed in Figure 5.38.

At high enough strain, the cylinders become metastable between two split cylinders and a single strained cylinder. Based on the strain values themselves, the split cylinders appear to be more energetically favorable, but this observation does not take into account surface energy and thus the reason for the observed coexistence of these phases is better understood from the transition SCFT simulations from Figure 5.39. Once the region with two cylinders is reached, the maximum strain the cylinders have is reduced dramatically since the two cylinders share the overall strain from the template. One would expect these trends to continue at higher commensurations assuming the correlation length for parallel cylinder formation remains less than L_x. Similar strain profiles have been observed in confined lamellae systems with the single feature accommodating the most strain and a drop occurring for higher numbers of features[149,191]. Based on these results, design of a given density multiplication pattern is possible by simply controlling the width of the HSQ pattern and the distance between HSQ lines such that the HSQ line width and BCP line pattern width can be controlled independently. In the next section, these results will be compared with some experimental results using such HSQ lines.

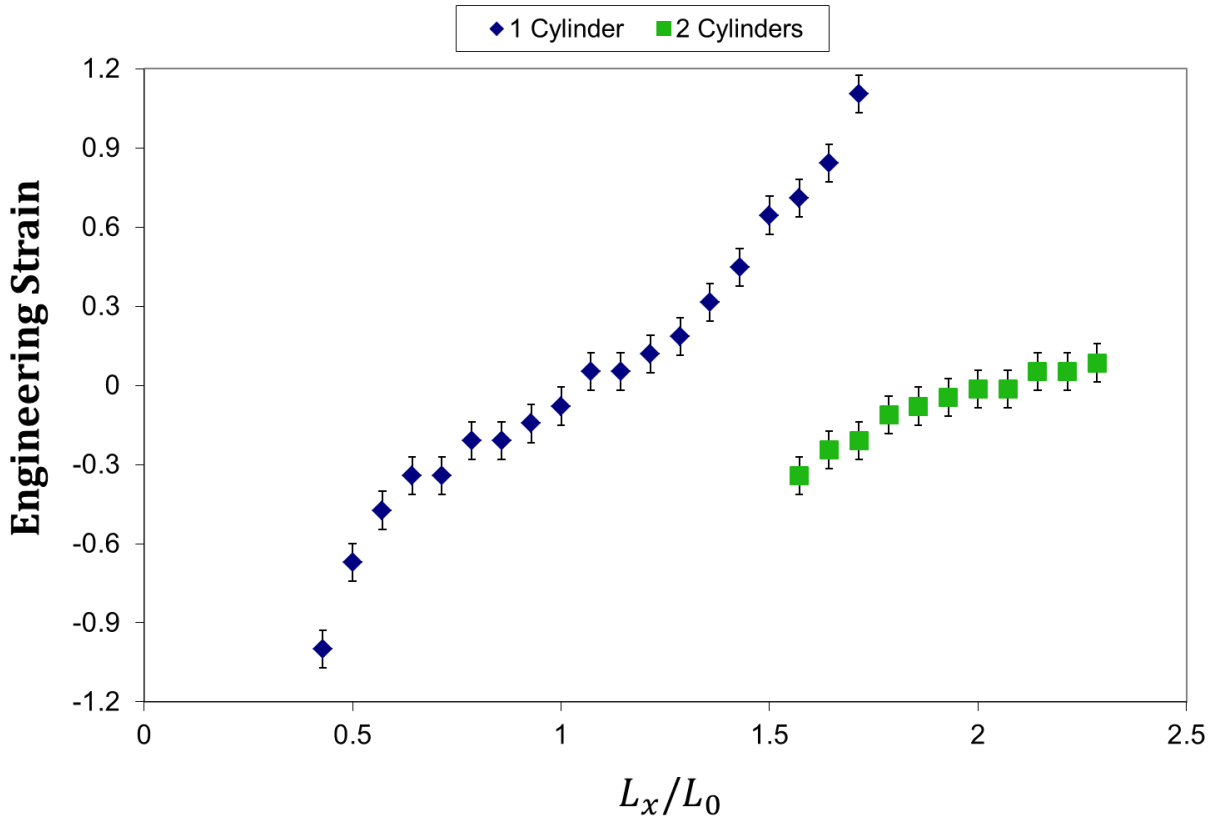

Figure 5-40: Engineering strain in the L_x direction of the cylinders versus the normalized template line width L_x/L_0 based on SCFT simulations cylinder diameters. The cylinders can strain up to $L_x/L_0 \cong 1.5$ before a single cylinder becomes too energetically unfavorable and a transition region is observed for $L_x/L_0 \cong 1.57$ to 1.71 where a single strained and two slightly compressed cylinders are metastable. For $L_x/L_0 \cong 1.79$ to 2.29 double cylinders with low strain are observed.

5.5.2 Experimental Results and Comparison

Experiments were performed by Amir Tavakkoli K.G. and Kevin Gotrik where HSQ line patterns with varying line spacing distance L_x between the lines were used to control the line width of the patterned PDMS cylinder between the HSQ. Three different line spacing distances $L_x = 28$ nm, 40 nm, and 36 nm were patterned with HSQ and are shown with oxidized PDMS cylinders from BCP DSA in Figure 5.41. These values correspond to normalized L_x/L_0 values of 0.74, 1.05, and 0.95 respectively with corresponding engineering strain values of $-0.21, 0.05,$ and 0.32. The first two values are relatively close to the predicted values from the SCFT calculations. The third value is way off from the predicted value suggesting the BCP is in tension with positive strain in a region where

negative strain was observed in the simulations. The likely reason for this discrepancy is that the experimental lines have varying thickness that couples with the height of the template. The simulations always assumed a height tall enough that the cylinders were essentially confined from each other. If the height is lower in the experiment, then cylinders between neighboring lines may perturb each other and increase in diameter. Since the lines in Figure 5.41.c are thinner than in Figure 5.41.b, they are likely shorter as well and thus not fully confining the neighboring cylinders.

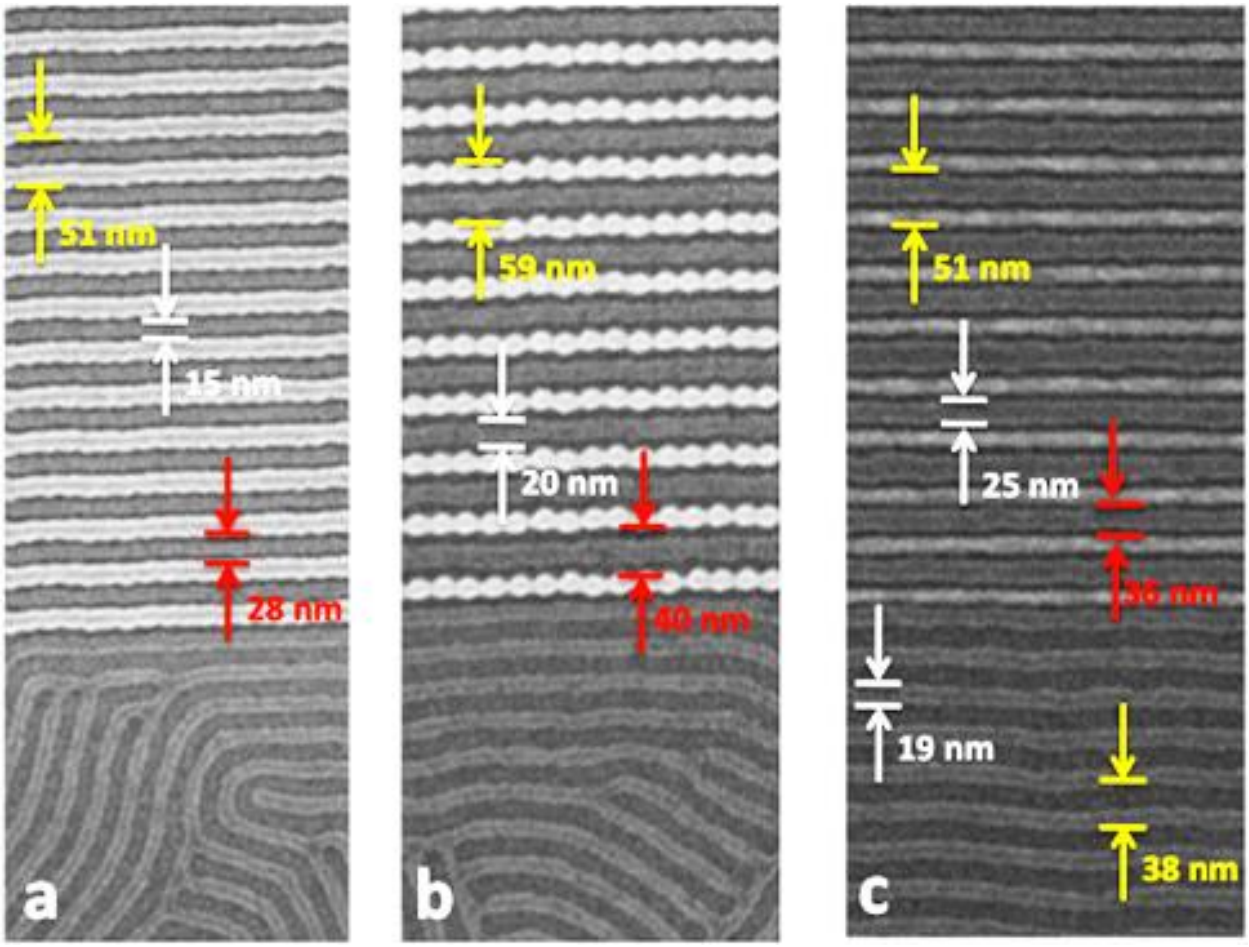

Figure 5-41: SEM images of experimental results using HSQ lines to pattern PDMS cylinders from a PS-PDMS BCP. White area is HSQ and grey area is oxidized after etching PDMS cylinders. Three different post spacing distances L_x are shown with a) L_x = 28 nm. b) L_x = 40 nm. c) L_x = 36 nm. Yellow lines mark the total period of HSQ lines or PDMS lines in c), white lines mark the width of PDMS cylinders, and red lines mark the post spacing distances L_x. The HSQ lines in c) are not as thick as in b) which is likely the cause of discrepancies between the measured engineering strain values with simulation calculated strains.

As the line spacing distance L_x was increased in the experiments, a transition to two cylinders between a single set of HSQ lines was observed. This transition is demonstrated in Figure 5.42. The same transition profiles were observed in the simulations by seeding holes in the high strain region for single cylinders as shown previously in Figure 5.39. The line spacing distances here in the experiment are slightly lower than those observed in the simulation. However, as discussed previously the line height in the experiments may be less than L_0 implying the cylinders are not completely confined as they are in the simulations leading to interactions between neighboring cylinders and thus reducing the maximum strain the cylinders can accommodate before transitioning to two cylinders. Despite quantitative differences, the simulation trends agree well with the experiments.

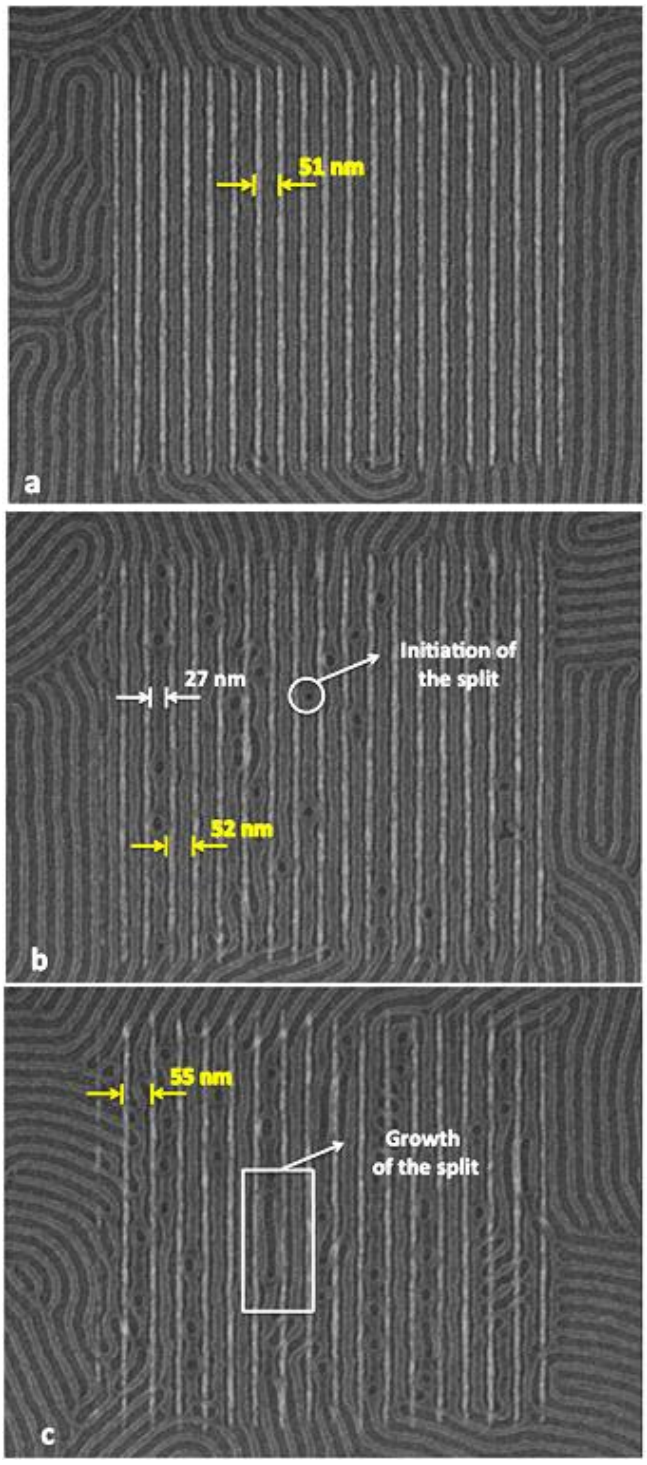

Figure 5-42: Experimental results with SEM images showing the effect of increasing the line spacing distance L_x above a critical value such that instead of having a single confined cylinder between two lines of HSQ as in (a), a transitional structure with holes was observed at intermediate L_x as in (b), and at large enough L_x double layers of cylinders began to form as in (c). Yellow numbers are the HSQ periods and white numbers are the PDMS diameters.

5.6 Confinement Studies

The effect of a confining geometry is one of most well studied cases of BCP DSA. There have been numerous studies of BCPs confined to cylindrical pores, spherical pores, and between parallel plates[67,91,134–140,142,152,159,165,199]. Here several simulation studies are presented with circular and square holes functionalized to be preferential to one block. Additionally, notch type defects are added to the confinement shapes to influence the chirality and directionality of spiral type features inside the holes. These studies simply serve to demonstrate that under highly confined conditions BCP DSA can lead to very reproducible structures that are nontrivial to produce with nondirect writing methods.

5.6.1 Simulation Results in 2D

Schematic diagrams of the unit cells used in 2D hole confinement simulations are shown in Figure 5.43. Both circular and square confining holes were considered in various sets of simulations. External field constraints kept polymer volume from evolving in the outside regions that dictated the confining DSA shape similar to other topographic boundary conditions presented. Around the edge of these shapes an exchange field constraint dictated whether the hole surface was neutral $W = 0$ or preferential to a block $W = \pm 10$. The total number of grid points were held constant at 64 by 64 and commensuration effects were modeled by changing the circle hole diameter parameter d or square hole side length s in terms of the natural period L_0. Ranges d/L_0 examined were from 0.4 up to 8.7. Simulation parameters were generally $f = 0.5$ (target 2D line patterns) with effective $\chi N = 14$ or 18 unless otherwise noted to model approximate implicit solvent annealing conditions of cylinder forming PS-PDMS.

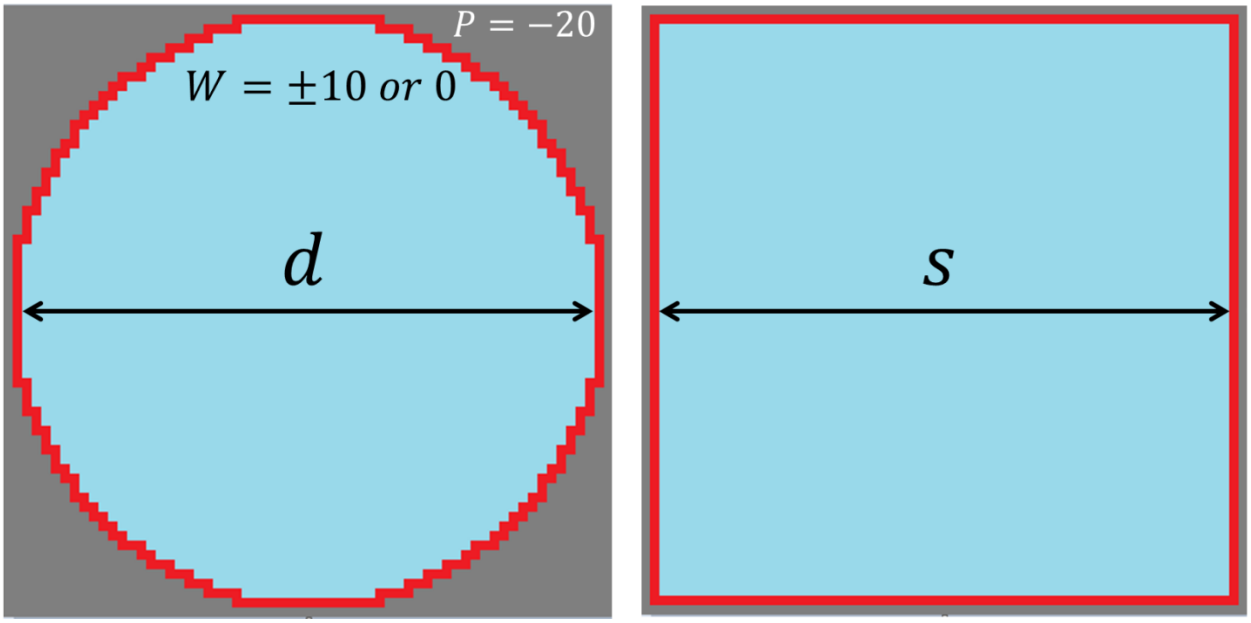

Figure 5-43: Schematic boundary conditions used for circular (left) and square (right) hole confinement simulations. Grey area was topographical constraints to the pressure fields to keep polymer density from evolving, red area is brush layer surface attraction modification through chemical potential field constraints, and teal area is free of field constraints where the BCP evolved unconstrained locally.

A set of simulations was performed varying d/L_0 from 0.4 to 8.7 for a PDMS preferential circular hole as shown in Figure 5.44. Similar experimental studies had been performed previously[200]. As d/L_0 increased, transitions between no internal morphology, a PDMS wetting ring, a PDMS dot, a PDMS ring within the wetting ring, a PDMS dot within a ring within the wetting ring, and so forth were observed. These various morphology states are color coded in Figure 5.44 depending on the number of internal features plus wetting layer. The main effect causing these transitions with increasing d/L_0 was the commensuration of the number of PDMS features with the size of the circular hole plus the circular geometry forcing the lines to curve.

To gain a more detailed understanding of these transitions, free energy curves were calculated as a function of d/L_0 by taking all nine distinct morphologies observed over the range, performing SCFT calculations seeding and holding the density fields constants to get the corresponding chemical potential fields, and calculating the corresponding free energy. These calculations do not represent saddle point solutions necessarily since the density fields are fixed and not allowed to evolve but instead let the full free energy space be

explored. The free energy curves generated from these calculations are shown in Figure 5.45. As d/L_0 increases, the curve with the lowest free energy transitions between the corresponding observed morphologies as expected from the original SCFT calculations, thus giving credence to the explanation that the structures are commensurate at different equilibrium spacing distances where each free energy curve has a local minimum.

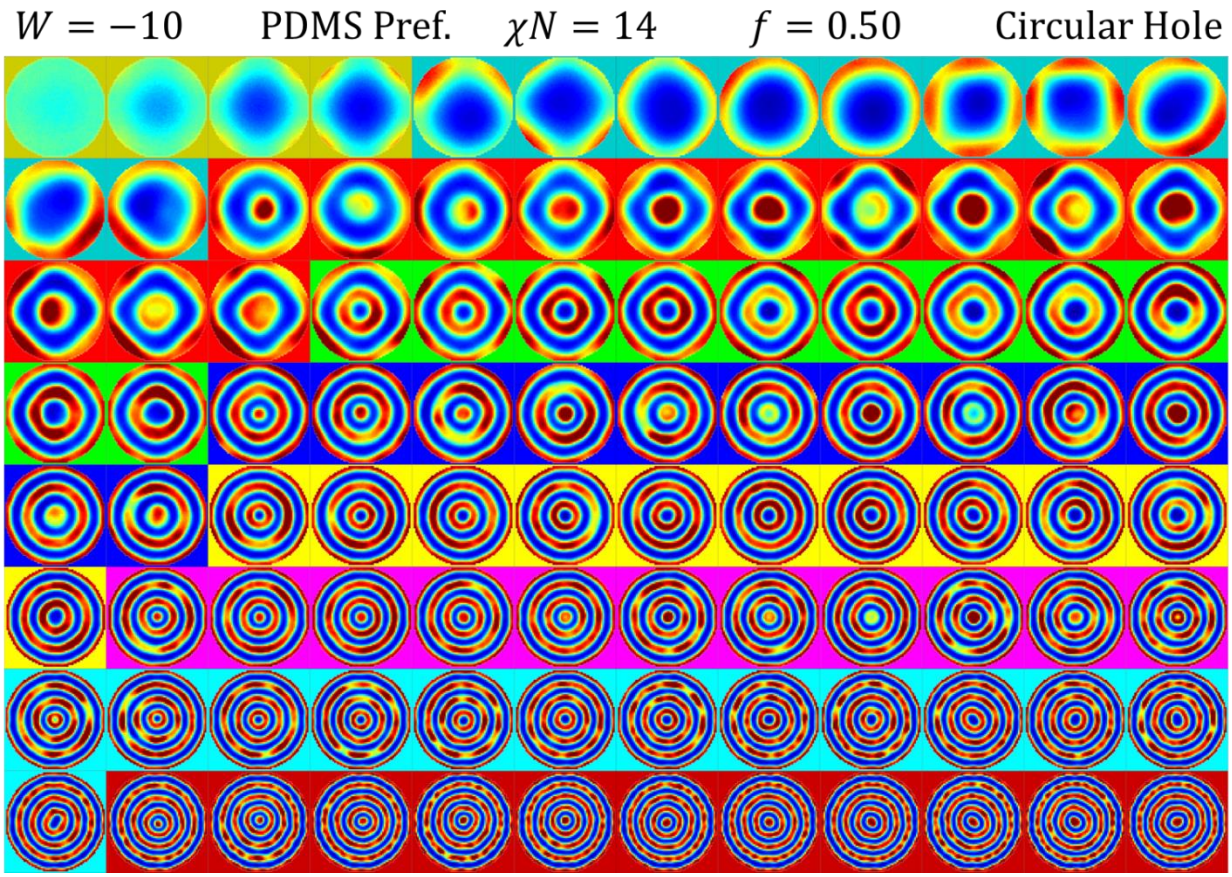

Figure 5-44: Various PS-PDMS circularly confined line morphology results under PDMS ring preferential boundary conditions. Going from the upper left corner to the right and then down rows, d/L_0 varies from 0.4 to 8.7. Nine different commensurate alternating ring and ring surrounding dot structures (color coded for clarity and to correspond to Figure 5.45 energy curves) are observed as d/L_0 increases.

Simulations with square symmetry holes with PDMS preferential walls were performed for a similar range of s/L_0 starting from 0.4 and going up to 8.7. The volume fraction here was raised to $f = 0.61$ to try to correspond better with experimental results perfomed by Hong Kyoon Choi. The square hole simulations were more prone to defective structures likely due to higher strain penalties in the sharp corner of the simulation cells.

Key structures observed consistently without defect are shown in Figure 5.46. These agree well with experimental observations at similar commensurations.

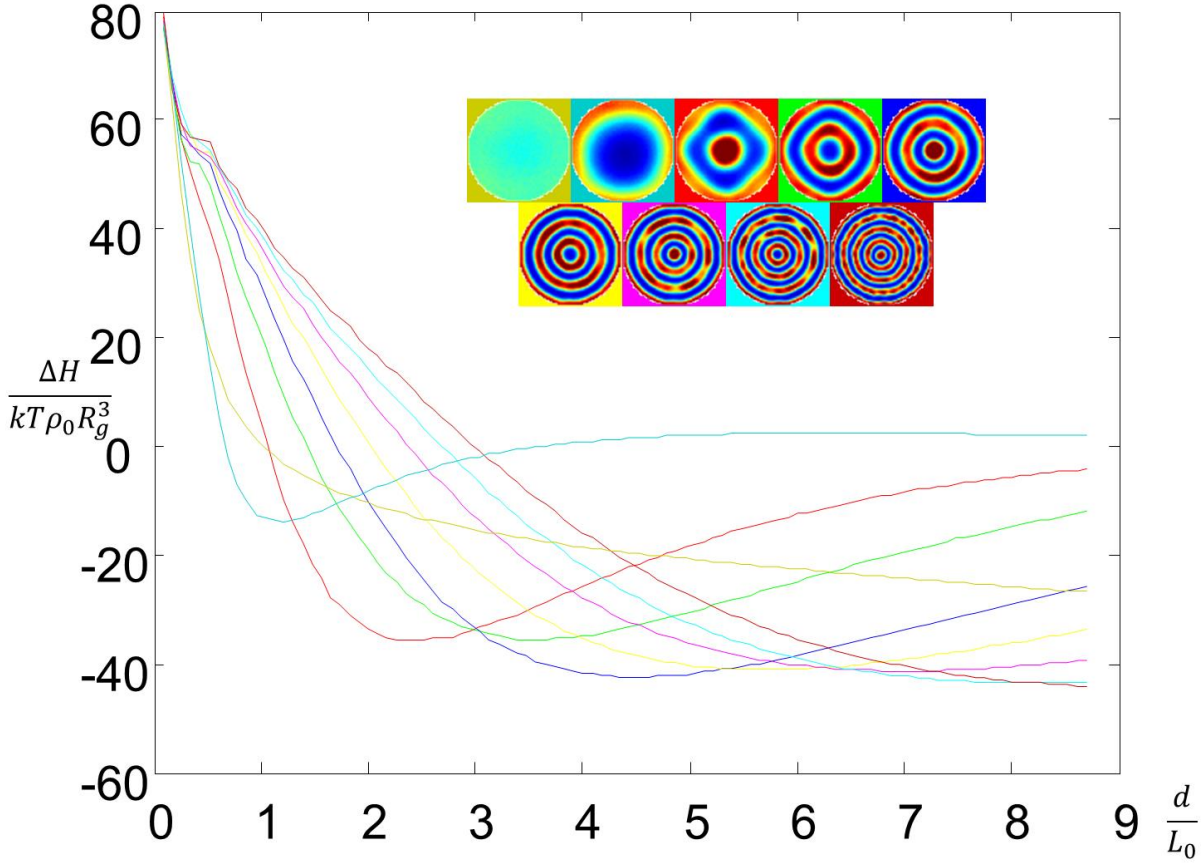

Figure 5-45: Normalized free energy curves $H/kT\rho_0 R_g{}^3$ for nine different ring and ring around dot alternating structures plotted as a function of d/L_0. The Δ symbol signifies these energy values are the difference from a purely disordered state. Calculations of the curves were done seeding the simulations with the nine structures from the first set of simulations and holding the density fields constant to obtain the corresponding chemical potential fields needed to calculate the free energy Hamiltonian. Curves are color coded to match the color code of the morphologies in Figure 5.44.

To demonstrate the controllability of spiral chirality and direction in circular holes of the PDMS lines confined by the holes, two unit cells with notch templates of different size were examined as shown in Figure 5.47. These notch templates were chosen to be of a right triangular shape to induce the nucleation of a line pattern of the corresponding surface wetting condition and then curve back around in the hole due to the circular boundary conditions. The results at commensurate d/L_0 spacing distances for both notch sizes are shown in Figure 5.48. For the smaller notch, the ring patterns were not induced to nucleate

until very larger commensurations of $d/L_0 = 6.00$ whereas the larger notch enabled the formation of a spiral pattern for commensurations as low as $d/L_0 = 3.00$. These results demonstrate the ability of pattern chirality control by adding a simple extra topographical feature and experimental verification has recently been performed showing the notches do indeed lead to the chiral spirals. The next section will examine 3D hole thickness effects as a final variable for hole confinement effects.

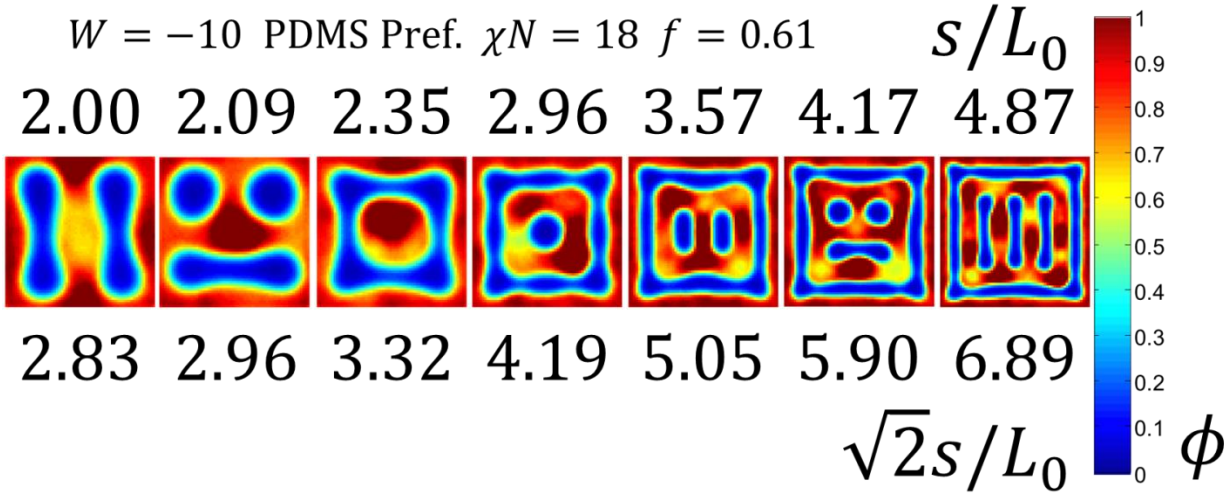

Figure 5-46: Seven different morphologies observed in simulations of PDMS preferential wall square hole confinement simulations. Top number is the side wall length and bottom number is the diagonal length. The square symmetry thus has a richer range of commensuration values with these two different directions, but this can simply lead to more defective structures due to higher strains in the different directions.

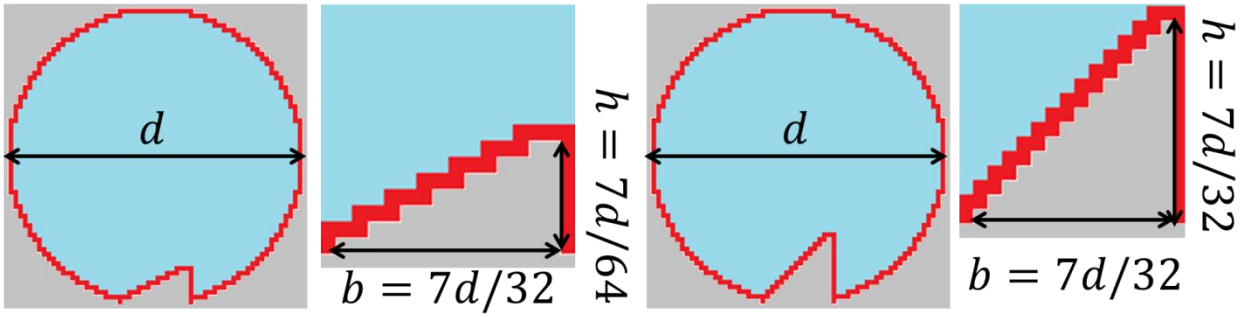

Figure 5-47: Schematics of unit cells with notch templates added to induce chirality and direction of ring patterns in circular hole confinement templates. Left: Full unit cells. Right: Close-up of notches with dimension details of the notch (base width b and height h) in terms of the hole diameter d. Top: Shorter notch template. Bottom: Larger notch template.

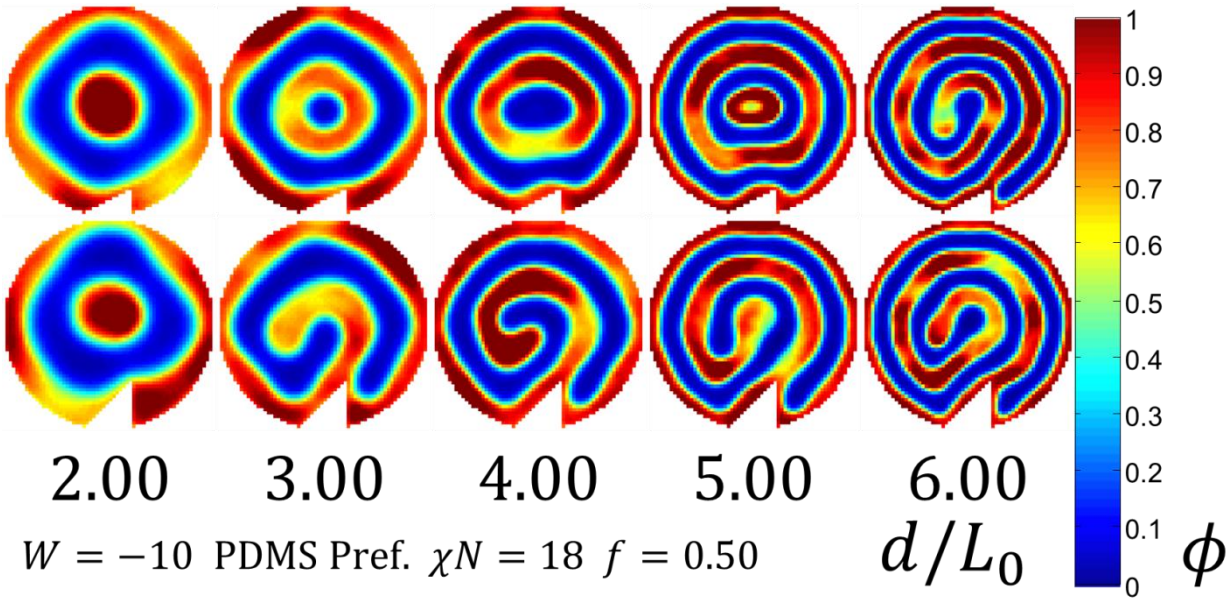

Figure 5-48: Five different morphologies observed in simulations of PDMS preferential wall circular hole confinement simulations with notch template to induce a spiral pattern with a particular chirality. Top row of results had a smaller height notch that simply compressed the ring and dot structures for low commensurations but did induce a spiral structure with a right-handed chirality for a commensuration of d/L_0 = 6.00. Bottom row of results had a larger height notch that induced a right-handed chirality spiral structure for commensurations as low as d/L_0 = 3.00.

5.6.2 Simulation Results in 3D

Simulations were performed with circular boundary conditions in 3D with a thickness of $4L_0$ by extending the 64 by 64 unit cell with $N_z = 32$ grid points and setting the thickness constant. The main point of the simulations were to see if independent layers of features would form or if there would be potential connections between layers of features. Diameters d/L_0 from 1.2 to 3.9 were explored at the specified simulation conditions as shown in Figure 5.49 and 4.0 to 6.6 were explored at the specified simulation conditions as shown in Figure 5.50. Similar trends seen in the 2D simulations were observed with alternating ring and dot surrounded by ring structures seen in the top-down cut through views of the results. However, the morphologies in the thickness direction did indeed produce connections due to the thickness not being between commensurations due to the neutral top boundary conditions with PDMS preferential bottom conditions. The curved perforated lamellae structure as shown in the zoomed image in Figure 5.51 is likely

stabilized due to the compressive strain of the incommensurate thickness since the boundary conditions would correspond to 3.5 layers of features. The space for these confined structures is very large with just changing the diameter of the features and thickness, thus there is plenty of opportunity in future studies to find optimal conditions for different desired confined features.

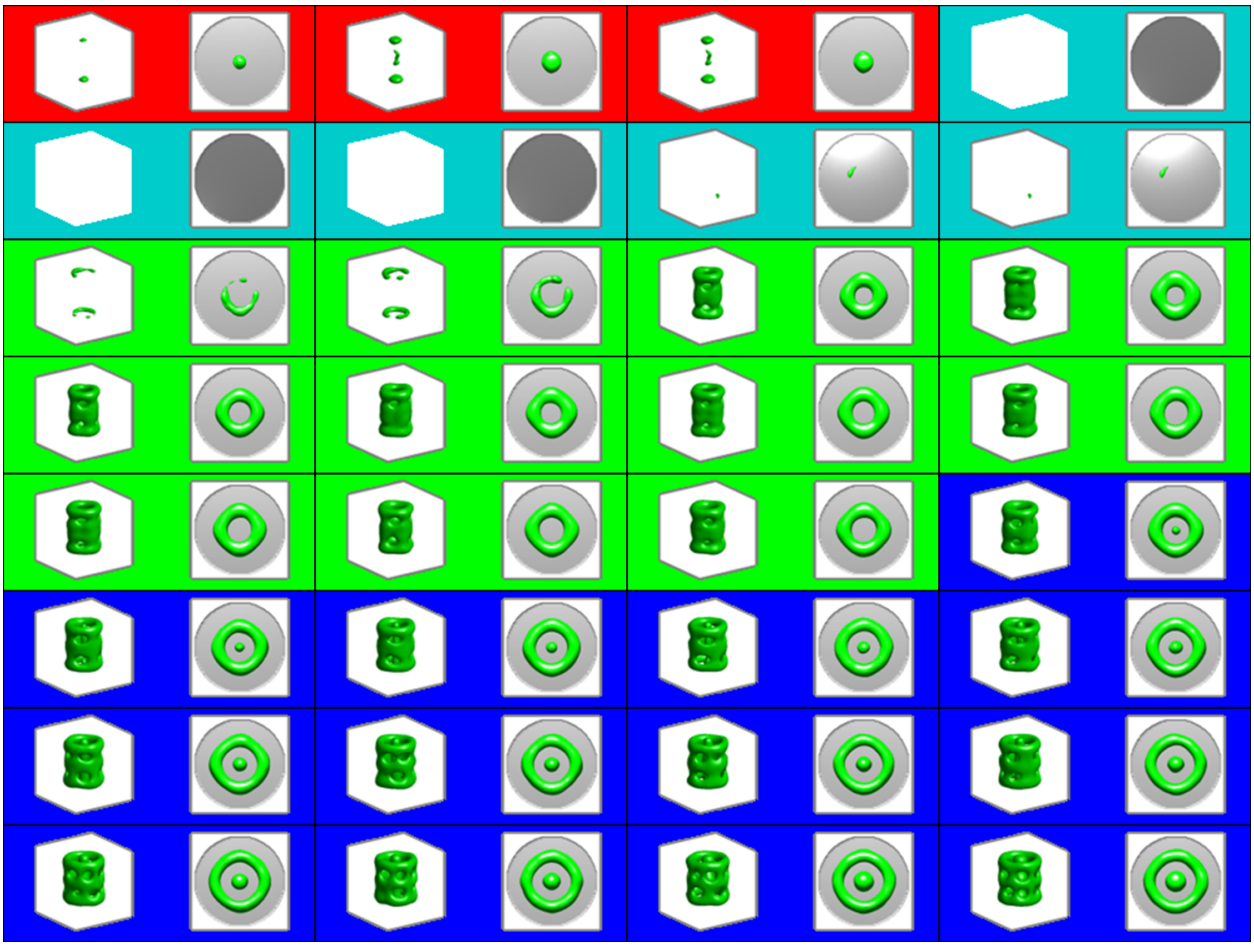

Figure 5-49: 3D simulation results of a $4L_0$ thick hole of a cylindrically confined cylinder forming PS-PDMS with neutral top surface conditions and PDMS preferential surface conditions on the rest of the surfaces. From upper left corner to right and then down results are shown from d/L_0 = 1.2 to 3.9. Left images are 3D side view with boundary conditions cut away and right images are top-down cut through views. General trends are for more concentric features to form as d/L_0 increases to different commensurations. Simulation parameters are χN = 18 and f = 0.36. Plots are of ϕ = 0.5 isosurfaces. Color coding is analogous to 2D results in Figure 5.44 only considering the top-down morphology appearance. Interestingly the preferential layer only phase (teal) in 3D occurs between a single sphere (red) and ring (green), possibly due to the bottom wetting layer (not shown).

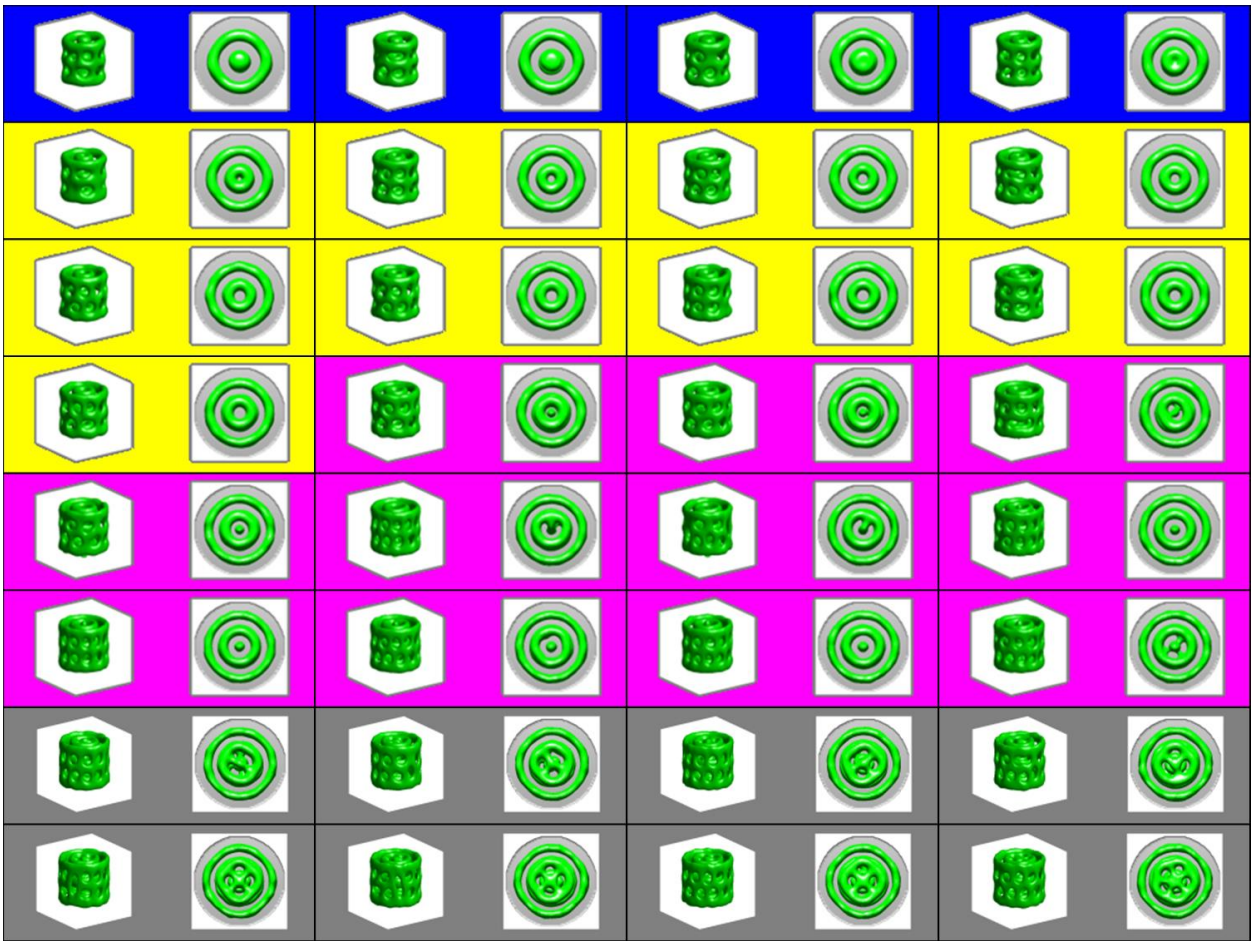

Figure 5-50: 3D simulation results of a $4L_0$ thick hole of a cylindrically confined cylinder forming PS-PDMS with neutral top surface conditions and PDMS preferential surface conditions on the rest of the surfaces. From upper left corner to right and then down results are shown from d/L_0 = 4.0 to 6.6. Left images are 3D side view with boundary conditions cut away and right images are top-down cut through views. General trends are for more concentric features to form as d/L_0 increases to different commensurations. Simulation parameters are χN = 18 and f = 0.36. Plots are of ϕ = 0.5 isosurfaces. Color coding is analogous to 2D results in Figure 5.44 only considering the top-down morphology appearance. The phase at the highest diameters (grey) was not observed in 2D simulations in terms of top-down views of 3D results where the ring in the center started having interconnections like confined perforated lamellae rings. Also, the double ring with single sphere phase (pink) had defects in different layers sometimes with the internal ring sometimes connecting to the internal sphere or cylinder going through the rings.

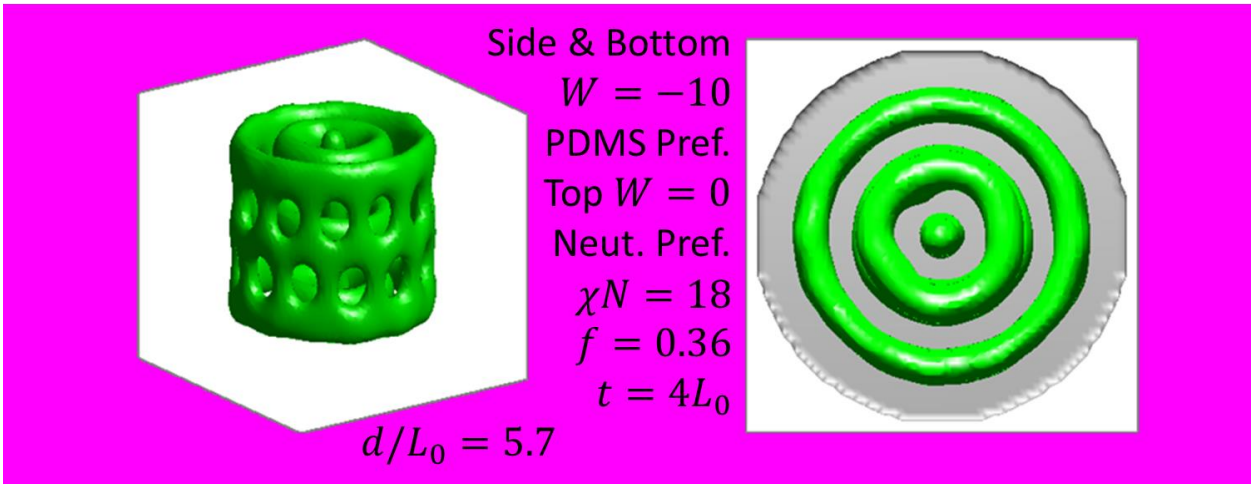

Figure 5-51: 3D simulation result for d/L_0 = 5.7 of a $4L_0$ thick hole of a cylindrically confined cylinder forming PS-PDMS with neutral top surface conditions and PDMS preferential surface conditions on the rest of the surfaces. Left image is 3D side view with boundary conditions cut away and right image is a top-down cut through view. A perforated lamellae structure formed in the thickness direction in the outer most ring due to the thickness being commensurate with 3.5 layers of cylinders thus confining the ring to the metastable perforated lamellae structure. Inner most single dot feature is a cylinder that goes through all rings, although in other cases it is made of separated spheres. Simulation parameters are listed inset in the figure. Plots are of ϕ = 0.5 isosurfaces.

5.7 Summary

As demonstrated by the wide variety of morphologies with long correlation lengths, DSA is a powerful tool in locally controlling BCP self-assembly. Templates can be formed from BCP patterns themselves as evidenced by the hierarchical templating, directly written using EBL into arrays of post features, lines, or confining holes, and eventually removed during etching by using the proper resist. As long as the size of the template is controllable to be on the order of magnitude of the BCP, the templates can integrate into the BCP morphologies and allow the formation of an almost limitless array of patterns.

Still, all the work presented in this chapter was limited to periodic patterns except in the case of locally confined structures. In general these boundary conditions can be made as complex as the coarse graining of the simulations and imagination of the engineers and scientist making the DSA templates allow. The notch being added to the confined hole features is one such example of an extended possibility with the design of DSA templates in the simulations. Posts of a multitude of shapes and sizes can all theoretically be examined,

though physically fabricating all such patterns is limited by lithography direct writing resolution limits. As long as the structures formed are due to commensuration effects and are equilibrium structures, the methods presented in this chapter can examine how to form such structures reproducibly. If kinetic pathways play a role in the structures formed, future dynamical simulation methods will need to be applied to such systems.

In the cases of periodic templates, the confinement limits the patterns to be local features repeated over the sample with a given periodicity. In the next chapter, inverse design principles and algorithms will be presented that allow the local effects of confinement to be combined with the periodic nature of post templating methods to produce locally arbitrarily complex patterns that are in principle concatenable. All the principles of commensuration with topographical features will remain important for this work, but by increasing the degrees of freedom in terms of post location while constraining how SCFT simulations are performed, a different paradigm of approaching BCP DSA is achieved where fewer simulations need to be performed in order to find the conditions necessary for a given target structure density profile.

Chapter 6

Inverse Design Simulations for Directed Self-Assembly

6.1 Introduction

For the cases of BCP directed self-assembly (DSA) presented in the previous chapter, structures that were obtained were generally periodic in nature and required either an experiment or simulation to determine the morphology the BCP would self-assemble into at a given set of topographical conditions. For periodic patterns this "forward" approach is fine as the underlying pattern and template generally have similar symmetry and thus optimization of the DSA template amounts to finding the proper commensuration conditions. For more complex patterns needed in integrated circuit (IC) technologies where local bends, junctions, and terminations are required in the pattern[6,17], the complexity of the DSA template required to template the BCP to form such structures precisely becomes complex as well[1]. In such systems, simply varying post pitch distances and post size is no longer straight forward since each local feature requires a special arrangement of the template to ensure reproducibility and this arrangement changes depending upon the neighboring features that themselves have special templating requirements. Thus the problem of identifying the required DSA template for a given target structure cannot simply be done through screening many potential forward simulations but requires a more focused approach.

In this chapter, two distinct approaches to this problem of inverse template design will be explored. In the first method, a simple template type is chosen as a basis for DSA that can have individual features changed locally[201]. By then constraining the system to where these local features can be changed, design rules for the various features of terminations, bends, and junctions are developed using a tile based system. Effects of

neighboring tiles affecting the formation of key features are analyzed through reproducibility statistics and free energy analysis in simulations. These design rules show good promise for making simple IC patterns, but further optimization of the design rules is necessary for the method to be generally applicable.

The second method uses an optimization algorithm that takes in a target structure and outputs a potential DSA template solution to obtain the structure based on input constraints that solution should satisfy[50]. This inverse design algorithm uses the established methods of SCFT as the basis for optimizing and verifying the template solutions. Energy minimization and target structure fidelity functions are used as optimization criterion in the simulations to guide the algorithm with a Monte Carlo (MC) like process. Since there are multiple solutions that satisfy the necessary criterion for the target structure, a single solution may not be the best solution for all criteria that can be optimized so simulations are run multiple times with different initial post configurations to account for degenerate energy solutions. By optimizing all these parameters that describe what the final templated solution should satisfy, other simulation parameters such as volume fraction, χN, post size, and number of post template features can be optimized as well to find the best solution template that yields the target structure reproducibly[51]. General design rule principles can be derived from the solution templates as well besides just using the algorithm itself to design template features for an arbitrary pattern. An overview comparison between an inverse design approach and forward direct method for DSA is shown in Figure 6.1.

Both the design rule approach and inverse design algorithm approach is verified experimentally using PS-PDMS cylinder forming BCPs with PDMS functionalized HSQ posts. The experimental verification shows the methods indeed allow for the production of complex IC patterns and as long as the simulation method parameters or design rules are optimized the methods allow for very precise control of local features in BCP DSA. In this chapter, the design rule approach will be examined first for a system using square arrays of PDMS functionalized HSQ posts and their reproducibility be examined in terms of free energy SCFT simulations. Next the inverse design algorithm will be presented in terms of how the algorithm works with various nuances of the implementation in the context of

SCFT simulations. Results for different target structures using the inverse design algorithm will be presented and compared with experimental verification as appropriate. Finally, future algorithm modifications will be discussed to make the algorithm faster, optimize more parameters per simulation, and yield target structures with higher reproducibility.

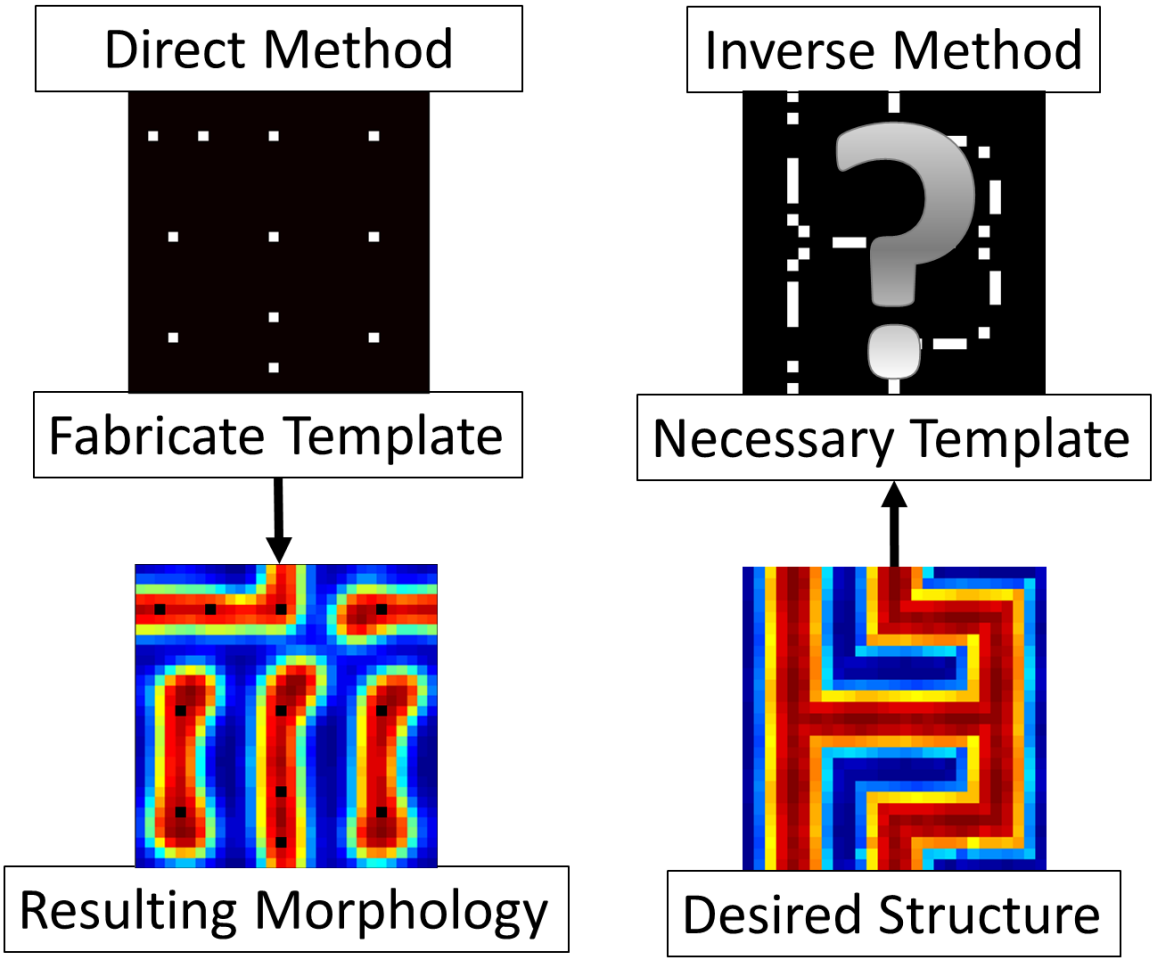

Figure 6-1: Comparison of forward direct method of DSA (left) with inverse design method (right). In the direct method, a template with a set of features is fabricated first experimentally or as boundary conditions for a simulation. The experiment or simulation is performed and the resulting morphology observed and characterized to gain insight into how the structures formed. In the inverse method, the desired structure is created using density fields in the context of the SCFT framework. This structure is then used in the inverse optimization algorithm to find a solution of template feature positions that represent the necessary template to produce the desired structure. Design rules can be extracted from either method[50].

6.2 Design Rule Approach

In order to use DSA of BCPs to produce arbitrarily complex patterns needed for IC applications, the template needs to be designed in a way that is simple compared to the final complex pattern and yet contain all the key information necessary for the BCP to assemble into a complex pattern without being a direct copy of the final pattern. In the design rule approach, a simple HSQ post template with square symmetry is chosen based on the current simplicity of electron beam lithography (EBL) to write such patterns[201]. By replacing individual posts with sets of double post template features, lines, bends, and terminations formed by the BCP are all able to be selectively placed in locally desired positions on the substrate with a simple set of design rules. These different post templates are grouped into four tile combinations used to generate different combinations of complex line and bend patterns. Reproducibility of these features is examined both experimentally and through simulation free energy studies based on observed defect structures.

In general, to form aperiodic features of bends, lines, terminations, and junctions from BCPs, an aperiodic template is necessary. Other work has demonstrated the formation of arrays of bends, T-junction, and jogs as well as isolated features all forming from a PS-PMMA lamellae forming BCP templated by chemical patterns[17,202] or for PS-PDMS cylinders forming BCPs templated by HSQ posts[1]. In these cases the templates were simply intuitive one-to-one templates that essentially could be considered just directly writing the final pattern. Thus for practical implementation the template features need to be constrained to be simple enough that there is an actual benefit to using the template to direct the BCP self-assembly rather than just directly writing the final pattern.

In the approach presented here, square arrays of HSQ posts produced by EBL are used as the basis for the DSA of the BCPs. These experiments were performed by Jae-Byum Chang and Hong Kyoon Choi. A 45.5 kg/mol PS-PDMS BCP is spun cast onto these substrates and solvent annealed to an equilibrium morphology that is reactive ion etched to remove any PDMS top surface and PS matrix leaving an oxidized PDMS pattern. The center to center spacing distance between posts is commensurate with the natural cylindrical period L_0 of the BCPs used such that a monolayer of cylinders forms over the

post grid with lines oriented randomly in either the P_x or P_y direction with a combination of termination and bend defects to account for changes in the direction of the cylinders. Scanning electron microscopy (SEM) images of the results of the DSA of commensurate square array of posts showing these cylinders is shown in Figure 6.2 along with an inset image of the square array of posts used to template the BCP. From this result, the goal for implementing design rules is to alter the initial plain square array to selectively control where the bends, lines, and terminations occur and how they are oriented. By altering the grid by selectively replacing certain posts with a set of double posts features, the design rules are developed. The final pattern produced has an increased throughput of areal features since the template post features only occupy a fraction of area of the final pattern.

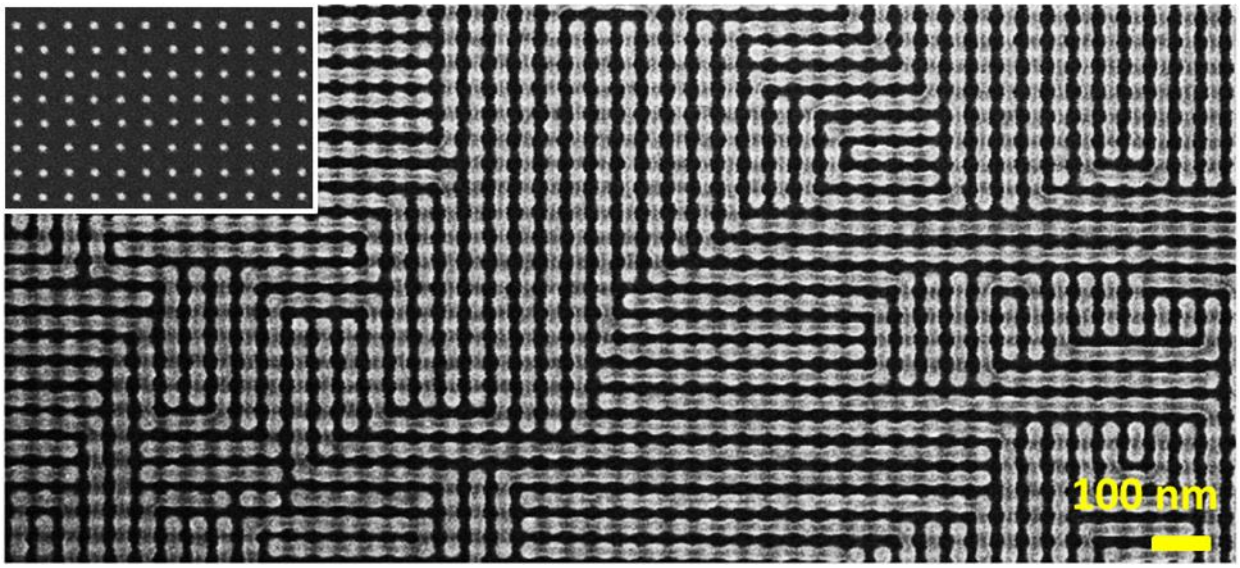

Figure 6-2: SEM image of PDMS cylinders that self-assembled on an array of square symmetry HSQ posts functionalized by PDMS brush. Orientations were equally random between P_x and P_y directions with bends and terminations appearing where directions changed. The natural period of the cylinders is L_0 = 39 ± 2 nm. Inset is an SEM image of the HSQ square post array used in the DSA of the BCP with spacing $P_x = P_y = L_0$, h_{post} = 28 ± 1 nm, and D_{post} = 10 ± 1 nm. Yellow scale bar in lower right corner is 100 nm for both inset and SEM image[201].

The way the double post features were added to the square grid to allow for the development of design rules and how these design rules were defined is shown in Figure 6.3. To make controlled patterns manageable, the grid of square input features is broken up into tiles containing three by three arrays of square posts with the center post being

replaced by a double post either oriented along the P_x or P_y direction as shown in Figure 6.3.a. In addition to the square lattice being divided as tiles, design cells defined by four neighboring double post features forming a square were defined as shown in Figure 6.3.a as well. Having this layout, design rules based on experimental and simulation studies of how BCPs self-assemble on closely spaced double dot features were used to develop local design rules shown in Figure 6.3.b and for the four non-degenerate combinations of tile features under symmetry operations as shown in Figure 6.3.c through Figure 6.3.f. Experimental results for these different tiles are shown in Figure 6.3.g through Figure 6.3.n.

In order to distinguish the four unique design cells, a notation for the orientation of the double posts in the corners was introduced. Going from upper right to upper left to lower left to lower right, the double posts are labeled as $A_1A_2A_3A_4$ where A is the alignment direction and denoted as X if aligned along the P_x axis or Y if aligned along the P_y axis. This gives the notation for the four unique design cells as $Y_1Y_2Y_3Y_4 \equiv Y^4$, $X_1X_2Y_3Y_4 \equiv X^2Y^2$, $X_1Y_2Y_3Y_4 \equiv XY^3$, and $Y_1X_2Y_3X_4 \equiv$ YXYX. The experimental results shown in Figure 6.3 were the most common observed patterns for each design cell. These most common patterns agreed with those predicted on the basis of the design rules. However, for the YXYX cell, the predicted pattern never agreed with the observed pattern and there were many degenerate patterns observed. The likely reason for these observations were the high symmetry of terminations in the predicted pattern that are energetically unfavorable compared to just lines forming across the posts. Thus usually only one termination formed at most in these particular cells and lines or bends accommodated the rest of the pattern. Since there was no predictability or reproducibility with the YXYX pattern, the design cell should not be included in forming target structures.

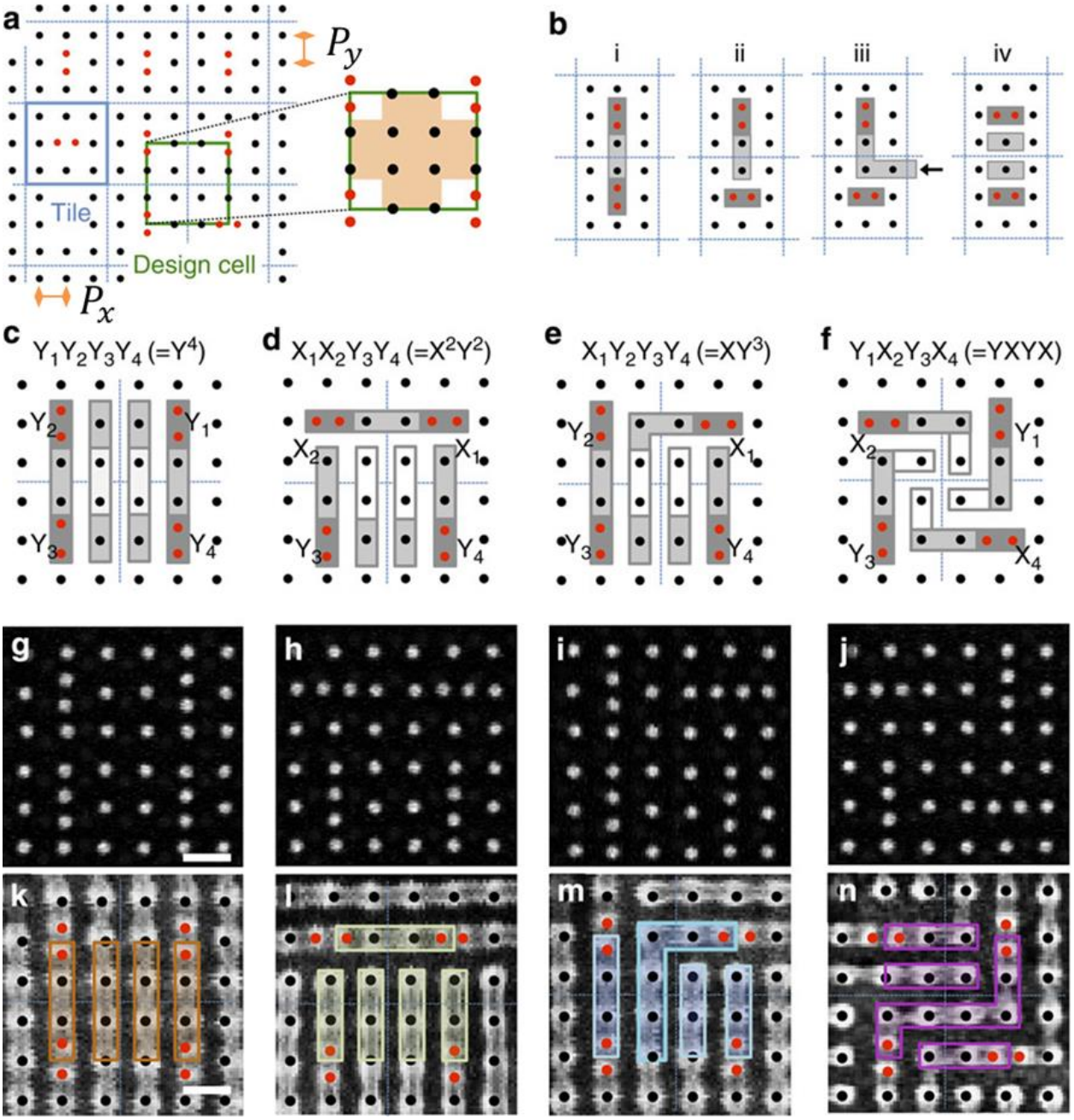

Figure 6-3: (a) Layout of the square template used for developing design rules. Single posts are denoted by black dots and double posts by red dots. Tiles (outlined in blue) with three by three sets of posts were defined with the center post being replaced by a double post oriented either along the P_x or P_y direction (lattice vectors denoted by orange distances). Design cells (outlined in green) are defined by the corners of a square with the four nearest sets of double posts. For the highlighted design cell, the shaded region will be primarily templated by the double posts in that cell. For (b-f), dark rectangles represent cylinders on double posts, light grey represent cylinders templated between double posts based on basic design rules, and white rectangles represent cylinders in the center of the design cell

templated by single posts between the double posts. (b) Four basic design rules: i) Two aligned parallel sets of double posts will align cylinder along the double post direction. ii) & iii) A double post perpendicular to a neighboring double post will either yield a termination or bend depending on neighboring posts. iv) Parallel double posts orthogonal to posts between them have cylinders align in their direction between them. (c-f) Four different design cells schematics with predicted patterns using design rules from (b). (g-j) SEM images of post templates used for the four different design cells. (k-n) SEM images of the results of BCP DSA where PDMS cylinders formed predicted patterns except in the case of (n) where the symmetry constraints where too energetically unfavorable to form the predicted structure with four terminations. Schematic colored overlay highlighted the cylinder patterns. Scale bars for SEM images are 50 nm[201].

Demonstration of the design rules to form a given complex pattern was done for two design patterns as shown in Figure 6.4 with both containing a mix of terminations, lines, and bends. The predicted morphology made by concatenating various design cells in compatible ways is shown in Figure 6.4a-b using the design rules. Only Y^4, X^2Y^2, and XY^3 design cells were used in these patterns. The HSQ post arrays used for these patterns are shown in Figure 6.4.c-d. The resulting experimental results of PDMS cylinders are shown in Figure 6.4.e-f and agree with very high yield with 97% of the grid points agreeing in the left sample and 99% in the right sample. SCFT simulations were done showing that the predicted pattern was indeed a saddle point solution to the SCFT conditions meaning the structures formed here are local equilibrium structures at best (global minimum structure verification for such large systems is hard to demonstrate since each grid area contributes only a fraction of the total free energy). These SCFT results are shown in Figure 6.4.g-h. The high grid point yield of the experimental results and agreement with the SCFT and design rule results suggests that the design rule approach can be very powerful in making various target structures. The only drawback of the approach is that there is a finite combination of concatenable design cells that have compatible boundary conditions and thus general structures are not possible. Such structures either require a different set of design cells that have more possible motif features to access all possible combinations of generated structures or allowing arbitrary locations of the post motifs. Such arbitrary position allowance will be discussed in the context of the inverse design algorithm in the following sections.

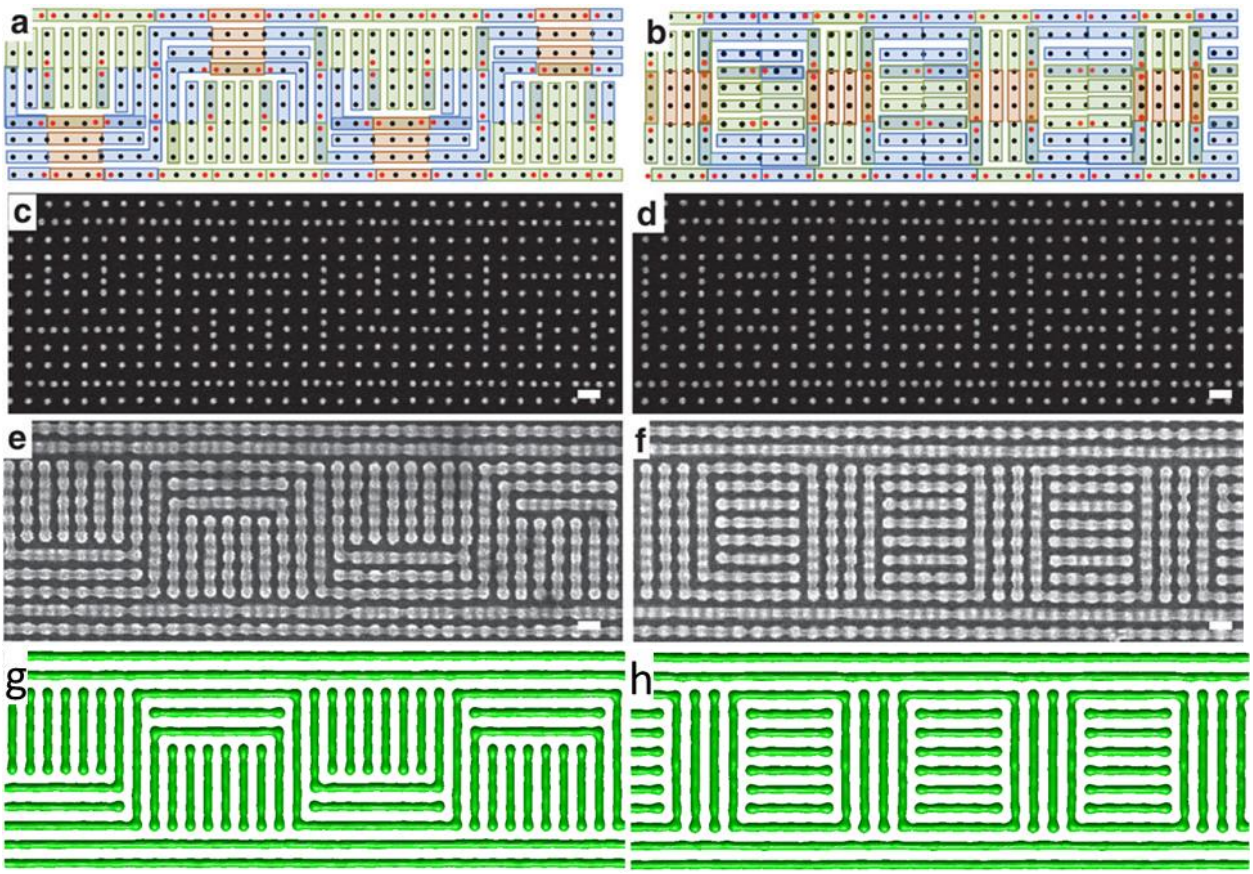

Figure 6-4: Demonstration of design rule approach using two design structures. (a-b) Design structure layout made from concatenation of different design cells (color coded). (c-d) SEM images showing the HSQ post templates used for making the design structures in (a-b). (e-f) Experimental result SEM images showing the PDMS cylinders self-assembled on the HSQ post template from (c-d). Structure in (e) had 97% grid points match the design pattern and structure in (f) had 99% of the grid points match the design pattern. (g-h) Simulation results of design structures showing $\phi = 0.5$ density isosurfaces that were verified through SCFT calculations to be saddle point solutions and thus consistent that the design patterns are indeed equilibrium solutions. Scale bars shown here are 50 nm[201].

For the SCFT simulations performed here, boundary conditions with concatenated design cells were used as shown in Figure 6.5. The boundary conditions used had the surface layers preferential to PDMS with $\mu_A = -\mu_B = W_{BL} = -5$ and pressure field conditions for the posts with $\mu_A = \mu_B = P = 20$. The top surface layer was constrained to be preferential to PDMS as well based on observations of the formation of a PDMS wetting layer. The grid cells used were of size N_x by N_y by N_z with these values varying depending on how many design cells were concatenated. The grid size at the coarse-graining used had a single post area consist of N_x by $N_y = 9$ by 9 as shown in Figure 6.5.a-b. Double post

areas are also schematically shown in Figure 6.5.a-b and were also N_x by $N_y = 9$ by 9. $N_z = 20$ to correspond to roughly $2L_0$ thick films observed in experiment. 9 grid points corresponded to L_0. Two post sizes were considered to best match the post diameters used in experiment with one having a single grid point for the pressure region surrounded by 8 grid points for the brush layer region and the other having a 3 grid point diameter (5 total grid points in a cross shape) surrounded by 16 grid points for the brush layer region. In real units these correspond to an ≈ 8 nm and ≈ 16 nm including brush layer, respectively. The experimental post diameter was 10 ± 1 nm so these tested diameters are around the range of the experimental values within the coarse graining of the simulations. Post heights were set to $0.78L_0 \cong 30$ nm corresponding to experimental observed thickness of HSQ. General simulation cells were formed by concatenating the 9 by 9 single and double post areas together with periodic boundary conditions imposed in the x and $y-$directions. A design cell simulation had at a minimum N_x by $N_y = 54$ by 54 grid points and additionally considering various reflective boundary conditions N_x by $N_y = 108$ by 108 grid points. Larger simulations thus had some multiple of these grid points. Schematics for the boundary conditions of a single XY^3 design cell with no symmetry considerations assumed is shown in Figure 6.5.c and Figure 6.5.d with the brush layer conditions and post conditions, respectively.

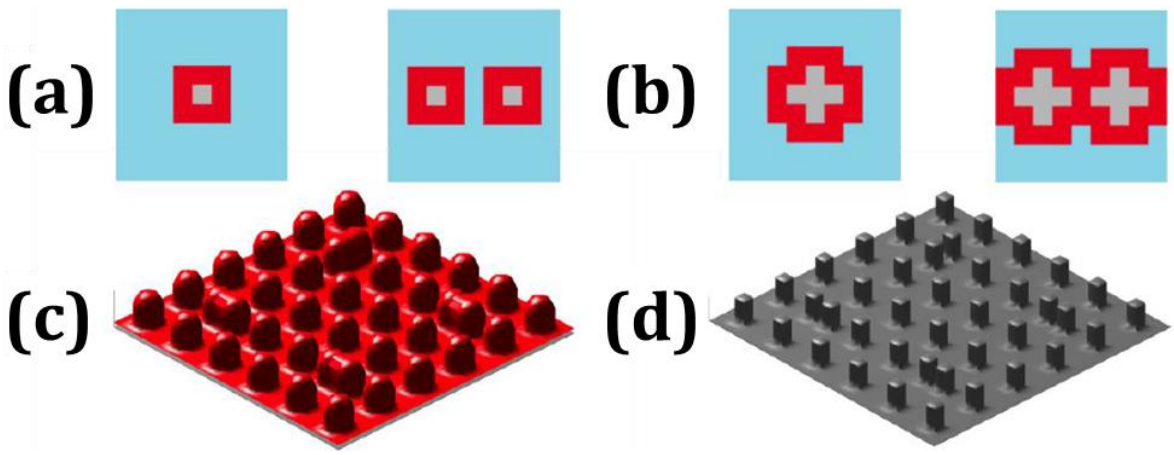

Figure 6-5: Blue regions are free of constraints, red are PDMS preferential brush layer, and grey are repulsive posts. (a) Cross-sections of the 9 by 9 grids for a single post (left) and double post (right) boundary conditions corresponding to ≈ 8 nm diameter post plus brush layer. (b) Cross-sections of the 9 by 9 grids for a single post (left) and double post (right) boundary conditions corresponding to ≈ 16 nm diameter post plus brush layer. (c) 3D periodic boundary conditions schematic of the PDMS brush layer for the XY^3 design cell with no symmetry constraints. (d) 3D periodic boundary conditions schematic of the posts for the XY^3 design cell with no symmetry constraints[201].

For these large cell simulations, defective structures formed in the simulation analogous to those observed in experiment. Thus, to make meaningful comparisons between the simulations and experimental results, free energy studies were performed. In these simulations, the results of preliminary simulations are used to make density field structures corresponding to all those observed in the experiments. The density fields are then seeded as the initial conditions in the simulations and held constant until the corresponding chemical potential fields are found such that the structure satisfies the saddle point condition. In such simulations Ω_- is relaxed first until constant followed by Ω_+ for better numerical stability. To make sure these energy studies are consistent with experimental parameters, simulations of the first design structure in Figure 6.4 considering the base repeat cells were performed over a range of volume fractions and post heights to find the optimal simulation parameters where the structure occurred. By seeding the simulations with the design structure and allowing the fields to relax, a range of volume fractions and post heights where the design structure was a saddle point solution was found and the lowest free energy post height and volume fraction values chosen for further

simulations. These values were $f = 0.36$ and $h_{post} = 0.78L_0$. These free energies are shown in Figure 6.6 and density plots are shown in Figure 6.7 as a function of f and h_{post}.

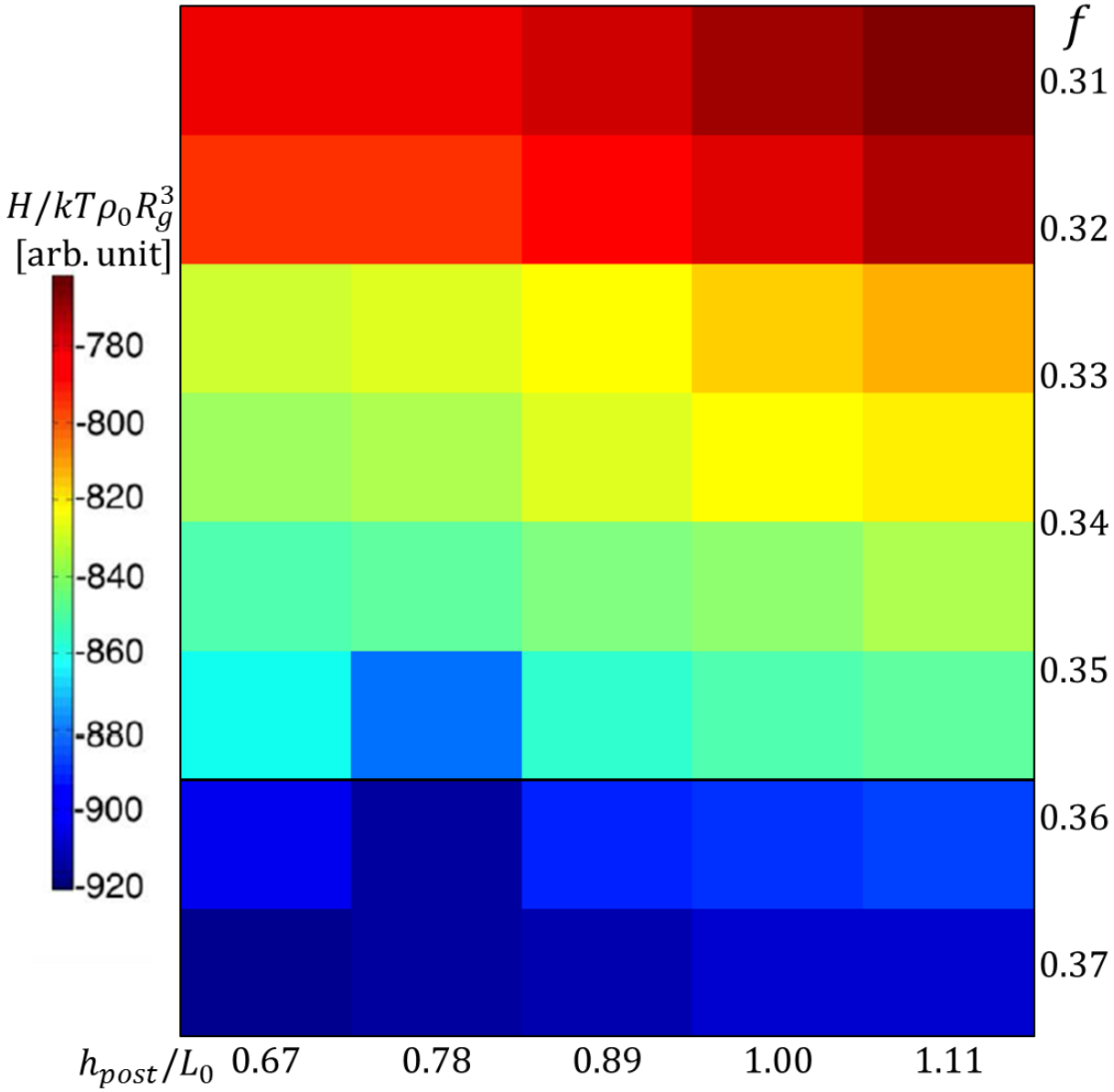

Figure 6-6: Total normalized free energy $H/kT\rho_0 R_g^3$ as a function of h_{post}/L_0 and f for the first design structure from Figure 6.4. In general, the free energy decreased with increasing volume fraction and increased with post height. The lowest free energy at the lowest volume fraction that the structure was stabilized occurred at f = 0.36 and h_{post}/L_0 = 0.78. χ_{eff} = 0.112 and N = 125 or $(\chi N)_{eff}$ = 14 for these simulations using implicit solvent annealing assumptions[201].

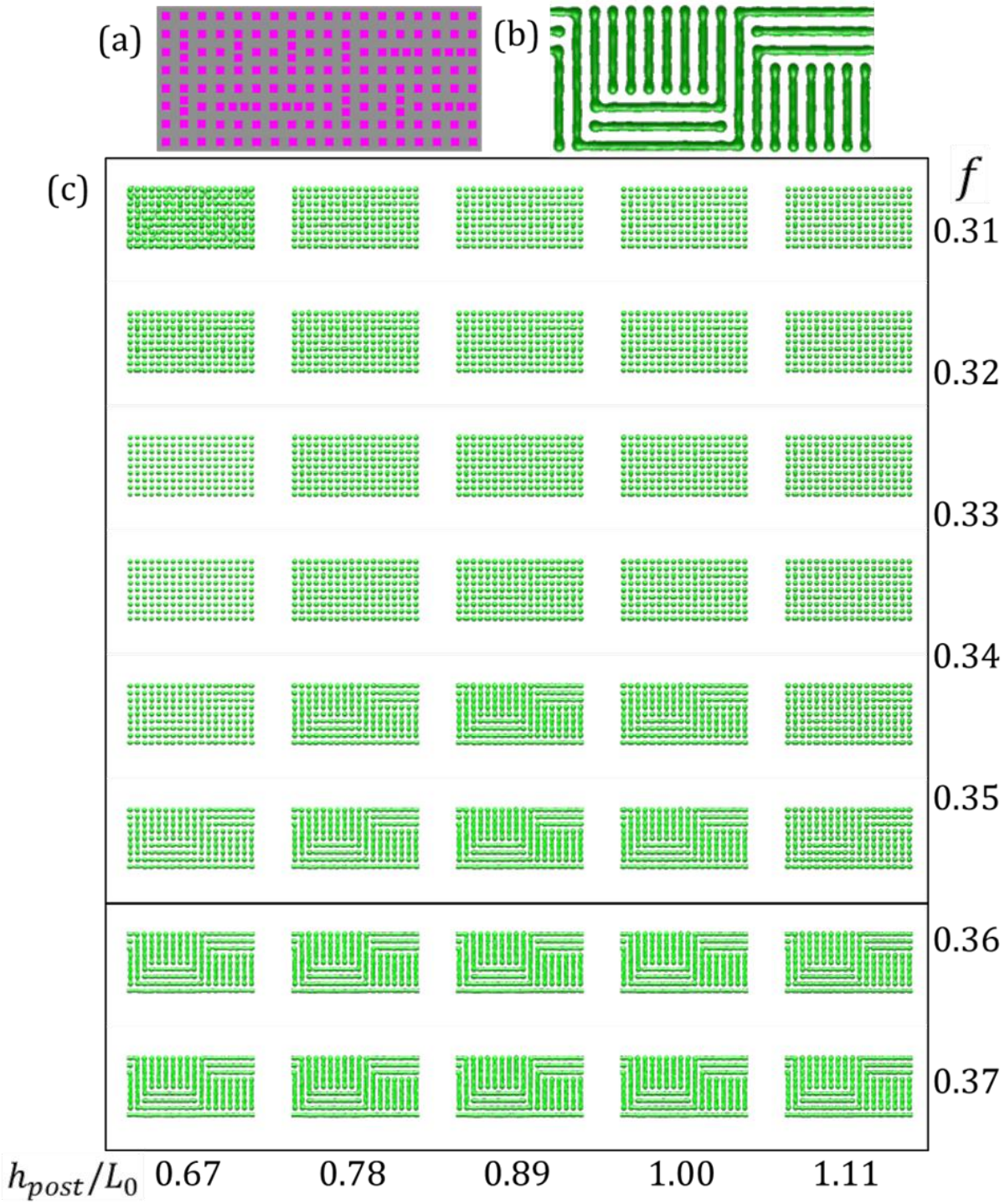

Figure 6-7: (a) Post configuration used to template base repeat unit of first design structure from Figure 6.4. (b) Design structure base repeat unit from Figure 6.4 for reference. (c) Phase diagram as a function of h_{post}/L_0 and f using first design structure from Figure 6.4. For $f \geq 0.36$, the structure remained implying the design structure was a saddle point solution at these conditions and thus a potential equilibrium structure. $\phi = 0.5$ isosurfaces are shown in green[201].

For comparing the free energies of different structures observed for the XY^3 and X^2Y^2, the 5 most commonly observed structures from experiment were seeded with appropriate internal reflective boundary conditions that were consistent between the simulations. Since the boundary conditions of the neighboring design cells influence the total free energy of the system, a consistent set of boundary conditions has to be chosen for comparison purposes and thus only the relative free energies between the structures can be compared. Schematic diagrams for these different seeded structures are shown in Figure 6.8. Each simulation cell contains nine total design cells. For the X^2Y^2 case, six of the cells are X^2Y^2 with three being reflective symmetry conditions and the other three design cells are X^4 for a buffer layer of features as shown in Figure 6.8.a. For the XY^3 case, four of the cells are XY^3 with four fold rotational symmetry with two extra being Y^2X^2 and three extra being Y^4 for buffer layers of features as shown in Figure 6.8.b. The buffer layers of features are the same across the five tested structures for each design cell type and thus will contribute equally to the free energy allowing for the relative free energies to be compared. These simulation cells are all of size 81 by 81 by 20 grid points large. The same underlying post lattice was used across the five structures in each case as shown on the left side of the Figure 6.8. The free energy of each structure was calculated holding the seeded density fields constant and letting the corresponding Ω_- field first relax and then the Ω_+ field relax. Simulation parameters were based on the optimized parameters of $h_{post} = 0.78L_0$, $f = 0.36$, and $(\chi N)_{eff} = 14$.

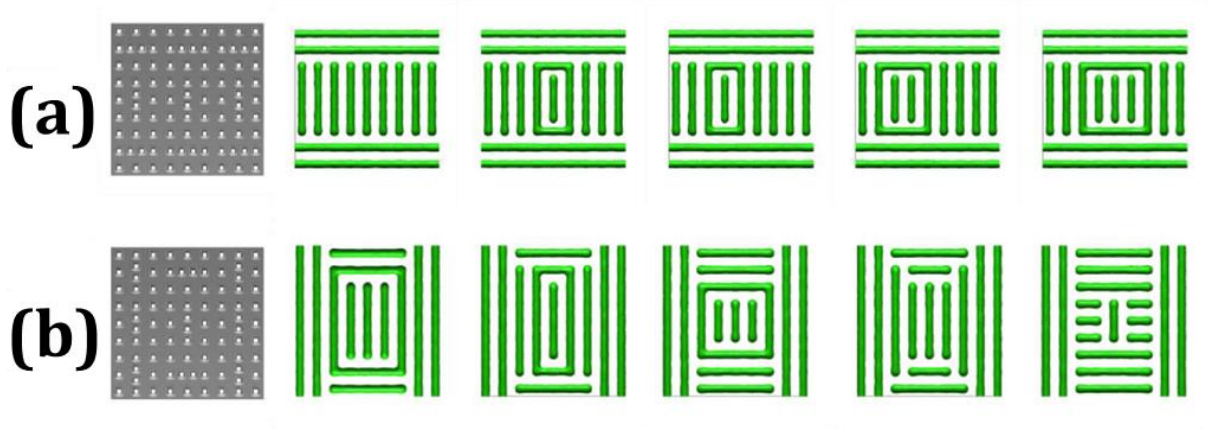

Figure 6-8: Green ϕ = 0.5 constant density isosurfaces are plotted. (a) Left: X^2Y^2 post template used for comparing free energies from SCFT simulations. Template contains six X^2Y^2 design cells with three X^4 buffer layers. Right: Five different morphologies observed in experiment for X^2Y^2 templates with appropriate symmetry considerations for reflective and rotational boundary conditions in addition to buffer layer structures. From left to right the morphology was less frequently observed in experiments. (b) Left: XY^3 post template used for comparing free energies from SCFT simulations. Template contains four XY^3 design cells with two X^2Y^2 and three X^4 buffer layers. Right: Five different morphologies observed in experiment for XY^3 templates with appropriate symmetry considerations for reflective and rotational boundary conditions in addition to buffer layer structures. From left to right the morphology was less frequently observed in experiments[201].

In the experiments, a large array of combinations of X^4, X^2Y^2, and XY^3 design cells were fabricated and BCP applied and solvent annealed on the pattern. In the resulting observations, all the X^4 simulations yielded the predicted pattern of aligned cylinders. Similar results were always observed in simulations with no alternative structures observed when seeded with random initial conditions. The X^2Y^2 and XY^3 structures had many alternative defect structures form in the experiment. The predicted structure using the design rules occurred over 60% of the time, but other structures appeared with relative commonality. The top five structures observed for each design cell correspond to the same structures seeded in the simulation from Figure 6.8. The plots of the count % for each structure and their corresponding relative free energy calculated using SCFT are shown in Figure 6.9.

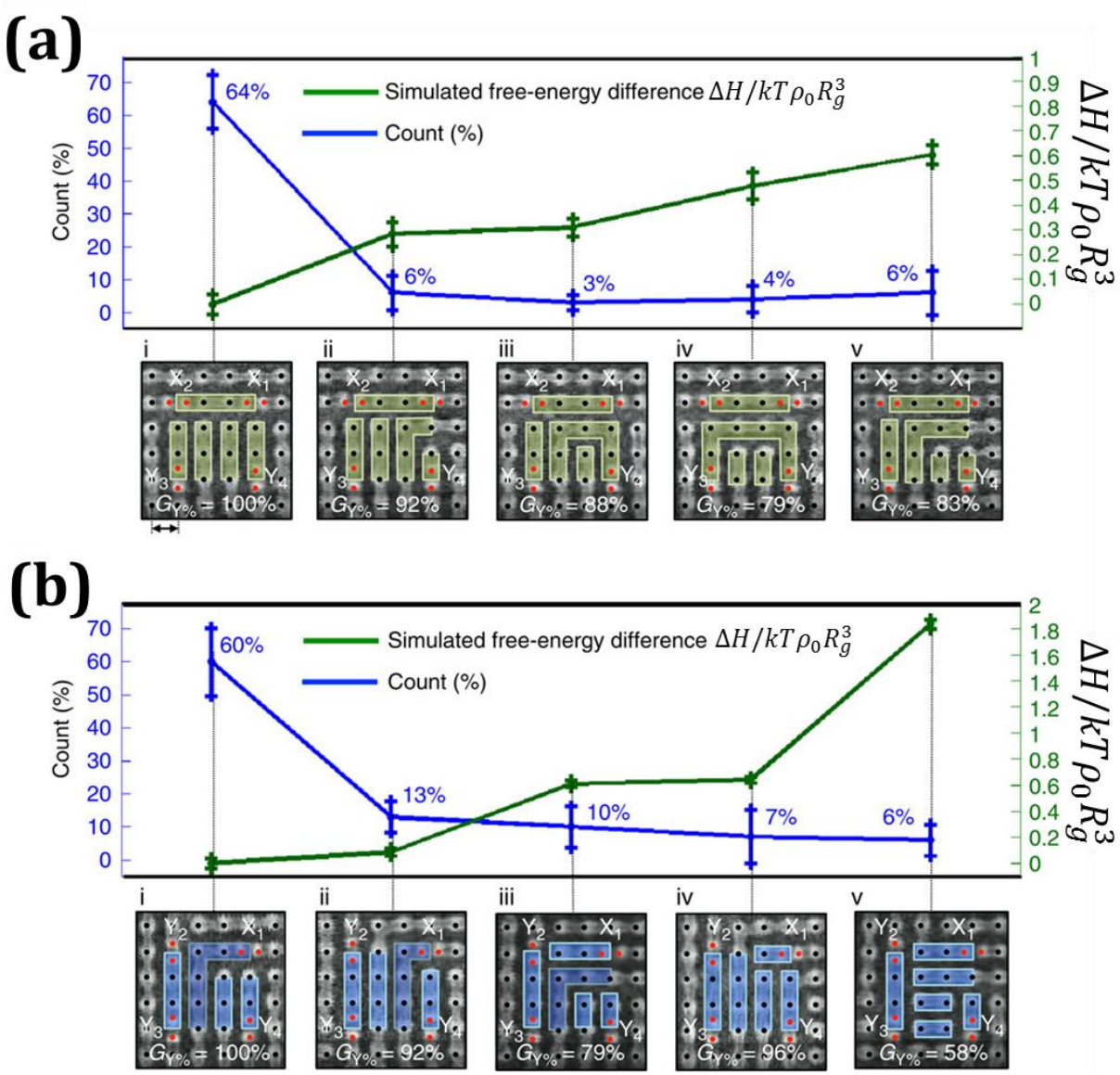

Figure 6-9: The percentage of observed design cells (Count) that formed the pattern (SEM images) shown below the count (%) plot (blue) and the free energy difference calculated from SCFT simulations using the seeded structures from Figure 6.8 (green). In general, as the free energy of the structure increased, the observed counts decreased. However, there is not a strict quantitative relationship between these values implying that other effects including neighboring unit cell effects (experiments were not strictly done with the same boundary conditions as simulations) and kinetic effects not captured in the simulations may affect the observed morphologies. $G_{Y\%}$ is the percentage of grid points in the design cell that had the same connections based on the design rules. Error bars are ± 1 standard deviation. (a) X^2Y^2 design cell results. (b) XY^3 design cell results[201].

The general trend between the count % and the free energy of the structures observed is that the most commonly observed structures had the lowest relative free

energy and increasing the free energy resulted in much lower observed counts. However, although the general trend is observed, there is not an exact quantitative relationship between the values. This implies that the most commonly observed structures are likely equilibrium structures, but that other factors influence the local final morphology whether that be different boundary conditions, kinetic effects not captured in the simulations, fluctuations in film thickness, or explicit details of the solvent incorporation. The simulation parameters may not be exactly optimized as well for exact correspondence. Still, the evidence from the trend is that thermodynamic considerations are the main driving force in the structure formation.

The design rules presented here demonstrate the ability to form complex patterns necessary for IC patterning applications. Still, the three design cells demonstrated with high reproducibility have their own limitations. Three and four way junctions were not produced in any of the design cells identified. However, three-way T-junctions were observed when a defect occurred due to a missing post as shown in Figure 6.10. The limitations of the current design rule approach are due to the post template being limited to square array geometry with only two kinds of motifs, single and double posts. To address general pattern design, allowing posts to be located anywhere on the substrate should allow for any generally complex pattern to form within the limits of IC pattern design. In the next section, an inverse algorithm that uses such a general post template condition will be introduced that allows for the determination of the post template required to obtain a given target structure with all possible IC pattern features.

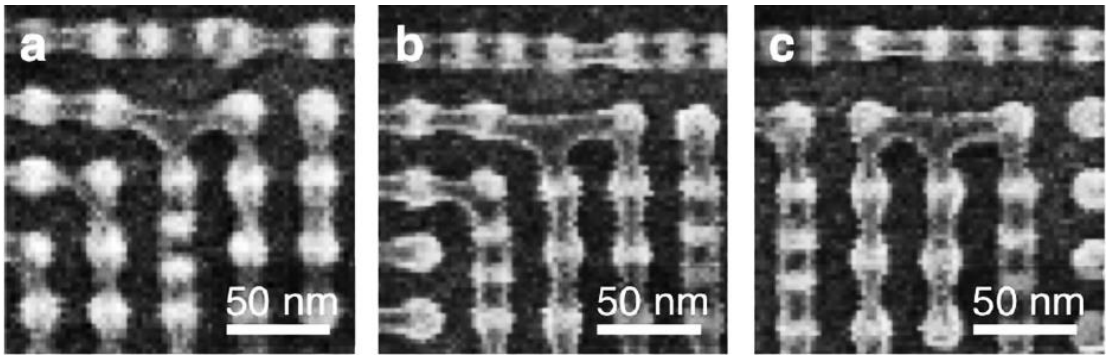

Figure 6-10: Three-way T-junction formation examples. In general, these features were observed only when a single post was missing. (a) Post was missing two grid points above double post. (b) Post was missing two grid points above and one right of double post. (c) Post was missing two grid points above and one left of double post[201].

6.3 Inverse Design Algorithm

To examine the possibilities of general BCP DSA with brush functionalized post motifs, an inverse design algorithm in an SCFT framework was developed that finds the topographical template needed for a desired target pattern through a random optimization algorithm akin to a MC algorithm. Time spent scanning large parameter spaces using forward simulations or experiments is reduced tremendously using this algorithm and is best suited for systems where the final pattern needed is already determined but the DSA template to produce that pattern is not known.

Other self-assembling systems have been explored through inverse design processes, such as Torquato and others investigating colloidal self-assembly and using an inverse design process to find the intercolloid potential that allows the colloids to form a particular symmetry pattern and be a free energy minimum state[203,204]. Only recently has the inverse design problem been examined in BCP systems, initially in simple systems such as designing holes for contact vias through a process of determining the template size necessary to get proper hole number, size, and distribution.

Aside from this recent work on determining the templates required for making contact vias and bends in specific locations[72,205,206], there has been limited study of the inverse problem for BCP DSA. There is great utility in using an inverse design method in BCP self-assembly for general applications besides just enhancing nanolithography DSA systems, as the method makes template and material synthesis more efficient, renders feasible solutions for implementation and testing, and can enable the creation of heterogeneous and hierarchical mesocale materials. The recent advent of inverse design algorithms allows the determination of the spatial configuration of post or chemical template motifs to obtain a target pattern[50,207]. In the method presented here[50], topographic post motifs attractive to one of the blocks in a diBCP system are seeded in a target structure and a stochastic minimization algorithm determines the optimal positions of the posts. Compared to the design rule approach in the previous section[201], the posts can occupy any point in space on the template substrate rather than being confined to a square lattice allowing for general structure formation.

For general target structures, there is no *a priori* guarantee a set of f, χ, and N for the BCP will be able to self-assemble into a given target structure with a DSA template. In essence, in order to guarantee a DSA template solution exists these parameters need to be optimized as well in addition number of posts n_{posts} and the position of those posts. The parameters can be guessed approximately if the density of post features needed for a target structure can be deduced based on the area fraction of the target pattern, but this may not always be intuitive. If guessing is not an option, the better method is to scan a range of parameters and find where the inverse solutions optimize a set of conditions the target structure solutions should satisfy.

For the inverse design algorithm, the system consists of a fixed number of topographical posts n_{posts} with diameter d and if a 3D system were examined height h. These posts are seeded with random initial positions $R_i = \{x_i, y_i\}$ for the ith post on a 2D grid of size N_x by N_y defined by the size of the target structure being investigated. These posts motifs are made to model experiment posts made from HSQ or carbonized PMMA produced from EBL functionalized with hydroxyl terminated homopolymer of PS or PDMS[49,56–58,60,201]. A schematic diagram of four different post sizes used with different coarse-graining is shown in Figure 6.11. The smallest of these posts corresponds to 3 by 3 grid with the center point being the hard post feature and the surrounding 8 grid points being the brush layer constraints. The post feature size thus corresponds to $L_0/9$ as the coarse-graining in the simulations had L_0 assigned to 9 grid points, and accounting for the brush layer is roughly $2L_0/9$ considering the brush layer only adds an effective half a grid point in size since the density fields are allowed to evolve in those regions and thus the entire grid point volume is not considered brush layer but some is considered the appropriate BCP block. The larger posts shown were tested in forward experiments only, but in principle can be used in inverse studies explicitly with the appropriate constraints that they not be allowed to overlap for different post configuration moves. The post field constraints consist of $\mu_A = \mu_B = P = 20$ for the central hard part of the post to keep the evolving polymer density ≈ 0 while the brush layer region has a fixed preferentiality of $\mu_A = -\mu_B = W = \pm 5$ depending on if the posts are preferential to the majority B block or

minority A block, respectively. This brush layer condition leads the appropriate block density to have a value ≈ 1.

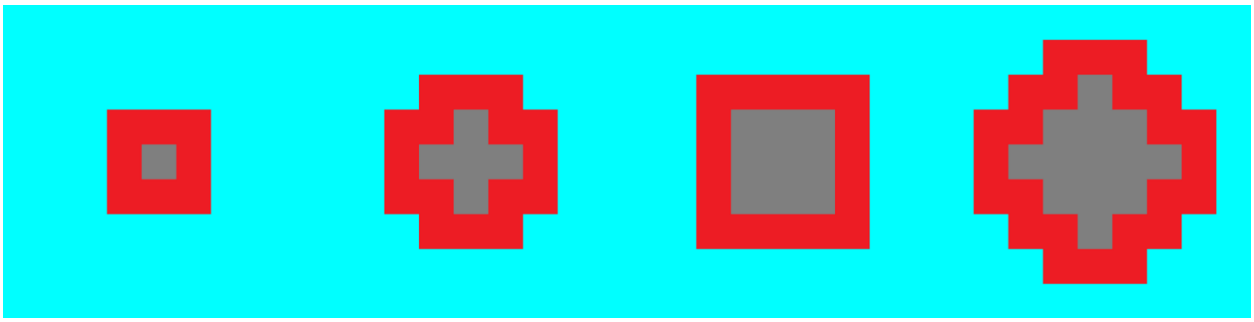

Figure 6-11: Four different post sizes used in simulations. Going left to right: Post consists of 1, 5, 9, and 13 total grid points (center grey region) surrounded by a brush layer consisting of 8, 16, 12, and 24 total grid points (red outer region)[51].

In the simulations, the main model parameters were χ, N, and f. The experimental system the model was tailored towards was a 45.5 kg/mol PS-PDMS BCP with $f = 0.335$ forming cylinders in the bulk studied previously[57–60,201]. 2D simulations are performed here for the initial demonstrations of the algorithm, although in principle 3D simulations can be done under constraints of choosing an appropriate post height. An initial guess volume fraction of $f = 0.44$ was chosen to correspond to the area fraction of features observed in experiment, but this value was later optimized depending on the target structure and solvent annealing conditions. $(\chi N)_{eff} = 14$ to correspond to the effective value encountered during solvent annealing under the coarse-graining used in the simulations. This effective χN considers the effects of the solvent reducing the bulk χ value in proportion to the incorporated solvent volume fraction and coarse-graining of the chain[59,117].

The steps in the inverse design algorithm are now outlined. The criterion defined as representing an inverse solution is a configuration of posts under the constraint of the seeded target structure that minimizes the free energy of the system. Thus the algorithm will seek to systematically change the post configuration until one that minimizes the free energy of the system under the target structure constraints is found. The steps in the process are shown schematically in Figure 6.12 with an example target structure denoted TS1. The steps described here are particularly for 2D systems, but in general can be applied

to 3D systems as well using a different post movement scheme if full 3D DSA conditions are to be examined rather than just posts confined to a 2D substrate with a fixed height.

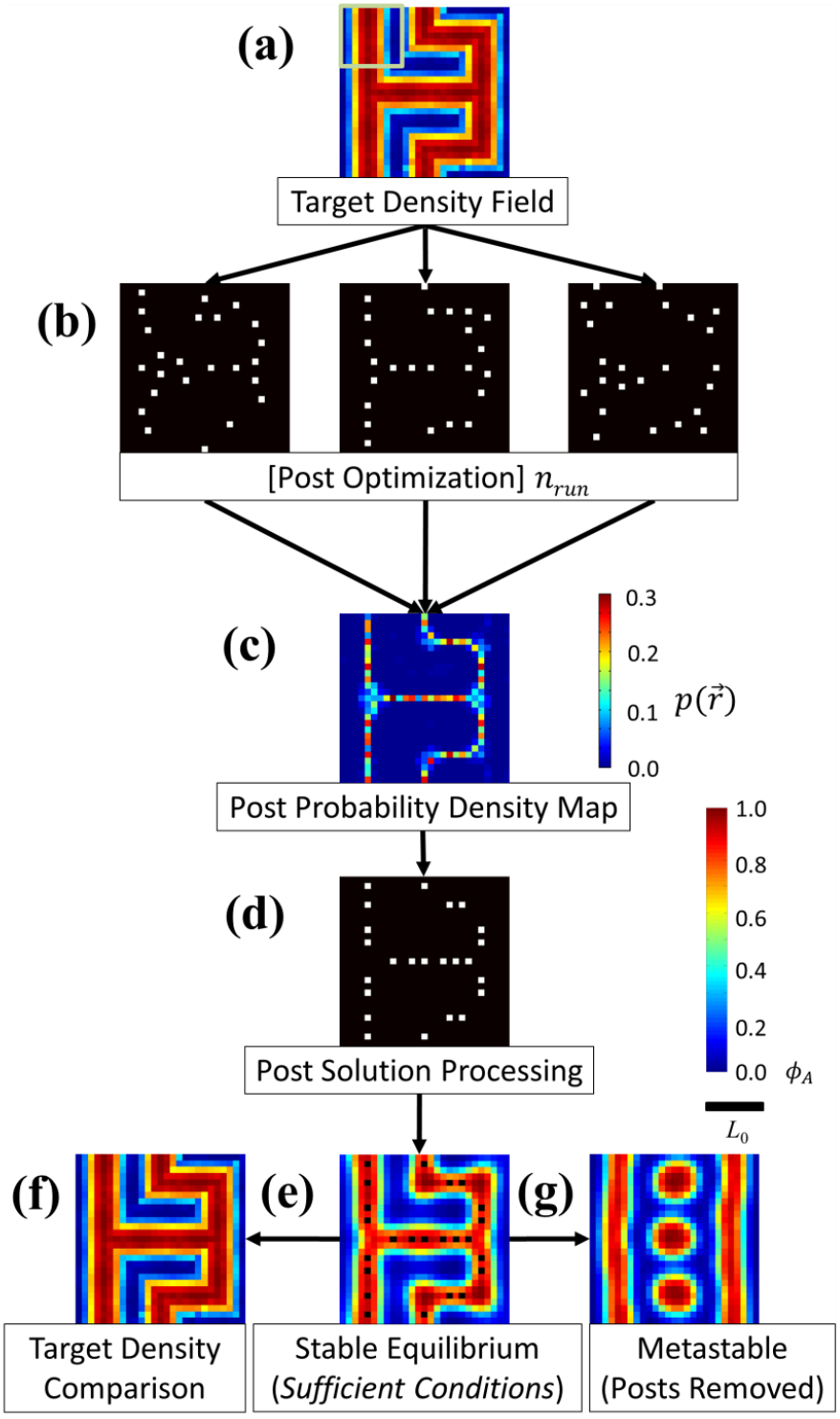

Figure 6-12: Summary of the inverse design algorithm with simulation results of a given target structure that has three-way junctions and bends. L_0 scale bar and ϕ_A density color

bar are on the right side of (d). (a) Target structure density field used to initialize inverse simulations. The green box outlines a primitive cell area used in developing target structures for IC patterns. (b) Three separate post configuration solutions found during n_{run} = 2,100 inverse simulations. (c) Statistically weighted post probability density map $p(\vec{\mathbf{r}})$ calculated using results of n_{run} = 2,100 inverse simulations with color bar of $p(\vec{\mathbf{r}})$ values on the right. (d) Inverse solution found using n_{posts} = 24 to set threshold on $p(\vec{\mathbf{r}})$. (e) Final structure obtained using (d) as post configuration for a forward SCFT simulation with random initial conditions demonstrating the *sufficient conditions* of the inverse design algorithm solution are met as the solution has correct topology of the target structure. (f) Original target structure from (a) reshown for direct comparison with (e). (g) Forward simulation result starting with solution in (f) and then removing posts allowing fields to relax demonstrating the target structure is not a saddle point solution without the posts and thus the posts are necessary for the target structure to form[50,51].

Target structures in the simulations are initialized using density field solutions of small primitive cells. In the cases studied here, N_x by $N_y = 9$ by 9 primitive cells with dimensions L_0 by L_0 were made from an initial forward SCFT with only periodic boundary conditions such that the solution formed a line structure in 2D. Larger cells for more detail can be used in future work at the cost of computational efficiency. The ϕ_A and ϕ_B densities of this structure was then used to develop all the potential local features that could be concatenated in IC circuit patterns including lines, terminations, bends, three-way junctions, four-way junctions, and isolated dot features. For the studies here, four-way junction and dot features were not explicitly included in target structures and thus should be examined in future work. To characterize the volume fraction at which these different features all occurred, energy calculation simulations were performed seeding the SCFT simulations with the density fields of the component features with appropriate reflective or rotational boundary conditions accounted and holding those density fields constant to get the corresponding chemical potential fields to calculate the free energy at that volume fraction. Plots for four different feature types are shown in Figure 6.13 along with the f that minimized the free energy. Since the unit cell size had an odd number of points and the Kuhn monomer sizes for the PDMS and PS were different, line patterns were minimized slightly less than $f = 0.5$ due to these assymetries. Using an even grid and equal Kuhn segment lengths should have lines with minimum energy at $f = 0.5$.

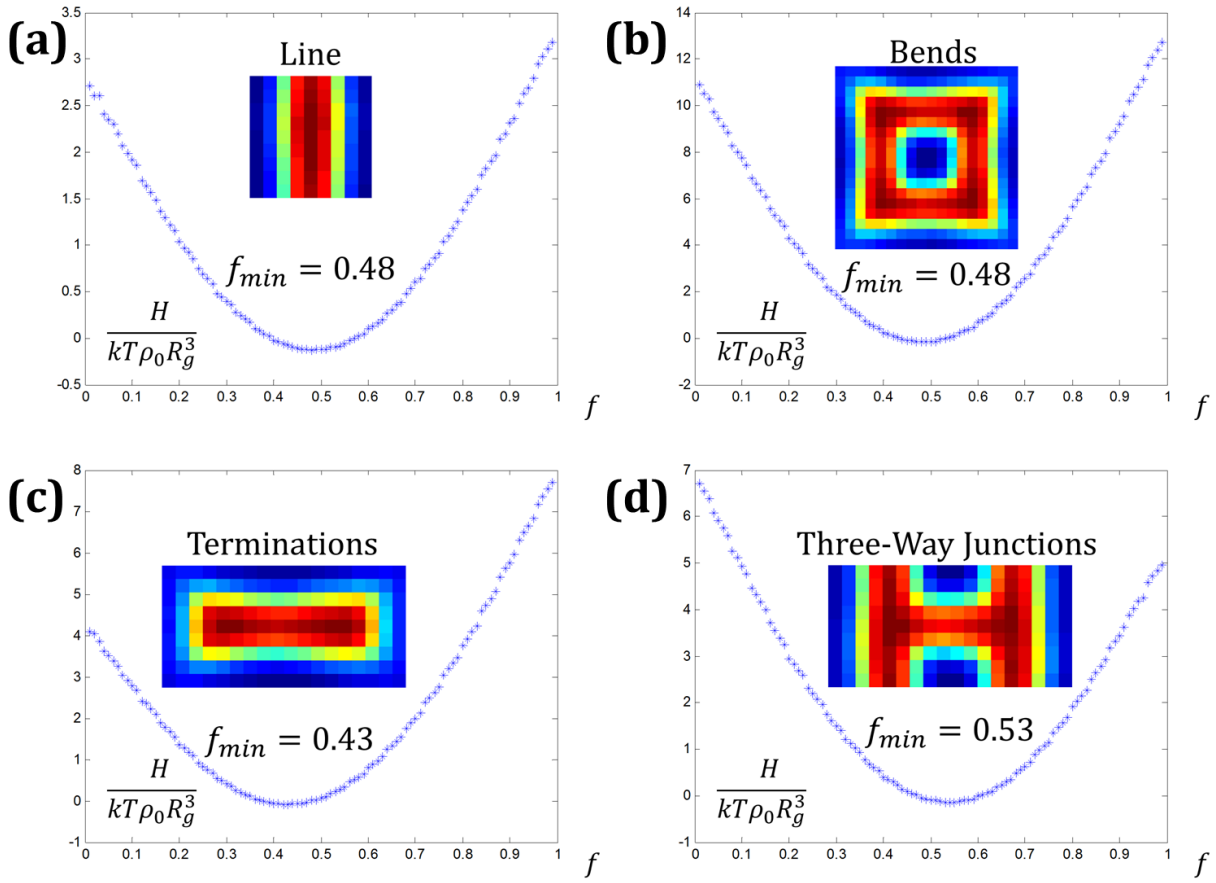

Figure 6-13: Free energy curves as a function of volume fraction for four essential IC features when coarse-grained to a 9 by 9 grid. (a) Line patterns have a free energy minimum at f = 0.48. (b) Bend patterns (with reflective and rotational symmetry accounted in an 18 by 18 unit cell) have a free energy minimum at f = 0.48. (c) Termination patterns (with reflective symmetry accounted in an 18 by 9 unit cell) have a free energy minimum at f = 0.43. (d) Three-way junction patterns (with reflective symmetry accounted in an 18 by 9 unit cell) have a free energy minimum at f = 0.53[51].

The f values at which the minimum free energy occurred make intuitive sense. Line and bend structures should be very close to $f = 0.5$ since the features should have equal amounts of area for connected space. The values did not exactly equal 0.5 for the asymmetry reasons previously mentioned. For terminations, the observed $f = 0.43$ makes sense as terminations take up less volume in the minority features. Similarly, three-way junctions having $f = 0.53$ higher than the line and bend pattern minimum f makes sense as more minority volume is needed to make the junctions.

Using only these different base IC pattern features, all tested target structures were developed such as TS1 in Figure 6.12.a with four bends, three lines, and two three-way junctions. Having a target structure developed, the system is then seeded with a fixed number of posts n_{posts} with a random spatial configuration to ensure the final configuration was not biased by the initial conditions. For TS1, $n_{posts} = 24$ is shown. The number of posts used is either chosen based on the expected density of posts needed to get the overall target structure close to the free energy equilibrium minimum volume fraction accounting for all feature types present or can be scanned through multiple values and compared to find which result yields the best target structures by additional characterization criteria. Since the algorithm uses the free energy as the way of sampling the post configurations and each post in the system adds energy to the system that is not exactly constant due local interaction effects, different n_{posts} configurations cannot be compared directly in a single simulation and thus must be examined separately.

Having been initialized, a single inverse simulation was carried out as follows. A forward SCFT simulation was performed with the initial post configuration and densities held constant until the chemical potential fields were relaxed which took $n_{iter} = 250$ normal iterations. The free energy H/kT was then calculated as follows

$$\frac{H}{kT} = \frac{\rho_0 R_g^3}{N}\left(\int d\vec{\mathbf{r}}\left((2f-1)\,\Omega_- + \frac{\Omega_-^2}{\chi N} - \Omega_+\right) - V\ln(Q[\Omega_+, \Omega_-])\right)$$

which was previously defined in Chapter 2 for diBCP systems. This value of the free energy is then kept as the free energy of the initial post configuration, H_0.

For finding a solution post configuration, a simple stochastic random walk algorithm is performed as follows. Each post with label i is cycled through n_{scan} times. When each post is selected, that post is moved in a random direction and distance determined by a random number generator with a maximum move distance $d_{movemax}$. If the position the post would move to is already occupied by a post (including brush layer area), a new position is selected until a valid move is found. After being moved, a new forward simulation holding the density fields constant over the new post configuration is performed. The free energy is calculated for this new configuration and the index j here

represents the jth complete inverse calculated energy such that H_j is calculated. This H_j is the compared with H_0. If $H_j < H_0$, the new post configuration is saved as a potential solution and the simulation continues with the next post in the series of i posts. If $H_j \geq H_0$, the configuration is rejected, and the current post is moved again. Each current post is moved for a total of n_{move} times at most unless a lower energy configuration is found and thus the next post selected as the current post. Each time a configuration is accepted, the current H_j becomes the new H_0.

Based on these criteria, the maximum single SCFT iterations n_{maxi} that would be performed if no configurations were accepted as lower energy configurations by the algorithm would be $n_{maxi} = n_{iter} n_{move} n_{scan}$. However, the actual total number of iterations will be lower since a given post only moves n_{move} times if a lower energy state is not found. A plot of the free energy versus total forward SCFT iteration steps is shown in Figure 6.14 for one simulation result of TS1. Here $n_{scan} = 5$ and $n_{move} = 20$ such that $n_{maxi} = 25{,}000$. Notice that the simulation ended closer to 14,000 iterations which is accounted for by the fact there were 45 instances where a new configuration was accepted and thus the post in those cases were not moved a full $n_{move} = 20$ times. The final accepted post configuration had the density field constraint lifted to ensure the solution fulfilled the *necessary conditions* of an inverse design solution and that the target structure was maintained after relaxing the fields.

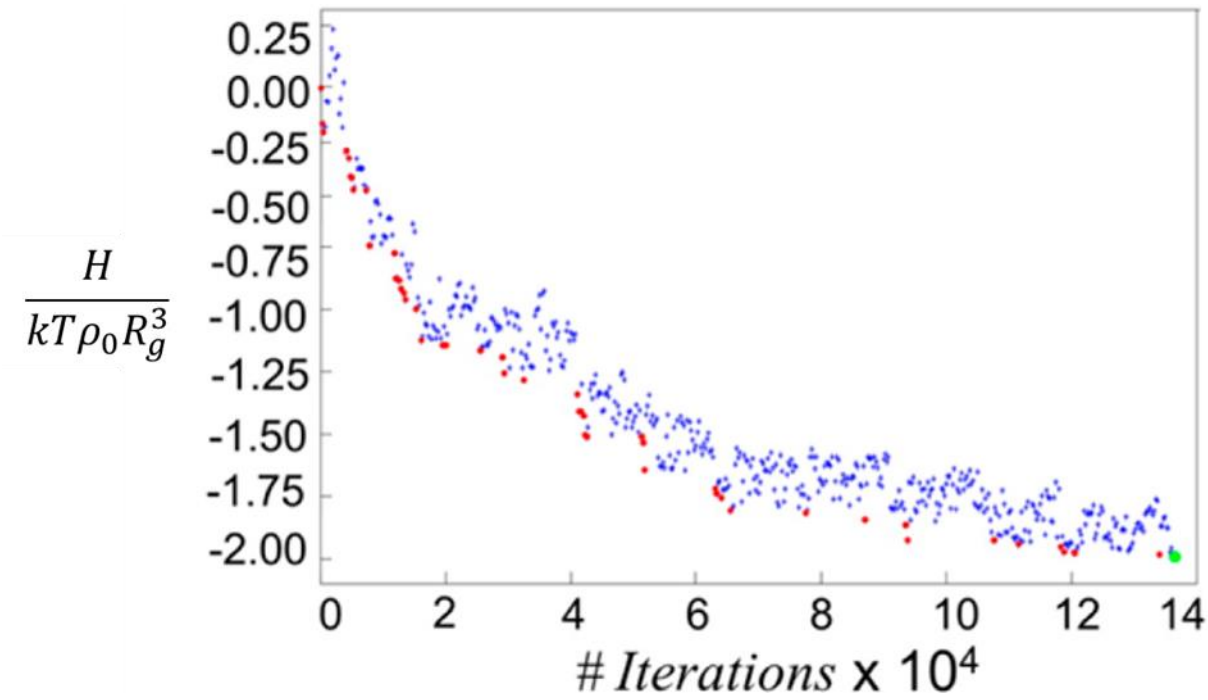

Figure 6-14: Free energy $H/kT\rho_0 R_g^3$ versus number of forward SCFT iterations for an inverse simulation with TS1 as the target struccture. Each point represents n_{iter} = 250 of these iterations. Blue points were where a new post configuration was not accepted, red points are where the calculated H was lower than the previous H_0 and thus the configuration accepted as a new candidate solution for the target structure, and the final green point was the last accepted candidate solution for the number of iterations performed and thus had the lowest H for this particular inverse simulation[50].

For a given inverse simulation, the possibility of the simulation not converging to the global minimum energy post configuration is highly likely for a few reasons. BCP systems inherently exhibit many degenerate or metastable morphologies at a given set of conditions and thus multiple post configurations may be local energy minimum solutions. The post movement algorithm presented at this point is one of the simplest possible algorithms and is highly biased by the initial configuration of the posts such that if posts are configured in a way that they cannot move out of a local energy well with just single post moves then the system will always be stuck with those positions. Algorithm modifications to alleviate these problems will be discussed in a couple of sections. There is also the possibility of multiple post configurations having the same global energy minimum and being solutions to the inverse design problem for a given target structure. Also, the value of n_{scan} and n_{move} need to be large to ensure convergence to a low energy solution,

but in practice for simulation speed these values need to be small. All these issues taken together mean a single inverse design simulation alone cannot be used to obtain the best solution for the system.

The approach taken to get around these issues is to perform n_{run} multiple inverse simulations for a given target structure and statistically weighting the post locations of those solutions based on the free energies of those solutions. Three example solutions for TS1 are shown in Figure 6.12.b. For TS1, $n_{run} = 2{,}100$ simulations were performed. The values of $H/kT\rho_0 R_g^3$ for these simulations was -1.99 ± 0.24 indicating large spread in the configuration energies due to the reasons previously mentioned. To obtain a meaningful way of statistically averaging these solutions, a post probability density map $p(\vec{\mathbf{r}})$ was calculated using a simple Boltzmann weighting such that

$$p(\vec{\mathbf{r}}) = \frac{\sum_m^{n_{run}} g_m(\vec{\mathbf{r}}) e^{\frac{-H_{min,m}}{kT}}}{\sum_m^{n_{run}} e^{\frac{-H_{min,m}}{kT}}}$$

where m represents the mth simulation, $H_{min,m}$ is the minimum free energy of the mth simulation, and $g_m(\vec{\mathbf{r}})$ represents the post configuration solution of the mth simulation such that

$$g_m(\vec{\mathbf{r}}) = \begin{cases} 1 \text{ if post accepted at } \vec{\mathbf{r}} \\ 0 \text{ if post rejected at } \vec{\mathbf{r}} \end{cases}$$

meaning $g_m(\vec{\mathbf{r}})$ is a matrix of 0s and 1s where a 1 represent a post is centered and located at that position and 0 means no post is centered at that position. A plot of $p(\vec{\mathbf{r}})$ for TS1 is shown in Figure 6.12.c and thus larger values of $p(\vec{\mathbf{r}})$ represent areas where posts should go to obtain the target structure and lower values of $p(\vec{\mathbf{r}})$ represent areas posts should not be placed.

Actual templates cannot be made by probable locations, so using the original n_{posts}, a threshold probability p_{thresh} is determined such that if $p(\vec{\mathbf{r}}) \geq p_{thresh}$ is converted to values of 1 and $p(\vec{\mathbf{r}}) < p_{thresh}$ is converted to values of 0, there will be n_{posts} values of one left in the matrix representation of $p(\vec{\mathbf{r}})$ and thus that matrix corresponds to the composite inverse template solution from all simulations performed. The composite solution for $n_{posts} = 24$ corresponding to $p_{thresh} = 0.2$ for TS1 is shown in Figure 6.12.d. In addition to

using p_{thresh} for selecting post positions from $p(\vec{\mathbf{r}})$, symmetry is considered for TS1 and values across the mirror plane in the structure averaged when selecting post positions. This composite solution was then tested several times with forward SCFT simulations and the resulting structure formed consistently as shown in the solution in Figure 6.12.e allowed the final deeming of the post configuration as a solution to the inverse design problem of TS1. Comparing this structure with the original TS1 shown in Figure 6.12.f shows that the solution does indeed give the correct desired topology. This testing means the solution satisfies the *sufficient conditions* needed for the inverse design algorithm to be viable. Removing the posts, the system relaxes to a different morphology as shown in Figure 6.12.g implying the posts are necessary to form and stabilize the target structure.

As presented, the current algorithm works under the condition that a solution exists for the combination of χ, N, f, n_{posts}, and preferentially of the posts chosen. For a general set of these parameters, just as in bulk systems cylinders are only a solution under a range of χN and f, so too are given target structures under a range of the correct control variable combinations. For TS1 as presented in the algorithm test, intuitive guess parameters where chosen based on the f of the composite features. To optimize these parameters in general, an additional optimization scheme is added to the algorithm. Here the root-mean square density difference "fidelity" function ξ and an inverted normalized version Ξ of the function are introduced as additional criterion to optimize in addition to the free energy of the system. For minority block preferential posts, ξ is defined as $\xi \equiv \int d\vec{\mathbf{r}} \sqrt{\left(\phi_{B,soln} - \bar{\phi}_B\right)^2}$ where $\phi_{B,soln}$ is the B majority block density of the post configuration solution for a particular set of conditions and $\bar{\phi}_B$ is the B majority block density of the target structure. Since the posts will occupy the minority volume in this case, the B densities are used in the fidelity definition. Alternative fidelity functions can be defined for other post preferentiality combinations. The other fidelity function is defined as $\Xi \equiv \min(\xi)/\xi$ where $\min(\xi)$ represents the smallest value of ξ found over a given set of simulation conditions. Generally for the best solutions, ξ should be minimized and Ξ maximized and close to 1 as possible. For a given set of simulation, $\Xi = 1$ represents the best solution from that set. By varying n_{posts} and f, several fidelity factors for TS1 were found. Two examples are shown in Figure

6.15 to illustrate how ξ changes with these parameters corresponding to 3 and 39 posts with $f = 0.32$ and $f = 0.52$. Both of these cases fail to have the proper topology of TS1, which is thus considered an additional criterion η that should be satisfied.

When a solution satisfies the topology constraints of the target structure, $\eta = 1$ and the solution is deemed an inverse solution. When a solution does not satisfy the topology constraints of the target structure, $\eta = 0$ and the solution is not deemed an inverse solution. Thus the two solutions in Figure 6.15 both have $\eta = 0$. The density field for the $n_{posts} = 3$ case is labeled as $\phi_B(\vec{\mathbf{r}}; \mathbf{R_{3,0.32}})$ and for the $n_{posts} = 39$ case as $\phi_B(\vec{\mathbf{r}}; \mathbf{R_{39,0.52}})$. In these two cases, $\xi\left(\phi_B(\vec{\mathbf{r}}; \mathbf{R_{3,0.32}})\right) > \xi\left(\phi_B(\vec{\mathbf{r}}; \mathbf{R_{39,0.52}})\right)$ and thus $\Xi\left(\phi_B(\vec{\mathbf{r}}; \mathbf{R_{3,0.32}})\right) < \Xi\left(\phi_B(\vec{\mathbf{r}}; \mathbf{R_{39,0.52}})\right)$. The absolute value of ξ for $\phi_B(\vec{\mathbf{r}}; \mathbf{R_{39,0.52}})$ is quite small as the structure is closely similar to TS1, but the system was oversaturated with posts such that extra connections formed and thus $\eta = 0$. This demonstrates that a low ξ by itself does not guarantee $\eta = 1$ and thus both conditions need to be considered when optimizing solutions in terms of the full BCP parameter space.

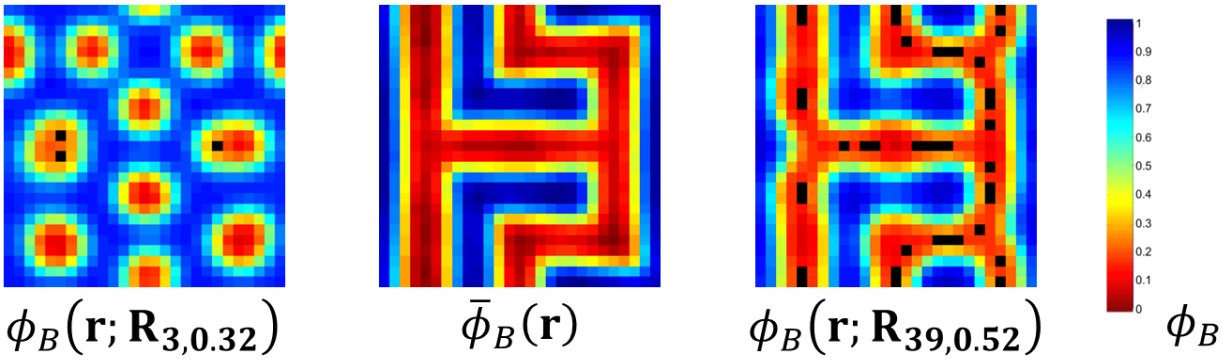

Figure 6-15: Two inverse solutions for TS1 (middle) with n_{posts} = 3 and f = 0.32 (left) and n_{posts} = 39 and f = 0.52 (right). Densities are plotted as darker blue regions corresponding to richer B regions and red to richer A regions and black dots represent posts. The fidelity factor ξ is much lower for the structure on the right than the left and thus a better overall solution, but still the pattern does not satisfy the topology constraints of the target structure due to the extra connections forming on the right side[51].

To gauge the computational efficiency of the inverse design algorithm, several simulations of different n_{post} and total grid size N_x by N_y were performed. In these simulations, parallel line patterns were seeded as the target structure and four input cell sizes were used with nL_0 by nL_0, where n was varied from 1 to 4 such that the

corresponding number of grid points N_x by $N_y = 9n$ by $9n$. n_{posts} was varied over the range 1 to 20 except for the $n = 1$ case as placing more than 5 posts in the system resulted in simulations crashing due to too few available lattice sites for posts to consistently move into new positions at the small unit cell size. For each combination of n cell size and n_{post}, $n_{run} = 200$ simulations were performed and the time to find a potential inverse solution t recorded and averaged amongst the 200 simulations.

Applying a least squares fit to the data, the relationship $t = an_{posts}N_xN_y \ln(N_x) \ln(N_y)$ was found to hold where a was a fitting parameter for the CPUs used and statistical chain length of $N_s = 125$ selected. The evaluated value of a was 4.97 miliseconds per simulation. Plots of the fit lines for the four n cell size cases are shown in Figure 6.16 with the labeling Fit n. The data shows that for the simulations performed on 2.66 GHz Intel ® Xeon ® CPUs, an $n = 1$ cell simulation took 1.95 seconds per post, an $n = 2$ cell simulation took 12.7 seconds per post, an $n = 3$ cell simulation took 38.0 seconds per post, and an $n = 4$ cell simulation took 82.7 seconds per post. These times are very reasonable for performing many n_{run} simulations with different n_{posts} for statistical averaging and analysis and thus the algorithm as presented is quite computationally efficient. Increasing the simulation to 3D will likely increase this time by a factor of $N_z \ln(N_z)$ thus further optimization of the algorithm itself may be necessary for 3D inverse simulations to be computationally efficient. Also, n_{iter} was set to a minimum value of 1 for these calculations such that the relaxed fields were simply calculated from seeded values of the exchange fields corresponding to the seeded target structure density fields, so in general using larger n_{iter} to get better comparison of relaxed field structures will increase the total simulation time by that factor as well.

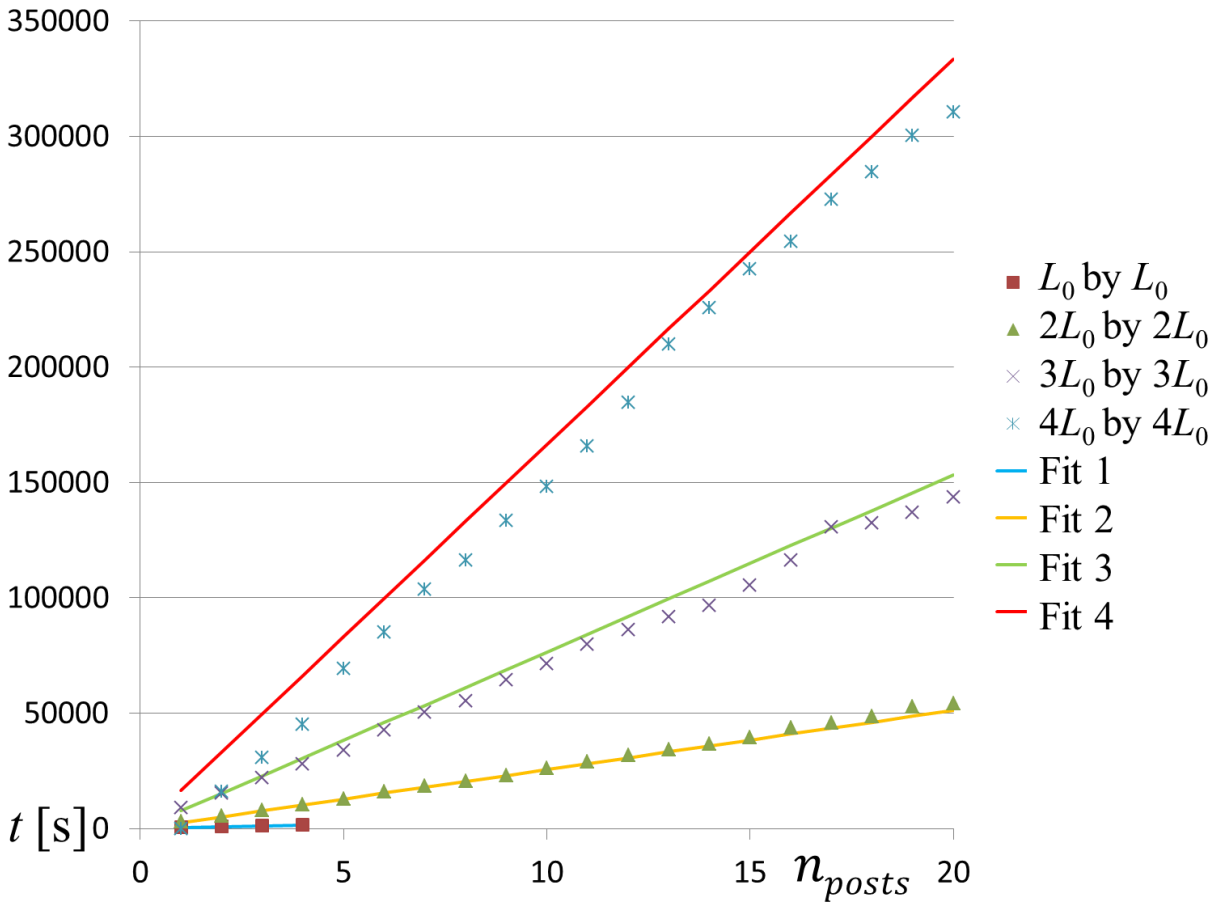

Figure 6-16: Plot of the time t in seconds for n_{run} = 200 inverse simulations to finish versus n_{posts} for four different cell sizes of N_x by N_y = 9n by 9n with parallel line target structures. Line fits are color coded as blue for n = 1, orange for n = 2, green for n = 3, and red for n = 4. Measured time data points are coded as brown squares for n = 1, green triangles for n = 2, violet × crosses for n = 3, and teal * stars for n = 4[51].

6.4 Inverse Design Results and Discussion

To demonstrate the capabilities of the inverse design algorithm, simulations were performed for different target patterns[51]. As a first level demonstration, the inverse design process was evaluated in simulations that varied parameters such as number of posts n_{posts} and volume fraction f to find optimal regions in parameter space where solutions for those patterns existed. The parameters used to reach these target patterns was further optimized computing fidelity function values for each pattern result and selecting the parameters that optimized the fidelity and preserved topology.

For a second level demonstration of the inverse design process, the best solutions and corresponding parameters from the simulations were converted to real experimental templates to show that the results from the simulations could be applied to real systems and thus form a basis for designing templates for real IC patterns. In the experiments, the posts were fabricated with HSQ using EBL and had a minimum finite size of ≈ 14 nm. The ideal post sizes used in the simulations were much smaller with values closer to ≈ 4 nm (not including brush layer). Thus post size effects were accounted for in simulations by taking the best solutions for the optimal post size and performing forward simulations with three larger post sizes at those positions. Future work can examine these larger posts in the inverse simulations directly rather than after the fact. The experimental system used for process verification was a 45.5 kg/mol cylinder forming PS-PDMS solvent annealed to equilibrium. By solvent annealing, the effective volume fraction could be controlled to better match the optimal volume fraction of a given pattern from the simulations.

For this whole inverse design demonstration process, two specific target structures were used as shown in Figure 6.17 which outlines the process. The top structure was the previously discussed TS1 and the bottom structure based on the expected pattern combining four XY^3 templates through four rotations in the design rule studies[201], designated as TS2 for target structure two, contains terminations and bends. These two structures were ideal for initial testing as one focuses on forming three-way junctions and the other structure on forming isolated lines with terminations, both essential features in IC patterns. The density fields of these two target structures are shown in Figure 6.17.a. For the inverse simulation, an effective $\chi N = 14$ was used as previously discussed to account for a lower effective χ during the solvent annealing and lower N from coarse graining in the simulations.

Good fidelity and correct topology solutions from the inverse simulations are shown in Figure 6.17.b where $n_{posts} = 24$ for TS1 and $n_{posts} = 72$ for TS2 with black squares indicating the positions of posts. By accounting for the diameter of the posts using more grid points to occupy post volume, additional solutions were obtained by taking the smaller post solution and eliminating unnecessary posts or replacing two close posts with a single larger post. Solutions using larger post size d but a smaller n_{posts} are thus shown in Figure

6.17.c. Having these more realistic post solutions, the post templates were converted to inputs for EBL and HSQ patterns of the posts were made as shown in Figure 6.17.d. Finally, applying the BCP thin film, annealing the sample, and removing the majority block resulted in the SEM images of patterns that matched the target structures experimentally in terms of topology as shown in Figure 6.17.e. Thus these results show the inverse design algorithm can indeed be used for the fabrication of complex patterns. Each of these steps in the overall process will be discussed in more detail in the next two subsections.

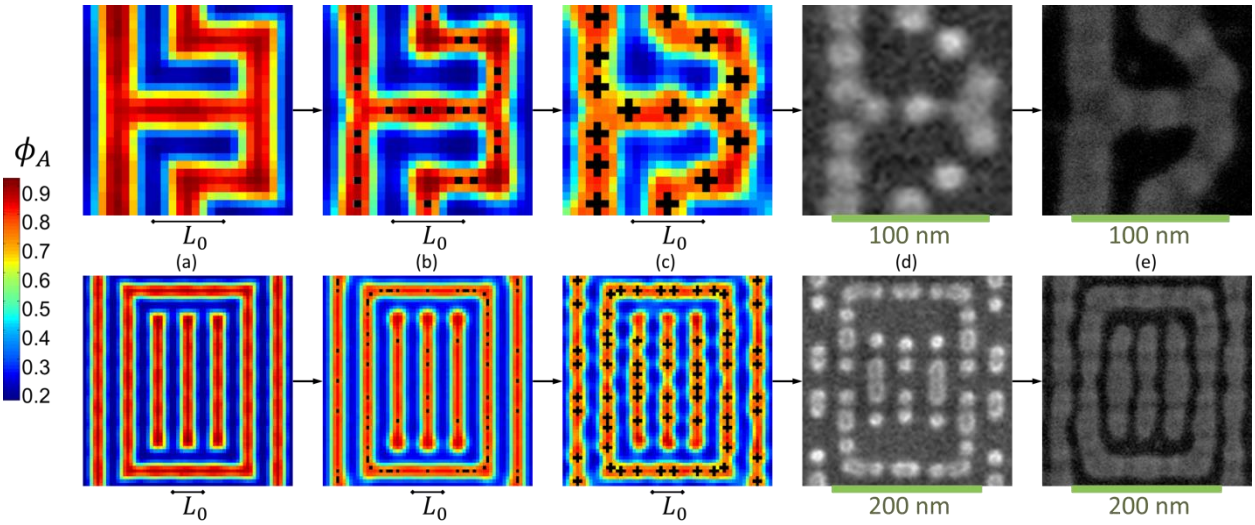

Figure 6-17: Entire inverse design process overview for (top) TS1 containing lines, bends, and three-way junctions with total size $3L_0$ by $3L_0$ and (bottom) TS2 containing lines, bends, and terminations with total size $7L_0$ by $7L_0$. (a) Density field target structures produced from concatenating essential IC circuit component patterns. These structures were used to test and optimize the inverse design algorithm. (b) Post template solutions (black) using inverse design algorithm for corresponding target structures in (a). (c) Post template solutions found taking best inverse design solutions of single grid posts and replacing those posts with larger posts moving or removing the posts positions appropriately such that the system still formed the correct topology using forward simulations. (d) SEM images showing the HSQ post patterns made using EBL. Patterns are based on those in (c). Post overlap is still an issue despite trying to account for the larger post size beforehand. (e) SEM images of the oxidized PDMS pattern on HSQ left from the self-assembly of a PS-PDMS cylinder forming BCP on the post templates in (d) demonstrating they have the same topology as the input target structures in (a) and thus the overall inverse design process works[51].

6.4.1 Simulation Results

The two most influential parameters in determining whether a given target structure will have a valid solution is the number of posts n_{posts} and volume fraction f. Thus for the two target structures examined the effects of these parameters on Ξ and η were studied in depth. For both target structures, f was varied from 0.28 all the way up to 0.72 with increments of 0.04. For TS1, values of n_{posts} from a single post to 40 posts in increments of 1 post were examined. For TS2, the four fold symmetry in the system was used to simplify the inverse calculations such that the unit cell actually tested was $4L_0$ by $4L_0$ with n_{posts} varying from 1 to 40 with increments of 1. The results of these simulations were they converted to the full $7L_0$ by $7L_0$ cells using rotational and reflective symmetry operations to mirror and place posts in all four quadrants of the total unit cell bringing the total n_{posts} values examined to a range of 4 to 160 in increments of 4. Post configuration solutions were found at each set of n_{posts} and f tested and the solutions used in several forward SCFT simulations. The density field results of these forward simulations were averaged spatially to create a composite structure for which Ξ and η were determined. Phase diagrams for $\Xi = \Xi(n_{posts}, f)$ and $\eta\Xi = \eta(n_{posts}, f)\Xi(n_{posts}, f)$ for TS1 and TS2 are shown in Figure 6.18 and Figure 6.19, respectively. For these simulations, $n_{run} = 200$. In these phase diagram, there were enveloped regions where good inverse design solutions where found with good fidelity and correct topology. For TS1, this region was between $f = 0.44$ to 0.56 and $n_{posts} = 15$ up to 40. For TS2, this region was between $f = 0.40$ to 0.48 and $n_{posts} = 68$ up to 160.

As shown in Figure 6.18 and Figure 6.19, the fidelity function Ξ is close to 1 for the best fidelity solution matches between simulations with template solutions and the target structure. The black regions in the lower halves of the figures indicate regions where there was not a topology match between the target structure and forward template simulations ($\eta = 0$) thus implying either no solution to produce the target structure exists at those combinations of n_{posts} and f or the inverse simulations failed to converge to a good template solution for the finite $n_{run} = 200$. The bright regions in this diagram thus represent good inverse solutions.

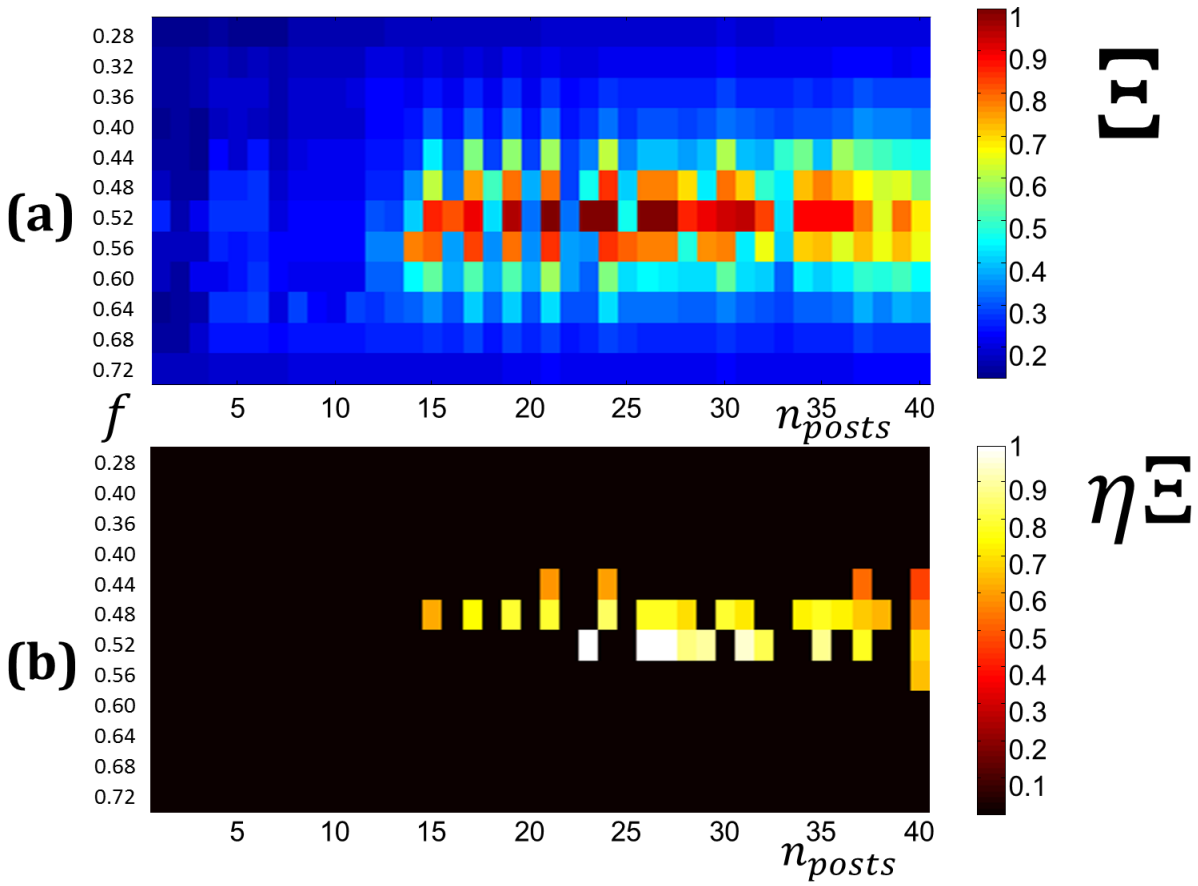

Figure 6-18: (a) TS1 $\Xi = \Xi(n_{posts},f)$ phase diagram. The best solution in terms of just fidelity occurred when $n_{posts} = 21$ and $f = 0.52$. (b) TS1 $\eta\Xi = \eta(n_{posts},f)\Xi(n_{posts},f)$ phase diagram. The best solution in terms of fidelity and topology occurred when $n_{posts} = 26$ and $f = 0.52$[51].

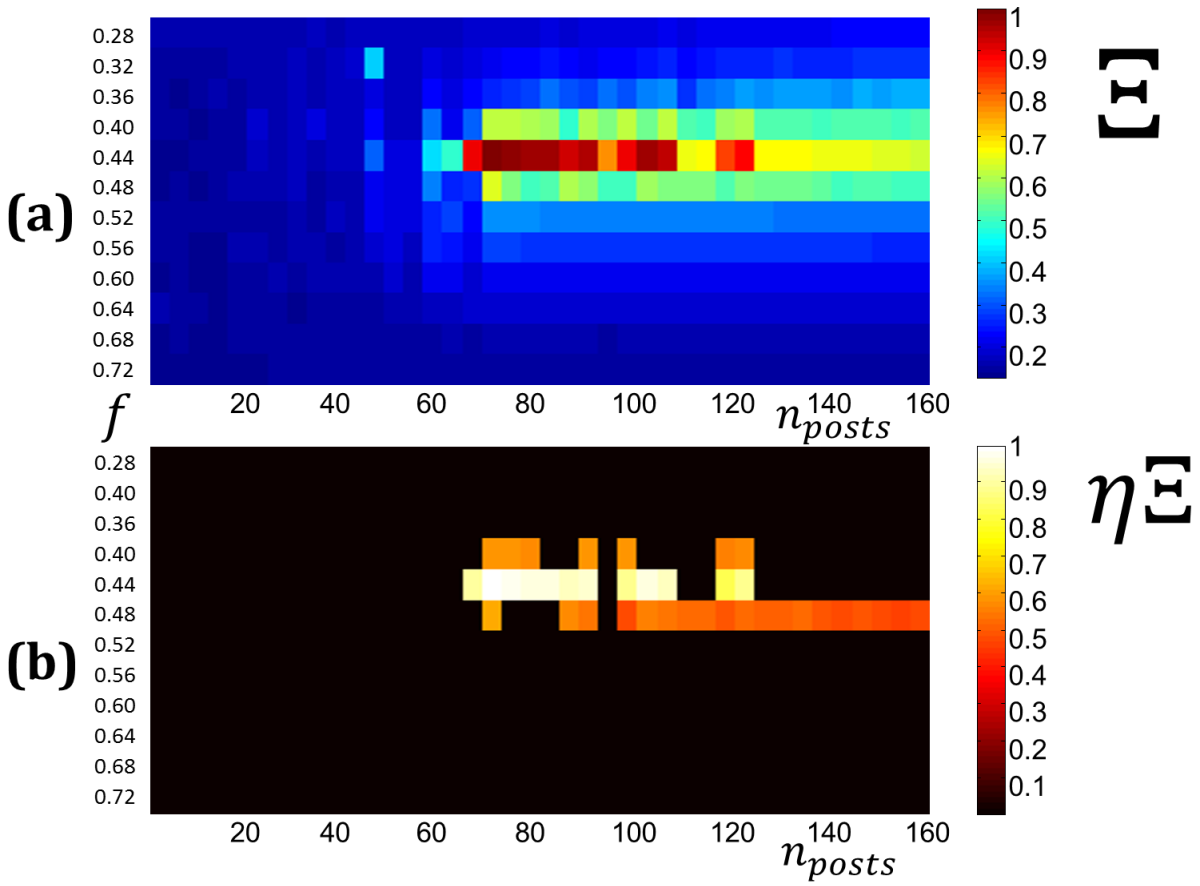

Figure 6-19: (a) TS2 $\Xi = \Xi(n_{posts},f)$ phase diagram. The best solution in terms of just fidelity occurred when n_{posts} = 72 and f = 0.44. (b) TS2 $\eta\Xi = \eta(n_{posts},f)\Xi(n_{posts},f)$ phase diagram. The best solution in terms of fidelity and topology occurred when n_{posts} = 72 and f = 0.44. There is a long region for f = 0.48 where topology is conserved at the cost of poor fidelity with increasing n_{posts} suggesting the system is very stable at this volume fraction as long as there are enough posts in the system[51].

Select examples of different forward simulation for TS1 and TS2 are shown in Figure 6.20 and Figure 6.21, respectively, to show how fidelity and topology are coupled in more depth. As seen in these figures, the general issues in whether the target structure formed with good fidelity or not was based on whether there were enough or too many posts to form the target structure under the given f of the PS-PDMS.

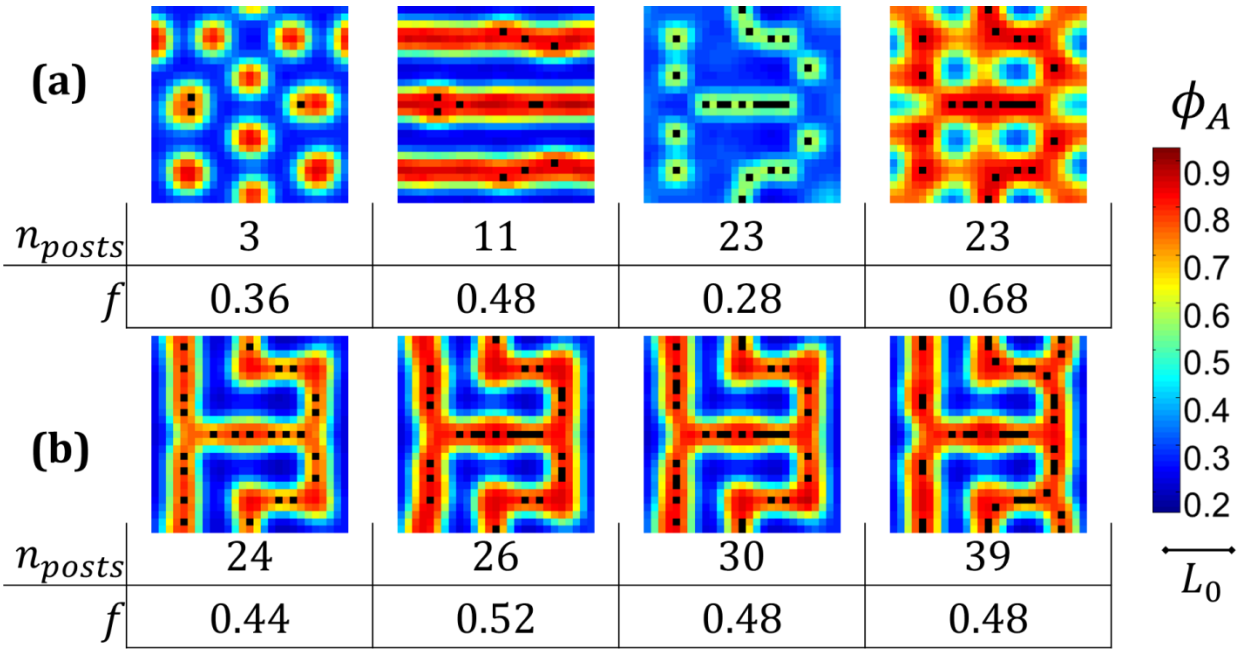

Figure 6-20: (a) Poor fidelity template solutions for TS1 using inverse design simulations. From left to right: n_{posts} = 3 and f = 0.36 resulted in too few posts and not enough PDMS to form TS1, instead forming dot patterns. n_{posts} = 11 and f = 0.48 resulted in too few posts to form TS1, instead forming lines. n_{posts} = 23 and f = 0.28 resulted in not enough PDMS to form TS1, instead just having weak phase segregation around the post template regions. n_{posts} = 23 and f = 0.68 resulted in too much PDMS to form TS1, forming a connected network structure with PS dots instead. (b) Good fidelity template solutions for TS1 using inverse design simulations. From left to right: n_{posts} = 24 and f = 0.44 resulted in correct topology with good fidelity for making TS1. n_{posts} = 26 and f = 0.52 resulted in correct topology with the best observed fidelity for making TS1. n_{posts} = 30 and f = 0.48 resulted in correct topology with good fidelity for making TS1. n_{posts} = 39 and f = 0.48 resulted in good fidelity for TS1, but extra connections formed mismatching the target structure topology due to the system being oversaturated with posts[51].

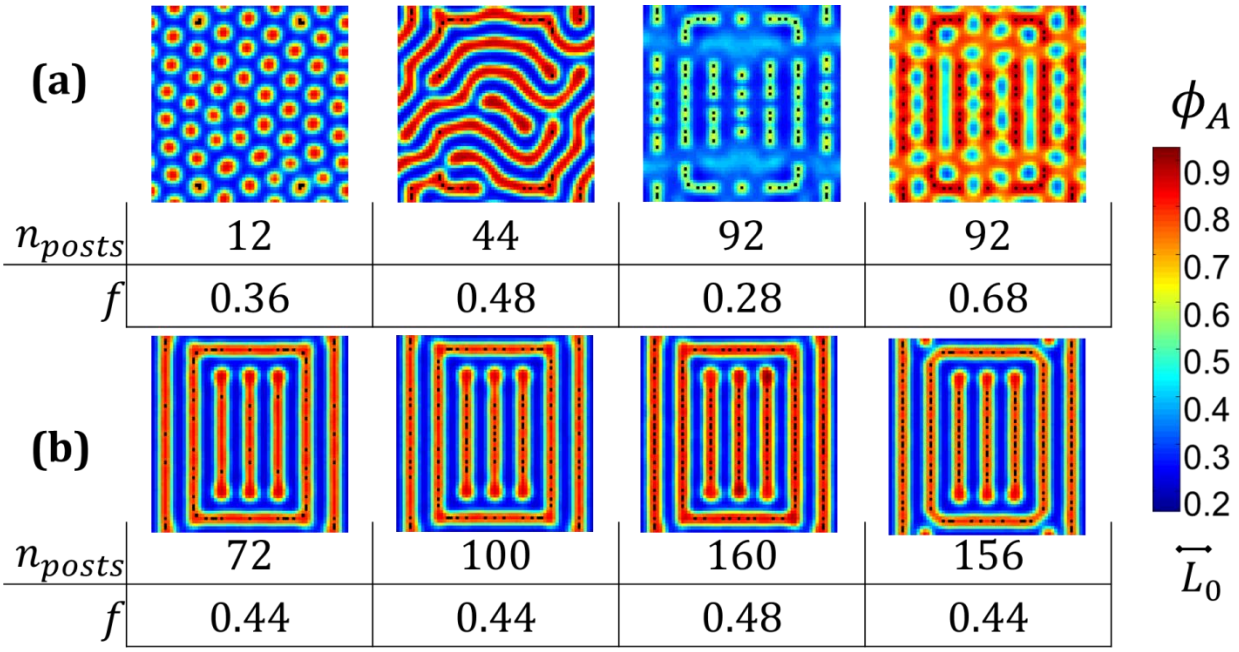

Figure 6-21: (a) Poor fidelity template solutions for TS2 using inverse design simulations. From left to right: n_{posts} = 12 and f = 0.36 resulted in too few posts and not enough PDMS to form TS2, instead forming dot patterns. n_{posts} = 44 and f = 0.48 resulted in too few posts to form TS2, instead forming line patterns. n_{posts} = 92 and f = 0.28 resulted in not enough PDMS to form TS2, instead just having weak phase segregation around the post template regions. n_{posts} = 92 and f = 0.68 resulted in too much PDMS to form TS2, forming a connected network structure with PS dots instead. (b) Good fidelity template solutions for TS2 using inverse design simulations. From left to right: n_{posts} = 72 and f = 0.44 resulted in correct topology with the best observed fidelity for making TS2. n_{posts} = 100 and f = 0.44 resulted in correct topology with good fidelity for making TS2 n_{posts} = 160 and f = 0.48 resulted in correct topology with good fidelity for making TS2. n_{posts} = 156 and f = 0.44 resulted in good fidelity for TS2, but extra dot features formed around the corners of the PDMS ring part of the structure due to strain from large n_{posts}[51].

To examine where these optimal combinations of parameters should exist, free energy calculations of the target structures as a function of f were performed and analyzed. These calculations are analogous to the ones done for component features in Figure 6-13. A plot of the free energy $H/kT\rho_0 R_g^3$ as a function of f for TS1 is shown in Figure 6-22 and for TS2 is shown in Figure 6-23. From these plots, TS1 had a free energy minimum at $f = 0.55$ and TS2 had a free energy minimum at $f = 0.45$.

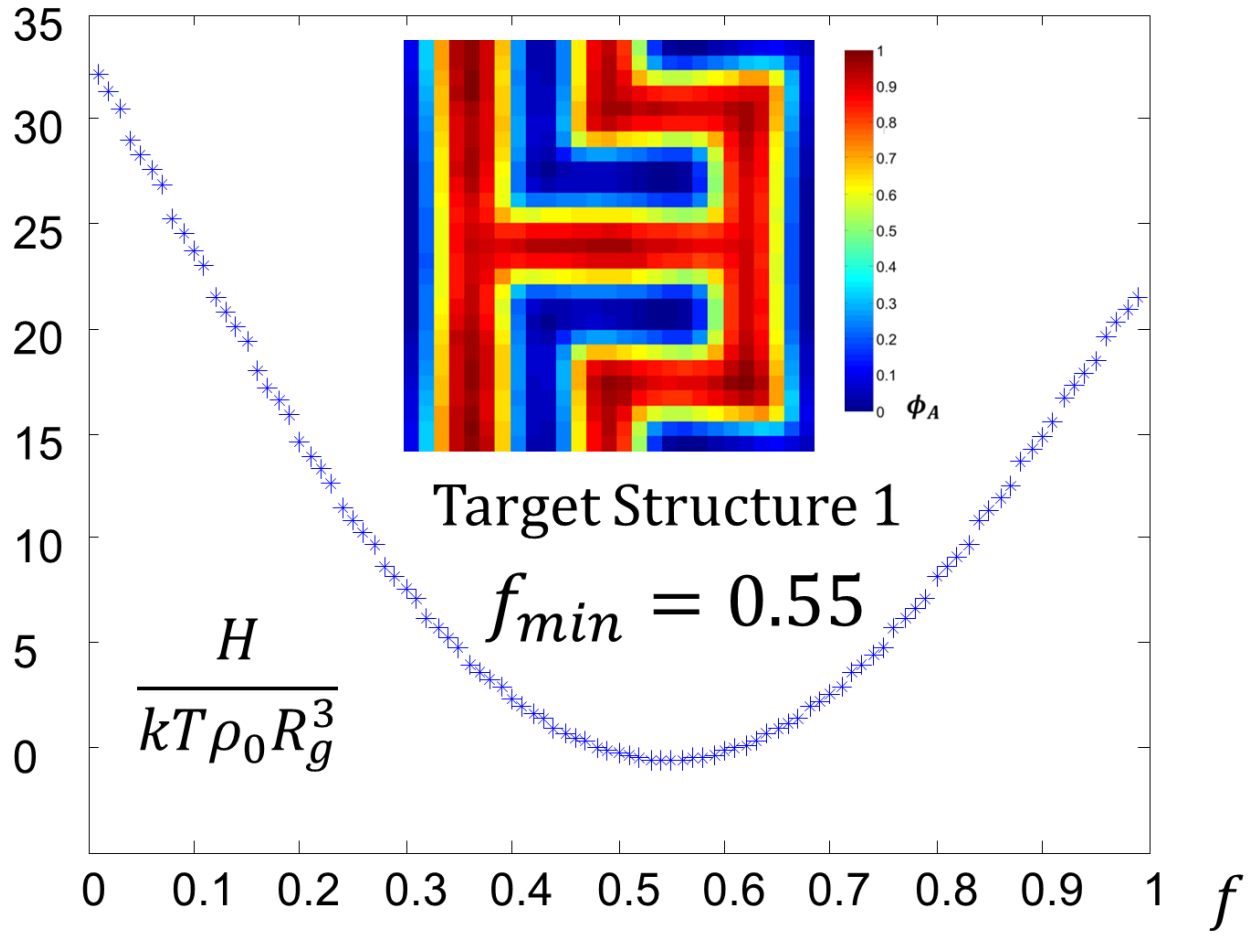

Figure 6-22: Free energy $H/kT\rho_0 R_g{}^3$ as a function of f for TS1. Minimum H occurred when f = 0.55 which makes sense as there are two three-way junctions in the pattern[51].

To use these results for where the minimum free energy occurred as a function f to compare with the results of the inverse solutions, the best solutions found in terms of fidelity Ξ and topology η are identified. For TS1, the best Ξ with $\eta = 1$ occurred at $n_{posts} = 26$ and $f = 0.52$ as seen in Figure 6.18. For TS2, the best Ξ with $\eta = 1$ occurred at $n_{posts} = 72$ and $f = 0.44$ as seen in Figure 6.19. By defining an effective fraction the posts motifs add to the system f_{posts}, effective volume fractions of PDMS f_{eff} can be defined and compared with the free energy minimum of f. Since each post occupies one grid point in the simulation unit cell of size N_x by N_y, $f_{posts} = n_{posts}/N_x N_y$. For larger posts, this becomes $f_{posts} = A_{posts} n_{posts}/N_x N_y$ were A_{posts} is the number of grid points in a post.

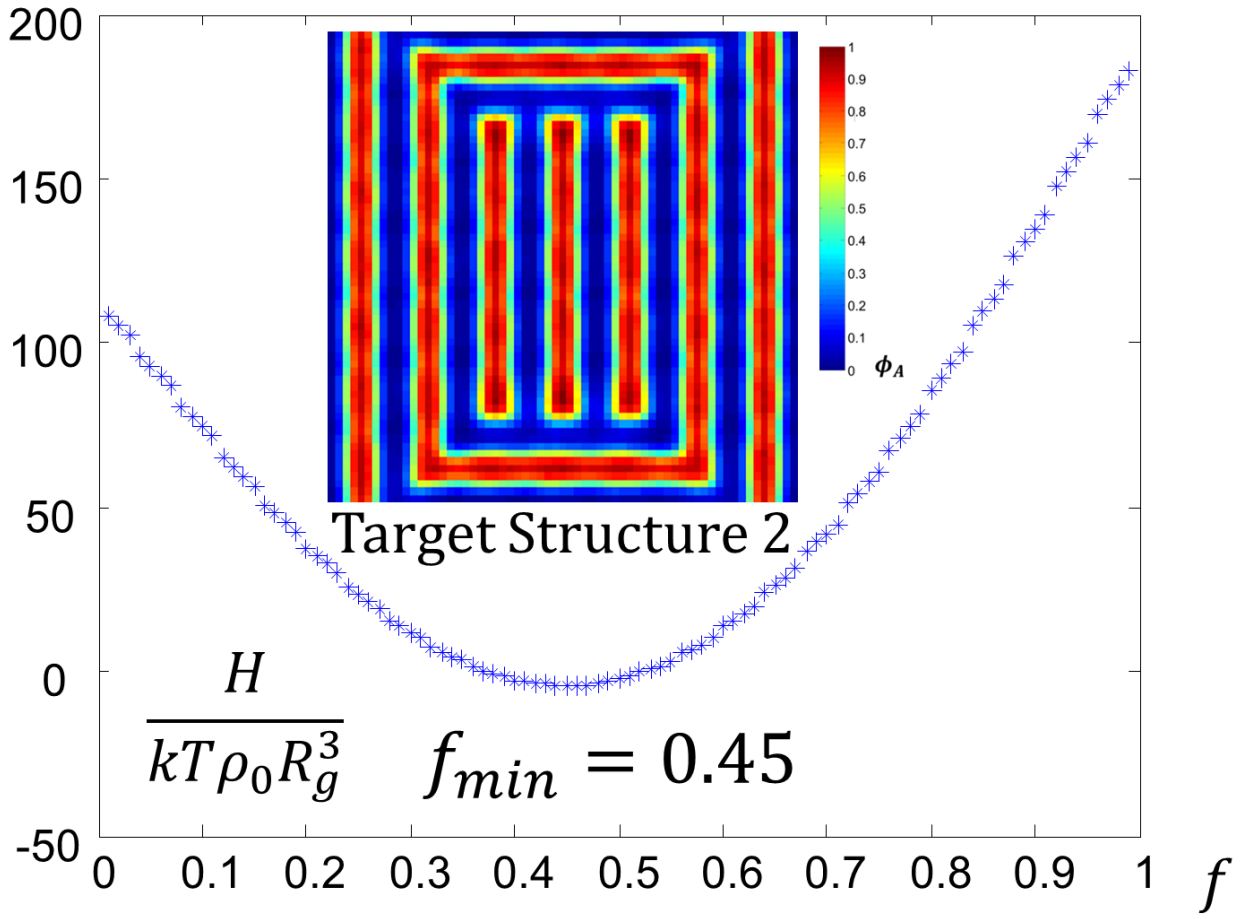

Figure 6-23: Free energy $H/kT\rho_0 R_g^3$ as a function of f for TS2. Minimum H occurred when f = 0.45 which makes sense as there are multiple terminations in the pattern[51].

For TS1 at the best fidelity solution, N_x by $N_y = 27$ by 27, so $f_{posts} = 26/729 \cong 0.036$. Since the posts are preferential to the PDMS block and thus reside in those regions, $f_{eff} = f + f_{posts}$. For TS1 at the best fidelity solution, $f_{eff} = 0.52 + 0.036 \cong 0.556$ which is almost equal to the observed free energy minimum f value of 0.55. For TS2 at the best fidelity solution, N_x by $N_y = 63$ by 63, so $f_{posts} = 72/3969 \cong 0.018$ and thus $f_{eff} = 0.44 + 0.018 \cong 0.458$ shich is almost equal to the observed free energy minimum f value of 0.45. The close values between f_{eff} for the best inverse solutions and the free energy minimum f calculated for the structure suggests the envelope region where template solutions exist are determined by the sum of post volume and PDMS volume being close to this value.

Using the experimental measured value of $L_0 = 39$ nm, the effective diameter of the single grid point posts are 4.3 nm for the center hard part of the post (not including brush

layer). This value is much smaller than the minimum post diameter of ≈ 14 nm of the HSQ posts produced from EBL, so before comparing these solutions with experiments post diameter size effects were explored. Four different diameters $d \cong 4, 12, 17, \text{and } 20$ nm were examined in additional forward SCFT simulations varying f from 0.44 to 0.52 for both TS1 and TS2. Potential overlap of posts with increasing post size was handled by removing or moving a post from the optimal inverse solutions that were closer than $L_0/3 \cong 12$ nm as shown in Figure 6.24. Effective double posts that were only one grid point or ≈ 4 nm apart had a single post replace the double posts at the center of the original two posts. When many posts were close or right next to each other, posts were removed or moved until the final local post configuration had no posts closer than $L_0/3$. For TS1, the solution with $n_{posts} = 24$ at $f = 0.44$ from the initial inverse design study before optimization was used for making these reduced post templates[50] while the best fidelity solution for TS2 at $n_{posts} = 72$ and $f = 0.52$ was used. Performing this post removal and moving process, TS1 had a solution reduced to 15 posts and TS2 had a solution reduced to 52 posts. For comparative purposes, three additional templates with some select double post features preserved were used in these forward simulation studies corresponding to $n_{posts} = 17, 19, \text{and } 21$ for TS1 and $n_{posts} = 56, 60, \text{and } 64$ for TS2. These altered templates are of course not the same as those found by the inverse design solution as they do not satisfy the free energy minimization condition. However, as shown in the forward simulation results of Figure 6.25, they did give correct topology at certain f.

The correct topology being observed for some of these modified solutions at the smallest post size of one grid point suggests the free energy minimization constraint is not the only constraint that should be optimized in the inverse design algorithm. This issue will be discussed in more detail in the future algorithm modifications section. As post size increased, line edge roughness in the PDMS patterns increased with the PDMS forming a corona around the posts such that TS1 tended to have less sharp corner bends and more round corner bends while in TS2 the PDMS patterns tended to break up around the posts rather than forming full line connections in addition to incorrect connectivity. The posts in these larger diameter patterns still overlap in some cases even after the modifications and this will also be seen in the experimental patterns.

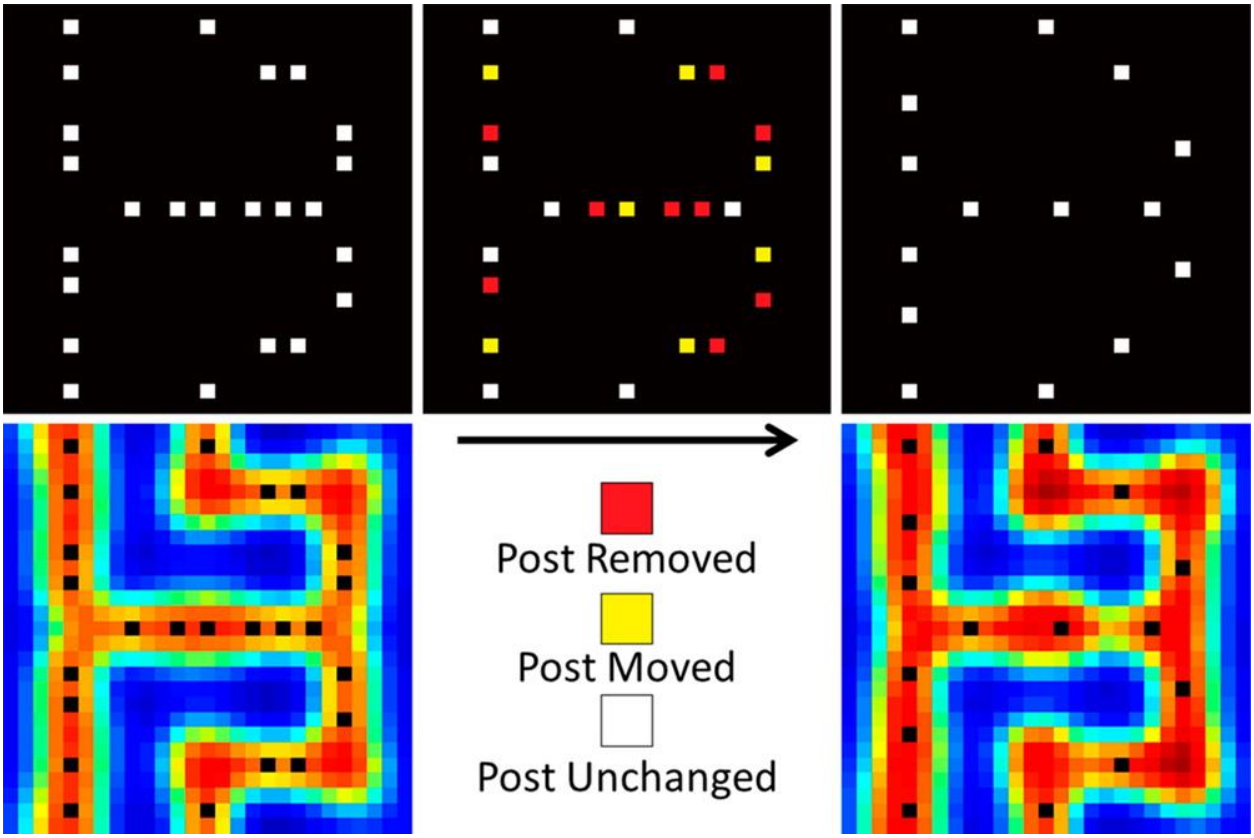

Figure 6-24: Steps used to alter inverse design solution templates to prepare solutions for experimental verification since post size in experiments is larger. (Top-Left) TS1 inverse post configuration solution from n_{posts} = 24 and f = 0.44. (Top-Middle) Red post are to be removed and yellow posts are to be moved one point over to centralize where a nearby post was removed. (Top-Right) n_{posts} = 15 post configuration after altering n_{posts} = 24 solution. (Bottom-Left) PDMS density map forward simulation result using n_{posts} = 24 template. (Bottom-Right) PDMS density map forward simulation result using n_{posts} = 15 template altered from n_{posts} = 24 template with f = 0.48. At this higher f the altered post template was able to yield the correct topology for TS1[51].

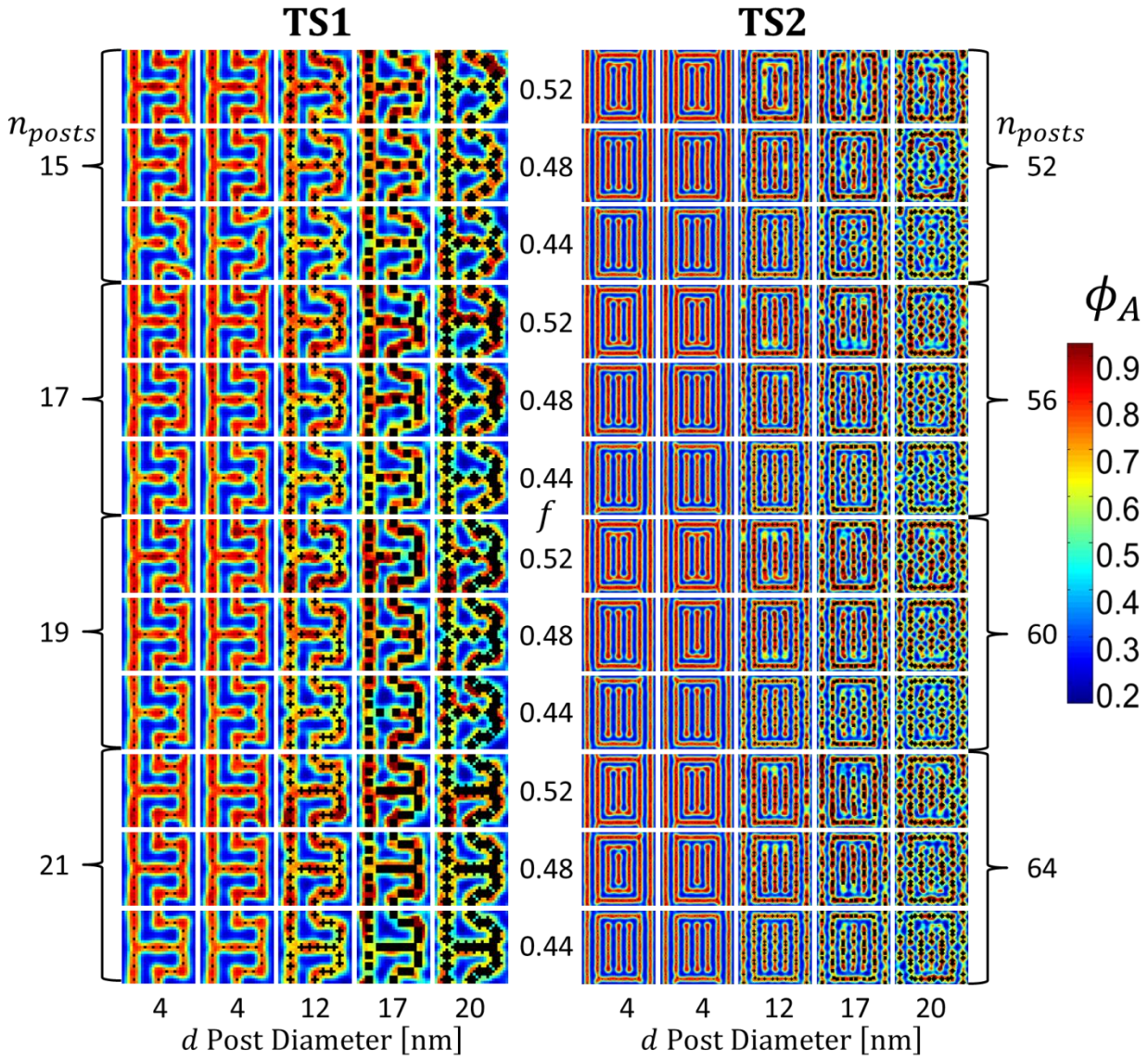

Figure 6-25: Additional forward simulation results varying n_{posts}, f, and d with altered post configuration solution templates using the rules from Figure 6.24. Smallest n_{posts} configurations used these rules strictly and higher n_{posts} left some double posts in the template (Left) Results for TS1. (Right) Results for TS2. Two separate simulation results are shown for d = 4 nm to illustrate the variability in results on initial conditions of the simulations[51].

For reference, an example of a forward simulation result at most of the conditions tested for the inverse design algorithm post configuration solutions are shown for TS1 in Figure 6.26 and for TS2 in Figure 6.27. The values of $f = 0.28$ and $f = 0.72$ were omitted since these solutions just had post feature wetting and no strong observable phase

separation. These represent the general morphology observed under those conditions as multiple simulations were performed for each case to examine defect structure formation.

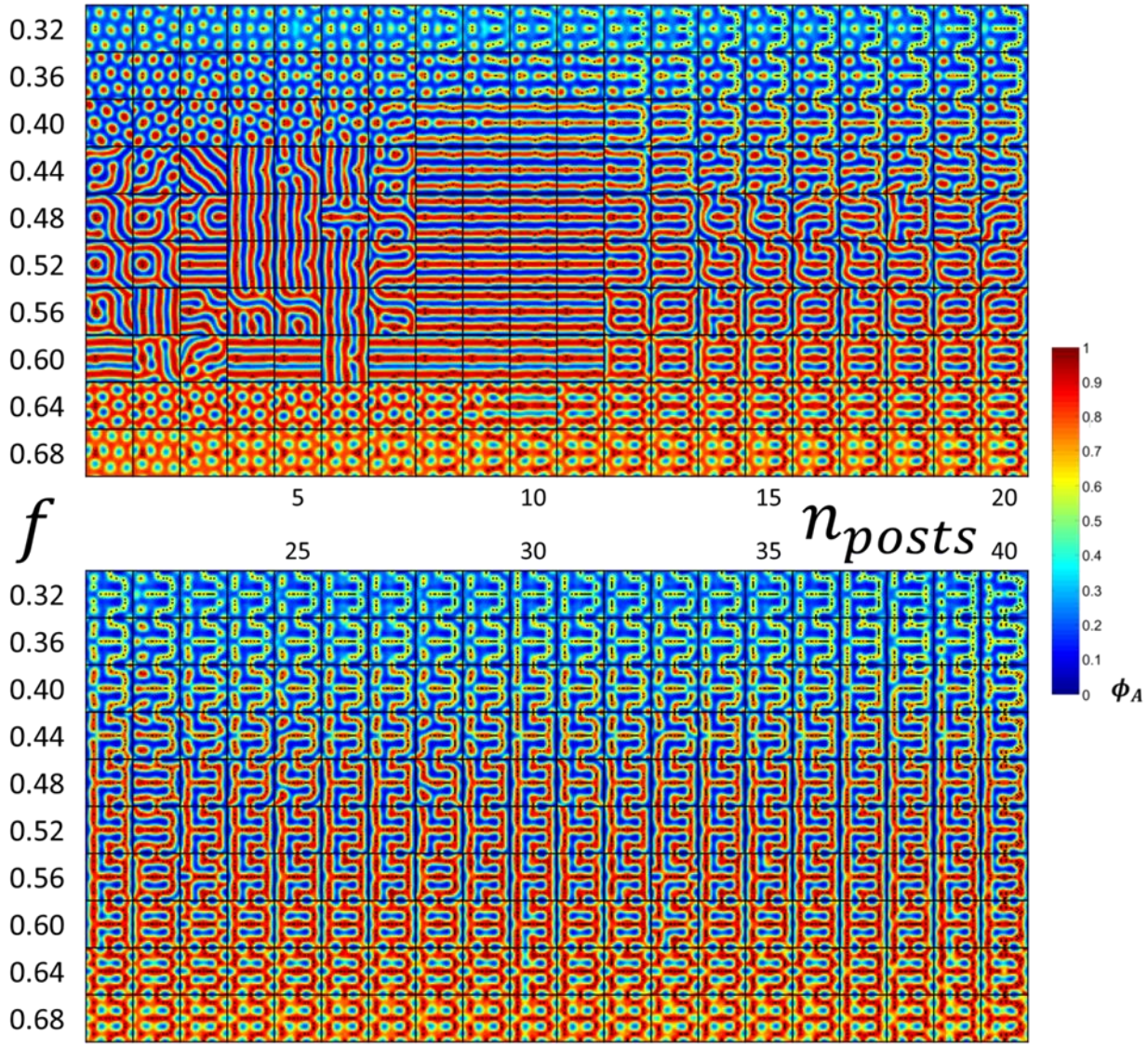

Figure 6-26: Forward SCFT simulation results for TS1 inverse design algorithm post configuration solutions for f = 0.32 to 0.68 with (Top) n_{posts} = 1 to 20 and (Bottom) n_{posts} = 21 to 40[51].

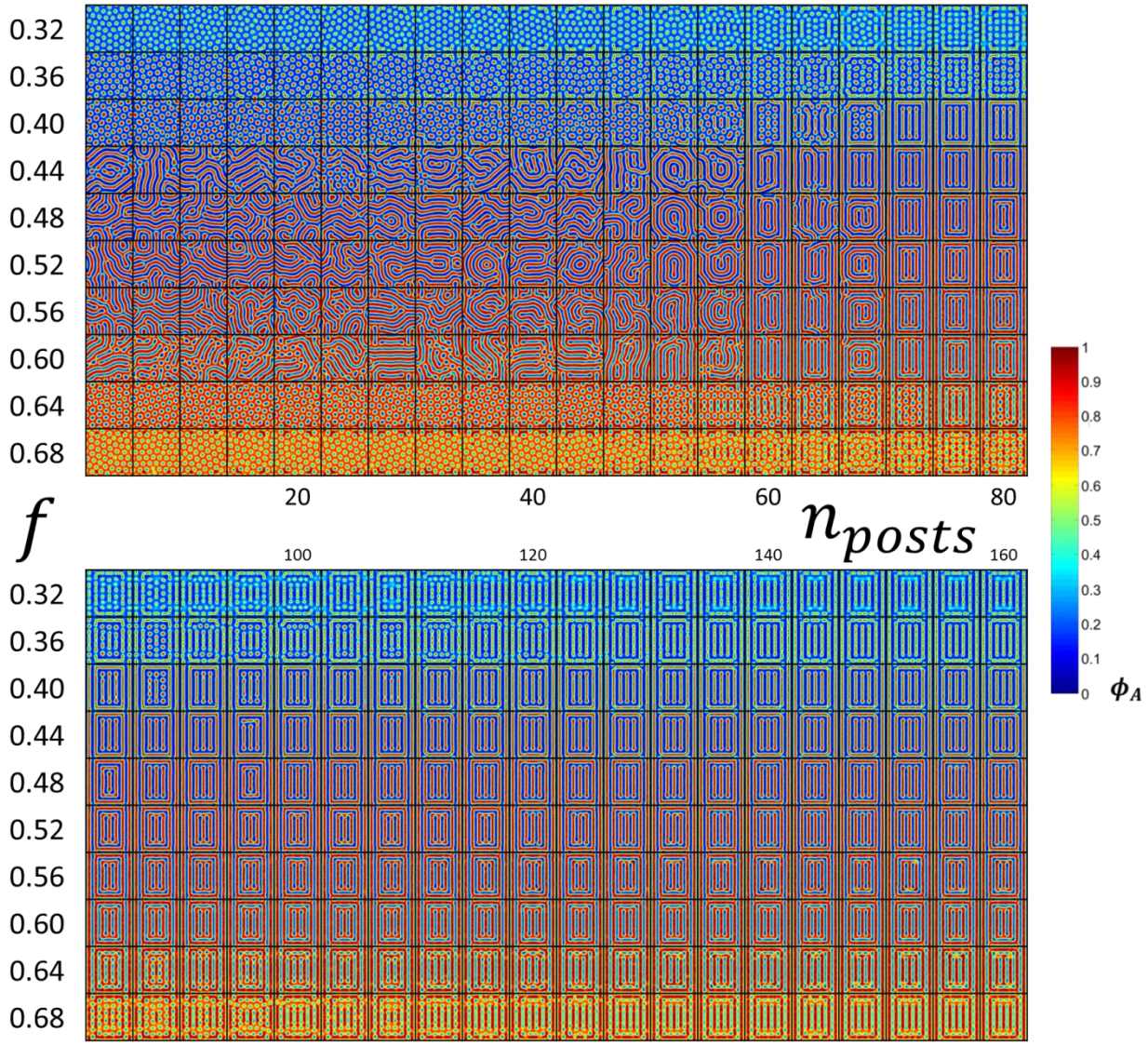

Figure 6-27: Forward SCFT simulation results for TS2 inverse design algorithm post configuration solutions for f = 0.32 to 0.68 with (Top) n_{posts} = 4 to 80 and (Bottom) n_{posts} = 84 to 160[51].

For TS2, a set of simulations were performed varying n_{posts} using the 4 altered templates from Figure 6.25 with 52, 56, 60, and 64 posts in addition to the best fidelity inverse solution with $n_{posts} = 72$ posts. In these simulations, the effective L per 9 grid points was varied from $0.78L_0$ to $1.20L_0$ to examine how commensuration affects the fidelity of solutions formed. As shown in Figure 6.28, the best solutions occurred near $L = L_0$. As shown in Figure 6.29, the fidelity Ξ is maximal for L slightly less than L_0 meaning the presence of the posts places the sample slightly in a compressed state.

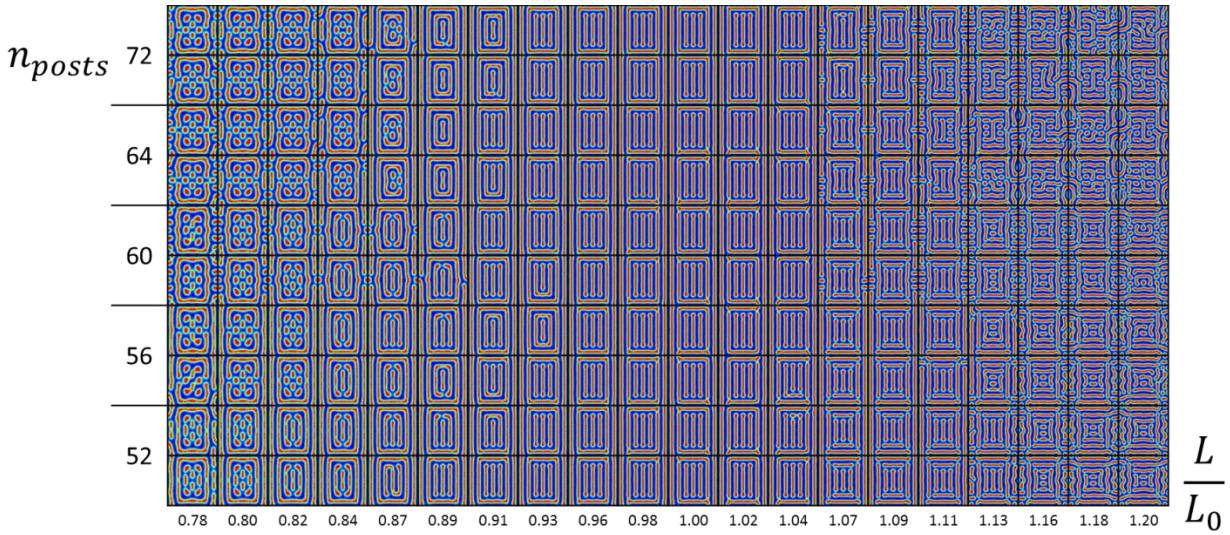

Figure 6-28: TS2 forward simulation results for five n_{posts} configurations varying L/L_0. Two simulation results are shown for each combination of n_{posts} and L/L_0[51].

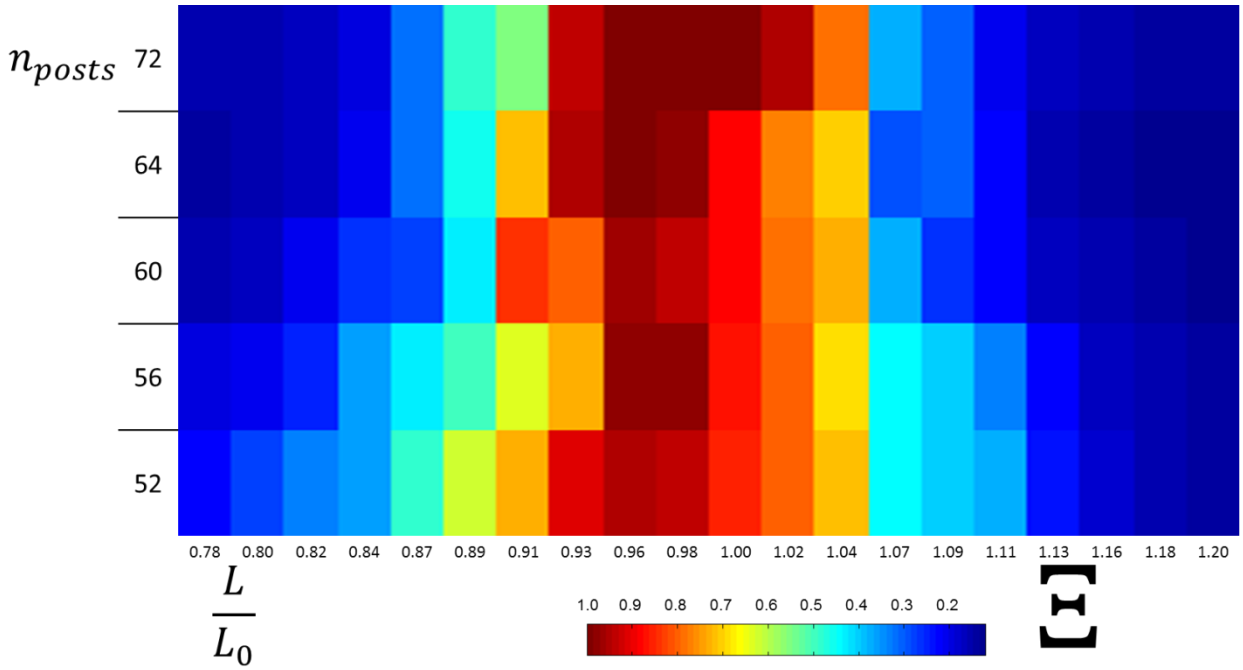

Figure 6-29: TS2 forward simulation Ξ fidelity map for five n_{posts} configurations varying L/L_0. The maximal Ξ values occur around L/L_0 = 0.96 and 0.98 implying the sample is under compressive strain with the posts present in terms of obtaining the best template if an L = L_0 post template were used[51].

In all of these simulation results, insight into design rules can be obtained that is not intuitive in terms of an empirical design process. Examples of empirically designed post template features expected to yield bend and junction features are contrasted with the

results of inverse design solutions in Figure 6.30. For PDMS preferential posts, bends might be thought to be produced having posts concentrated at the corner of the bend for guiding the PDMS domains around the corner. For three-way junctions, a T-shaped post at the center of the junction might be expected to produce the structure as shown in Figure 6.29.a, but does not promote the lines to connect. Actual inverse design results as shown in Figure 6.30.b demonstrate the assumptions are not exactly right but show the post templating features should be outside of the junction and bend areas. Similar experimental results were shown previously in the design rule work for the three-way junctions when posts were missing as in Figure 6.10[201]. These results show that intuitive "connect-the-dots" strategies are not the best way to go about getting desired results and thus use of inverse design simulations or developed design rules from simulations and experiments are the best route to obtaining general arbitrary morphologies. The next subsection will examine transferring these results to real experimental systems.

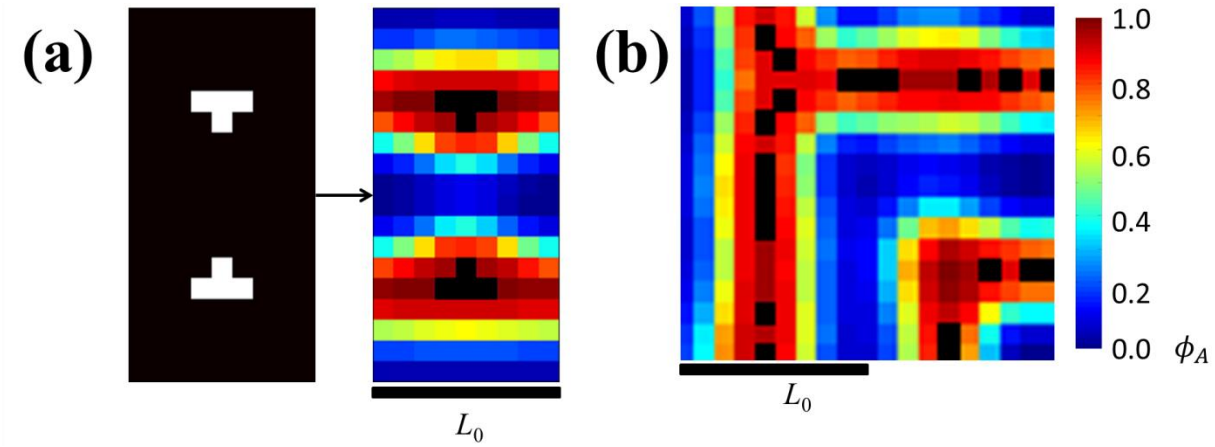

Figure 6-30: Example simulation results of how intuitive template design can fail to achieve target morphologies. (a) T-shaped post features empirically designed for trying to form three-way junctions fail to do so in simulations rather forming strained lines. (b) Examples of inverse design simulation results showing templating features that produced bends and junctions by having post features moved away from the center of the IC features[50].

6.4.2 Experimental Results and Comparison

For experimental verification of the results of the inverse design algorithm, HSQ (Dow Corning XR-1541, 2%) posts were fabricated using an Elionix F125 EBL system with posts and substrates functionalized with a 0.8 kg/mol PDMS hydroxyl terminated

homopolymer brush. Experiments were performed by Yi Ding and Wubin Bai. Room temperature HSQ was spun cast at 3000 rpm for 30 seconds to obtain 38 ± 2 nm thick films. The films were exposed with a raster scan of an electron beam at an acceleration voltage of 125 kV with a 1 nA beam current. The exposure time was varied from 70 to 200 μseconds/dot. After exposure in the Elionix, a salty development using a 4% NaCL and 1% NaOH DI water solution was used to develop the exposed HSQ. The films of HSQ were then rinsed in DI water for 2 minutes and isopropanol for 1 minute before being aired dried in nitrogen gas. After salty development, the samples were oxidized with oxygen plasma in an asher.

A 2 wt % cyclohexane solution of the brush was spun cast at 3000 rpm for 30 seconds onto the templated sample, thermally baked at 170°C and ≈ 20 Torr pressure for 18 hours for the brush to bond to the substrate and posts, and subjected to a toluene rinse to remove any remaining brush that did not bond to the substrate. Cylinder forming $f_{PDMS} = 0.335$ PS-PDMS from Polymer Source, Inc. with molecular weight 45.5 kg/mol and PDI ≅ 1.15 was spun cast onto the patterned substrate using a 1.5 wt % solution in propylene glycol monomethyl ether acetate (PGMEA) to a 38 nm thickness as measured by spectral reflectometry. Both pure toluene and 5 to 1 toluene to heptane solvent vapor combinations were used to solvent anneal the samples for 3 hours until equilibrium was reached in a beaker system with controlled ventilation to maintain a constant vapor pressure. The film was dried in a controlled fashion to keep the vapor pressure steadily decreasing. A quick 5 second CF_4 plasma reactive ion etch followed by a longer 22 second oxygen plasma etch was performed to remove any surface PDMS layer and PS matrix, respectively. The oxygen plasma also served to oxidize the PDMS patterns, making them give better contrast SEM images. The experimental details are similar to those of other HSQ template DSA processes[56–58,60,201].

In the EBL writing process, raster scans based on trajectory write points are input into the system with dwell times and dosages. Thus in order to convert the simulation post configuration results to a writable experimental template, the post configurations had to be converted to real space parameter coordinates. Since the simulations assumed periodic boundary conditions, arrays of these post configuration coordinates were designed for

better comparison with the simulation results by producing arrays of coordinates with total pattern unit cell size of 11 by 11 unit cells for TS1 and 7 by 7 unit cells for TS2. Example raster scan trajectories with the corresponding inverse design solutions and forward simulation results for two post sizes are shown in Figure 6.31 for TS1 and in Figure 6.32 for TS2. Several effective unit cell primitive cell periods L were assigned to the real space scan trajectories to ensure that the post patterns were commensurate with the experimental BCP natural period L_0 to account for any possible experimental error of L_0 not being exactly as expected from previous experiments due to solvent annealing conditions not be exactly calibrated. This L value was varied over 10 periods ranging from 34 nm to 43 nm using the four modified post solutions from Figure 6.25. Resulting HSQ post patterns using these conditions for select L values are shown in Figure 6.33.

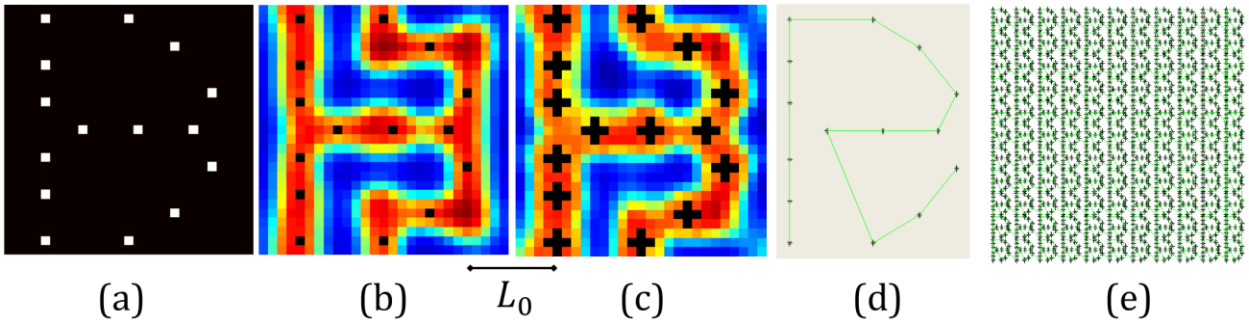

Figure 6-31: (a) Altered post configuration solution from inverse design algorithm with n_{posts} = 15 for TS1. (b) Forward SCFT simulation result using post configuration in (a). (c) Forward SCFT simulation result using post configuration in (a) but with larger posts. (d) Post coordinates with raster scan trajectory for making experimental template for TS1 using post configuration in (a) for verifying inverse design algorithm process. (e) Concatenated full raster scan trajectory post coordinates for making TS1 in experiments using an 11 by 11 array of unit cells to account for periodic boundary conditions used in the simulations[51].

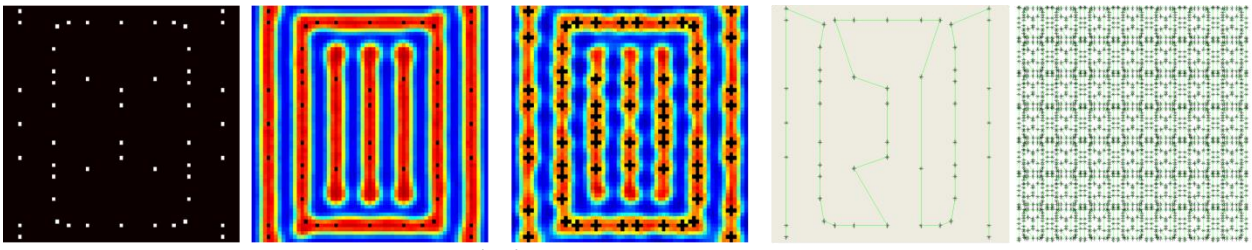

Figure 6-32: (a) Altered post configuration solution from inverse design algorithm with n_{posts} = 52 for TS2. (b) Forward SCFT simulation result using post configuration in (a). (c) Forward SCFT simulation result using post configuration in (a) but with larger posts. (d) Post coordinates with raster scan trajectory for making experimental template for TS2 using post configuration in (a) for verifying inverse design algorithm process. (e) Concatenated full raster scan trajectory post coordinates for making TS2 in experiments using a 7 by 7 array of unit cells to account for periodic boundary conditions used in the simulations[51].

The best experimental results in terms of corresponding to correct topology of the target structures TS1 and TS2 are shown in Figure 6.34. For TS1, the best patterns with fewest defects occurred near $L = 39$ nm for pure toluene samples ($\approx L_0$ based on previous experiments at these conditions) and $L = 42$ nm for 5 to 1 toluene to heptane samples. A frequently observed defect in the experiments for TS1 was an additional circular PDMS domain showing up between the corner bends at larger values of L. For TS2, the best patterns occurred at $L = 39$ nm ($\approx L_0$) under the 5 to 1 toluene to heptane condition. For TS2, the ring area of the pattern had the fewest observed defects and formed reproducibility across samples. The terminated line segments inside the pattern were harder to consistently produce across samples and formed connected defects in many samples. Also, the line patterns between ring structures showed breaks in the line at random locations similar to those observed in the larger post diameter forward simulations.

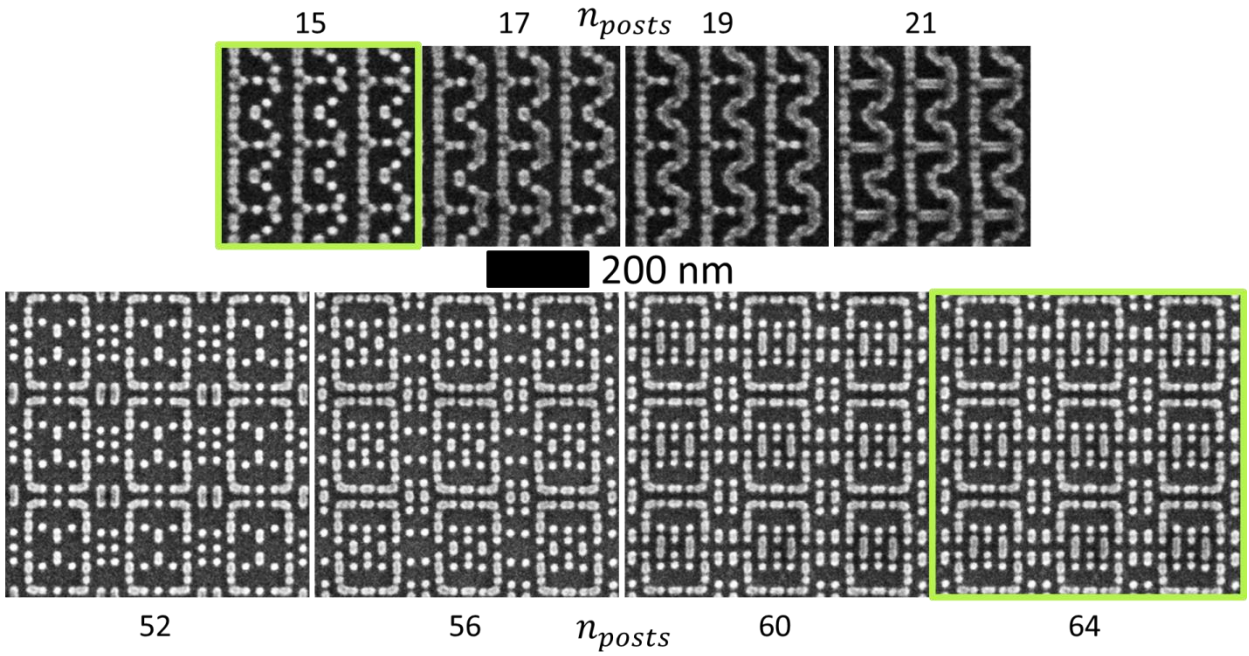

Figure 6-33: SEM images of HSQ patterns of posts corresponding to post solutions derived inverse design solutions. (Top) Patterns for TS1. (Bottom) Patterns for TS2. The patterns that gave the best experimental results have boxes around them. The pattern primitive cell spacing is L = 39 nm[51].

The solvent annealing conditions of 5 to 1 toluene to heptane correspond to higher effective PDMS volume fractions than pure toluene, although the volume fractions do not exactly relate to the 2D simulation f values explicitly as the presence of the posts affects the net effective f experienced by the BCP under the different annealing conditions. Since the effective 2D fractions in the simulations showed TS1 being stabilized at higher PDMS fractions, the fact the pattern occurred reproducibly for $L = 39$ nm for 5 to 1 toluene to heptane conditions corresponds well with these conditions increasing the effective PDMS volume. Conversely, for TS2 there were still disconnections at these conditions. However, TS1 occurred over a larger range of f in simulation compared to a very narrow range for TS2. This suggests that in future studies higher heptane concentration studies for TS2 should be performed to better establish a range where these patterns form reproducibly. The observed area fractions do not correspond to the 2D input f in the simulations due to 3D effects, so future studies should also try to focus more on 3D issues such as post height and air and substrate surface energy effects. Additionally, these samples are not entirely

under periodic boundary conditions, so future simulation studies should try to examine more realistic boundary conditions as well as concatenated target structures.

These results reiterate the ideas of design rules[201]. The observation that the absence of a post in the middle of three-way junction promotes the feature formation was again observed with both junctions in TS1. Bends were reliably reproduced by having dense post features coming into the bend as seen for TS2 such that the ring structures were stabilized. Terminations were the hardest IC feature attempted in these target patterns to reproducibly control and place as seen in the defects of TS2 as the structure would often rather form connected bends. Terminations formed more reliably increasing toluene (decreasing volume fraction) but at the cost of being able to produce continuous line patterns well. Thus future studies need to really focus on combination effects of effective volume fraction and local post feature density for different desired IC components.

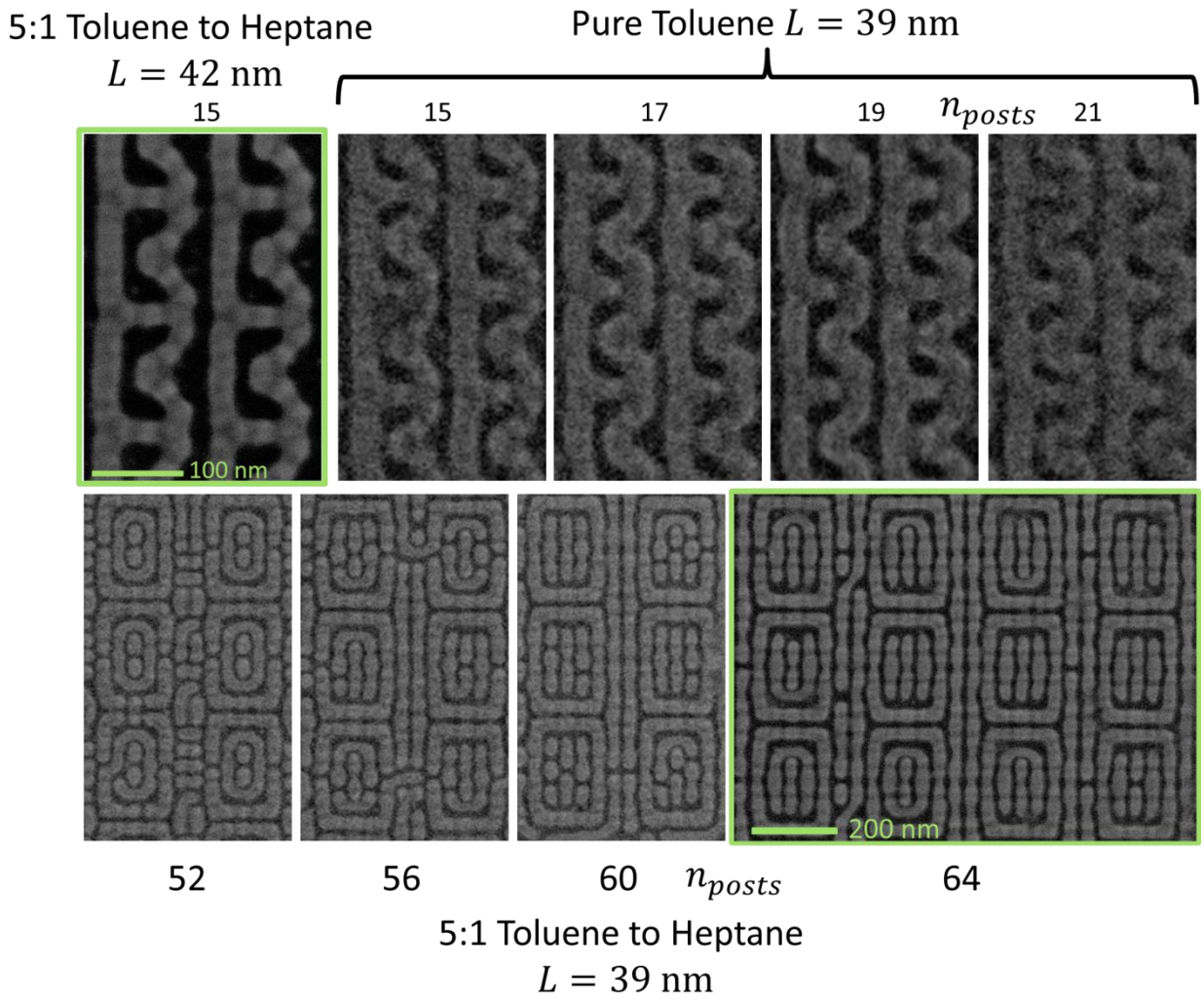

Figure 6-34: SEM images of oxidized PDMS self-assembled features templated by HSQ post patterns derived from inverse design simulations after reactive ion etching the samples. (Top) TS1 results under different L values and solvent annealing conditions. All TS1 patterns shown had correct topology over most of the sample. The best experimental result in terms of topology is highlighted, although the periodicity of this sample is larger than expected due to the effective fraction from the solvent vapor annealing conditions used. (Bottom) TS2 results under L = 39 nm with a 5 to 1 toluene to heptane annealing condition. The largest n_{posts} = 64 template gave the best results, but not completely optimized as there were many local defects[51].

Many additional experimental results for TS1 are shown in Figure 6.35 through Figure 6.42 with $L = 36$ to 43 nm and $n_{posts} = 15$ to 21 in increments of 2 and many results for TS2 are shown in Figure 6.43 through Figure 6.52 with $L = 34$ to 43 nm and $n_{posts} = 52$ to 64 in increments of 4. These templates correspond to the ones derived and

altered from the inverse simulations. TS1 was overall more robust in reproducibility over this range of parameters compared to TS2.

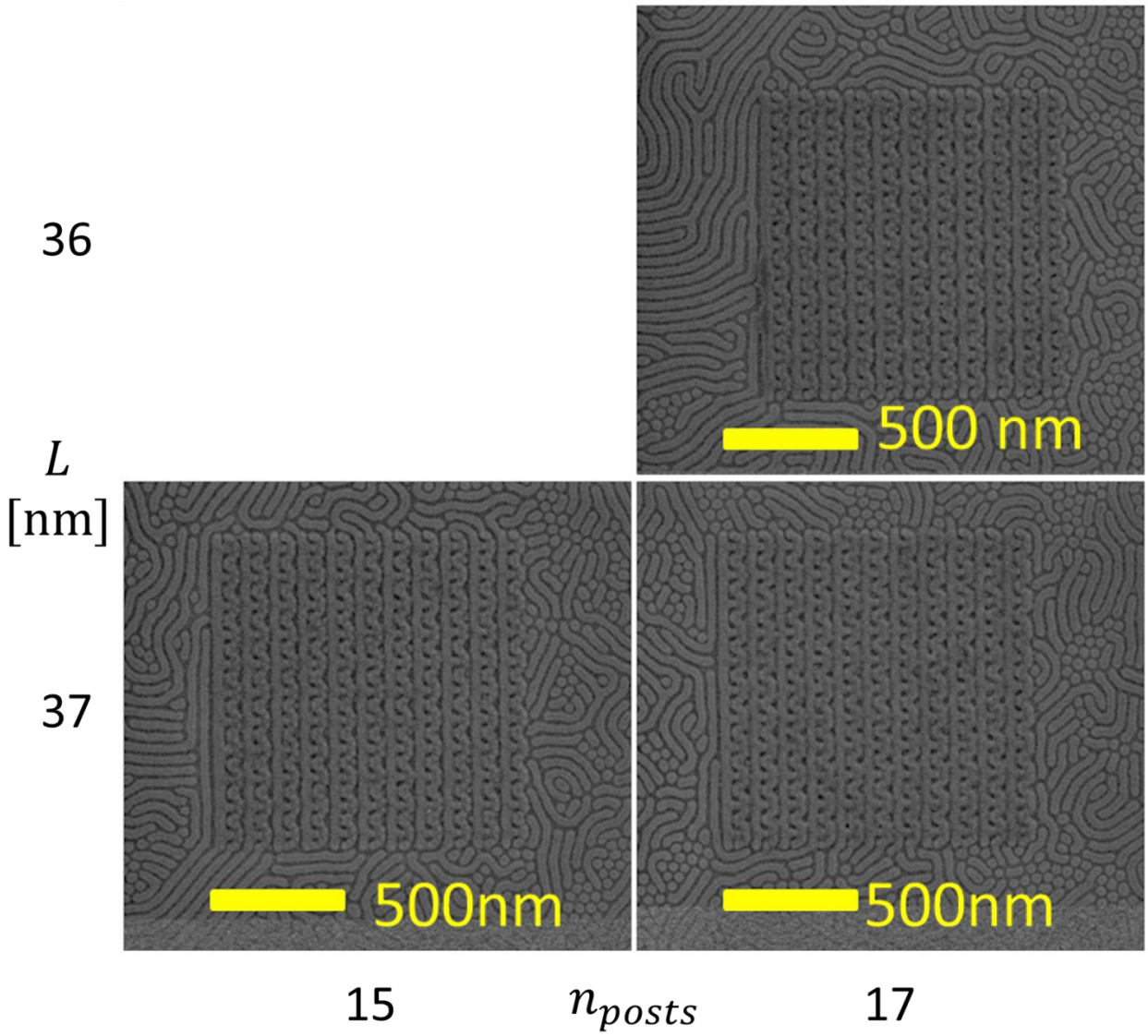

Figure 6-35: SEM images of PDMS patterns formed on templates designed for forming TS1 over a range of n_{posts} and L. Whole template areas are shown. Solvent annealing conditions are pure toluene vapor[51].

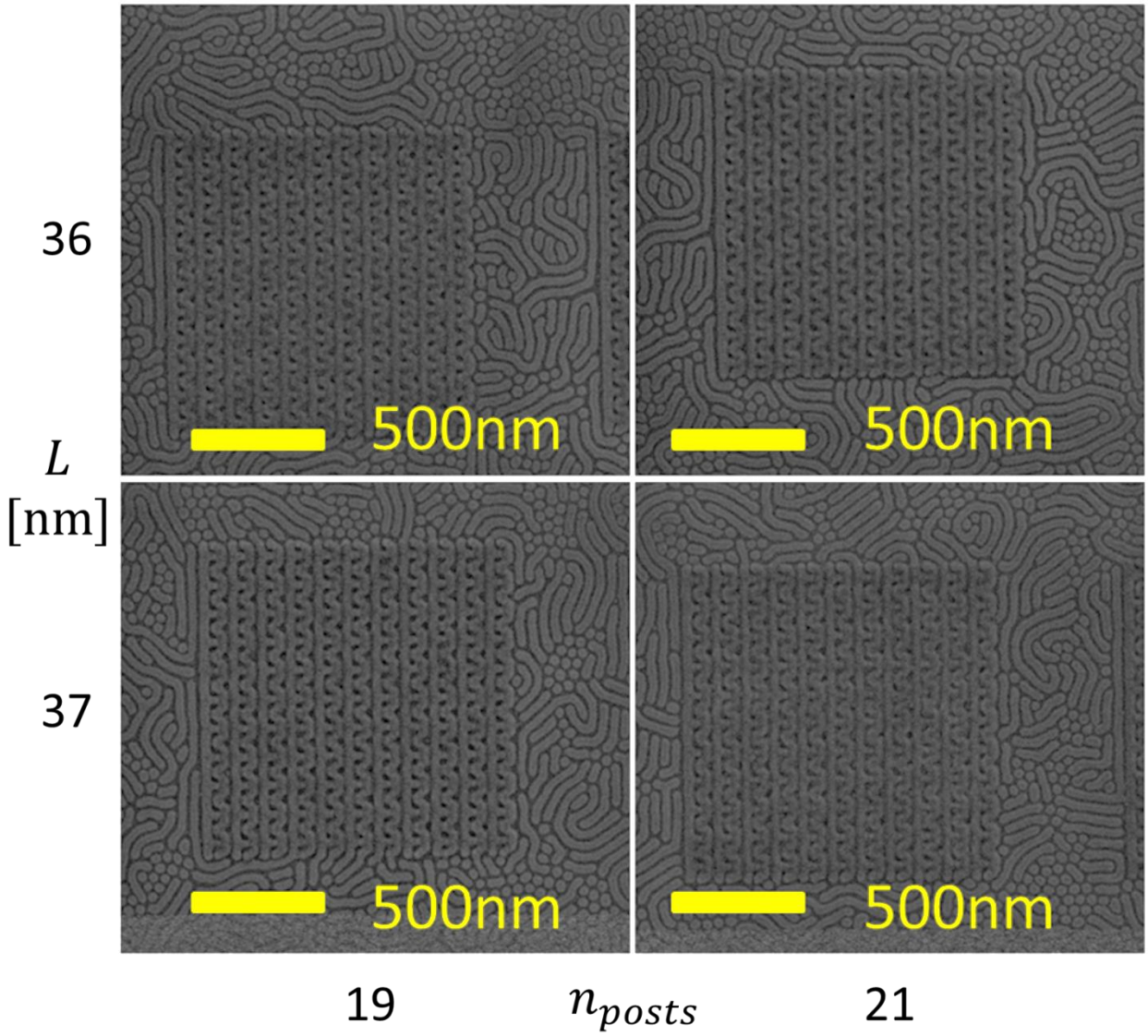

Figure 6-36: SEM images of PDMS patterns formed on templates designed for forming TS1 over a range of n_{posts} and L. Whole template areas are shown. Solvent annealing conditions are pure toluene vapor[51].

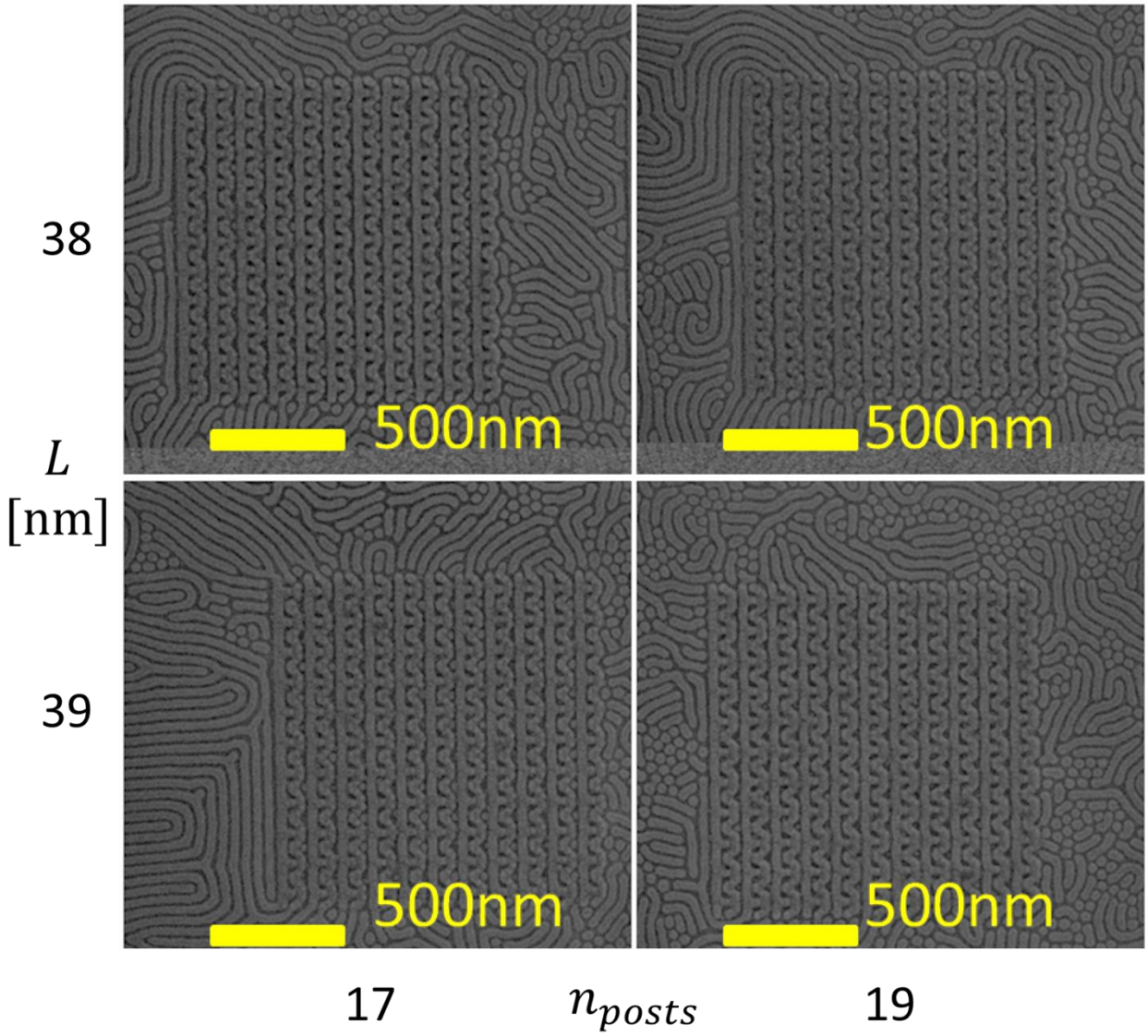

Figure 6-37: SEM images of PDMS patterns formed on templates designed for forming TS1 over a range of n_{posts} and L. Whole template areas are shown. Solvent annealing conditions are pure toluene vapor[51].

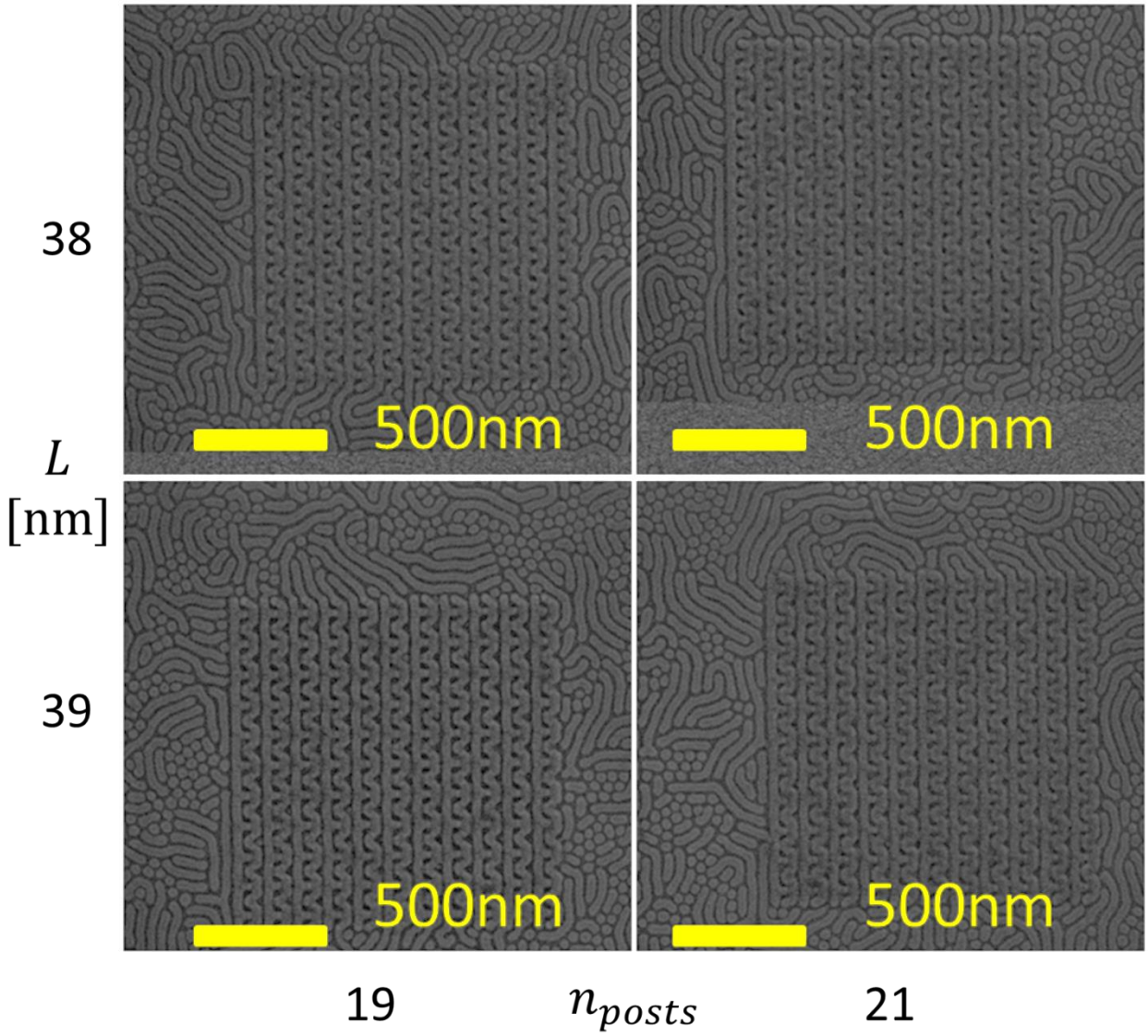

Figure 6-38: SEM images of PDMS patterns formed on templates designed for forming TS1 over a range of n_{posts} and L. Whole template areas are shown. Solvent annealing conditions are pure toluene vapor[51].

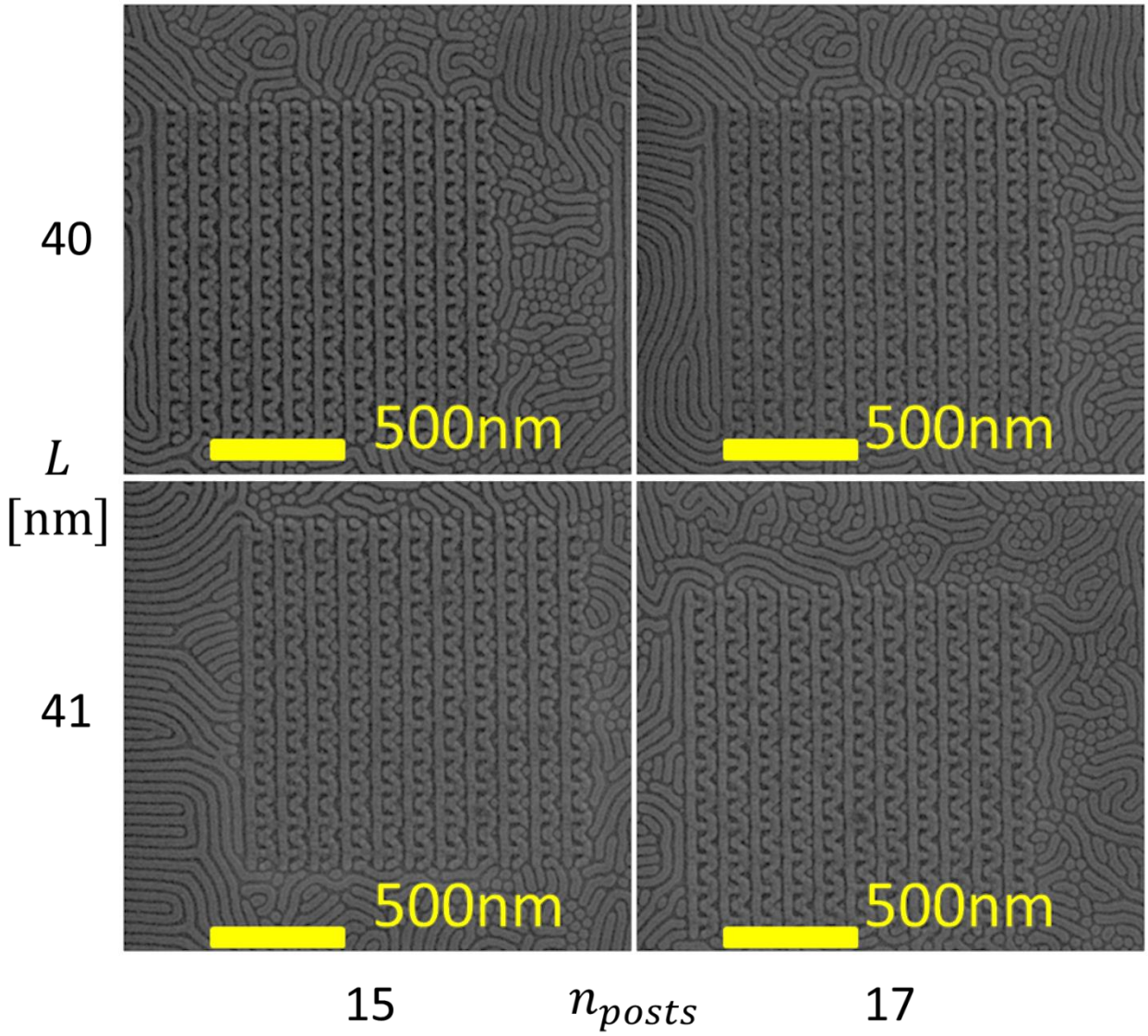

Figure 6-39: SEM images of PDMS patterns formed on templates designed for forming TS1 over a range of n_{posts} and L. Whole template areas are shown. Solvent annealing conditions are pure toluene vapor[51].

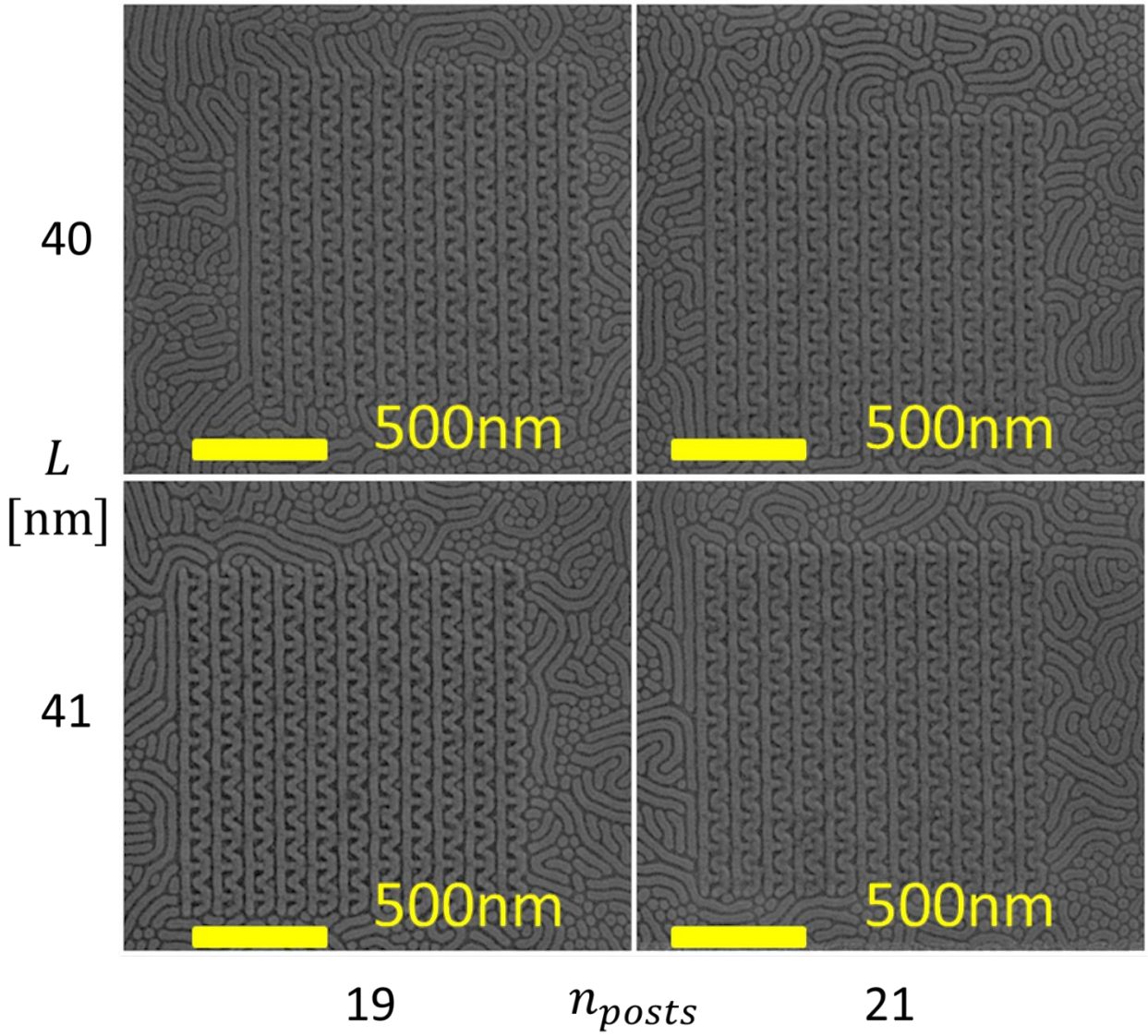

Figure 6-40: SEM images of PDMS patterns formed on templates designed for forming TS1 over a range of n_{posts} and L. Whole template areas are shown. Solvent annealing conditions are pure toluene vapor[51].

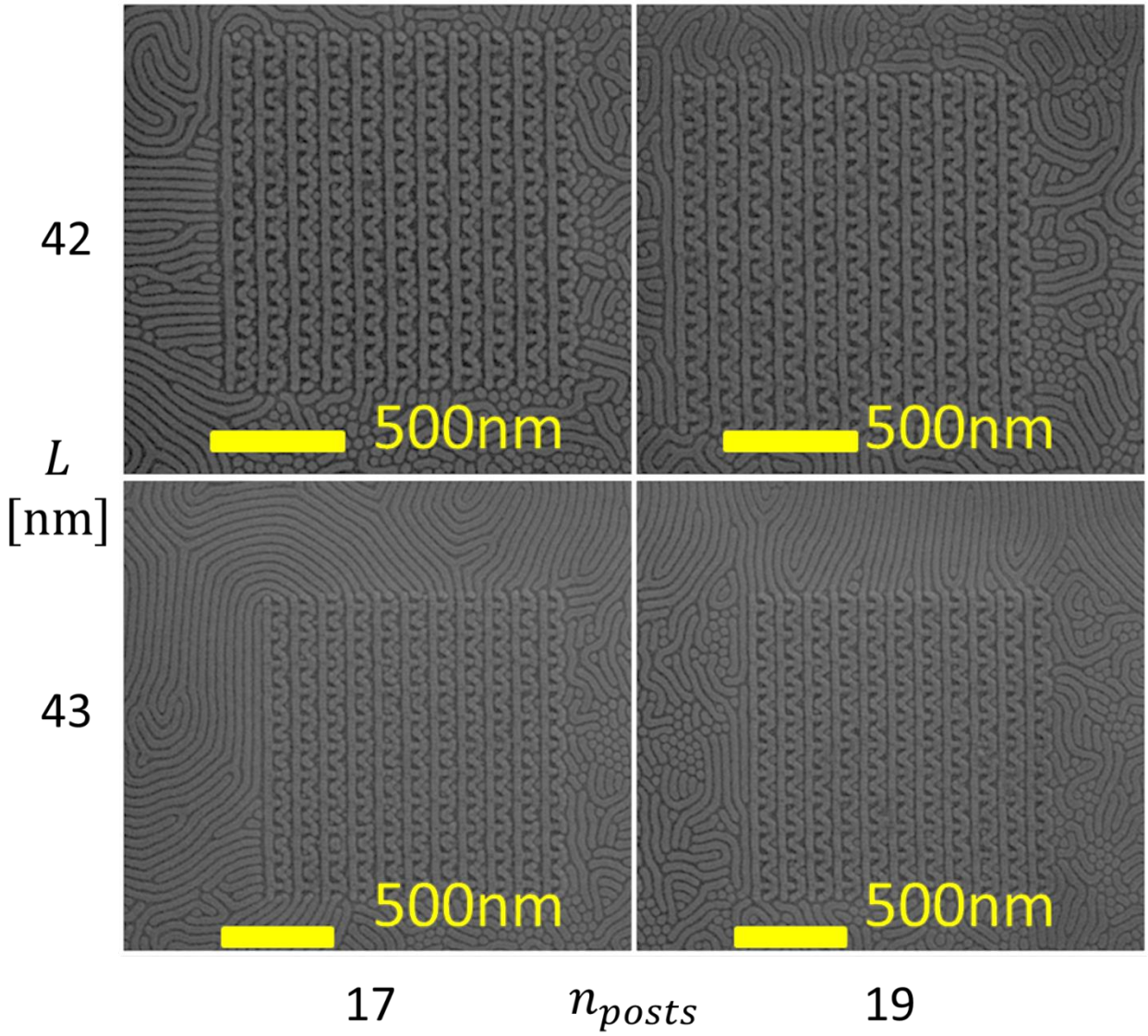

Figure 6-41: SEM images of PDMS patterns formed on templates designed for forming TS1 over a range of n_{posts} and L. Whole template areas are shown. Solvent annealing conditions are pure toluene vapor[51].

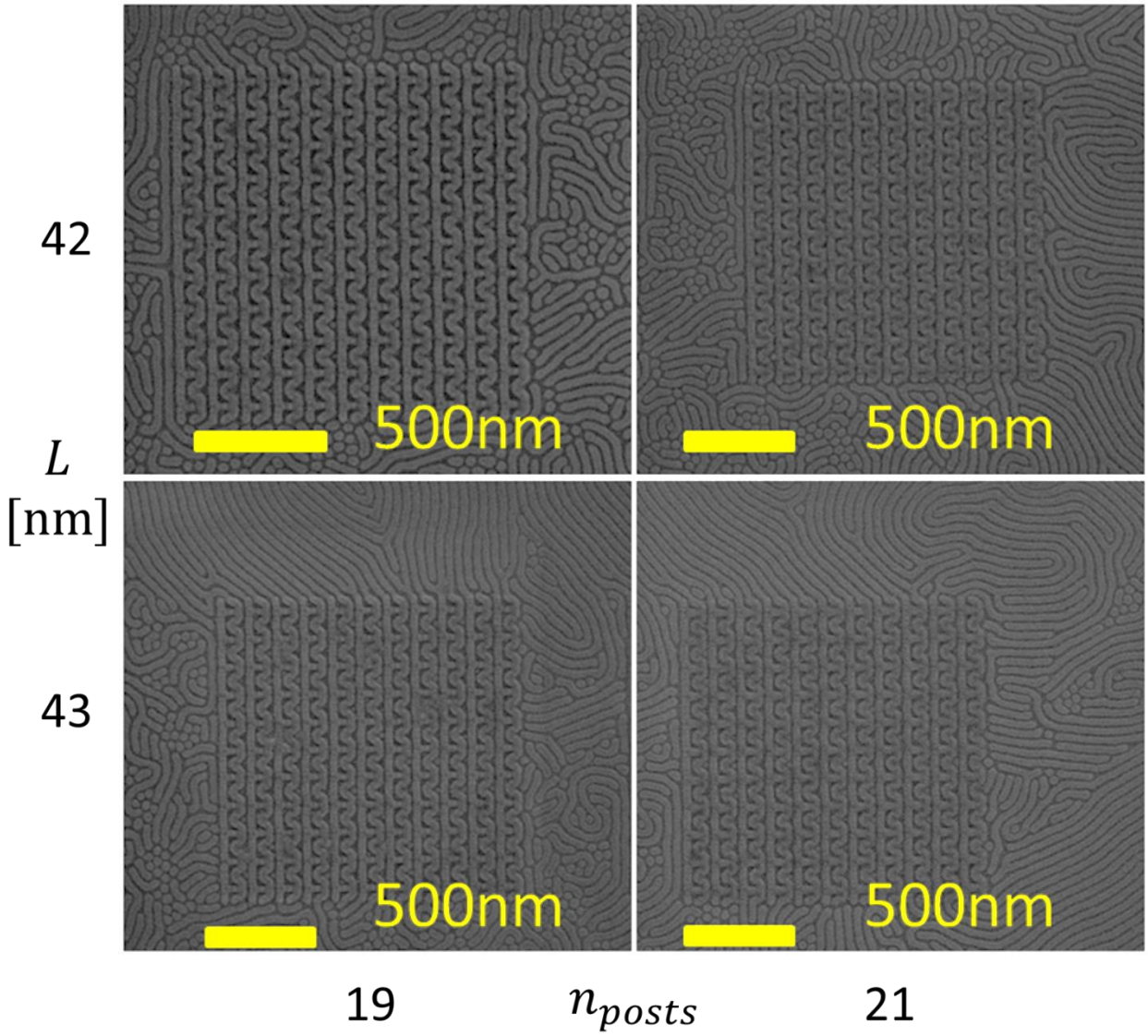

Figure 6-42: SEM images of PDMS patterns formed on templates designed for forming TS1 over a range of n_{posts} and L. Whole template areas are shown. Solvent annealing conditions are pure toluene vapor[51].

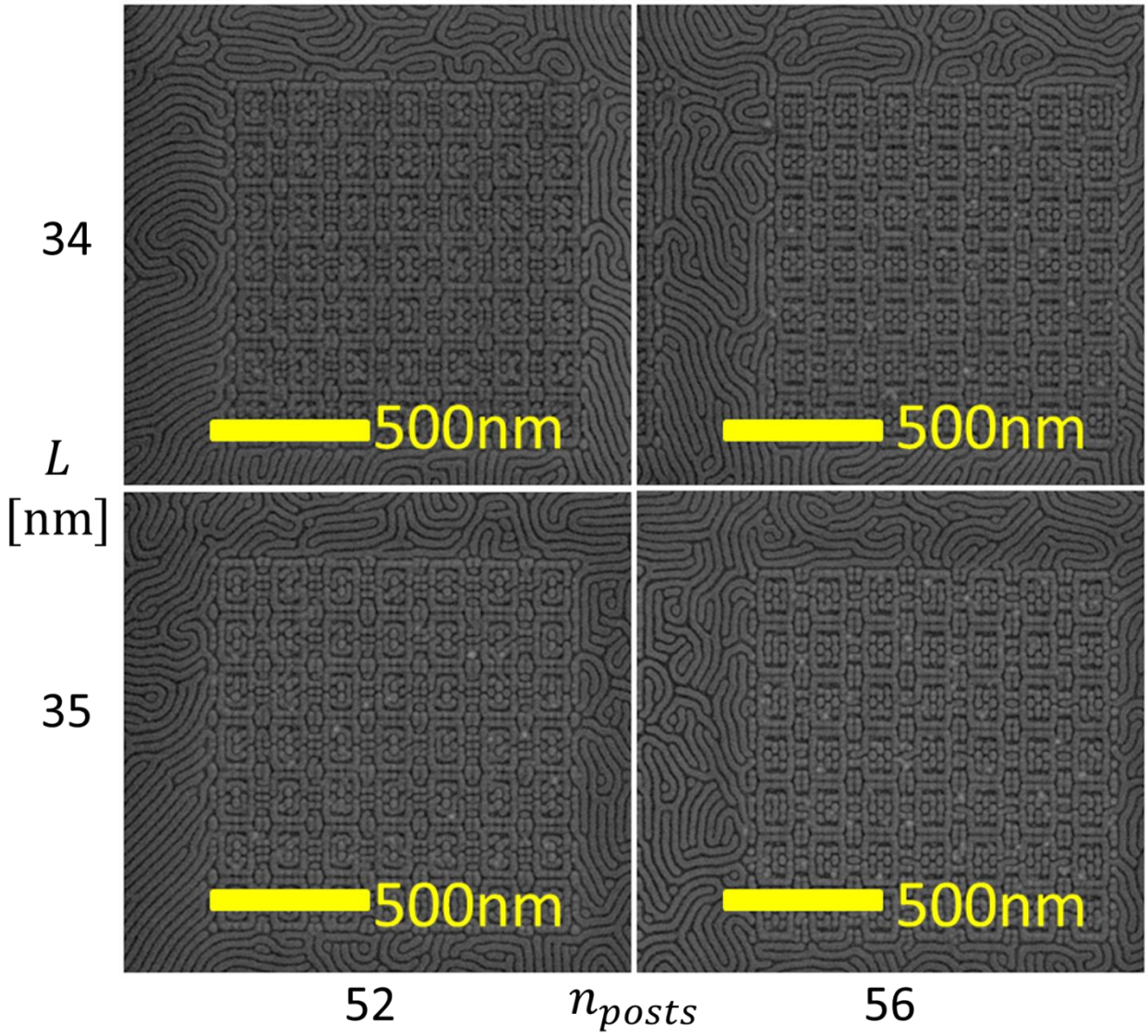

Figure 6-43: SEM images of PDMS patterns formed on templates designed for forming TS2 over a range of n_{posts} and L. Whole template areas are shown. Solvent annealing conditions are 5 to 1 toluene to heptane vapor[51].

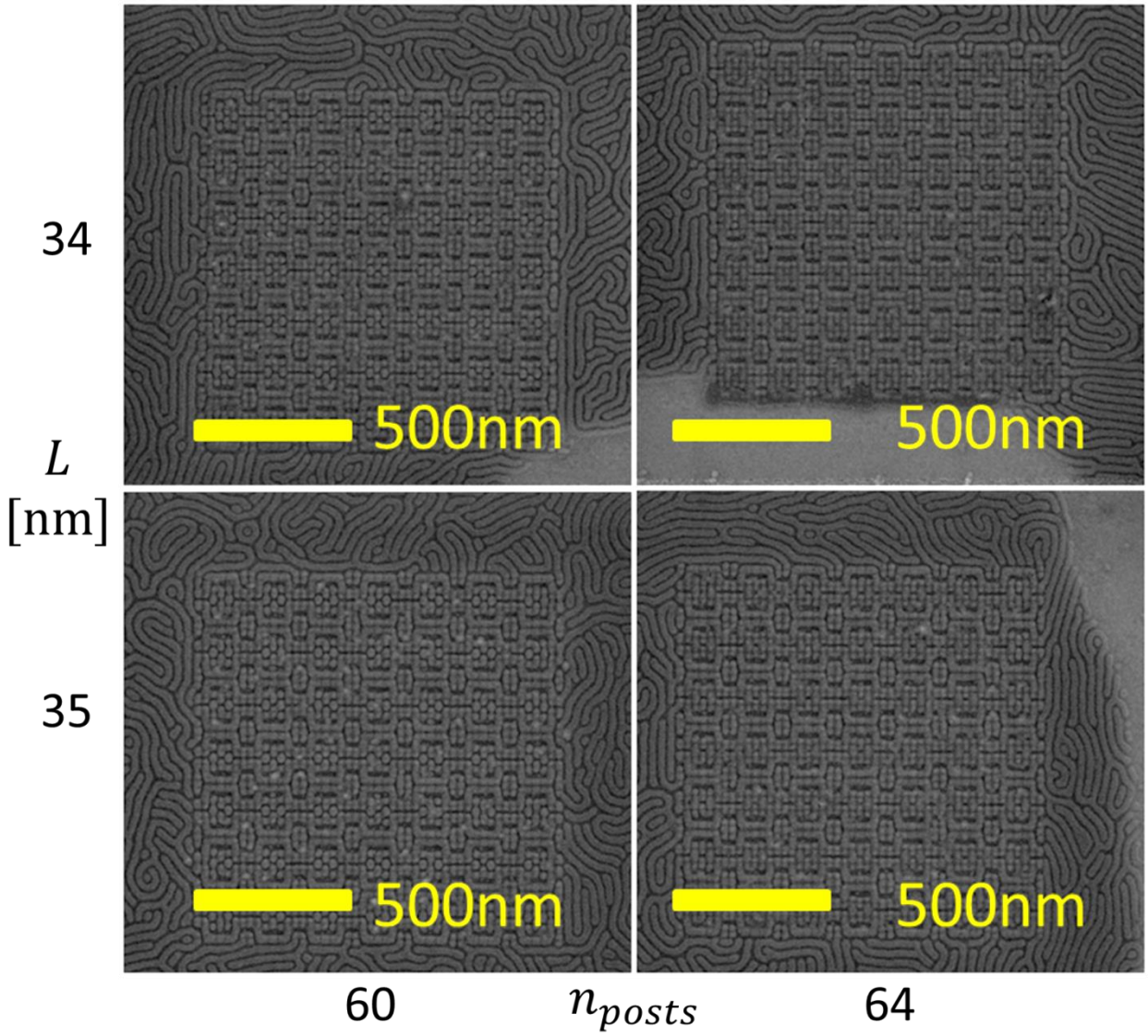

Figure 6-44: SEM images of PDMS patterns formed on templates designed for forming TS2 over a range of n_{posts} and L. Whole template areas are shown. Solvent annealing conditions are 5 to 1 toluene to heptane vapor[51].

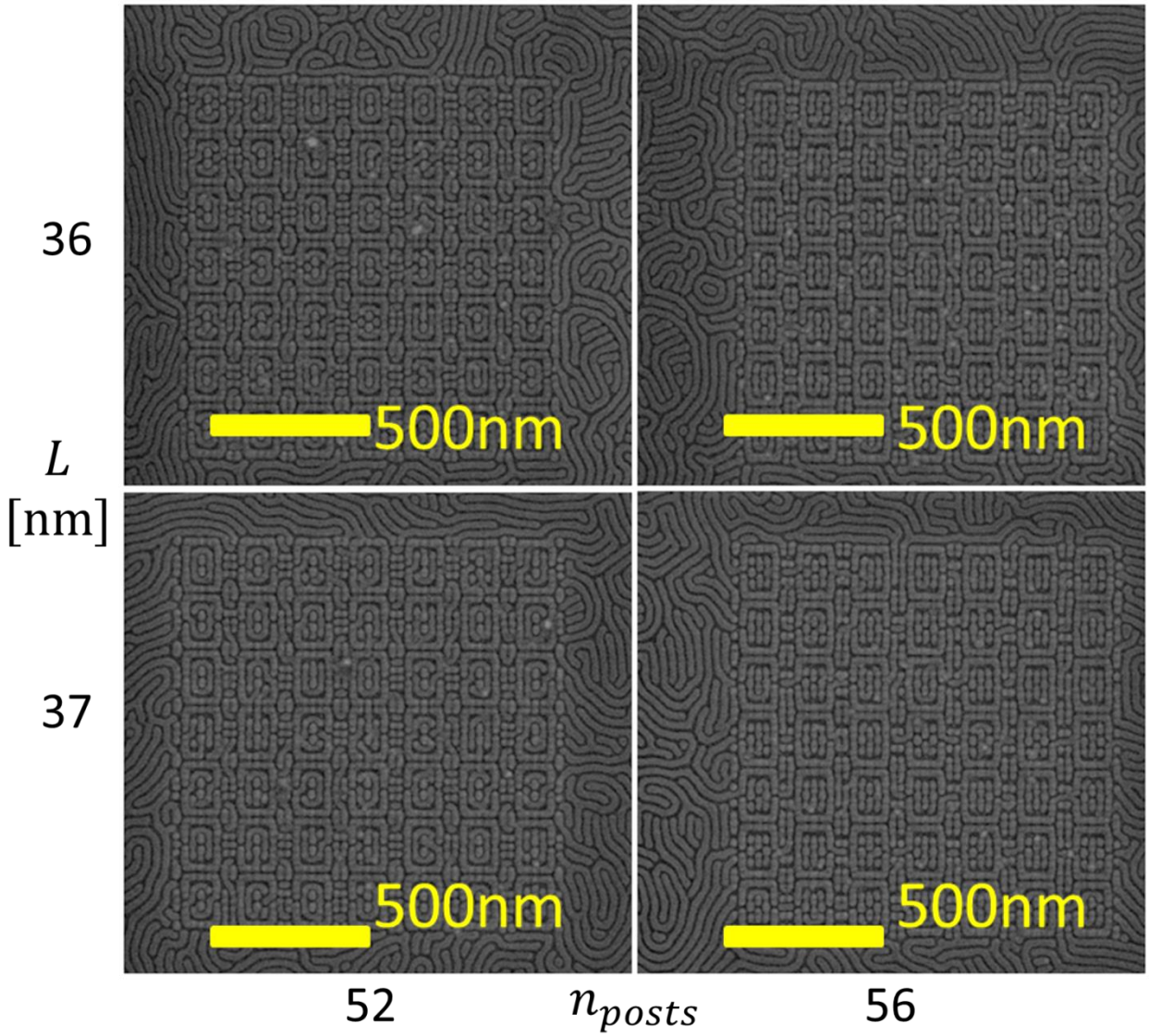

Figure 6-45: SEM images of PDMS patterns formed on templates designed for forming TS2 over a range of n_{posts} and L. Whole template areas are shown. Solvent annealing conditions are 5 to 1 toluene to heptane vapor[51].

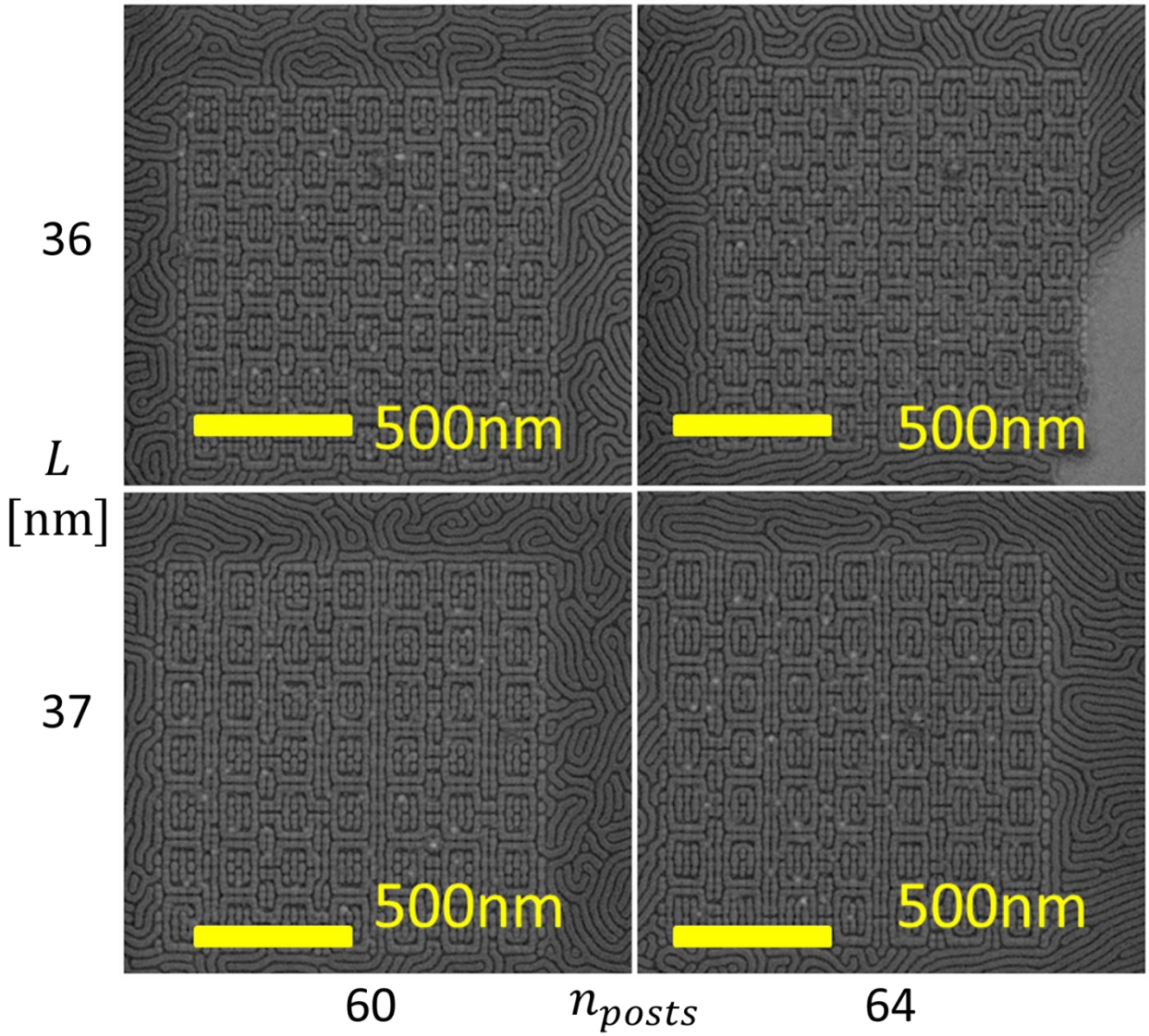

Figure 6-46: SEM images of PDMS patterns formed on templates designed for forming TS2 over a range of n_{posts} and L. Whole template areas are shown. Solvent annealing conditions are 5 to 1 toluene to heptane vapor[51].

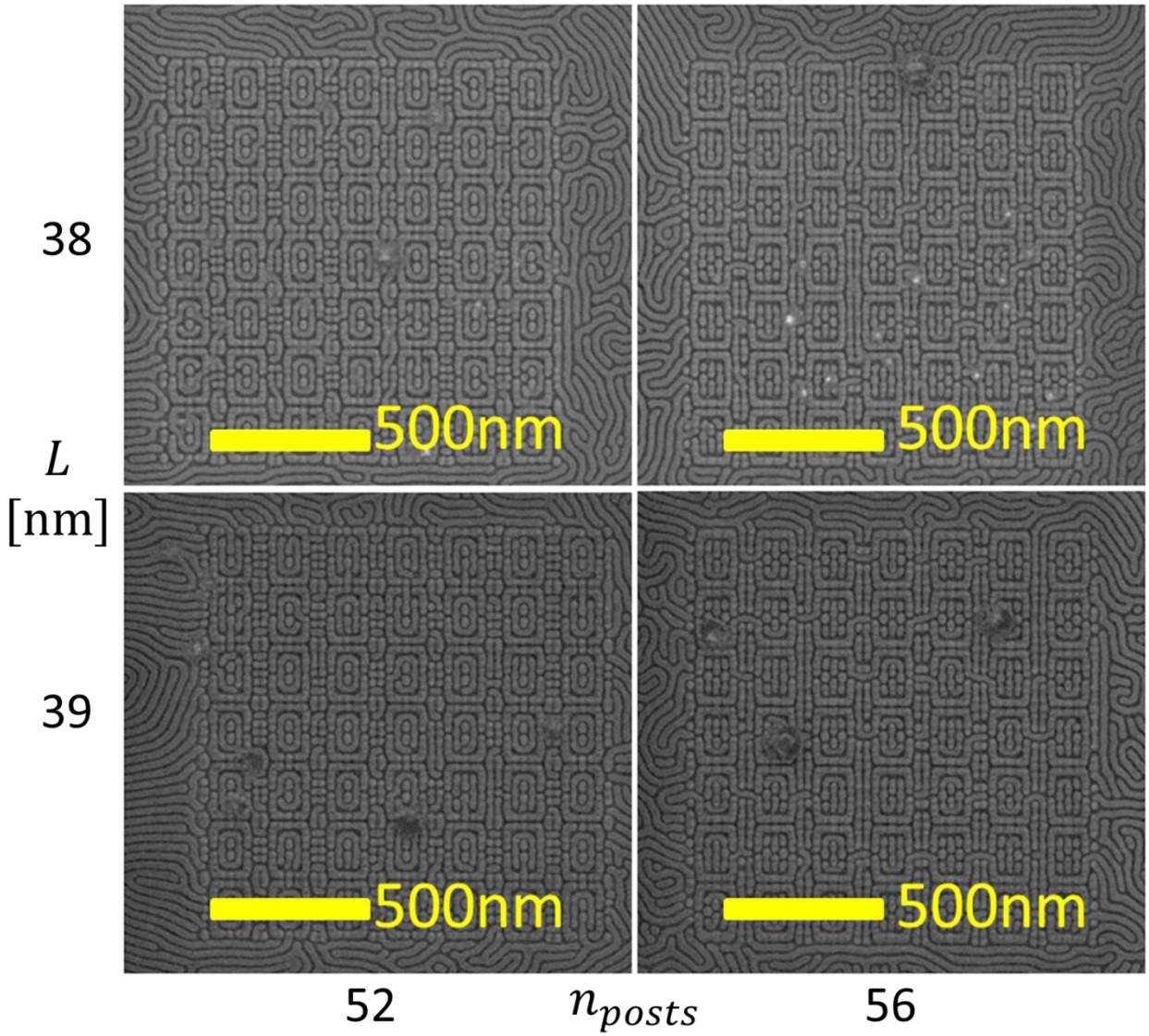

Figure 6-47: SEM images of PDMS patterns formed on templates designed for forming TS2 over a range of n_{posts} and L. Whole template areas are shown. Solvent annealing conditions are 5 to 1 toluene to heptane vapor[51].

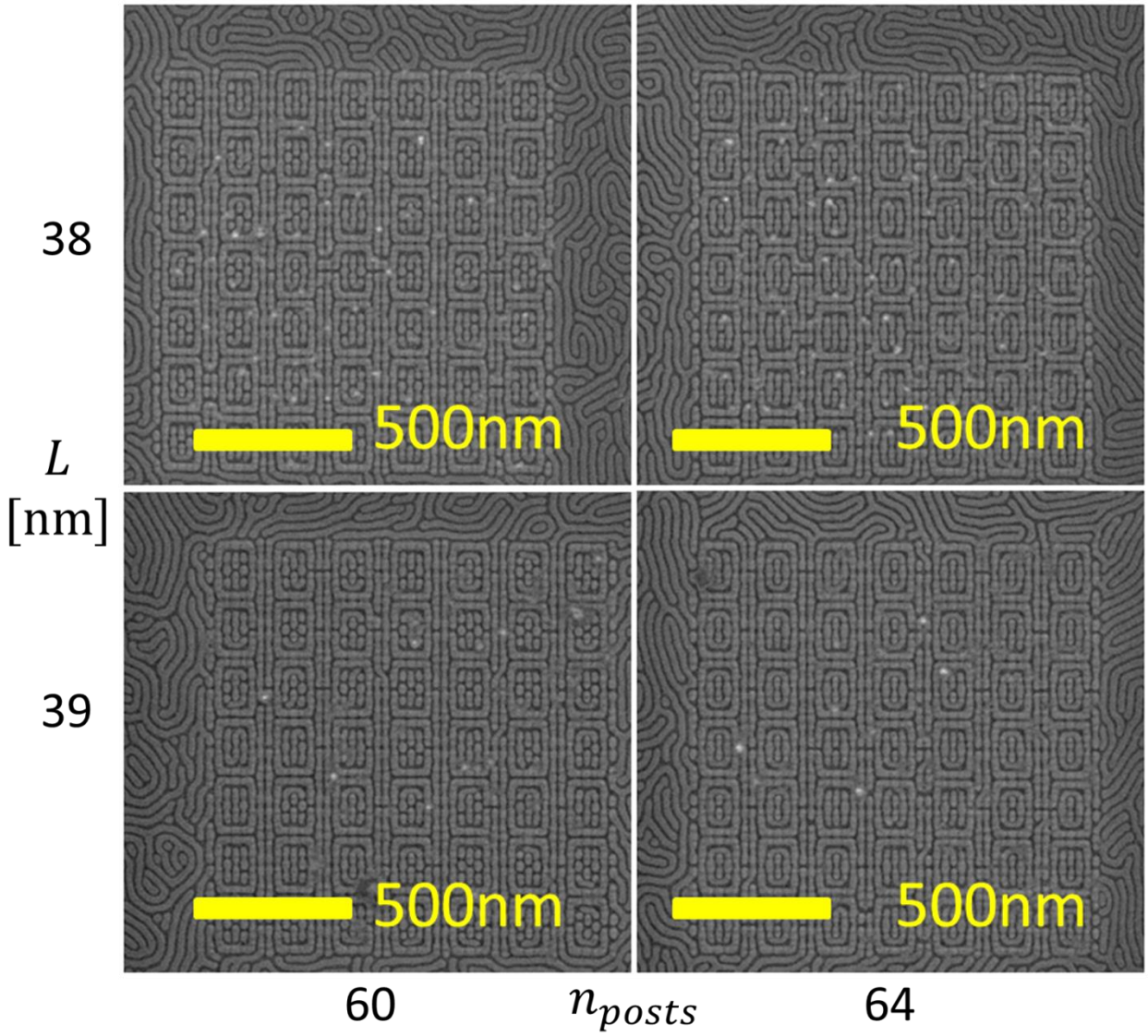

Figure 6-48: SEM images of PDMS patterns formed on templates designed for forming TS2 over a range of n_{posts} and L. Whole template areas are shown. Solvent annealing conditions are 5 to 1 toluene to heptane vapor[51].

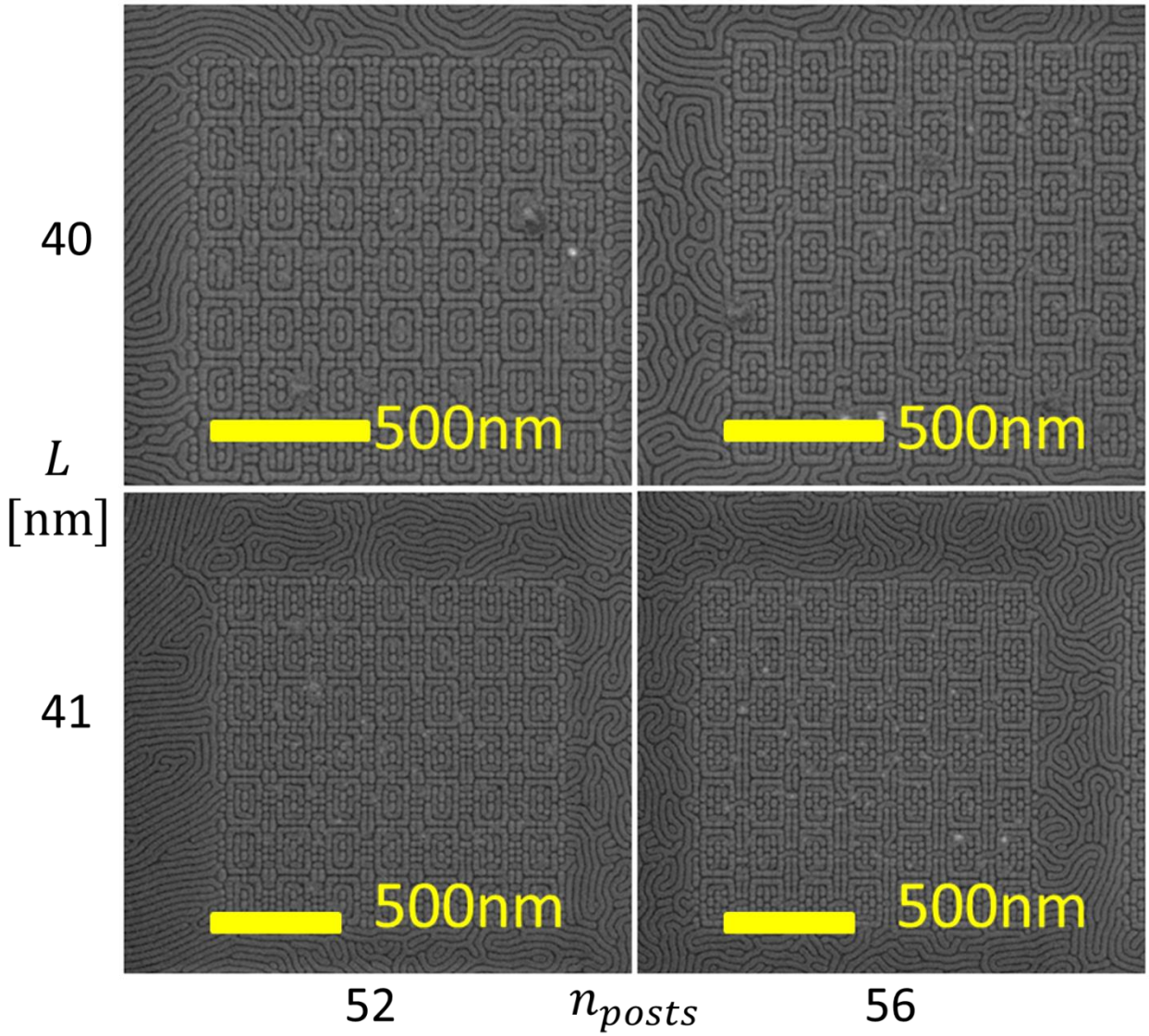

Figure 6-49: SEM images of PDMS patterns formed on templates designed for forming TS2 over a range of n_{posts} and L. Whole template areas are shown. Solvent annealing conditions are 5 to 1 toluene to heptane vapor[51].

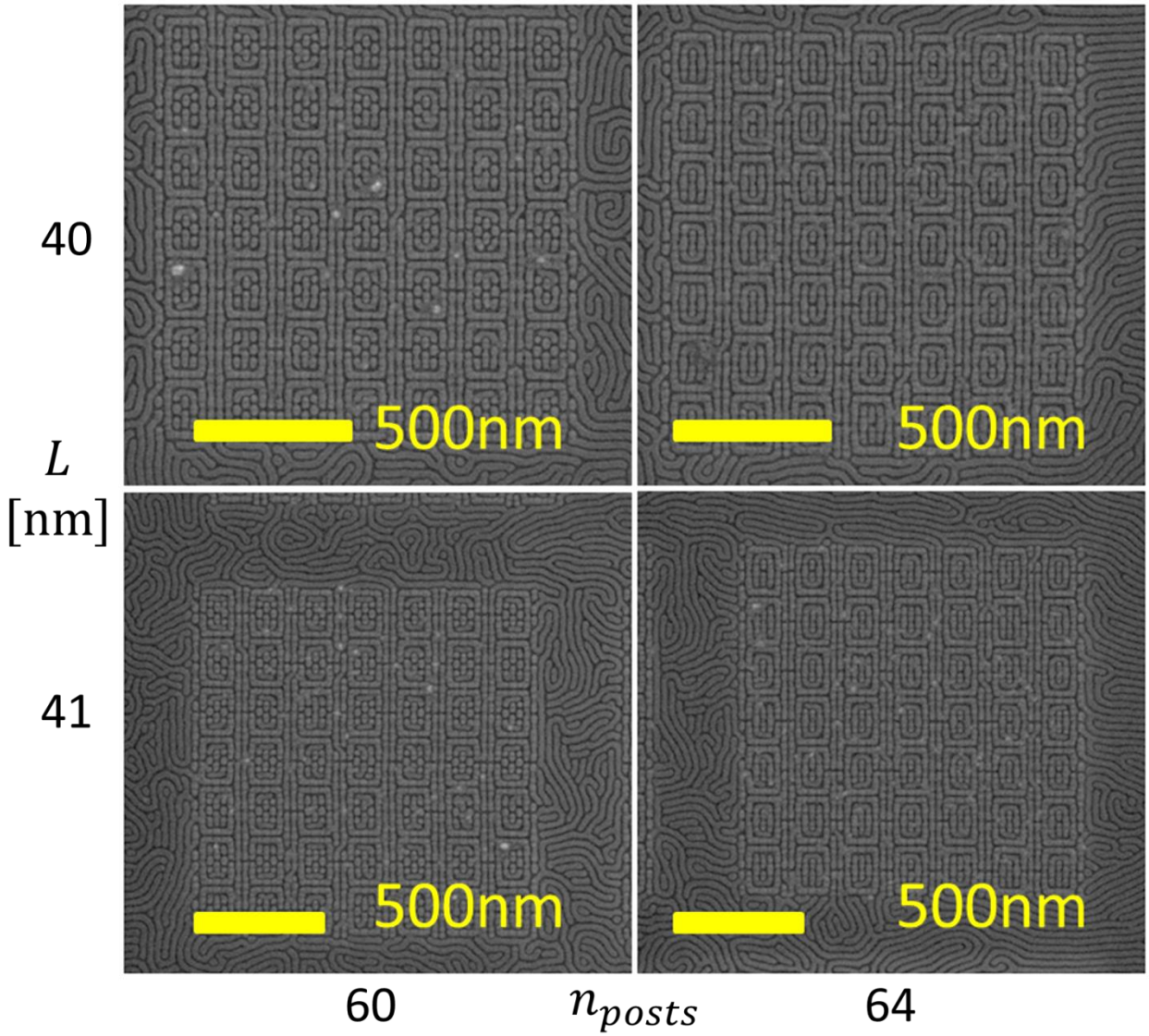

Figure 6-50: SEM images of PDMS patterns formed on templates designed for forming TS2 over a range of n_{posts} and L. Whole template areas are shown. Solvent annealing conditions are 5 to 1 toluene to heptane vapor[51].

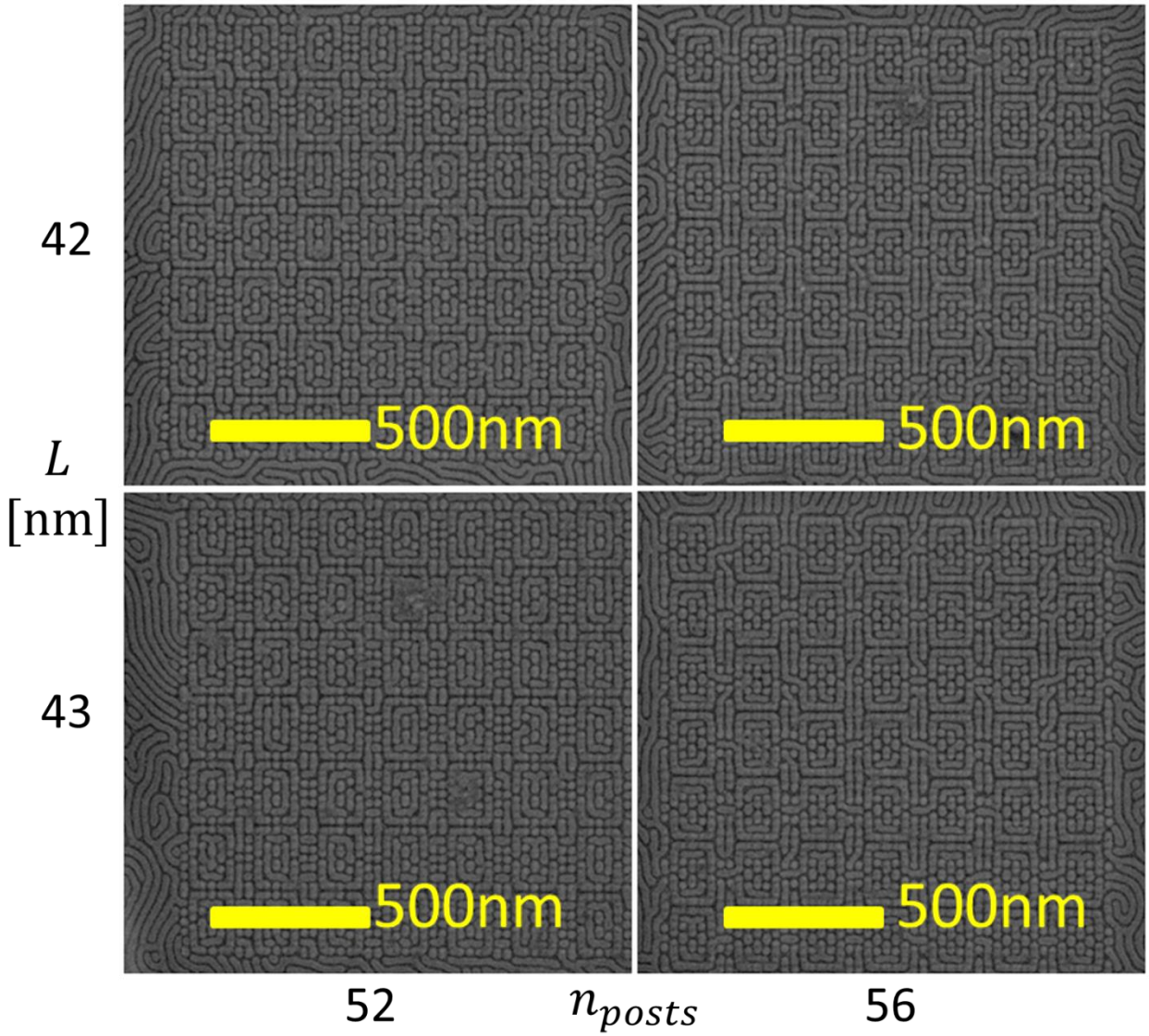

Figure 6-51: SEM images of PDMS patterns formed on templates designed for forming TS2 over a range of n_{posts} and L. Whole template areas are shown. Solvent annealing conditions are 5 to 1 toluene to heptane vapor[51].

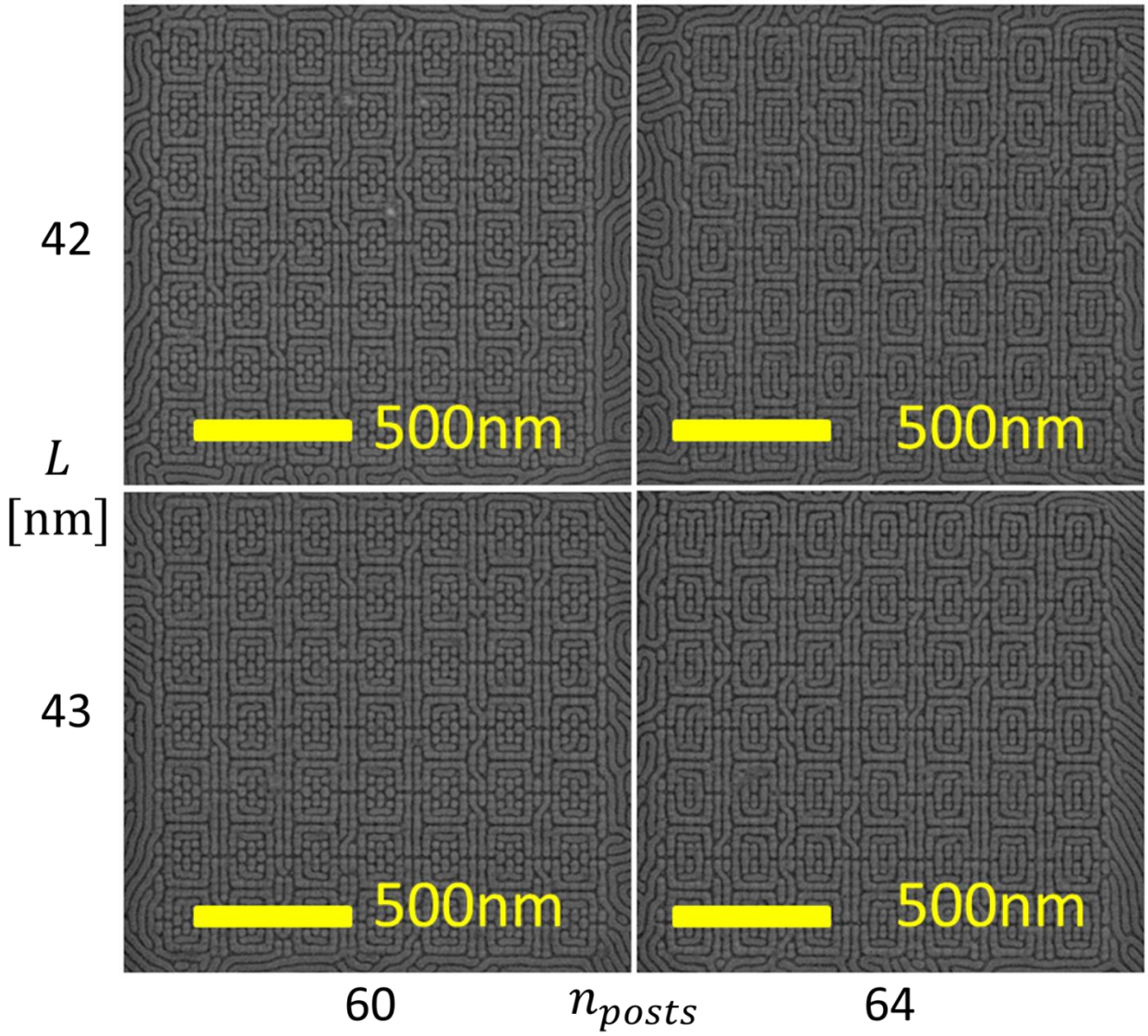

Figure 6-52: SEM images of PDMS patterns formed on templates designed for forming TS2 over a range of n_{posts} and L. Whole template areas are shown. Solvent annealing conditions are 5 to 1 toluene to heptane vapor[51].

6.5 Future Algorithm Modifications

The inverse design process as demonstrated shows great promise as a way of producing IC circuit patterns by only having to focus on a small range of patterns to produce desired target structures. Still, there remain many things that can be optimized in the algorithm. The current optimization scheme using a simple single post random walk move to find solution templates is limited in being able to converge toward consistent solutions for large

n_{posts} due to possibility for multiple posts with their original positions disallowing certain lower energy state solutions in terms of another post moving close to those posts.

In general, as shown in Figure 6.53, as n_{run} is increased, the post configuration solutions change when averaged over the many possible configurations found. In this particular case for TS1, increasing n_{run} from 150 to 2,100 drastically changes the post configuration solution template. Although both solutions are valid and converge to TS1 performing forward simulations, the $n_{run} = 2{,}100$ solution resulted in a $p_{thresh} = 0.2$ to keep 24 posts with mirror symmetry, whereas using that threshold value for the post probability density map for $n_{run} = 150$ results in many extra posts being kept in the system when accounting for symmetry implying extra degenerate posts were left in the system. Part of the reason for these issues is the post probability density map at low n_{run} is not completely symmetrical but becomes more symmetrical with larger n_{run} values. This demonstration shows that the algorithm itself can be improved upon by considering more complex move schemes such as an evolutionary algorithm as one recently proposed in solving the inverse design problem for chemically templated BCPs[207]. By using more advanced post configuration sampling algorithms, the necessary n_{run} needed to converge to an acceptable solution template should be greatly reduced.

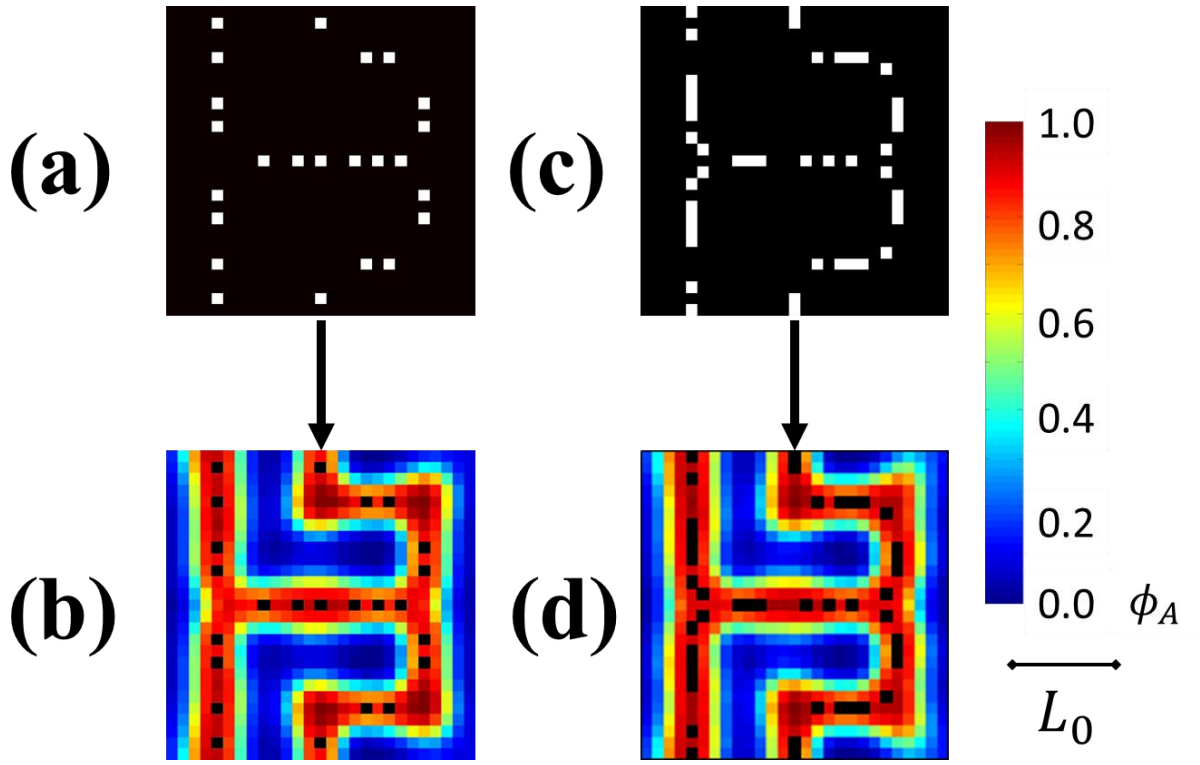

Figure 6-53: Comparison of inverse solutions for TS1 with n_{posts} = 24 and different n_{run} values. (a) n_{run} = 2,100 post configuration solution from inverse design algorithm. (b) Forward SCFT simulation result for post configuration solution in (a) showing TS1 is produced with correct topology. (c) n_{run} = 150 post configuration solution from inverse design algorithm. Low n_{run} value led to $p(\vec{\mathbf{r}})$ not being symmetrical and more than 24 posts being kept in the system when symmetry was accounted. (d) Forward SCFT simulation result for post configuration solution in (c) showing TS1 is produced with correct topology[50].

Another area for advancing the algorithm is using majority block preferential posts in addition to minority block preferential posts. There have already been many forward system studies on the effects of majority preferential posts[57,58,60] and thus applying such features in inverse design solutions is a simple progression in the field. As an example of a structure where majority preferential posts might be more beneficial to use in getting an inverse design solution, a square ring structure was tested using inverse simulations with both majority and minority preferential posts as shown in Figure 6.54. In this case, the minority preferential solution formed extra defect circular structures at the corners while the majority preferential solution formed the structure consistently with sharp corners. Thus there may be different solution space regions for different target structures

depending upon whether minority or majority preferential posts are used, or if possible a combination of both. There can even be a spectrum of neutral to slightly preferential posts tested, so in this regard there are many potential motif features that can be incorporated in the inverse design process simulations.

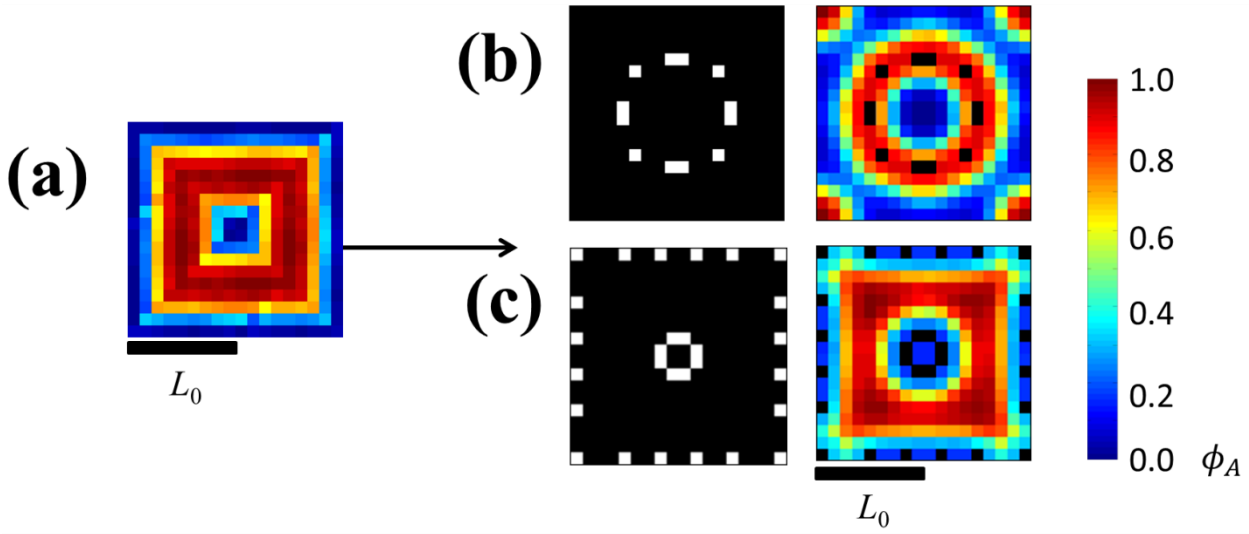

Figure 6-54: (a) Square ring target structure density map with size $2L_0$ by $2L_0$. (b) (Left) Inverse design solution for target structure in (a) using minority preferential posts where (Right) the resulting forward simulation results had defective dot structures rather than sharp corners. (c) (Left) Inverse design solution for target structure in (a) using majority preferential posts where (Right) the resulting forward simulation results produced the sharp corners of the target structure[50].

Converting the inverse design algorithm to 3D is already something possible but computationally expensive. By having the posts have a fixed height, similar move schemes can be applied to a thin film target structure with a fixed film thickness as shown in Figure 6-55. However, in order to get the best solution for such structures, film thickness and post height must also be optimized. Thus, not only does the computational time for these simulation increase by a factor $N_z \ln(N_z)$ but the parameter space that needs to be optimized increases as well. Since the 2D patterns already appear to give decent solutions, an alternative to full 3D inverse simulations is to just perform 3D forward simulations using post configurations derived from 2D inverse simulations and varying post height and film thickness trying to use appropriate 3D values of f. Examples of such simulations for TS1 are shown in Figure 6.56. By doing these simulations, parameters such as post height and film thickness can be optimized as well. Effects with post size can also be incorporated

initially into the inverse design simulations having the posts initially larger when performing the configuration sampling algorithm. Solvent annealing can be modeled explicitly rather than implicitly, especially if these 3D simulations are implemented.

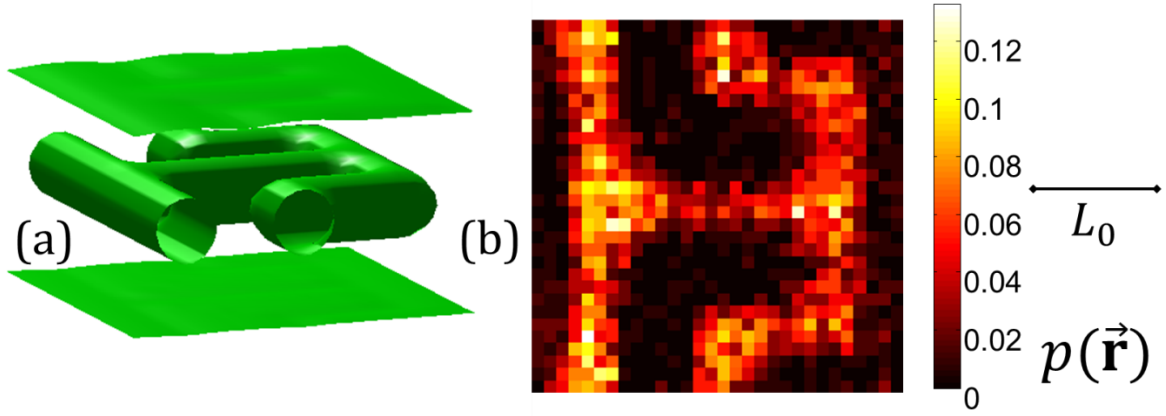

Figure 6-55: 3D inverse design simulation preliminary results. (a) TS1 represention in 3D showing the ϕ_A = 0.5 isosurface contours in green. Air and substrate wetting conditions are assumed to make PDMS surface layers and internal morphology is that of connected cylinders. (b) Post probability density map $p(\vec{\mathbf{r}})$ for several inverse simulations for 3D TS1 in (a) with several posts with post height L_0 in a $2L_0$ thick unit cell. The small number of simulations performed did not allow for a clear convergence to an obvious post configuration solution. Since many simulations are necessary for such a convergence and the 3D simulations are computationally expensive, an improved movement algorithm is necessary before continuing such 3D inverse simulations.

As made apparent by the fact a given target structure can have many potential inverse solutions, additional solution characterization criteria should be considered. An example of multiple post configuration solutions for the same number of posts is demonstrated in Figure 6.57 for another target structure containing three-way junctions and terminations where one solution was guessed using design rule principles for three-way junctions and the other determined by the inverse algorithm. In this example, $n_{posts} = 28$ for both post configurations, yet in the guess solution case no posts where required in the termination line regions, rather they were just templated by the surrounding PDMS lines. Possible distinguishing characteristics between solutions could be free energy, fidelity, and line edge roughness as the topology criterion is met for both.

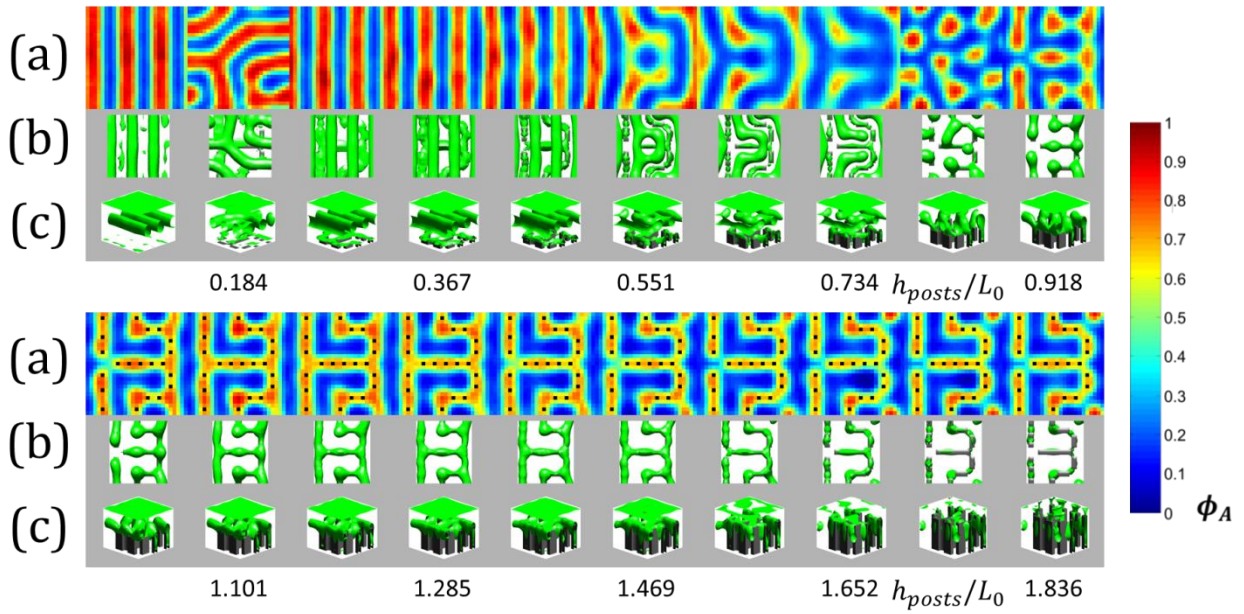

Figure 6-56: Forward 3D SCFT simulation results varying the height of the posts h_{posts}/L_0 using the altered n_{posts} = 15 solution for TS1 using a constant film thickness of $2L_0$ (N_z = 20) thought to be commensurate with a monolayer of PDMS cylinders with a top and bottom PDMS surface wetting layer. As h_{posts}/L_0 increases, the morphology changes from a commensurate monolayer of cylinders to something similar to the target structure, although there are always defects. The closest structures to the target structure occurs for $h_{posts}/L_0 \geq 1$. (a) 2D cross-section using density color bar on right for ϕ_A showing density of PDMS half way up film thickness. (b) Top-down view of 3D density isosurfaces for ϕ_A = 0.5 in green. (c) Side view of 3D density isosurfaces for ϕ_A = 0.5 in green and posts colored grey.

Already the fidelity function ξ and Ξ as well as topology criterion η help to distinguish better solutions after the inverse algorithm has been performed over a set of parameters. In future work, the fidelity function can be incorporated into the inverse algorithm itself to try to optimize the solutions during the inverse simulation with respect to n_{posts} and f rather than afterwards. As an example, rather than accepting solutions based on minimizing the free energy H, ξ was minimized as the optimization criteria for TS1 and as shown in Figure 6.58 that both H and ξ decreased through the course of the simulation. This coupled decrease implies both parameters should be considered as optimization parameters in a single inverse design simulation. Other such parameters that characterize line edge roughness or other feature distinguishing quantitative functions can be used as well.

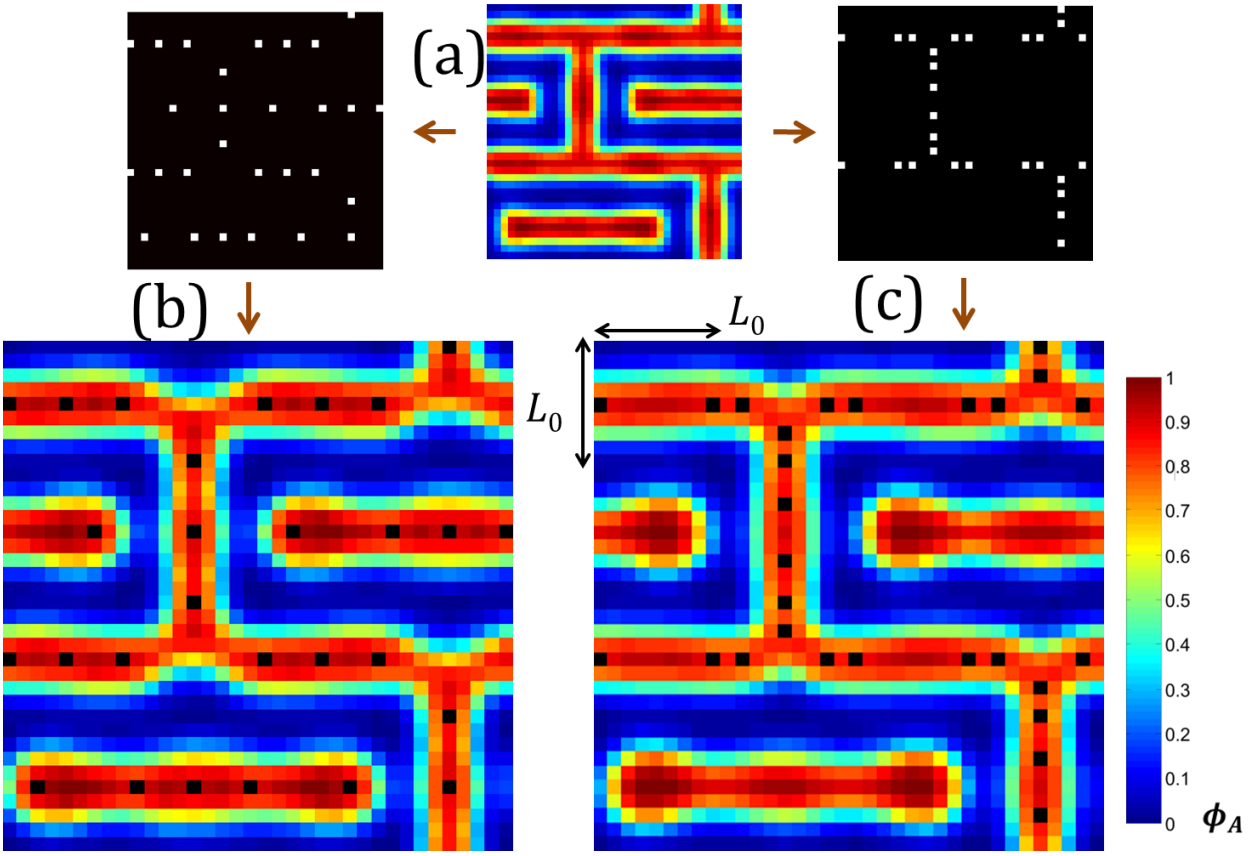

Figure 6-57: Demonstration of multiple potential solutions to the inverse problem for a given target structure. (a) Target structure with three-way junctions, lines, and terminations. (b) Inverse design algorithm solution determined for the target structure with n_{posts} = 28 and f = 0.44 with (Top) post configuration positions and (Bottom) forward simulation result showing correct topology for the target structure. (c) Guess solution using the design rule principles learned for forming three-way junctions by having posts near the junction but not inside the junction using 28 posts at f = 0.44 with (Top) guessed post configuration and (Bottom) forward simulation result showing correct topology for the target structure.

One other advancement of the algorithm that can be performed in how each H or ξ comparison value is calculated. Rather than performing hundreds of individual SCFT iterations until the corresponding chemical potential fields are relaxed for the held constant target densities, target structure chemical potential fields can be used instead that simply have the post features added to their values and a single forward SCFT iteration performed to develop the corresponding relaxed density fields. Such a method cuts computational time down by a factor of 100 or better, but only works as good as the developed chemical potential fields correspond to the actual target structure density fields.

Using the density fields as the target structures in general is the conservative approach since they are more easily developed than chemical potential fields.

All these areas of potential improvement show that these inverse design algorithms are still in their infancy in implementation. However, the fact the resulting solutions are already adequate enough to produce some experimental target patterns means there is great potential for continuing to develop the algorithms to investigate the large parameter space of BCP DSA. Once all these future modifications are implemented, the potential for solving for any necessary template to produce an arbitrary complex pattern will be greatly enhanced and the ability to use BCPs to form IC circuit patterns at the smallest length scales will be limitless.

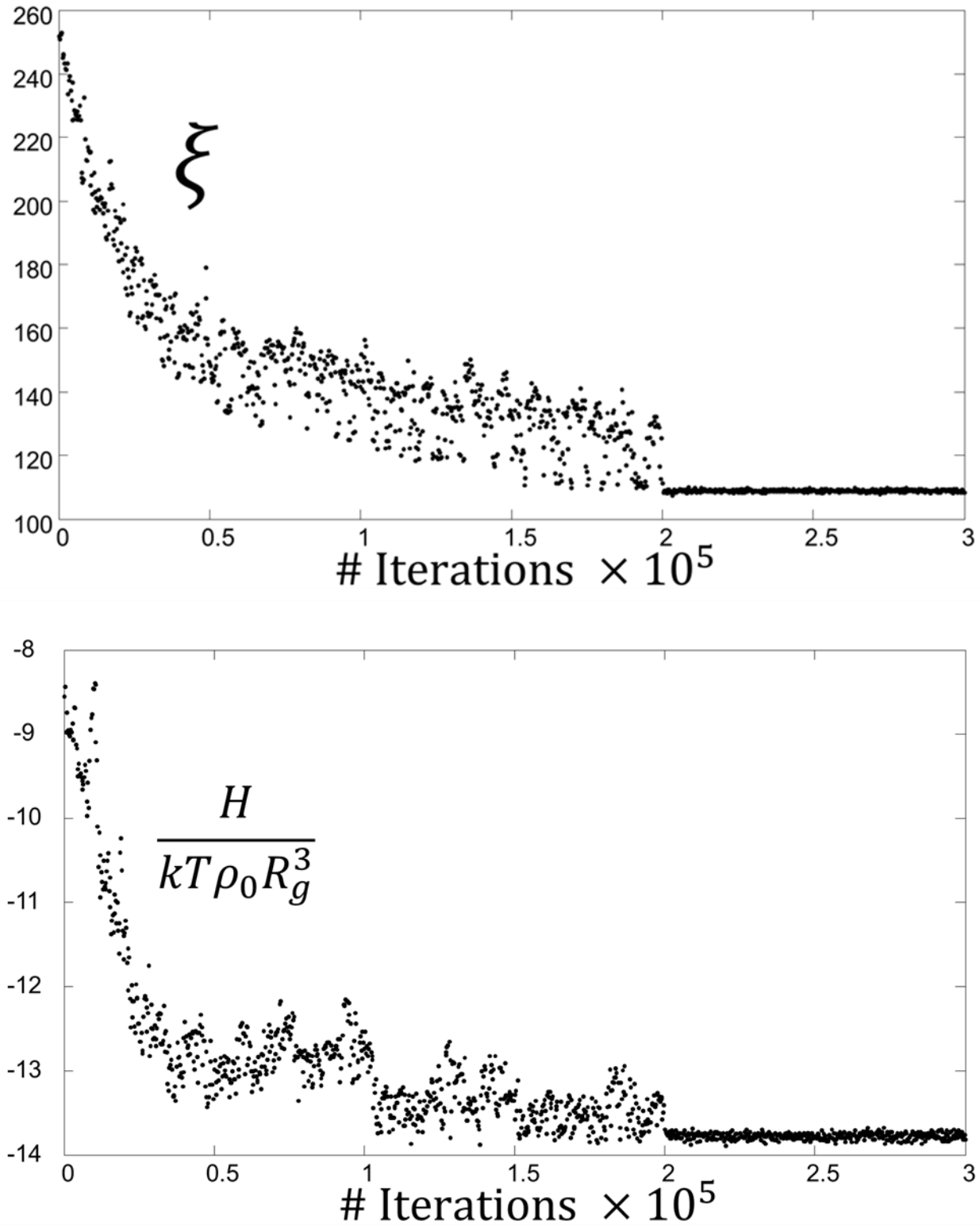

Figure 6-58: (Top) Plot of ξ as a function of individual SCFT iterations in an inverse design algorithm simulation for TS1 where ξ is minimized as the optimization criterion for accepting or rejecting post configurations rather than the free energy H. (Bottom) Plot of

corresponding $H/kT\rho_0 R_g^3$ as a function of individual SCFT iterations for an inverse simulation where ξ was the optimization variable minimized rather than H. Interestingly H decreases as the fidelity factor ξ is minimized implying both parameters are essential in optimizing the solutions toward the best inverse design solutions.

6.6 Summary

A method for determining the necessary DSA template to produce a given target pattern containing essential IC circuit components such as lines, bends, junctions, and terminations concatenated in an complex fashion using an inverse design algorithm has been computationally and experimentally demonstrated. Using an SCFT framework with posts modeled as chemical potential field boundary conditions, forward simulation results test and show that post configuration solutions can be found under a wide range of parameters of f and n_{posts} for different target structures after obtaining the inverse algorithm solution. Optimization under these parameters is performed through fidelity and topology considerations. Design rules for obtaining essential component structures that are not intuitive are easily inferred from the results and can be combined with the inverse design algorithm itself to enhance the design process for general lithographic patterns.

Compared with the inferred design rule method using a restricted square array of posts with double post motifs, the inverse design method appears to be more generally applicable for arbitrary patterns containing essential IC components. While the square array design rule method has the advantage of template fabrication being well controlled and more easily parallelizable for template writing, the method has higher rates of defect structures for various combinations of design structure components whereas the reproducibility rate for the inverse design method is very high if the most optimum template is found as was the case for TS1. Still, both methods need optimization in different ways to better optimize the methods such as the fact TS2 had issues with stabilizing terminations with the current size of post features while the square array design rule method needs less restrictions on motif location to generate all essential IC components. In essence, each method aids the other as design rules can be inferred from the inverse design

algorithm and the square array approach gives insight into better ways of fabricating posts in close proximity that come about in solutions of the inverse design method.

Experimental confirmation of the inverse design method using cylinder forming PS-PDMS gives great validity to the method showing the importance of f and the volume of the posts in obtaining the desired pattern, although there are still many places where the model is not completely adequate in explaining experimental behavior. Many areas for optimizing the algorithm to alleviate these discrepancies exist including using more advanced sampling algorithms such as evolutionary algorithms as opposed to the current simple stochastic random walk algorithm, using majority and neutral preferential post features in the design process, performing inverse and forward confirmation simulations in 3D, using larger post sizes closer to real EBL fabricated posts in the inverse simulations themselves, modeling solvent explicitly, using additional target structure comparison criteria functions such as the fidelity functions in the algorithm itself rather than afterwards on a larger parameter space, and optimizing parameters like f besides the post positions in the inverse simulations themselves rather than by keeping them constant and running multiple inverse simulations over many values of those parameters. Still, as currently implemented the algorithm has already demonstrated great potential in solving many DSA problems not easily solved by empirical methodology.

Chapter 7

Conclusion and Future Work

7.1 Suggested Future Work

The work presented in this thesis has demonstrated the potential of BCP DSA to fabricate patterns for IC circuits and other complex devices with feature components that can be shrunk in size to sub-10 nm[2,10,12,34,47,64,67,72,142,156,171,172,194,205,206,208–212]. Through the use of a variety of computational methodologies in an SCFT framework, simulations have enabled the prediction of morphologies under a wide range of boundary conditions[48,213–222]. As outlined in Chapter 2, this theoretically framework[53,54] has allowed the modeling of solvent vapor annealing demonstrated in Chapter 3 both implicitly and explicitly[59,223]. As discussed in Chapter 4, thin film systems can be handled easily using proper assumptions about film thickness and surface energy constraints[55]. As discussed in Chapter 5, adding topographical template features to direct the self-assembly in these thin films allows for seemingly limitless possible combinations of local morphologies by controlling template boundary condition parameters[49,56–58,60,61,200]. As discussed in Chapter 6, by inverting the design process of these topographical templates by starting with the target self-assembled patterns rather than constrained templates, almost any concatenable pattern with a subset of base components can be designed and template rules for making that pattern achieved through inverse design simulations[50,51,201]. Combining all the nuances of the various simulation parameters allows for a great design tool in experimental fabrication where reliance on trial and error is not affordable.

There are still many areas that the simulation methods can be advanced to progress the prediction accuracy of the patterns produced in thin film BCP DSA. Depending on the solvent annealing conditions used and film thickness, dynamics of quenching can have a

drastic effect on the morphology formed and thus incorporating such effects into simulations is now becoming a great area of study. Although there appears to be an unlimited number of combinations of patterns available using just BCP DSA with inversely designed templates, an even greater number of such possible patterns would be possible using triBCP or *n*-species systems as well as blending systems with multiple components; modeling such DSA systems has been limited and thus a great area of research can be conducted on such systems. In the same regard, adding functionalized nanoparticles to the system serves to increase the complexity of patterns produced as well as adding functionality to the final patterns; developing appropriate modeling methods for account for both DSA features and nanoparticles in the same simulations is yet another emerging area of research.

Most of the experimental comparison of the SCFT models with experiments demonstrated in the studies presented were to samples that had been modified or damaged in some way through etching processes for examination and thus do not correspond to the BCP swollen thin films the model seeks to capture. Thus designing new experiments to directly compare in situ results of real thin films without damaging the samples will be extremely beneficial to making the models better predictors of the actual structures formed in addition to having the possibility of altering the models to account for such destructive effects of post processing applications. Ultimately, the methods need to be fully applied to sub-10 nm systems exclusively, so suggestions on making both the model and experiments move toward the DSA of super high χ systems is examined. All of these suggestions for future work serve to advance the capabilities of both the simulation methods in having better accuracy in predicting the final patterns produced from the BCP DSA as well as influence the way experiments are done to improve the actual experimental results.

7.1.1 Dynamical SCFT Simulations

Recent in situ studies using GISAXS have shown there to be two different regimes in solvent annealing[117]. In one regime, swelling reaches a local equilibrium structure with order if the effective χ of the system does not result in the system going below the $(\chi N)_{ODT}$ value that

is collapsed during the quench step of the solvent annealing. In the other regime, so much solvent is incorporated into the system that the system goes into a disordered state and thus if the system is quenched from this state the final morphology of the system is solely dependent upon the dynamics of the quench. Recent simulation methods using a particle based Monte Carlo approach have shed some light into these processes[127]. There has also been some attempts at a dynamical SCFT model to account for quench dynamics from the disordered state[87].

For future work, such quenching dynamical effects should be examined. By having a method to examine the final structure after quenching, better direct comparison with various experimental methods can be performed especially if the quenching step has a great effect on the final morphology which is very likely the case for systems swollen above the $(\chi N)_{ODT}$. Recent experimental methods have used thermal heating to control quenching the sample[224], and thus modeling such quench paths would be beneficial to understanding the final morphology. Additionally, behavior during swelling can also be examined using methods that allow for thin film growth during the simulation increasing solvent volume as the film swells. Results between fixed thickness simulations and swelling simulations can be compared to see how different the final states are between the different approaches; if there is little quantitative and qualitative difference computational time can be saved performing the simpler fixed thickness simulations.

7.1.2 Multicomponent and n −Species Systems

Although a wide array of patterns have been demonstrated using just diBCPs, there are many benefits to going to larger numbers of species and components in the system. Adding extra species such as by using ABC triBCPs[80,225,226] allows for more functionality in the final pattern as different polymers can be used that have special properties for final device application and they can be left in the final pattern as opposed to the case in diBCPs where one block is generally a sacrificial block that etched away and the other block left to give structure to the pattern. Adding additional components such as homopolymers or blends of different BCPs with different architectures can allow great control of local volume fraction of the different blocks and help alleviate strain as seen in previous studies[6].

Modeling such systems has been a challenge in terms of SCFT framework as the potential for numerical instability increases with number of species and corresponding chemical potential fields in the system. Additionally the parameter space increases greatly as well as for every n distinct species in the system there are $n-1$ independent volume fractions and $(n^2-n)/2$ distinct χ parametrs. Recent progress in simulation methods have eliminated such instabilities by using relaxation schemes that converge more slowly allowing for the implementation of DSA simulations of such structures. Still, in these methods the full χ matrix of all χ in the system has to be considered with a relaxation scheme for the n independent chemical potential fields plus an incompressibility constraint added. Little simulation study has been done on DSA systems with more than two species or blend systems, thus future work should definitely examine these systems and the potential for greater control of fine morphological details as seen in many experimental studies[175,227,228].

7.1.3 Nanoparticle Inclusion

There has been a great interest in adding nanoparticles to BCP systems as the BCPs can help in the local placement of the nanoparticles based on the interactions of the surface chemistry of the particle ligands with the different blocks[178,179]. Recent progress in modeling these particles has been done in both considering the particles as movable boundary conditions similar to the topographical features in the DSA simulations[229] as well as more recent methods where a traditional solvent particle partition function is expanded using a size distribution profile[230,231]. Although methods for modeling such systems have been developed, there remains a wide parameter space to study in terms of how precise controlled placement of individual particles can be and how to prevent local aggregation and phase separation from the system. Additionally, combining these particles with multicomponent BCP systems besides simple diBCP systems is another area future studies can explore. Depending upon the functionality of the particles, experimental imaging of the resulting combined nanoparticle arrays and BCP patterns may be able to be done with novel methodology that is tuned to the functionality of the nanoparticles themselves. For

all these reasons, future work needs to investigate such systems in more detail to gain a deeper understanding of the control parameter space for these systems.

7.1.4 Direct Experimental Comparison Methods

In order for the simulation methods as presented to be useful, experimental validation must be performed. For the studies presented, most experimental methodology requires the essential destruction of the sample by having to etch one of the blocks away such as the case of scanning electron microscopy. Other methods such as atomic force microscopy can image thin film morphologies to some degree if there is enough contrast in the stiffness of the two blocks, but still in these cases the samples have already been quenched from solvent annealing and thus the morphologies predicted by the simulations will not exactly correspond.

One recent approach to the issue is through the use of x-ray scattering experiments. In particular to note are two scattering types. In situ grazing incidence small angle x-ray scattering (GISAXS) has been used to get real time structure data of thin film polymer ordering during solvent vapor annealing swelling experiments[117], but this data is limited to large structure periodicity. Another approach is the use of resonant soft x-ray scattering (RSoXS) where scattering data is produced using the resonance functionality of the different chemical functional groups in a BCP to produce high enough scattering intensity peaks to get the fine structure details at large reciprocal space values in the scattering data necessary for such fine detail structures[232]. By taking the resulting scattering intensity plot in terms of reciprocal space parameters, a reconstruction of the morphological domains can be made using an iterative Markov Chain Monte Carlo process. Results have already been made using a lamellae forming PS-PMMA BCP, and thus future work can be done on other thin film systems such as cylinder forming PS-PDMS. There is the potential for the experiment to be done in situ with solvent annealing as well to get the swollen state structure as well as information about the local ordering of selective solvents.

The scattering approaches show great promise as a way of quantitatively verifying simulation results for the internal structure of the microphase separated BCP domains, but require indirect methods that need optimization in order to get the real space structure

due to the scattering data being an indirect measure of the structure. As a direct measurement technique, recent progress has been made using 3D transmission electron microscopy tomography to image many slices of a given BCP thin film and compile those slices into a direct 3D image[233]. As a demonstration of the method, a sample of the mesh grid forming pattern found under the right commensurate conditions with rectangular arrays of majority functionalized topographical posts with a double layer of BCP was imaged after being quenched and the resulting tomography reconstructed image is shown in Figure 7.1.

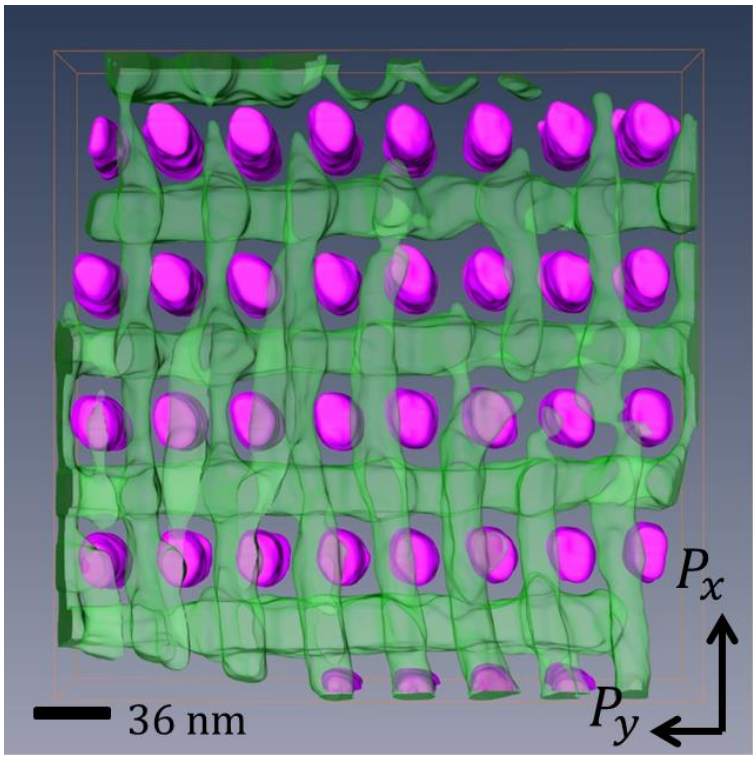

Figure 7-1: Image showing 3D structure of connected mesh grid PDMS cylinders (colored green) templated by HSQ posts (colored magenta) with the long post axis P_x and short post axis P_y labeled. Image was produced using 3D transmission electron microscopy tomography with a thin film solvent vapor annealed sample of cylinder forming 45.5 kg/mol PS-PDMS. The image clearly shows connections between the top and bottom cylinders before reactive ion etching the PS matrix. Scale bar is shown[233].

From the results clear connections between the top and bottom cylinders in the mesh exist as predicted by the SCFT simulations. At the same time, the new data show the bottom cylinder touching the substrate or at least extremely close to the substrate which was not predicted in the model. This new result suggests that the surface chemistry in the

substrate region may be more neutral than the posts. For the tomography experiment, the substrate had to be made of silicon nitride rather than oxide, which shows a slightly different bonding behavior to the brush layer than the silicon oxide and HSQ. Thus extra simulations over a range of post heights and surface energy conditions were performed to find regimes where the mesh grid structure formed with the connection as shown in Figure 7.2. From these results, there exists a range of parameters where the structure formed successfully with the neutral surface conditions best matching the experimental findings of the 3D tomography data. This demonstration of a direct comparison method, assuming the quench step just results in collapse of the structure in the z −direction, shows that there needs to be continued direct measurement correspondence between simulation results and experimental results to ensure that model parameters are correct and thus establish a feedback between modeling and experiment to create more accurate models in the future.

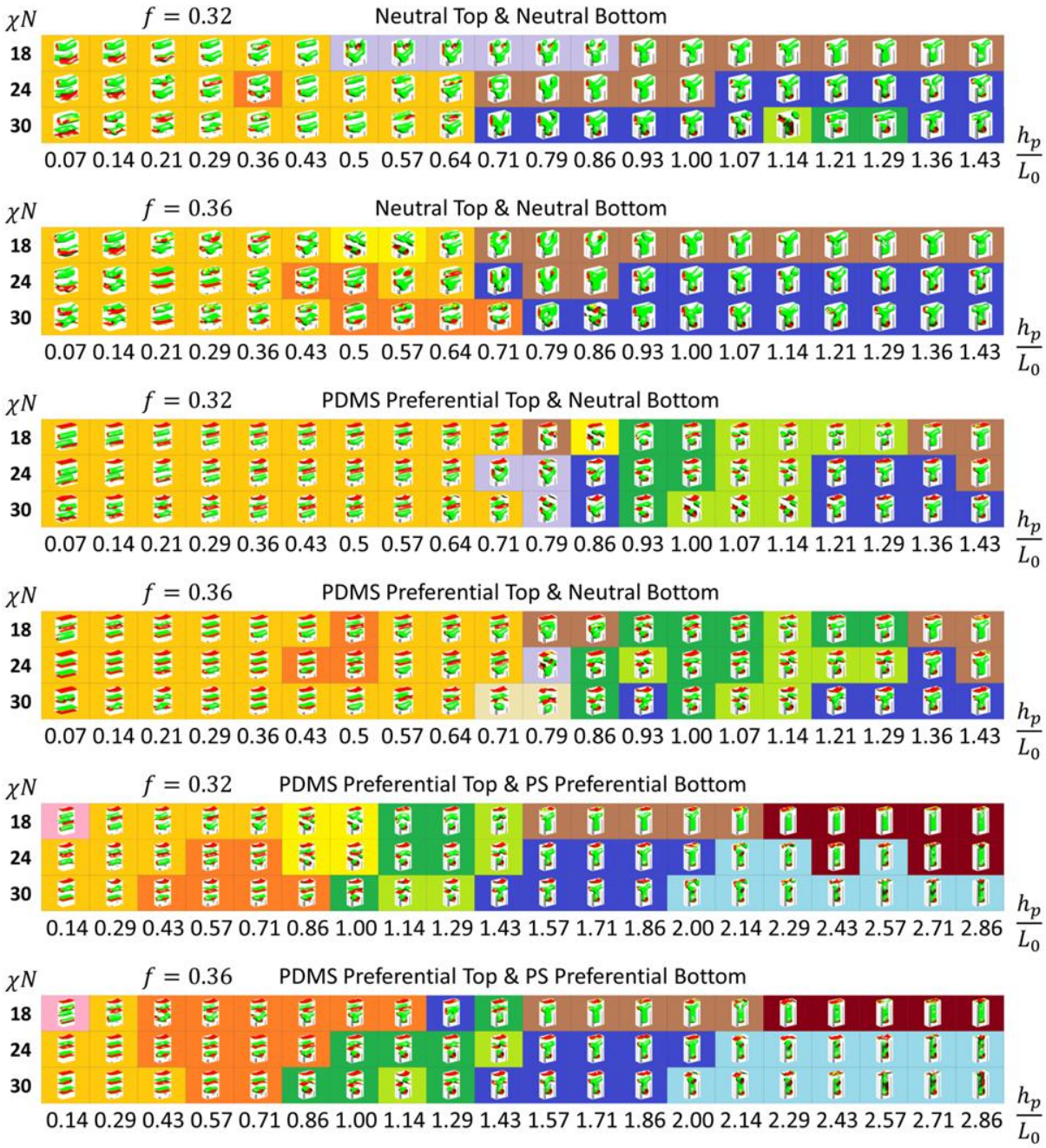

Figure 7-2: SCFT simulation results for a variety of top and bottom surface preferentiality conditions, effective χN = 18, 24, and 30, f = 0.32 and 0.36, and a range of normalized post heights h_p/L_0 for a double layer BCP on a rectangular array of posts with periods P_x = $1.71L_0$, P_y = L_0, and d_{post} = $0.71L_0$. The structure of interest, a mesh grid with connected top and bottom layers, occurred in the dark blue regions. An unconnected mesh grid structure appears in green regions. Other morphologies were color coded and grouped but were not of interest for experimental comparison since the posts in experiment did not expand over this full range of heights. The region best corresponding to the 3D tomography data is for h_p/L_0 = 0.93, χN = 30, neutral top and bottom conditions, with f = 0.36[233].

7.1.5 High Flory-Huggins Interaction Parameter Systems

The sub-10 nm features that are ultimately desired to be created using BCP DSA need very high χ parameters in order to achieve such length scales. Since L_0 scales as $L_0 \cong a\chi^{1/6}N^{2/3}$ and ordered structures theoretically cannot form below $(\chi N)_{ODT} = 10.5$ for lamellae forming BCPs[41,52], this gives two constraints for sub-10 nm domains that $a\chi^{1/6}N^{2/3} \leq$ 20 nm (since 10 nm feature sizes is half the period) and $\chi N \geq 10.5$. In general these constraints can be solved to give upper and lower bounds on the values of χ where microphase segregation can occur with the lower bound of $\chi \geq 10.5/N$ and the upper bound being $\chi \leq (L_0/a)^6/N^4$. Plots for $L_0 = 20$ nm, $L_0 = 10$ nm, and $L_0 = 5$ nm are shown in Figure 7.3 assuming $a = 1$ nm with a region corresponding roughly to where 16 kg/mol PS-PDMS self-assembled features should exist highlighted (since the exact experimental χ is not known in solvent annealing experiments and since the N here corresponds to arbitrary Kuhn segments of length $a = 1$ nm a region is given rather than a point).

Using the assumption that N corresponds to the double chemical repeat unit Kuhn monomer such that for most carbon backbone polymers $a \cong 1$ nm, solving these equation simultaneously gives an upper bound on N of $N \leq 183$ and lower bound for $\chi \geq 0.0575$ for $L_0 = 20$ nm. For PS-PDMS, this corresponds to a maximum molecular weight of 32.6 kg/mol. For half this pitch, $L_0 \leq 10$ nm to get 5 nm size features, $N \leq 46$ and $\chi \geq 0.23$, or a maximum molecular weight of 8.8 kg/mol PS-PDMS BCP. Thus to get a factor of a half increase in feature size, the molecular weight has to be reduced by close to a factor of 4 and χ increased by close to a factor of 4. For comparison, the ≈ 17 nm period resulting in ≈ 8.5 nm feature sizes in the PDMS preferential rectangular post studies had a molecular weight of 16 kg/mol, and a χ somewhere between 0.14 and 0.27 for PS-PDMS in the bulk, implying that these small feature sizes should theoretically be reachable[56]. However, going much below 5 nm feature sizes will be difficult as getting to 2.5 nm features would require an increase in χ to a value over 1 which has not yet been experimentally confirmed repeatedly. Thus, future works should examine both ways to synthesize such high χ polymers as well as to how to model such systems effectively.

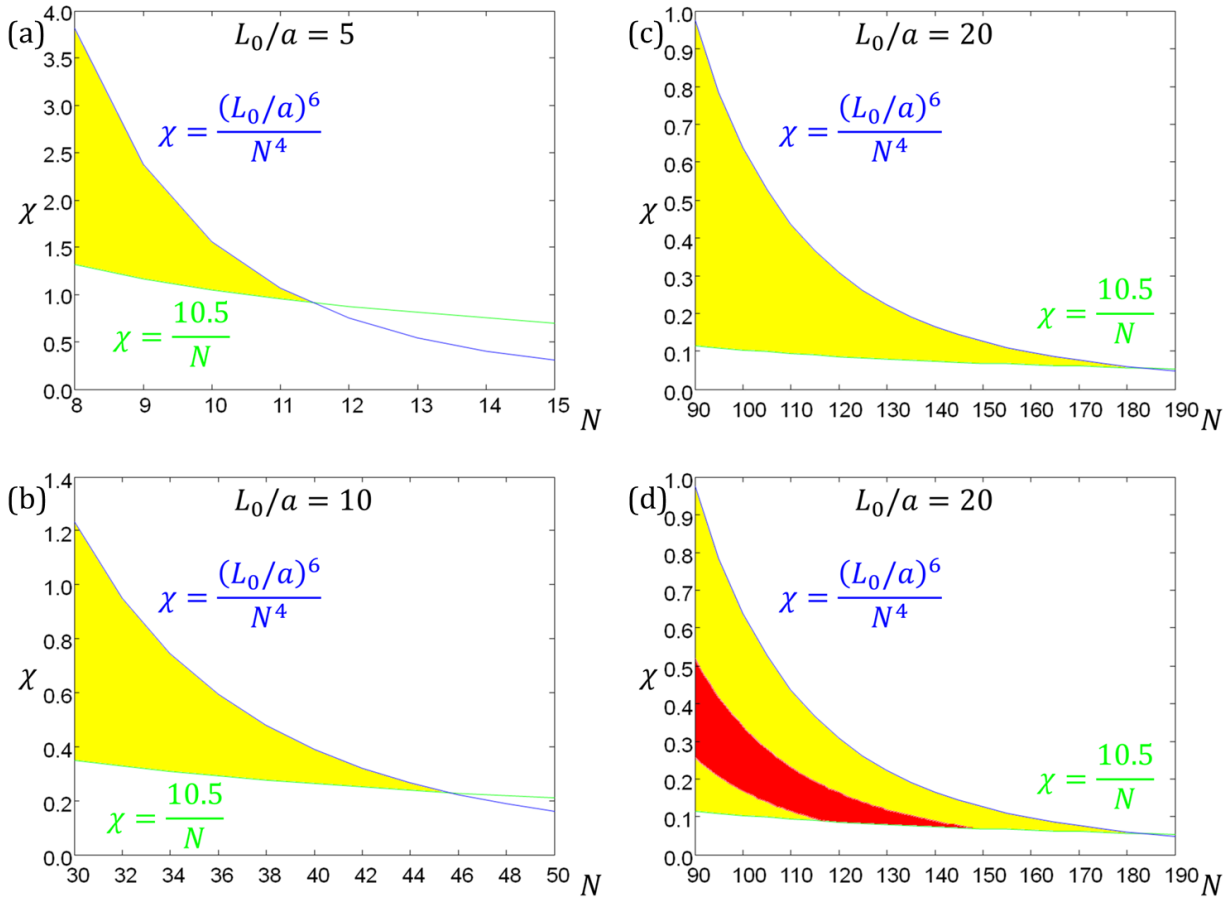

Figure 7-3: Plots of χ versus N (effective degree of polymerization assuming two chemical repeat units constitutes a Kuhn monomer) with upper boundary curves (blue) derived from the relationship $L_0 = a\chi^{1/6}N^{2/3}$ and lower boundary curves (green) from $\chi N = 10.5$ as the order-disorder transition value for $f = 0.5$ lamellae. Yellow regions are where microphase segregation is possible with L_0 values smaller than the chosen value for the plot assuming $a = 1$ nm. (a) Plot for $L_0/a = 5$ meaning feature sizes are 2.5 nm or less. N must be smaller than 12 and χ greater than 0.95 to achieve such small features. (b) Plot for $L_0/a = 10$ meaning feature sizes are 5 nm or less. N must be smaller than 46 and χ greater than 0.23 to achieve such small features. (c) Plot for $L_0/a = 20$ meaning feature sizes are 10 nm or less. N must be smaller than 183 and χ greater than 0.058 to achieve features this size. (d) Plot for $L_0/a = 20$ from (c) with red region added to indicate expected regime corresponding to experimental observations for 16 kg/mol PS-PDMS used in experiments. Upper bound of the curve is $L_0/a = 18$ and lower bound is $L_0/a = 16$ where the expected period is ≈ 17 nm.

7.2 Looking Ahead

The use of BCP DSA to create a variety of patterns for IC, memory storage, and other patterned media device technologies with sub-10 nm feature sizes is very promising as a

next generation technological process. The ability to model these systems has been greatly advanced through SCFT simulations in finding the equilibrium morphologies of the systems under a variety of thin film and topographical boundary conditions with both thermal and solvent vapor annealing processes used to drive the system to those morphologies. Many challenges still remain for these models to predict exact quantitative details of the experiments and ultimately manufactured samples.

From the simulation side of things, dynamical effects in solvent vapor annealing processes need to be incorporated explicitly to account for instances where the conditions no longer support equilibrium structure formation in the annealing times performed. Full scale 3D inverse design simulations under a parallel code structure can be used with such effects accounted to find the DSA templates and optimal control variable parameters needed to produce any desired pattern based on essential circuit features. Essentially combining all the various modeling conditions explored in this thesis will allow the future production of lithographic templates for manufacturing a wide variety of the next generation set of devices necessary for the continued miniaturization and optimization of computer technology.

From the experiment side of things, fabrication methods for decreasing template feature sizes will be immensely useful. Combining sacrificial topographical templating with hierarchical methodology can be used to create BCP post like features that can be used to template another smaller molecular weight BCP if post size itself cannot be physically reduced. Parallel direct write lithography techniques are another potential future technology that can aid in this endeavor, though their utility will be based on how arbitrary the generated pattern needs to be as there is a point where the direct write techniques could just write the whole pattern if spot size of the produced features can be reduced to a small enough size. If such spot size reductions are not possible, then self-assembly of super high χ BCPs should be explored thoroughly using the suggested techniques listed to reduce feature sizes using multiple hierarchical patterning steps that can eliminate the original patterns to reduce the overall feature sizes.

The methods explored in this study are not limited to BCP systems but have applications in other fields as well. With the advances of hard particle inclusions in the

systems, SCFT studies of colloid solutions could eventually be possible as one example where charge interaction potentials would need to be added to the system. The inverse algorithm as presented is not limited to just post configurations and can be applied to other system features that govern different types of target solutions for other systems leading to a family of algorithms for solving problems in the field of optimization. The computational requirements to perform large scale 3D simulations can eventually be reduced if the methods presented do indeed lead to the fabrication of better memory storage devices and IC devices due to increased computing speed and storage space density. In other words, by using simulations to guide experiments to make better computing technology, more efficient simulations can be done in the future to advance the next generation devices for more advanced technology.

The parameter space is wide and the problems innumerable that the modeling methodology presented in this thesis has yet to explore. Thus continued work toward the advancement of these methods and the technology that is created thanks to knowledge gained from the simulations is necessary to better humanity and the world as a whole.

Appendix A

Supplementary Information

A.1 Simulation Data Archive and Code Information

For information on raw simulation data availibity and specific versions of the SCFT code, please contact Adam Floyd Hannon at thegreyfloyd@gmail.com.

A.2 Special Appendix

This appendix was removed March 22nd, 2014 at Mount Auburn Hospital, Cambridge, MA.

Bibliography

[1] Yang, J. K. W.; Jung, Y. S.; Chang, J.-B.; Mickiewicz, R. A.; Alexander-Katz, A.; Ross, C. A.; Berggren, K. K. *Nat. Nanotechnol.* **2010**, *5*, 256–260.

[2] Bita, I.; Yang, J. K. W.; Jung, Y. S.; Ross, C. A.; Thomas, E. L.; Berggren, K. K. *Science* **2008**, *321*, 939–943.

[3] Stoykovich, M. P.; Nealey, P. F. *Mater. Today* **2006**, *9*, 20–29.

[4] Xiao, S.; Yang, X.; Edwards, E. W.; La, Y.-H.; Nealey, P. F. *Nanotechnology* **2005**, *16*, S324–S329.

[5] Park, S.-M.; Stoykovich, M. P.; Ruiz, R.; Zhang, Y.; Black, C. T.; Nealey, P. F. *Adv. Mater.* **2007**, *19*, 607–611.

[6] Stoykovich, M. P.; Müller, M.; Kim, S. O.; Solak, H. H.; Edwards, E. W.; de Pablo, J. J.; Nealey, P. F. *Science* **2005**, *308*, 1442–1446.

[7] Cohen, R. . *Curr. Opin. Solid State Mater. Sci.* **1999**, *4*, 587–590.

[8] Cheng, J. Y.; Ross, C. A.; Thomas, E. L.; Smith, H. I.; Vancso, G. J. *Adv. Mater.* **2003**, *15*, 1599–1602.

[9] Cheng, J. Y.; Rettner, C. T.; Sanders, D. P.; Kim, H.-C.; Hinsberg, W. D. *Adv. Mater.* **2008**, *20*, 3155–3158.

[10] Ruiz, R.; Kang, H.; Detcheverry, F. A.; Dobisz, E.; Kercher, D. S.; Albrecht, T. R.; de Pablo, J. J.; Nealey, P. F. *Science* **2008**, *321*, 936–939.

[11] Park, S.; Lee, D. H.; Xu, J.; Kim, B.; Hong, S. W.; Jeong, U.; Xu, T.; Russell, T. P. *Science* **2009**, *323*, 1030–1033.

[12] Kim, S. O.; Solak, H. H.; Stoykovich, M. P.; Ferrier, N. J.; de Pablo, J. J.; Nealey, P. F. *Nature* **2003**, *424*, 411–414.

[13] Wilmes, G.; Durkee, D.; Balsara, N.; Liddle, J. *Macromolecules* **2006**, *2*, 2435–2437.

[14] Segalman, R. A.; Hexemer, A.; Kramer, E. J. *Macromolecules* **2003**, *36*, 6831–6839.

[15] Segalman, R. A.; Hexemer, A.; Kramer, E. J. *Phys. Rev. Lett.* **2003**, *91*, 196101.

[16] Segalman, R.; Yokoyama, H.; Kramer, E. *Adv. Mater.* **2001**, *13*, 1152–1155.

[17] Stoykovich, M. P.; Kang, H.; Daoulas, K. C.; Liu, G.; Liu, C.-C.; de Pablo, J. J.; Müller, M.; Nealey, P. F. *ACS Nano* **2007**, *1*, 168–175.

[18] Sundrani, D.; Darling, S. B.; Sibener, S. J. *Nano Lett.* **2004**, *4*, 273–276.

[19] Black, C. T.; Bezencenet, O. *IEEE Trans. Nanotechnol.* **2004**, *3*, 412–415.

[20] Cheng, J. Y.; Mayes, A. M.; Ross, C. A. *Nat. Mater.* **2004**, *3*, 823–828.

[21] Park, S.; Craig, G.; La, Y. *Macromolecules* **2007**, *40*, 5084–5094.

[22] Rockford, L.; Liu, Y.; Mansky, P.; Russell, T.; Yoon, M.; Mochrie, S. *Phys. Rev. Lett.* **1999**, *82*, 2602–2605.

[23] Xiao, S.; Yang, X.; Park, S.; Weller, D.; Russell, T. P. *Adv. Mater.* **2009**, *21*, 2516–2519.

[24] Ruiz, R.; Sandstrom, R.; Black, C. *Adv. Mater.* **2007**, *19*, 587–591.

[25] Ruiz, R.; Ruiz, N.; Zhang, Y.; Sandstrom, R. L.; Black, C. T. *Adv. Mater.* **2007**, *19*, 2157–2162.

[26] Xiao, S.; Yang, X.; Lee, K. Y.; ver der Veerdonk, R. J. M.; Kuo, D.; Russell, T. P. *Nanotechnology* **2011**, *22*, 305302.

[27] Jeong, S.-J.; Moon, H.-S.; Shin, J.; Kim, B. H.; Shin, D. O.; Kim, J. Y.; Lee, Y.-H.; Kim, J. U.; Kim, S. O. *Nano Lett.* **2010**, *10*, 3500–3505.

[28] Tang, Q.; Ma, Y. *Soft Matter* **2010**, *6*, 4460.

[29] Moore, G. E. *Proc. IEEE* **1998**, *86*, 82–85.

[30] Sanders, D. P. *Chem. Rev.* **2010**, *110*, 321–360.

[31] Yang, J. K. W.; Berggren, K. K. *J. Vac. Sci. Technol. B Microelectron. Nanom. Struct.* **2007**, *25*, 2025–2029.

[32] Black, C. T. *Appl. Phys. Lett.* **2005**, *87*, 163116.

[33] Cheng, J.; Jung, W.; Ross, C. A. *Phys. Rev. B* **2004**, *70*, 064417.

[34] Yi, H.; Bao, X.-Y.; Zhang, J.; Bencher, C.; Chang, L.-W.; Chen, X.; Tiberio, R.; Conway, J.; Dai, H.; Chen, Y.; Mitra, S.; Wong, H.-S. P. *Adv. Mater.* **2012**, *24*, 3107–3114.

[35] Thurn-Albrecht, T. *Science* **2000**, *290*, 2126–2129.

[36] Jung, Y. S.; Jung, W.; Tuller, H. L.; Ross, C. A. *Nano Lett.* **2008**, *8*, 3776–3780.

[37] Bai, J.; Zhong, X.; Jiang, S.; Huang, Y.; Duan, X. *Nat. Nanotechnol.* **2010**, *5*, 190–194.

[38] Liang, X.; Wi, S. *ACS Nano* **2012**, *6*, 9700–9710.

[39] Zschech, D.; Kim, D. H.; Milenin, A. P.; Scholz, R.; Hillebrand, R.; Hawker, C. J.; Russell, T. P.; Steinhart, M.; Gösele, U. *Nano Lett.* **2007**, *7*, 1516–1520.

[40] Leibler, L. *Macromolecules* **1980**, *13*, 1602–1617.

[41] Bates, F. S.; Fredrickson, G. H. *Annu. Rev. Phys. Chem.* **1990**, *41*, 525–557.

[42] Bates, F. S.; Fredrickson, G. H. *Phys. Today* **1999**, *52*, 32–38.

[43] Flory, P. J. *Principles of Polymer Chemistry*; Cornell University Press: Ithaca, New York, 1953.

[44] Jung, Y. S.; Ross, C. A. *Adv. Mater.* **2009**, *21*, 2540–2545.

[45] Albert, J. N. L.; Bogart, T. D.; Lewis, R. L.; Beers, K. L.; Fasolka, M. J.; Hutchison, J. B.; Vogt, B. D.; Epps, T. H. *Nano Lett.* **2011**, *11*, 1351–1357.

[46] Herr, D. J. C. *J. Mater. Res.* **2011**, *26*, 122–139.

[47] Luo, M.; Epps, T. H. *Macromolecules* **2013**, *46*, 7567–7579.

[48] Ginzburg, V. V.; Weinhold, J. D.; Trefonas, P. *J. Polym. Sci. Part B Polym. Phys.* **2013**, doi: 10.1002/polb.23365.

[49] Mickiewicz, R. A.; Yang, J. K. W.; Hannon, A. F.; Jung, Y.; Alexander-katz, A.; Berggren, K. K.; Ross, C. A. *Macromolecules* **2010**, *43*, 8290–8295.

[50] Hannon, A. F.; Gotrik, K. W.; Ross, C. A.; Alexander-Katz, A. *ACS Macro Lett.* **2013**, *2*, 251–255.

[51] Hannon, A. F.; Ding, Y.; Bai, W.; Ross, C. A.; Alexander-Katz, A. *Nano Lett.* **2014**, *14*, 318–325.

[52] Matsen, M.; Schick, M. *Phys. Rev. Lett.* **1994**, *72*, 2660–2663.

[53] Fredrickson, G. *The Equilibrium Theory of Inhomogeneous Polymers*; Oxford University Press: Oxford, New York, 2005.

[54] Fredrickson, G. H.; Ganesan, V.; Drolet, F. *Macromolecules* **2002**, *35*, 16–39.

[55] Alexander-Katz, A.; Fredrickson, G. H. *Macromolecules* **2007**, *40*, 4075–4087.

[56] Chang, J.-B.; Son, J. G.; Hannon, A. F.; Alexander-Katz, A.; Ross, C. A.; Berggren, K. K. *ACS Nano* **2012**, *6*, 2071–2077.

[57] Tavakkoli K G, A.; Hannon, A. F.; Gotrik, K. W.; Alexander-Katz, A.; Ross, C. A.; Berggren, K. K. *Adv. Mater.* **2012**, *24*, 4249–4254.

[58] Tavakkoli K. G., A.; Gotrik, K. W.; Hannon, A. F.; Alexander-Katz, A.; Ross, C. A.; Berggren, K. K. *Science* **2012**, *336*, 1294–1298.

[59] Gotrik, K. W.; Hannon, A. F.; Son, J. G.; Keller, B.; Alexander-Katz, A.; Ross, C. A. *ACS Nano* **2012**, *6*, 8052–8059.

[60] Tavakkoli K G, A.; Nicaise, S. M.; Hannon, A. F.; Gotrik, K. W.; Alexander-Katz, A.; Ross, C. A.; Berggren, K. K. *Small* **2013**, *10*, 493–499.

[61] Son, J. G.; Hannon, A. F.; Gotrik, K. W.; Alexander-Katz, A.; Ross, C. A. *Adv. Mater.* **2011**, *23*, 634–639.

[62] Lodge, T.; Dalvi, M. *Phys. Rev. Lett.* **1995**, *75*, 657–660.

[63] Kim, S. H.; Misner, M. J.; Russell, T. P. *Adv. Mater.* **2004**, *16*, 2119–2123.

[64] Bates, C. M.; Seshimo, T.; Maher, M. J.; Durand, W. J.; Cushen, J. D.; Dean, L. M.; Blachut, G.; Ellison, C. J.; Willson, C. G. *Science* **2012**, *338*, 775–779.

[65] Jeong, J. W.; Hur, Y. H.; Kim, H.-J.; Kim, J. M.; Park, W. I.; Kim, M. J.; Kim, B. J.; Jung, Y. S. *ACS Nano* **2013**, *7*, 6747–6757.

[66] Detcheverry, F. A.; Liu, G.; Nealey, P. F.; de Pablo, J. J. *Macromolecules* **2010**, *43*, 3446–3454.

[67] Detcheverry, F. A.; Nealey, P. F.; de Pablo, J. J. *Macromolecules* **2010**, *43*, 6495–6504.

[68] Tada, Y.; Yoshida, H.; Ishida, Y.; Hirai, T.; Bosworth, J. K.; Dobisz, E.; Ruiz, R.; Takenaka, M.; Hayakawa, T.; Hasegawa, H. *Macromolecules* **2012**, *45*, 292–304.

[69] Edwards, E. W.; Montague, M. F.; Solak, H. H.; Hawker, C. J.; Nealey, P. F. *Adv. Mater.* **2004**, *16*, 1315–1319.

[70] Park, S.-M.; Craig, G. S. W.; La, Y.-H.; Nealey, P. F. *Macromolecules* **2008**, *41*, 9124–9129.

[71] Daoulas, K. C.; Müller, M.; Stoykovich, M. P.; Park, S.-M.; Papakonstantopoulos, Y. J.; de Pablo, J. J.; Nealey, P. F.; Solak, H. H. *Phys. Rev. Lett.* **2006**, *96*, 036104.

[72] Doerk, G. S.; Liu, C.-C.; Cheng, J. Y.; Rettner, C. T.; Pitera, J. W.; Krupp, L. E.; Topuria, T.; Arellano, N.; Sanders, D. P. *ACS Nano* **2013**, *7*, 276–285.

[73] Van Kampen, N. G. *Stochastic processes in physics and chemistry*; Elsevier: Amsterdam, The Netherlands, 1992; Vol. 11.

[74] Rice, S. O. In *Selected Papers on Noise and Stochastic Processes*; 1954; pp. 133–294.

[75] Zimm, B. H.; Stockmayer, W. H.; Fixman, M. *J. Chem. Phys.* **1953**, *21*, 1716–1723.

[76] Doi, M.; Edwards, S. F. *The Theory of Polymer Dynamics*; Oxford University Press: Oxford, England, 1986.

[77] De Gennes, P. G. *Scaling Concepts in Polymer Physics*; Cornell University Press: Ithaca, New York, 1979.

[78] Carlen, E.; Carvalho, M. C.; Loss, M. *Linear Algebra: From the Beginning*; 1st ed.; Freeman, W. H. & Company: New York, NY, 2006.

[79] Detcheverry, F.; Kang, H.; Daoulas, K.; Muller, M.; Nealey, P. F.; de Pablo, J. J. *Macromolecules* **2008**, *41*, 4989–5001.

[80] Sides, S. W.; Fredrickson, G. H. *Polymer* **2003**, *44*, 5859–5866.

[81] Yeung, C.; Shi, A. *Macromol. Theory Simulations* **1996**, *298*, 291–298.

[82] Reister, E.; Müller, M.; Binder, K. *Phys. Rev. E. Stat. Nonlin. Soft Matter Phys.* **2001**, *64*, 041804.

[83] Hasegawa, R.; Doi, M. *Macromolecules* **1997**, *30*, 5490–5493.

[84] Müller, M.; Schmid, F. *Adv. Comput. Simul. Approaches Soft Matter Sci. II Adv. Polym. Sci.* **2005**, *185*, 1–58.

[85] Fraaije, J. G. E. M. *J.Chem. Phys* **1993**, *99*, 9202–9212.

[86] Fraaije, J. G. E. M.; Vimmeren, B. A. C. van; Maurits, N. M.; Postma, M.; Evers, O. A.; Hoffmann, C.; Goldbeck-Wood, G. *J. Chem. Phys.* **1997**, *106*, 4260–4269.

[87] Paradiso, S. P.; Delaney, K. T.; García-Cervera, C. J.; Ceniceros, H. D.; Fredrickson, G. H. *ACS Macro Lett.* **2014**, *3*, 16–20.

[88] Press, W. *Numerical recipes 3rd edition: The art of scientific computing*; Cambridge University Press: New York, NY, 2007.

[89] Smith, S. W. In *The Scientist and Engineer's Guide to Digital Signal Processing*; 1997; pp. 225–232.

[90] Chen, H.; Kim, Y.; Alexander-Katz, A. *J. Chem. Phys.* **2013**, *138*, 104123.

[91] Wang, Q. *Macromol. Theory Simulations* **2005**, *14*, 96–108.

[92] Petrus, P.; Lísal, M.; Brennan, J. K. *Langmuir* **2010**, *26*, 14680–14693.

[93] Yin, Y.; Sun, P.; Chen, T.; Li, B.; Jin, Q.; Ding, D.; Shi, A.-C. *ChemPhysChem* **2004**, *5*, 540–548.

[94] Lodge, T. P.; Dalvi, M. C. *Phys. Rev. Lett.* **1995**, *75*, 657–660.

[95] Kim, H. C.; Russell, T. P. *Jounal Polyer. Sci. Part B Polym. Phys.* **2001**, *39*, 663–668.

[96] Horvat, A.; Lyakhova, K. S.; Sevink, G. J. A.; Zvelindovsky, A. V; Magerle, R. *J. Chem. Phys.* **2004**, *120*, 1117–1126.

[97] Kim, E.; Choi, S.; Guo, R.; Ryu, D. Y.; Hawker, C. J.; Russell, T. P. *Polymer* **2010**, *51*, 6313–6318.

[98] Bucholz, T. L.; Loo, Y.-L. *Macromolecules* **2006**, *39*, 6075–6080.

[99] Russell, T.; Jr, R. H.; Seeger, P. *Macromolecules* **1990**, *23*, 890–893.

[100] Yan, H.; Blanford, C. F.; Lytle, J. C.; Carter, C. B.; Smyrl, W. H.; Stein, A. *Chem. Mater.* **2001**, *13*, 4314–4321.

[101] Cavicchi, K. A.; Berthiaume, K. J.; Russell, T. P. *Polymer* **2005**, *46*, 11635–11639.

[102] Peng, J.; Kim, D. H.; Knoll, W.; Xuan, Y.; Li, B.; Han, Y. *J. Chem. Phys.* **2006**, *125*, 64702.

[103] Paik, M. Y.; Bosworth, J. K.; Smilges, D.-M.; Schwartz, E. L.; Andre, X.; Ober, C. K. *Macromolecules* **2010**, *43*, 4253–4260.

[104] Di, Z.; Posselt, D.; Smilgies, D.-M.; Papadakis, C. M. *Macromolecules* **2010**, *43*, 418–427.

[105] Harant, A. W.; Bowman, C. N. *J. Vac. Sci. Technol. B Microelectron. Nanom. Struct.* **2005**, *23*, 1615–1621.

[106] Xuan, Y.; Peng, J.; Cui, L.; Wang, H.; Li, B.; Han, Y. *Macromolecules* **2004**, *37*, 7301–7307.

[107] Vogelsang, J.; Brazard, J.; Adachi, T.; Bolinger, J. C.; Barbara, P. F. *Angew. Chem. Int. Ed. Engl.* **2011**, *50*, 2257–2261.

[108] Phillip, W. A.; Hillmyer, M. A.; Cussler, E. L. *Macromolecules* **2010**, *43*, 7763–7770.

[109] Kim, S. H.; Misner, M. J.; Russell, T. P. *Adv. Mater.* **2004**, *16*, 2119–2123.

[110] Kim, S.; Briber, R.; Karim, A. *MRS Proc.* **2006**, *961*, 0961–O17–03.

[111] Mori, K.; Hasegawa, H.; Hashimoto, T. *Polymer* **1990**, *31*, 2368–2376.

[112] Hansen, C. M. *Hansen Solubility Parameters, A User's Handbook*; CRC Press: Boca Raton, FL, 2000.

[113] Bahadur, P.; Sastry, N. V. *Principles of Polymer Science*; Alpha Science International, Ltd.: Oxford, UK, 2005.

[114] Elbs, H.; Krausch, G. *Polymer* **2004**, *45*, 7935–7942.

[115] Helfand, E.; Tagami, Y. *J. Chem. Phys.* **1972**, *56*, 3592–3601.

[116] Hashimoto, T.; Shibayama, M.; Hiromichi, K. *Macromolecules* **1983**, *16*, 1093–1101.

[117] Gu, X.; Gunkel, I.; Hexemer, A.; Gu, W.; Russell, T. P. *Adv. Mater.* **2014**, *26*, 273–281.

[118] Jung, Y. S.; Ross, C. A. *Nano Lett.* **2007**, *7*, 2046–2050.

[119] Bang, J.; Kim, B. J.; Stein, G. E.; Russell, T. P.; Li, X.; Wang, J.; Kramer, E. J.; Hawker, C. J. *Macromolecules* **2007**, *40*, 7019–7025.

[120] Guo, R.; Huang, H.; Chen, Y.; Gong, Y.; Du, B.; He, T. *Macromolecules* **2008**, *41*, 890–900.

[121] Bosworth, J. K.; Paik, M. Y.; Ruiz, R.; Schwartz, E. L.; Huang, J. Q.; Ko, A. W.; Smilgies, D.-M.; Black, C. T.; Ober, C. K. *ACS Nano* **2008**, *2*, 1396–1402.

[122] Jeong, J. W.; Park, W. I.; Kim, M.; Ross, C. A.; Jung, Y. S. *Nano Lett.* **2011**, *11*, 4095–4101.

[123] Zwietering, T. N. *Chem. Eng. Sci.* **1959**, *11*, 1–15.

[124] Cholette, A.; Cloutier, L. *Can. J. Chem. Eng.* **1959**, *37*, 105–112.

[125] Cavicchi, K. A.; Russell, T. P. *Macromolecules* **2007**, *40*, 1181–1186.

[126] Albert, J. N. L.; Young, W.-S.; Lewis, R. L.; Bogart, T. D.; Smith, J. R.; Epps, T. H. *ACS Nano* **2012**, *6*, 459–466.

[127] Hur, S.-M.; Khaira, Gurdaman S. Nealey, P. F.; Muller, M.; de Pablo, J. J. In *APS*; 2014.

[128] Knoll, A.; Horvat, A.; Lyakhova, K. S.; Krausch, G.; Sevink, G. J. A.; Zvelindovsky, A. V; Magerle, R. *Phys. Rev. Lett.* **2002**, *89*, 035501.

[129] Ginsburg, N.; Robertson, W. W.; Matsen, F. A. *J. Chem. Phys.* **1946**, *14*, 511– 517.

[130] Chao, C.-C.; Ho, R.-M.; Georgopanos, P.; Avgeropoulos, A.; Thomas, E. L. *Soft Matter* **2010**, *6*, 3582.

[131] Saez, C.; Compostizo, A.; Rubio, R. G.; Colin, A. C.; Peiia, M. D. *J. Chem. Soc. Faraday Trans. 1 Phys. Chem. Condens. Phases* **1986**, *82*, 1839–1852.

[132] Kennemur, J.; Yao, L.; Bates, F.; Hillmyer, M. *Macromolecules* **2014**, *47*, 1411–1418.

[133] Ross, C. A.; Berggren, K. K.; Cheng, J. Y.; Jung, Y. S.; Chang, J.-B. *Adv. Mater.* **2014**, doi: 10.1002/adma.201400386.

[134] Stewart-Sloan, C. R.; Thomas, E. L. *Eur. Polym. J.* **2011**, *47*, 630–646.

[135] Wang, Q.; Yan, Q.; Nealey, P. F.; de Pablo, J. J. *J. Chem. Phys.* **2000**, *112*, 450–464.

[136] Wang, Q.; Nealey, P. F.; de Pablo, J. J. *Macromolecules* **2001**, *34*, 3458–3470.

[137] Wang, Q.; Nath, S. K.; Graham, M. D.; Nealey, P. F.; de Pablo, J. J. *J. Chem. Phys.* **2000**, *112*, 9996–10010.

[138] Wang, Q.; Yan, Q.; Nealey, P. F.; de Pablo, J. J. *Macromolecules* **2000**, *33*, 4512–4525.

[139] He, X.; Song, M.; Liang, H.; Pan, C. *J. Chem. Phys.* **2001**, *114*, 10510–10513.

[140] Meng, D.; Wang, Q. *Soft Matter* **2010**, *6*, 5891–5906.

[141] Tsori, Y.; Andelman, D. *Macromolecules* **2002**, *35*, 5161–5170.

[142] Yu, B.; Sun, P.; Chen, T.; Jin, Q.; Ding, D.; Li, B.; Shi, A.-C. *Phys. Rev. Lett.* **2006**, *96*, 138306.

[143] Feng, J.; Ruckenstein, E. *J. Chem. Phys.* **2006**, *125*, 164911.

[144] Li, W.; Wickham, R. A.; Garbary, R. A. *Macromolecules* **2006**, *39*, 806–811.

[145] Sevink, G. J. A.; Zvelindovsky, A. V.; Fraaije, J. G. E. M.; Huinink, H. P. *J. Chem. Phys.* **2001**, *115*, 8226–8230.

[146] Wu, Y.; Cheng, G.; Katsov, K.; Sides, S. W.; Wang, J.; Tang, J.; Fredrickson, G. H.; Moskovits, M.; Stucky, G. D. *Nat. Mater.* **2004**, *3*, 816–822.

[147] Shin, K.; Xiang, H.; Moon, S. I.; Kim, T.; McCarthy, T. J.; Russell, T. P. *Science* **2004**, *306*, 76.

[148] Henkee, C. S.; Thomas, E. L.; Fetters, L. J. *J. Mater. Sci.* **1988**, *23*, 1685–1694.

[149] Russell, T. P.; Lambooy, P.; Kellogg, G. J.; Mayes, A. M. *Phys. B Phys. Condens. Matter* **1995**, *213-214*, 22–25.

[150] Xiang, H.; Shin, K.; Kim, T.; Moon, S.; Mccarthy, T. J.; Russell, T. P. *J. Polym. Sci. Part B Polym. Phys.* **2005**, *43*, 3377–3383.

[151] Russell, T. P. *Curr. Opin. Colloid Interface Sci.* **1996**, *1*, 107–115.

[152] Yu, B.; Li, B.; Jin, Q.; Ding, D.; Shi, A.-C. *Soft Matter* **2011**, *7*, 10227.

[153] Coulon, G.; Collin, B.; Ausserre, D.; Chatenay, D.; Russell, T. P. *J. Phys.* **1990**, *51*, 2801–2811.

[154] Fasolka, M.; Mayes, A. *Annu. Rev. Mater. Res.* **2001**, *31*, 323–355.

[155] Albert, J. N. L.; Epps III, T. H. *Mater. Today* **2010**, *13*, 24–33.

[156] Ruiz, R.; Dobisz, E.; Albrecht, T. R. *ACS Nano* **2011**, *5*, 79–84.

[157] Park, C.; Cheng, J. Y.; Fasolka, M. J.; Mayes, A. M.; Ross, C. A.; Thomas, E. L.; De Rosa, C. *Appl. Phys. Lett.* **2001**, *79*, 848–850.

[158] Mark, J. E. *Physical Properties of Polymers Handbook*; 2007; p. 1076.

[159] Wang, Q. *J. Chem. Phys.* **2007**, *126*, 024903.

[160] Wang, Q.; Nealey, P. F.; de Pablo, J. J. *Macromolecules* **2002**, *35*, 9563–9573.

[161] Andersen, T. H.; Tougaard, S.; Larsen, N. B.; Almdal, K.; Johannsen, I. *J. Electron Spectros. Relat. Phenomena* **2001**, *121*, 93–110.

[162] Chan, C. M. *"Plasma Modification" in Polymer Surface Modification and Characterization*; Hanser Publishers: Munich, Germany, 1994; pp. 225–261.

[163] Huinink, H. P.; Brokken-Zijp, J. C. M.; van Dijk, M. A.; Sevink, G. J. A. *J. Chem. Phys.* **2000**, *112*, 2452–2462.

[164] Chen, P.; Liang, H.; Shi, A.-C. *Macromolecules* **2007**, *40*, 7329–7335.

[165] Yu, B.; Jin, Q.; Ding, D.; Li, B.; Shi, A.-C. *Macromolecules* **2008**, *41*, 4042–4054.

[166] Yin, Y.; Sun, P.; Jiang, R.; Li, B.; Chen, T.; Jin, Q.; Ding, D.; Shi, A.-C. *J. Chem. Phys.* **2006**, *124*, 184708.

[167] Yang, Y.; Qiu, F.; Zhang, H.; Yang, Y. *Polymer* **2006**, *47*, 2205–2216.

[168] Wu, N.; Zhang, X.; Murphy, J.; Chai, J.; Harris, K. D.; Buriak, J. M. *Nano Lett.* **2012**, *12*, 264–268.

[169] Bai, W.; Hannon, A. F.; Gotrik, K. W.; Choi, H. K.; Aissou, K.; Liontos, G.; Ntetsikas, K.; Alexander-Katz, A.; Avgeropoulos, A.; Ross, C. A. *Unpublished*.

[170] Kim, S.; Kim, B.; Meng, D.; Shin, D. *Adv. Mater.* **2007**, *19*, 3271–3275.

[171] Park, M.; Harrison, C.; Chaikin, P. M.; Register, R. A.; Adamson, D. H. *Science* **1997**, *276*, 1401–1404.

[172] Cheng, J. Y.; Ross, C. A.; Smith, H. I.; Thomas, E. L. *Adv. Mater.* **2006**, *18*, 2505–2521.

[173] Lazzari, M.; López-Quintela, M. A. *Adv. Mater.* **2003**, *15*, 1583–1594.

[174] Tang, C.; Lennon, E. M.; Fredrickson, G. H.; Kramer, E. J.; Hawker, C. J. *Science* **2008**, *322*, 429–432.

[175] Chuang, V. P.; Gwyther, J.; Mickiewicz, R. A.; Manners, I.; Ross, C. A. *Nano Lett.* **2009**, *9*, 4364–4369.

[176] Sivaniah, E.; Hayashi, Y.; Iino, M. *Macromolecules* **2003**, *36*, 5894–5896.

[177] Son, J. G.; Bulliard, X.; Kang, H. M.; Nealey, P. E.; Char, K. *Adv. Mater.* **2008**, *20*, 3643–3648.

[178] Chiu, J. J.; Kim, B. J.; Kramer, E. J.; Pine, D. J. *J. Am. Chem. Soc.* **2005**, *127*, 5036–5037.

[179] Son, J. G.; Bae, W. K.; Kang, H.; Nealey, P. F.; Char, K. *ACS Nano* **2009**, *3*, 3927–3934.

[180] Fink, Y.; Urbas, A. M.; Bawendi, M. G.; Joannopoulos, J. D.; Thomas, E. L. *J. Light. Technol.* **1999**, *17*, 1963–1969.

[181] Jung, Y. S.; Ross, C. A. *Small* **2009**, *5*, 1654–1659.

[182] Jung, Y. S.; Chang, J.-B.; Verploegen, E.; Berggren, K. K.; Ross, C. A. *Nano Lett.* **2010**, *10*, 1000–1005.

[183] Jeong, S.-J.; Kim, J. E.; Moon, H.-S.; Kim, B. H.; Kim, S. M.; Kim, J. B.; Kim, S. O. *Nano Lett.* **2009**, *9*, 2300–2305.

[184] Park, S. H.; Shin, D. O.; Kim, B. H.; Yoon, D. K.; Kim, K.; Lee, S. Y.; Oh, S.-H.; Choi, S.-W.; Jeon, S. C.; Kim, S. O. *Soft Matter* **2010**, *6*, 120–125.

[185] Jeong, S.-J.; Moon, H.-S.; Kim, B. H.; Kim, J. Y.; Yu, J.; Lee, S.; Lee, M. G.; Choi, H.; Kim, S. O. *ACS Nano* **2010**, *4*, 5181–5186.

[186] Park, S.-M.; Ravindran, P.; La, Y.-H.; Craig, G. S. W.; Ferrier, N. J.; Nealey, P. F. *Langmuir* **2007**, *23*, 9037–9045.

[187] Bang, J.; Kim, S. H.; Drockenmuller, E.; Misner, M. J.; Russell, T. P.; Hawker, C. J. *J. Am. Chem. Soc.* **2006**, *128*, 7622–7629.

[188] Turner, M.; Joanny, J. *Macromolecules* **1992**, *25*, 6681–6689.

[189] Tsori, Y.; Andelman, D. *Macromolecules* **2003**, *36*, 8560–8566.

[190] Finders, J.; Dusa, M.; Vleeming, B.; Hepp, B.; Maenhoudt, M.; Cheng, S.; Vandeweyer, T. *J. Micro/Nanolithography, MEMS MOEMS* **2009**, *8*, 011002.

[191] Lambooy, P.; Russell, T.; Kellogg, G.; Mayes, A.; Gallagher, P.; Satija, S. *Phys. Rev. Lett.* **1994**, *72*, 2899–2902.

[192] Cheng, J. Y.; Zhang, F.; Chuang, V. P.; Mayes, A. M.; Ross, C. A. *Nano Lett.* **2006**, *6*, 2099–2103.

[193] Matsen, M. W.; Bates, F. S. *Macromolecules* **1996**, *29*, 1091–1098.

[194] Hardy, C. G.; Tang, C. *J. Polym. Sci. Part B Polym. Phys.* **2013**, *51*, 2–15.

[195] Tang, C.; Bang, J.; Stein, G. E. *Macromolecules* **2008**, *41*, 4328–4339.

[196] Son, J. G.; Gwyther, J.; Chang, J.-B.; Berggren, K. K.; Manners, I.; Ross, C. A. *Nano Lett.* **2011**, *11*, 2849–2855.

[197] Bosworth, J. K.; Black, C. T.; Ober, C. K. *ACS Nano* **2009**, *3*, 1761–1766.

[198] Son, J. G.; Chang, J.-B.; Berggren, K. K.; Ross, C. A. *Nano Lett.* **2011**, *11*, 5079–5084.

[199] Tsori, Y.; Andelman, D. *Eur. Phys. J. E* **2001**, *5*, 605–614.

[200] Jung, Y. S.; Jung, W.; Ross, C. A. *Nano Lett.* **2008**, *8*, 2975–2981.

[201] Chang, J.-B.; Choi, H. K.; Hannon, A. F.; Alexander-Katz, A.; Ross, C. A.; Berggren, K. K. *Nat. Commun.* **2014**, *5*, 3305.

[202] Liu, G.; Thomas, C. S.; Craig, G. S. W.; Nealey, P. F. *Adv. Funct. Mater.* **2010**, *20*, 1251–1257.

[203] Torquato, S. *Soft Matter* **2009**, *5*, 1157–1173.

[204] Cohn, H.; Kumar, A. *Proc. Natl. Acad. Sci. U. S. A.* **2009**, *106*, 9570–9575.

[205] Seino, Y.; Yonemitsu, H.; Sato, H.; Kanno, M.; Kato, H.; Kobayashi, K.; Kawanishi, A.; Azuma, T.; Muramatsu, M.; Nagahara, S.; Kitano, T.; Toshima, T. *Proc. SPIE* **2012**, *8323*, 83230Y.

[206] Hinsberg, W.; Cheng, J.; Kim, H.-C.; Sanders, D. P. *Proc. SPIE* **2010**, *7637*, 76370G.

[207] Qin, J.; Khaira, G. S.; Su, Y. R.; Garner, G. P.; Miskin, M.; Jaeger, H. M.; de Pablo, J. J. *Soft Matter* **2013**, *9*, 11467–11472.

[208] Darling, S. B. *Prog. Polym. Sci.* **2007**, *32*, 1152–1204.

[209] Koo, K.; Ahn, H.; Kim, S.-W.; Ryu, D. Y.; Russell, T. P. *Soft Matter* **2013**, *9*, 9059–9071.

[210] Yu, B.; Sun, P.; Chen, T.; Jin, Q.; Ding, D.; Li, B.; Shi, A.-C. *J. Chem. Phys.* **2007**, *126*, 204903.

[211] Segalman R.A. *Mater. Sci. Eng. R Reports* **2005**, *48*, 191–226.

[212] Park, C.; Yoon, J.; Thomas, E. L. *Polymer* **2003**, *44*, 6725–6760.

[213] Reilly, M.; Ginzburg, V.; Smith, M. D. *Proc. SPIE* **2013**, *8682*, 86820G.

[214] Yi, H.; Latypov, A.; Wong, H.-S. P. *Proc. SPIE* **2013**, *8680*, 86801L.

[215] Yi, H.; Bao, X.-Y.; Tiberio, R.; Wong, H.-S. P. *Proc. SPIE* **2013**, *8680*, 868010.

[216] Laachi, N.; Delaney, K. T.; Kim, B.; Hur, S.-M.; Bristol, R.; Shykind, D.; Weinheimer, C. J.; Fredrickson, G. H. *Proc. SPIE* **2013**, *8680*, 868014.

[217] Chen, P.; Liang, H.; Xia, R.; Qian, J.; Feng, X. *Macromolecules* **2013**, *46*, 922–926.

[218] Xie, N.; Li, W.; Qiu, F.; Shi, A.-C. *Soft Matter* **2013**, *9*, 536–542.

[219] Takahashi, H.; Laachi, N.; Hur, S.-M.; Weinheimer, C. J.; Shykind, D.; Fredrickson, G. H. *Proc. SPIE* **2012**, *8323*, 83231N.

[220] Kriksin, Y. A.; Neratova, I. V.; Khalatur, P. G.; Khokhlov, A. R. *Chem. Phys. Lett.* **2010**, *492*, 103–108.

[221] Mishra, V.; Fredrickson, G. H.; Kramer, E. J. *ACS Nano* **2012**, *6*, 2629–2641.

[222] Hur, S.-M.; García-Cervera, C. J.; Kramer, E. J.; Fredrickson, G. H. *Macromolecules* **2009**, *42*, 5861–5872.

[223] Alexander-Katz, A.; Moreira, A. G.; Fredrickson, G. H. *J. Chem. Phys.* **2003**, *118*, 9030–9036.

[224] Gotrik, K. W.; Ross, C. A. *Nano Lett.* **2013**, *13*, 5117–5122.

[225] Tang, P.; Qiu, F.; Zhang, H.; Yang, Y. *Phys. Rev. E. Stat. Nonlin. Soft Matter Phys.* **2004**, *69*, 031803.

[226] Drolet, F.; Fredrickson, G. *Phys. Rev. Lett.* **1999**, *83*, 4317–4320.

[227] Son, J. G.; Gwyther, J.; Chang, J.-B.; Berggren, K. K.; Manners, I.; Ross, C. A. *Nano Lett.* **2011**, *11*, 2849–2855.

[228] Choi, H. K.; Gwyther, J.; Manners, I.; Ross, C. A. *ACS Nano* **2012**, *6*, 8342–8348.

[229] Kim, Y.; Chen, H.; Alexander-Katz, A. *Soft Matter* **2014**, *10*, 3284–3291.

[230] Koski, J.; Chao, H.; Riggleman, R. A. *J. Chem. Phys.* **2013**, *139*, 244911.

[231] Ginzburg, V. V. *Macromolecules* **2013**, *46*, 9798–9805.

[232] Sunday, D. F.; Hammond, M. R.; Wang, C.; Wu, W.; Kline, R. J.; Stein, G. E. *J. Micro/Nanolithography, MEMS, MOEMS* **2013**, *12*, 031103.

[233] Gotrik, K. W.; Lam, T.; Hannon, A. F.; Bai, W.; Alexander-Katz, A.; Liddle, J.; Ross, C. A. *Unpublished*.